

Computational Modelling of Solid Propellants

Micro-Structural Analysis and Homogenization

Andrés Daniel Yépez Calderón

Computational Modelling of Solid Propellants

Micro-Structural Analysis and Homogenization

by

Andrés Daniel Yépez Calderón

to obtain the degree of Master of Science
at the Delft University of Technology,
to be defended publicly on Wednesday May 26, 2021 at 15:00.

Student number: 4803396
Project duration: January 15, 2020 – May 26, 2021
Thesis committee: Prof. dr. ir. L. J. Sluys, TU Delft, Chair
Ir. A. H. Lasschuit, TU Delft, Daily supervisor
Dr. Ir. B. Šavija, TU Delft, Supervisor
Dr. Ir. J. Weerheijm, TNO, Supervisor

An electronic version of this thesis is available at <http://repository.tudelft.nl/>.

Preface

I would like to express my gratitude to the people who helped me during my thesis.

Mom and dad, thank you for believing in me even when I was not able to do it myself. This thesis would have not been possible without your loving and enduring support. I am forever grateful.

Ingrid, thank you for bringing good days to this tough period. You brought happiness to my life even when I was in constant distress by what seemed an unending thesis.

Marco, Jorge, Sebastian and all my other friends of TUD, thank you for the good times. You greatly contributed in making this masters a memorable experience.

I extend my gratitude to the members of my thesis committee for their supervision. Especially to Bram, who provided valuable guidance and detailed comments on this report.

*Andrés Daniel Yépez Calderón
Delft, May 2021*

Abstract

Energetic materials have widespread applicability in various fields of engineering as propellants, explosives, and pyrotechnics. The Netherlands Organisation for Applied Scientific Research (TNO) is investigating additive manufacturing of solid propellants. As part of this investigation, TNO developed a new polymer binder mix for solid propellants. The thermomechanical behavior of the solid propellants is not well understood yet. Therefore, TNO is interested in developing computational modelling schemes for characterizing their behavior. Computational schemes based on the finite element method (FEM) are developed in this thesis. They are calibrated with matrix-only and solid propellant uniaxial tension experiments provided by TNO (Figs. 1.4 and 1.5). The developed schemes are compared with the experiments to better understand the materials behavior and improve the computational models.

The macro-structural behavior of solid propellants is significantly affected by the behavior of the micro-structure. It is computationally unfeasible to directly consider the micro-structure in macro-structural FEM. Therefore, computational homogenization (CH) is employed for idealizing the micro-structure with representative volume elements (RVEs) at a finite number of macroscopic locations. Micro-structural behavior consists of numerous nonlinear thermomechanical processes. This thesis focuses in characterizing micro-structural matrix viscoelasticity, continuum matrix damage, and debonding. The brittle and rate dependent behavior of the matrix and the solid propellants is described with these thermomechanical processes. Other relevant processes such as temperature effects, nonlinear elasticity, anisotropy, and large strains are not considered.

The experiments exhibit a clear rate dependence throughout the entire loading process, and viscoelasticity is hypothesized to play a major role in this dependence. The matrix is idealized as isotropic and linear viscoelastic (LVE), even though the experiments exhibit anisotropic and state dependent behavior. The Generalised Maxwell model is employed for viscoelasticity, and parameters thereof are identified with nonlinear least squares fitting. The fitted matrix-only experiment is accurately approximated with the Generalised Maxwell model. However, the identified parameters approximate matrix-only experiments with different strain rates with less accuracy. Loss of accuracy occurs because of discrepancies between the experimental samples and because of the isotropy and LVE simplifications.

The experimental samples experience a brittle failure that is believed to be caused by matrix micro-crack damage. Lee's and Shin's continuum damage model for brittle particulate composites [20] is identified as a promising model for investigating the brittle nature of the matrix and the solid propellants. This model uses mathematical homogenization (MH) to describe particulate composites, but can also be used to describe the matrix-only. However, the model assumes physical constraints that are not valid for either the matrix or the solid propellants, and suffers from numerically unstable behavior. Two modified versions of the model, which relax the constraints and improve numerical stability, are proposed for modelling matrix damage in the matrix-only and in perfectly bonded solid propellants. One describes non-viscous damage and the other describes viscoelastic damage by applying the Generalised Maxwell model. The models assume that damage evolution is caused by micro-crack nucleation and growth. Both modified models are rate dependent, preventing loss of ellipticity. Because of experimental limitations, the parameters for crack nucleation and crack growth for negative hydrostatic stresses can not be identified. Crack growth is more relevant than crack nucleation for brittle damage, therefore the tensile behavior of the matrix can still be characterized. The fitted matrix-only experiment is accurately approximated with the modified viscoelastic damage model. However, the identified parameters approximate matrix-only experiments with different strain rates with less accuracy. Loss of accuracy occurs for the same reasons as for the viscoelasticity approximation and as a consequence of the technique employed for reducing numerical instabilities.

Particle debonding is observed in the failure planes of the solid propellants (Fig. 1.1), and is hypothesized to significantly affect their behavior. The Turon model [30] is employed for debonding by placing interface elements with a bilinear traction separation law (TSL) in the matrix-particle interfaces. A bilinear TSL is believed to be appropriate because the experiments suggest that interfacial softening can be approximated as constantly decreasing, provided that the matrix is appropriately modelled. It is shown that the Turon model can capture free surface propagation in RVEs only for heavily refined

meshes. Fine meshes are not feasible within a CH context, so free surface propagation is generally not captured. Early numerical nonconvergence was generally observed for physically reasonable debonding parameters. Therefore, debonding parameters that do not represent the solid propellants are employed in RVE simulations.

The micro-structure of the solid propellants is investigated by simulating several RVE geometries with different combinations of constitutive models. The effects of particular thermomechanical processes and microscopic geometric components can therefore be determined. The CH investigation of the macro-structure also considers different combinations of constitutive models and RVE geometries. Within a CH context physically representative debonding parameters can be used without causing early nonconvergence. The fitted solid propellant experiment is well approximated with the full CH damage-debonding-viscoelastic computational scheme. The approximation is not as accurate as the matrix-only approximation obtained with the damage-viscoelastic scheme, but is good considering the simplifications and scope of this thesis, and that free surface propagation is not well captured.

Matrix-only and solid propellant computational results confirm that viscoelasticity is a major source of rate dependence and that (continuum) matrix micro-crack damage causes brittle failure. They also suggest that continuum matrix damage is a significant source of rate dependence in the post-damage regime, and matrix-only experiments agree. Comparing the results for perfectly bonded solid propellants to the results for solid propellants with debonding and to the solid propellant experiments, it is clear that debonding indeed has a large effect in reducing the ultimate strength of the material. The full CH damage-debonding-viscoelastic scheme shows promise as a first step towards full characterization. Future work can improve the scheme by addressing the issue of free surface propagation and can build on it by including relevant thermomechanical processes that are not yet implemented. Recommendations on how to achieve this are given in the final chapter.

Contents

List of Figures	ix
List of Tables	xv
1 Introduction	1
1.1 General Overview	1
1.2 Aim of Research	2
1.3 Research Methodology	2
1.4 Thesis Overview	4
2 Literature Review	5
2.1 The Finite Element Method	5
2.2 Viscoelasticity	6
2.3 Continuum Damage	7
2.4 Cohesive Surface Modelling	8
2.5 Homogenization	9
3 Linear Elasticity and Linear Viscoelasticity in the Matrix	13
3.1 Theoretical Background	14
3.1.1 Linear Elasticity	14
3.1.2 The Generalised Maxwell Model	14
3.2 Elastic Behavior	15
3.3 Viscoelastic Behavior	18
3.4 Conclusion	22
4 Damage in the Matrix and in Perfectly Bonded Solid Propellants	23
4.1 Particle Reinforced Brittle Composite Model	24
4.1.1 Constitutive Behavior	24
4.1.2 Damage Evolution: Nucleation and Growth of Micro-Cracks	27
4.1.3 Finite Element Implementation and Extension to Viscoelasticity	28
4.2 Numerical Comparison	31
4.3 Non-Viscous Damage of the Matrix	33
4.3.1 Tension	34
4.3.2 Compression	39
4.3.3 Shear	41
4.3.4 Effects of Inclusion of Particles	42
4.3.5 Effect of Time Discretization	43
4.3.6 Effect of Mesh Discretization	49
4.4 Viscoelastic Damage of the Matrix	50
4.4.1 Behavior of the Matrix and Parameter Identification	50
4.4.2 Viscoelastic vs. Non-Viscous Damage for Matrix Characterization	55
4.4.3 Behavior of Perfectly Bonded Solid Propellants	55
4.5 Conclusion	56
5 Micro-Structural Behavior and Debonding in the RVE	59
5.1 Theoretical Background	60
5.1.1 The Turon Model for Interface Elements	60
5.1.2 Finite Element Formulation of Interface Elements	62

5.2	Linear Elastic Behavior	62
5.3	Damage-Viscoelastic Behavior	68
5.4	Debonding Behavior	76
5.4.1	Behavior of the Debonding Model	76
5.4.2	Mesh Refinement, Particle Size, and Particle Distribution	87
5.5	Damage-Debonding-Viscoelastic Behavior	96
5.6	Conclusion	104
6	Macro-Structural Behavior and Debonding in the Experimental Samples	105
6.1	First-Order Computational Homogenization	106
6.2	Linear Elastic Behavior	107
6.3	Behavior of the Debonding Model and Parameter Identification	112
6.4	Damage-Viscoelastic, Debonding, and Combined Damage-Debonding-Viscoelastic Behaviors	116
6.5	Conclusion	117
7	Conclusion and Recommendations	119
7.1	Conclusions	119
7.2	Recommendations	122
7.2.1	Constitutive Modelling within the Numerical Schemes Employed	122
7.2.2	Numerical Schemes and Related Constitutive Modelling	124
A	Numerical Comparison Results	127
B	Effect of Turon Model Parameters on Composites with Matrix Damage	129
B.1	Effect on the Micro-Structure	129
B.2	Effect on the Macro-Structure	138
C	Computational Homogenization Analyses Results	141
C.1	Damage-Viscoelastic Behavior	141
C.2	Debonding Behavior	144
C.3	Damage-Debonding-Viscoelastic Behavior	146
D	RVE Meshes	149
	Bibliography	157

List of Figures

1.1	Failure plane in TNO's solid propellant	2
1.2	Thrust function for different solid propellant geometries	2
1.3	Macroscopic BCs and dimensions: general	3
1.4	Matrix-only experiments	3
1.5	Solid propellants experiments	3
2.1	2D FE mesh	6
2.2	Full NR procedure	6
2.3	Loading-unloading viscoelastic behavior	7
2.4	Localization band formed by loss of ellipticity	8
2.5	Intrinsic and extrinsic TSLs	9
2.6	Four-noded interface element	9
2.7	Deformed RVEs in the micro-structure	10
3.1	Meshes utilized for elastic and viscoelastic simulations	13
3.2	BCs and dimensions: elasticity and viscoelasticity	14
3.3	Maxwell chain	15
3.4	Experimental responses and linear elastic simulations	17
3.5	Linear elastic stress fields	17
3.6	Single- and multi-element mesh viscoelastic approximations	19
3.7	Brittle case viscoelastic approximations	20
3.8	Ductile case viscoelastic approximations	21
3.9	Brittle case vs. ductile case viscoelastic comparison	21
3.10	Viscoelastic stress fields	21
4.1	Meshes utilized for the damage model simulations	23
4.2	BCs and dimensions: matrix damage	24
4.3	Damage model unstable behavior comparison	30
4.4	NR global iterations per time step for different choices of tangent stiffness	30
4.5	Damage model compliance combinations comparison	32
4.6	Stress-strain curve for different values of control parameter β	33
4.7	Stress-strain curve for first- and second-order contributions and $\phi = 0.1$	33
4.8	Response of specimen for different values of control parameter β	34
4.9	Response of brittle specimen for different values of ω_0 , γ , and N_0/V	35
4.10	Response of ductile specimen for different values of ω_0 , γ , and N_0/V	36
4.11	Response of specimen for different values of threshold stress σ_{n0}	37
4.12	Response of specimen for different values of initial rate of nucleation \dot{N}_0	37
4.13	Response of specimen for different values of σ_1	38
4.14	Damage model tension investigation damage fields	38
4.15	Damage model tension investigation stress fields	38
4.16	Response of specimen for different values of cohesive stress σ_0	39
4.17	Response of specimen for different values of friction coefficient μ	39
4.18	Compression response of specimen for different values of threshold crack density ω_{n0}	40
4.19	Damage model compression investigation damage fields. Brittle case and varying ω_{n0}	40
4.20	Damage model compression investigation damage fields. Ductile case and varying ω_{n0}	41
4.21	Shear response of specimen for different values of threshold crack density ω_{n0}	41
4.22	Damage model compression investigation damage fields. Brittle case and varying ω_{n0}	42
4.23	Damage model compression investigation stress fields	42
4.24	Response of specimen for different values of particle volume fraction ϕ without damage	43

4.25	Response of specimen for different values of particle volume fraction ϕ with damage . . .	43
4.26	Manipulation of strain rate with Δt and β comparison	44
4.27	Unstable response from manipulating strain rate with Δt and β comparison	45
4.28	Response of RVE for different strain rates	46
4.29	Damage fields for simulations of Fig.4.28	46
4.30	Modified damage model and phenomenological model comparison	47
4.31	Convergence to quasi-static loading for a single-element mesh	47
4.32	Rate dependence observed by Lee and Simunovic [21] for a single-element mesh	48
4.33	Response of RVE for different mesh refinements	49
4.34	Response for different meshes when N_0/V depends on element size	50
4.35	Damage fields for Mesh 3 when N_0/V depends on element size	50
4.36	Tension response of matrix for set 1 parameters and different strain rates	52
4.37	Tension response of matrix for set 2 parameters and different strain rates	53
4.38	Tension response of matrix for both sets of parameters and different strain rates	53
4.39	Matrix damage field for tension response. Set 1 parameters	53
4.40	Matrix damage field for tension response. Set 2 parameters	54
4.41	Compression response of matrix. Same response for both sets of parameters	54
4.42	Shear response of matrix for both sets of parameters and different strain rates	54
4.43	Response of perfectly bonded solid propellant for both sets of parameters and different strain rates	56
4.44	Perfectly bonded solid propellant damage field for both sets of parameters	56
5.1	BCs applied to the RVEs	60
5.2	Bilinear TSL proposed in Turon [30]	60
5.3	Micro: effect of mesh refinement. Linear elastic case	63
5.4	Stress and strain fields for RVE with normally distributed particle size. Linear elastic case, tension BCs, and varying mesh refinement	64
5.5	Micro: effect of particle distribution and Df for RVEs with uniformly distributed particle size. Linear elastic case	64
5.6	Micro: effect of particle distribution and Df for RVEs with normally distributed particle size. Linear elastic case	65
5.7	Micro: effect of $nfx1$ for RVEs with uniformly distributed particle size. Linear elastic case	65
5.8	Micro: effect of $nfx1$ for RVEs with normally distributed particle size. Linear elastic case	66
5.9	Stress fields for RVE with uniformly distributed particle size. Linear elastic case, tension BCs, and varying $nfx1$	66
5.10	Stress fields for RVE with uniformly distributed particle size. Linear elastic case, shear BCs, and varying $nfx1$	67
5.11	Micro: effect of mesh refinement. Damage-viscoelastic case	68
5.12	Stress and damage fields for RVE with normally distributed particle size. Damage-viscoelastic case, tension BCs, and varying mesh refinement	69
5.13	Micro: effect of particle distribution and Df for RVEs with uniformly distributed particle size. Damage-viscoelastic case	70
5.14	Micro: effect of particle distribution and Df for RVEs with normally distributed particle size. Damage-viscoelastic case	71
5.15	Micro: effect of $nfx1$ for RVEs with uniformly distributed particle size. Damage-viscoelastic case	72
5.16	Micro: effect of $nfx1$ for RVEs with normally distributed particle size. Damage-viscoelastic case	73
5.17	Damage fields for RVE with uniformly distributed particle size. Damage-viscoelastic case and varying $nfx1$	74
5.18	Damage fields for RVE with normally distributed particle size. Damage-viscoelastic case and varying $nfx1$	75
5.19	Stress-strain response and stress fields. Debonding damage regimes	77
5.20	Response of RVE for different values of mode I energy G_{Ic} . Debonding case	78
5.21	Response of RVE for different values of mode II energy G_{IIc} . Debonding case	79

5.22 Response of RVE for different values of mode I and mode II energies G_{Ic} and G_{IIc} . Debonding case	80
5.23 Response of RVE for different values of mode I strength τ_I . Debonding case	81
5.24 Response of RVE for different values of mode II strength τ_{II} . Debonding case	82
5.25 Response of RVE for different values of experimental parameter η when both strengths and both energies are equal to each other. Debonding case	83
5.26 Response of RVE for different values of experimental parameter η when both strengths are equal to each other but the energies are different. Debonding case	84
5.27 Response of RVE for different values of experimental parameter η when both energies are equal to each other but the strengths are different. Debonding case	85
5.28 Response of RVE for different values of dummy stiffness K . Debonding case	86
5.29 Micro: effect of mesh refinement. Debonding case	87
5.30 Stress and strain fields for RVE with normally distributed particle size. Debonding case, tension BCs, and varying mesh refinement	89
5.31 Micro: effect of particle distribution and Df for RVEs with uniformly distributed particle size. Debonding case	90
5.32 Micro: effect of particle distribution and Df for RVEs with normally distributed particle size. Debonding case	91
5.33 Micro: effect of $nfx1$ for RVEs with uniformly distributed particle size. Debonding case .	92
5.34 Micro: effect of $nfx1$ for RVEs with normally distributed particle size. Debonding case .	93
5.35 Stress fields for RVE with uniformly distributed particle size. Debonding case, tension BCs, and varying $nfx1$	94
5.36 Stress fields for RVE with normally distributed particle size. Debonding case, tension BCs, and varying $nfx1$	95
5.37 Micro: effect of mesh refinement. Damage-debonding-viscoelastic elastic case	96
5.38 Stress and damage fields for RVE with normally distributed particle size. Damage-debonding-viscoelastic case, tension BCs, and varying mesh refinement	97
5.39 Micro: effect of particle distribution and Df for RVEs with uniformly distributed particle size. Damage-debonding-viscoelastic case	98
5.40 Micro: effect of particle distribution and Df for RVEs with normally distributed particle size. Damage-debonding-viscoelastic case	99
5.41 Micro: effect of $nfx1$ for RVEs with uniformly distributed particle size. Damage-debonding-viscoelastic case	100
5.42 Micro: effect of $nfx1$ for RVEs with normally distributed particle size. Damage-debonding-viscoelastic case	101
5.43 Damage fields for RVE with uniformly distributed particle size. Damage-debonding-viscoelastic case and varying $nfx1$	102
5.44 Damage fields for RVE with normally distributed particle size. Damage-debonding-viscoelastic case and varying $nfx1$	103
6.1 Macroscopic meshes utilized for CH simulations	106
6.2 Macroscopic BCs and dimensions: CH	106
6.3 RVE subjected to periodic BCs	107
6.4 Macro: effect of mesh refinement. Linear elastic case	109
6.5 Macroscopic stress fields for RVE with normally distributed particle size. Linear elastic case and varying mesh refinement	110
6.6 Effect of mesh refinement when MH is utilized. Linear elastic case	110
6.7 Stress fields when MH is utilized. Linear elastic case and varying mesh refinement . . .	110
6.8 Macro: effect of particle distribution and Df . Linear elastic case	110
6.9 Macro: effect of $nfx1$. Linear elastic case	111
6.10 Response of macro specimen for different values of the critical energy release rates. Debonding case	113
6.11 Response of macro specimen for different values of the cohesive strengths. Debonding case	114
6.12 Response of macro specimen for different values of dummy stiffness K . Debonding case	114

6.13	Response of macro specimen for different values of the experimental parameter η . Debonding case	115
6.14	Computational approximation to the experiment for the identified debonding parameters	115
6.15	Comparison between CH results with varying $nfx1$ and MH results. Perfectly bonded solid propellants	116
6.16	Macroscopic response of solid propellants. CH damage-debonding-viscoelastic scheme and varying strain rate	117
A.1	First-order-only compliances and combination of first-order and second-order compliances for $\phi = 0.1$ and $\phi = 0.3$	127
A.2	Stress-strain response of element for first- and second-order contributions.	128
A.3	Response of element for different values of particle volume fraction ϕ	128
A.4	Response of element for different values of control parameter β	128
A.5	Response of element for different values of initial crack density ω_0	128
B.1	Response of RVE for different values of mode I energy G_{Ic} . Damage-debonding-viscoelastic case	129
B.2	Response of RVE for different values of mode II energy G_{IIc} . Damage-debonding-viscoelastic case	130
B.3	Response of RVE for different values of mode I and mode II energies G_{Ic} and G_{IIc} . Damage-debonding-viscoelastic case	131
B.4	Response of RVE for different values of mode I strength τ_I . Damage-debonding-viscoelastic case	132
B.5	Response of RVE for different values of mode II strength τ_{II} . Damage-debonding-viscoelastic case	133
B.6	Response of RVE for different values of experimental parameter η . Damage-debonding-viscoelastic case	134
B.7	Response of RVE for different values of experimental parameter η when both energies are equal to each other but the strengths are different. Damage-debonding-viscoelastic case	135
B.8	Response of RVE for different values of experimental parameter η when both strengths are equal to each other but the energies are different. Damage-debonding-viscoelastic case	136
B.9	Response of RVE for different values of dummy stiffness K . Damage-debonding-viscoelastic case	137
B.10	Response of macro specimen for different values of the critical energy release rates. Damage-debonding-viscoelastic case	138
B.11	Response of macro specimen for different values of dummy stiffness K . Damage-debonding-viscoelastic case	139
B.12	Response of macro specimen for different values of the cohesive strengths. Damage-debonding-viscoelastic case	139
B.13	Response of macro specimen for different values of the experimental parameter η . Damage-debonding-viscoelastic case	140
C.1	Macro: effect of mesh refinement. Damage-viscoelastic case	141
C.2	Macroscopic stress fields for RVE with normally distributed particle size. Damage-viscoelastic case and varying mesh refinement	142
C.3	Macro: effect of particle distribution and Df . Damage-viscoelastic case	142
C.4	Macro: effect of $nfx1$. Damage-viscoelastic case	143
C.5	Macro: effect of mesh refinement. Debonding case	144
C.6	Macroscopic stress fields for RVE with normally distributed particle size. Debonding case and varying mesh refinement	144
C.7	Macro: effect of particle distribution and Df . Debonding case	145
C.8	Macro: effect of $nfx1$. Debonding case	145
C.9	Macro: effect of mesh refinement. Damage-debonding-viscoelastic case	146
C.10	Macroscopic stress fields for RVE with normally distributed particle size. Damage-debonding-viscoelastic case and varying mesh refinement	146

C.11 Macro: effect of particle distribution and Df . Damage-debonding-viscoelastic case . . .	147
C.12 Macro: effect of nf_x1 . Damage-debonding-viscoelastic case	147
D.1 RVE with ID 0,10,50	150
D.2 RVE with ID 0,20,50	150
D.3 RVE with ID 0,30,10	150
D.4 RVE with ID 0,30,20	150
D.5 RVE with ID 0,30,30	151
D.6 RVE with ID 0,30,40	151
D.7 RVE with ID 0,30,50	151
D.8 RVE with ID 0,30,70	151
D.9 RVE with ID 0,30,80	152
D.10 RVE with ID 0,30,90	152
D.11 RVE with ID 0,30,100	152
D.12 RVE with ID 0,40,50	152
D.13 RVE with ID 0,20,20	153
D.14 RVE with ID 1,20,20	153
D.15 RVE with ID 2,20,20	153
D.16 RVE with ID 0,v1,50	154
D.17 RVE with ID 0,v2,10	154
D.18 RVE with ID 0,v2,30	154
D.19 RVE with ID 0,v2,40	154
D.20 RVE with ID 0,v2,50	155
D.21 RVE with ID 0,v2,90	155
D.22 RVE with ID 0,v3,50	155
D.23 RVE with ID 1,v2,50	155
D.24 RVE with ID 2,v2,50	156
D.25 RVE with ID 3,v2,50	156
D.26 RVE with ID 4,v2,50	156

List of Tables

3.1	Elastic properties of TNO's matrix and particles	18
3.2	Viscoelastic parameters for TNO's matrix material	19
4.1	Default damage parameters for damage model investigation	34
4.2	Mesh discretization investigation: Details for Meshes 1, 2, and 3	49
4.3	Damage parameters for TNO's matrix material	51
5.1	Default debonding parameters for micro-structural debonding model investigation	76
6.1	Debonding parameters for TNO's solid propellants	112
D.1	Details of RVE meshes where particle size is uniformly distributed	149
D.2	Details of RVE meshes where particle size is normally distributed	150

Introduction

1.1. General Overview

Energetic materials are a class of material that store chemical energy in their molecular structure. This energy can be released by external stimuli, e.g. mechanical loading, heat or shock [22]. Energetic materials have a wide range of practical applications. They can be used as propellants, explosives, or pyrotechnics [22]. Specific applications of energetic materials include demolition and ground improvement in civil engineering, propelling rockets in aerospace engineering, and military uses such as propelling and detonating bullets.

The Netherlands Organisation for Applied Scientific Research (TNO) is investigating additive manufacturing of solid propellants, an application of energetic materials, using *fused deposition modelling* (FDM), a method for 3D-printing solid objects, to improve control of the material's geometry. The solid propellants are particulate composites with a polymer matrix and stiff explosive crystals. The failure plane of TNO's solid propellant was investigated with an electron microscope, shown in Fig. 1.1. Thrust is generated by solid propellants when the flammable polymer burns, igniting the explosive crystals. The rate at which the propellants burn and create thrust depends on their surface area Fig. 1.2. Controlling the propellant's geometry, therewith the burning surface, is of great importance. The application of FDM motivated TNO to develop a new polymer binder mix for solid propellants.

As a consequence of their applications, solid propellants are often subject to complex loading conditions [4]. Furthermore, the dependence of the thermomechanical behavior of solid propellants on large deformations, strain rate, micro-geometry, and damage in the form of micro-cracks and debonding is not yet well understood. Therefore, this material is often characterized experimentally [4]. A more economical and time efficient alternative is to characterize solid propellants using computational modelling techniques. The behavior of solid propellants is complex because their micro-structural behavior and properties have a significant effect on their macro-structural response. Furthermore, their micro-structural behavior is also complex in its own right. Consequently, past and recent research efforts have been made in developing computational modelling techniques for solid propellants. This thesis investigates the effects and feasibility of utilizing specific modelling techniques and material models for characterizing solid propellants. Computational results are compared to available experimental data of TNO's material.

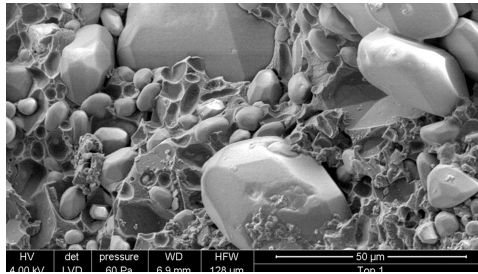


Figure 1.1: Electron microscope image of a failure plane in TNO's solid propellant [19]

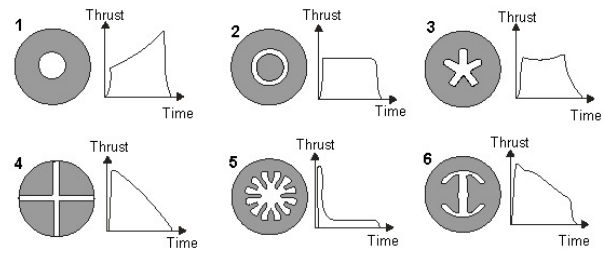


Figure 1.2: Thrust evolution in time for different solid propellant geometries [19]

1.2. Aim of Research

The aim of this research is to identify and test material models and homogenization techniques that are believed to be suitable for modelling solid propellants. Three sources of micro-structural material nonlinearities are investigated: matrix viscoelasticity, continuum damage of the matrix, and debonding of particles from the matrix. The primary focus is to investigate continuum damage. The effects of the manufacturing process (FDM) on the propellants is not in the current focus. The objective and focus of this thesis naturally gives rise to the following research questions:

RQ 1. *What are the effects of viscoelasticity and matrix continuum damage in solid propellants?*

RQ 2. *What is the effect of grain debonding in solid propellants?*

RQ 3. *How can the micro/macro transition of solid propellants be modelled computationally?*

1.3. Research Methodology

Considering the specific behavior of solid propellants, material models for capturing the micro-structure were identified. Namely, the well-known Maxwell model is employed for viscoelasticity, modified versions of the model developed by H.K. Lee and D.K. Shin [20] are proposed for continuum damage, and the model developed by A. Turon et. al [30] is employed for debonding. First-order computational homogenization is used to capture the behavior of the micro-structure in the macro-structural response of the material. The Maxwell model and the modified continuum damage models were implemented in the finite element method program of the Computational Mechanics group of TU Delft using the *Jem/Jive* libraries for C++. The existing implementations of the Turon interface model [30] and of first-order computational homogenization were utilized. Temperature, nonlinear elasticity, anisotropy, and large strains significantly affect the behavior of solid propellants. However, their effects are not investigated in this thesis.

Tension and compression experiments for different strain rates for the matrix-only and for the solid propellant materials were performed by A.H. Lasschuit at TNO. The material samples were fabricated by simply casting them in molds, so FDM was not performed. A.H. Lasschuit produced so-called preliminary and second round material samples, both of which had experimental flaws. Preliminary samples were slightly curved and second round experiments had embedded air bubbles. For most samples, additional experimental errors occurred during the loading process. The experimental load-displacement results obtained from these samples are shown in Fig. 1.4 for the matrix-only and in Fig. 1.5 for the solid propellants. Note that throughout the thesis, total displacements and strains in absolute value are shown in figures. The dimensions of the samples and the applied boundary conditions (BCs), as idealized in this thesis ¹ are shown in Fig. 1.3. The shear BCs weren't applied experimentally, but will be applied computationally.

Throughout the thesis preliminary tension experiments are the main subject of analysis. Preliminary experiments are considered because it is more sensible to characterize slightly curved samples with a homogeneous matrix than samples where the matrix is heterogeneous due to the existence of air bubbles. Tension experiments are considered because they show the effects of matrix and debonding

¹The actual shape of the experimental tension samples was a 'dogbone', not a rectangle. The idealized rectangle corresponds to the thin part of the dogbone.

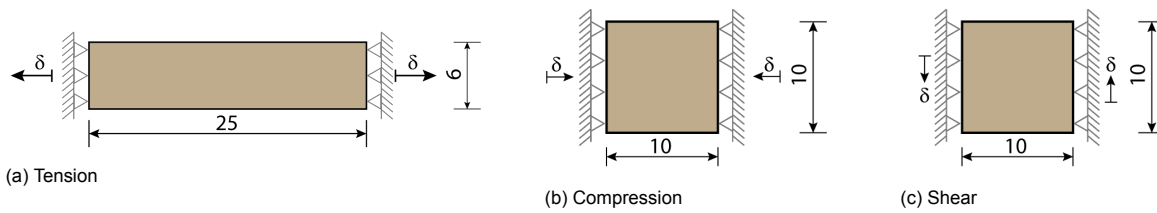


Figure 1.3: Macroscopic BCs and dimensions (dimensions in millimeters). Horizontal reactions are sampled for tension and compression and vertical reaction is sampled for shear

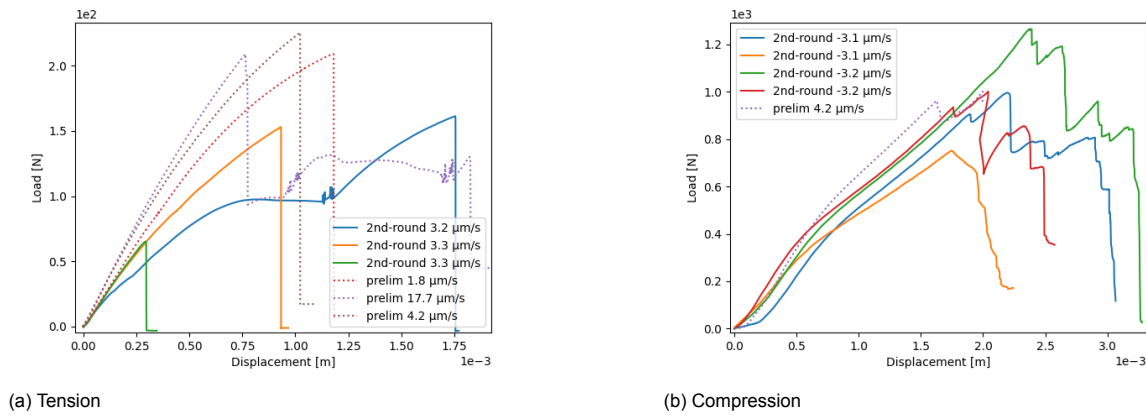


Figure 1.4: Matrix-only experiments

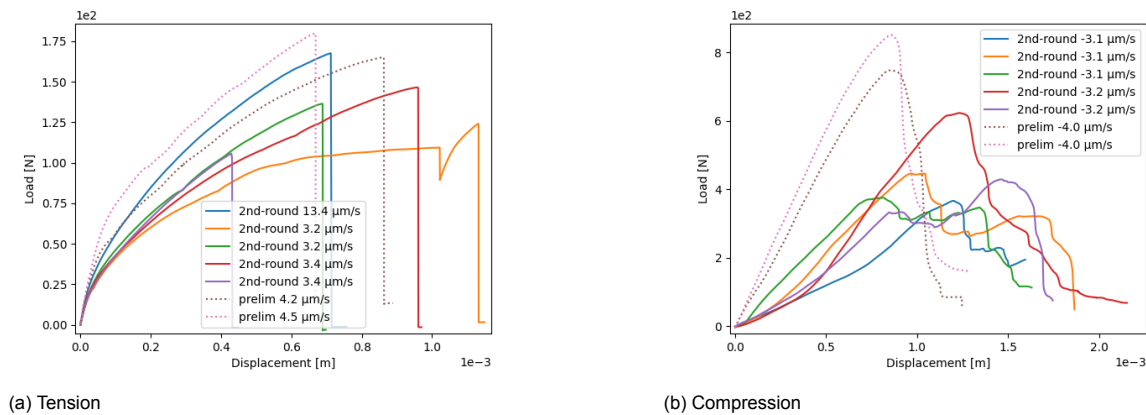


Figure 1.5: Solid propellants experiments

damage better than compression experiments. For compression experiments the samples always failed because they became larger than the load cell, and it is unclear to what extent start-up effects influenced their responses. Start-up effects trigger an initial response that is not characteristic of the actual material behavior and occur due to imperfections of the experimental procedures. Furthermore, the tension and compression behavior of the matrix are significantly different, and this thesis does not focus in characterizing the anisotropic behavior of the solid propellants.

The effects of computational homogenization and the chosen material models are determined by investigating the consequences of varying BCs, geometric configurations, material parameters, and mesh refinement. Furthermore, material parameters that can replicate the experiments are identified. The purpose of this is to determine the extent to which a model, or a combination of models, can reproduce the propellants' behavior. The available TNO experimental data is not sufficient to properly identify any of the additional material parameters introduced for matrix damage [20] or debonding [30], and it is not ideal to identify the parameters introduced by the Maxwell model. All computational analyses in this

thesis performed with multi-element meshes (i.e. meshes consisting of more than one element) were performed utilizing 3-noded triangular finite elements. Computational analyses performed with single-element meshes (i.e. meshes consisting of only one element) were performed with either 4-noded quadrilateral elements or 8-noded hexahedron elements. Infinitesimal strain theory was considered for all cases, and plane strain conditions were considered for all 2D analyses.

1.4. Thesis Overview

The thesis follows the logical order for identifying the parameters that the Maxwell viscoelastic model, the modified versions of the Lee and Shin continuum damage model [20], and the Turon interface model [30] introduce into the computational modelling schemes constructed to analyze solid propellants. Chapter 3 identifies the linear elastic and linear viscoelastic parameters. Chapter 4 explores the behavior of the modified continuum damage models and identifies the damage parameters. Chapters 3 and 4 also analyze the response of the matrix for the parameters identified in them. In Chapter 5, the responses of various RVEs with respect to the viscoelastic, the continuum damage, and the debonding models are explored. This chapter also explores the behavior of the debonding model at the RVE level. In Chapter 6, the responses of the solid propellants for various micro-structures and with respect to the different models are explored using CH. This chapter also explores the behavior of the debonding model at the macro-structural level and then identifies the parameters introduced by said model. Finally, Chapter 7 concludes the findings of the thesis and presents recommendations for further research.

2

Literature Review

This chapter introduces the general theory for concepts and numerical frameworks employed in this thesis. Specific models and frameworks are given as background information in Chapters 3–6, which make use of specialized theory.

2.1. The Finite Element Method

The finite element method (FEM) is a numerical method for solving partial differential equations (PDEs). With this method, the numerical frameworks for the computational modelling schemes are constructed and presented in this thesis. A brief summary of FEM for nonlinear solid mechanics is given here. The expressions given are for the 2D continuum case, but the extension to 3D continuum is straightforward. For a detailed description of the subject the reader is referred to a FEM textbook. For the expressions for interface elements see Section 5.1.2.

In solid mechanics, the quasi-static finite element (FE) continuum formulation arises from first spatially discretizing the so-called weak form of the strong equilibrium equation, which is given by

$$\nabla \cdot \Sigma + \rho \mathbf{g} = \mathbf{0} \quad (2.1)$$

Where $\nabla \cdot$ is the divergence operator, Σ is the second-order stress tensor, ρ is the material density, and \mathbf{g} is the gravity vector.

A spatially discretized 2D solid object, or a *mesh*, is shown in Fig. 2.1. The triangles represent *elements* and the dotted intersections represent *nodes*. The displacement field within a triangular element e with nodal displacements $\mathbf{a}_e = [a_x^1, a_y^1, \dots, a_x^n, a_y^n]^T$ is approximated as

$$\mathbf{u}_e(\mathbf{x}) = \mathbf{N}_e(\mathbf{x})\mathbf{a}_e \quad (2.2)$$

Where the matrix $\mathbf{N}_e(\mathbf{x})$ contains polynomials called shape functions. One shape function is associated to each node. The shape function matrix is given by

$$\mathbf{N}_e(\mathbf{x}) = \begin{bmatrix} N_1 & 0 & N_2 & 0 & \dots & N_n & 0 & 0 \\ 0 & N_1 & 0 & N_2 & \dots & 0 & N_n & 0 \end{bmatrix} \quad (2.3)$$

Kinematic and constitutive relations are introduced to the spatially discretized form to complete the formulation. The kinematic relation that arises from infinitesimal strain theory is

$$\epsilon_e(\mathbf{x}) = \mathbf{B}_e(\mathbf{x})\mathbf{a}_e \quad (2.4)$$

Where $\epsilon_e(\mathbf{x})$ is the strain field in Voigt notation and the kinematic matrix $\mathbf{B}(\mathbf{x})$ is given by

$$\mathbf{B}_e(\mathbf{x}) = \mathbf{L}\mathbf{N}_e \quad (2.5)$$

In which the linear differential operator \mathbf{L} is given by

$$\mathbf{L}^T = \frac{\partial \epsilon_e}{\partial \mathbf{u}_e} = \begin{bmatrix} \frac{\partial}{\partial x} & 0 & \frac{\partial}{\partial y} \\ 0 & \frac{\partial}{\partial y} & \frac{\partial}{\partial x} \end{bmatrix} \quad (2.6)$$

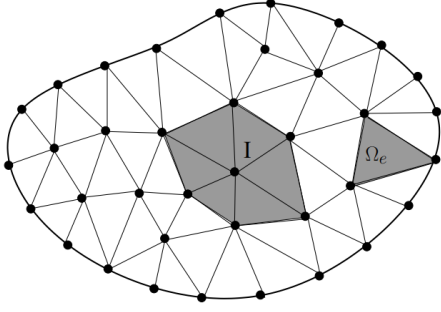


Figure 2.1: 2D FE mesh. Element domain Ω_e and elements that share node I are highlighted [26]

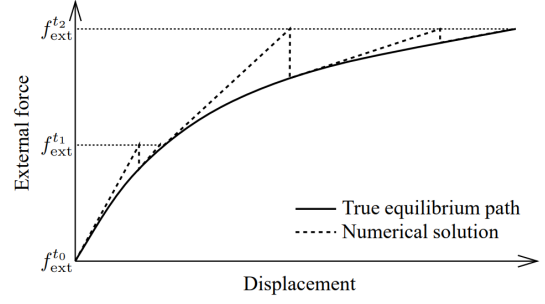


Figure 2.2: Full NR incremental-iterative procedure [10]

The constitutive relation is

$$\mathbf{C}^{tan} = \frac{\partial \sigma_e}{\partial \epsilon_e} \quad (2.7)$$

Where \mathbf{C}^{tan} is the tangent stiffness at a given moment of the loading process and σ_e is the stress field. Both are given in Voigt notation.

For nonlinear problems, the formulation is also discretized in so-called global time steps. These time steps describe the sequence of events of the quasi-static loading process. They do not represent a physical dependence in real time. The response of the solid is linearized within each time step. The FEM continuum formulation for nonlinear problems in solid mechanics is

$$\mathbf{K}\Delta\mathbf{a} = \mathbf{f}_{ext}^{t+\Delta t} - \mathbf{f}_{int}^t \quad (2.8)$$

Where $\Delta\mathbf{a}$ is the global nodal displacement difference between the current time step $t + \Delta t$ and the previous time step t . The internal force vector \mathbf{f}_{int} , the external force vector \mathbf{f}_{ext} , and the global stiffness \mathbf{K} are given by

$$\mathbf{f}_{int} = \sum_{e=1}^{n_e} \mathbf{z}_e^T \left(\int_{\Omega_e} \mathbf{B}_e^T \sigma_e \, d\Omega \right) \quad (2.9)$$

$$\mathbf{f}_{ext} = \sum_{e=1}^{n_e} \mathbf{z}_e^T \left(\int_{\Omega_e} \rho \mathbf{N}_e^T \mathbf{g} \, d\Omega + \int_{\Gamma_e} \mathbf{N}_e^T \mathbf{t} \, d\Gamma \right) \quad (2.10)$$

$$\mathbf{K} = \frac{\partial \mathbf{f}_{int}}{\partial \mathbf{u}} = \sum_{e=1}^{n_e} \mathbf{z}_e^T \left(\int_{\Omega_e} \mathbf{B}_e^T \mathbf{C} \mathbf{B}_e \, d\Omega \right) \mathbf{z}_e \quad (2.11)$$

In which, n_e is the number of elements in the mesh, \mathbf{t} is the external traction, and \mathbf{z}_e is the location matrix that reflects the topology of the discretization [9]. An element's domain is represented by Ω_e and its boundary by Γ_e . Computations are performed at locations within the elements called integration points (IPs), and results are then extrapolated from the IPs to the nodes. Integration is performed numerically with the results from the IPs. Going forward the subscript notation e is dropped for simplicity.

For this formulation, incremental-iterative solution procedures are utilized to avoid drifting¹ of the solution. This thesis uses displacement control and a full Newton-Raphson (NR) procedure for all analyses. The relative magnitude by which the solution is allowed to drift away in each time step is determined by the convergence criteria. An example of a full NR procedure is shown in Fig. 2.2.

2.2. Viscoelasticity

Viscoelasticity is the combination of elasticity and viscosity. It is exhibited when the molecular structure of a material is reordered upon loading. Elasticity describes a direct non-dissipative correspondence between stress and strain. When an elastic material is loaded and then unloaded, it returns to its original undeformed shape following the same load path it took during loading. Viscosity describes a

¹Accumulation of error for each time step

direct dissipative correspondence between stress and strain rate. When a viscous material is loaded and then unloaded, it continues deforming in the loading direction. A material is said to be viscoelastic when it exhibits both elastic and viscous properties.

Similarly to elastic materials, viscoelastic materials recover, at least partially, their original shape after a loading-unloading cycle. However, the loading path and unloading path are different. This means that like viscous processes, viscoelastic processes dissipate energy. Loading-unloading viscoelastic behavior is shown in Fig. 2.3. Viscoelastic properties are temperature-dependent, therefore it is important to account for energy dissipation. Similarly to elastic and viscous materials, viscoelastic materials are strain and strain rate-dependent, respectively. Strain rate dependence is shown in Figures 1.4a and 1.5a of Section 1.3, where stiffer responses are observed for higher strain-rates.

Viscoelasticity is classified as either linear or nonlinear. In linear viscoelasticity (LVE) constitutive behavior is independent of the state of the material, whereas in nonlinear viscoelasticity (NLVE) constitutive behavior depends on state. Essentially, the governing PDE is linear for LVE² and nonlinear for NLVE. LVE obeys the Boltzmann superposition principle, which states that total viscoelastic response can be additively decomposed into a discrete history of relaxation or creep responses. Mathematically, the superposition principle implies the following constitutive relation for the relaxation case

$$\sigma(t) = \mathbf{C}(t)\epsilon(0) + \int_0^t \mathbf{C}(t - \tilde{t}, \tilde{t})\dot{\epsilon}(\tilde{t})d\tilde{t} \quad (2.12)$$

Where $\dot{\epsilon}(\tilde{t})$ is the strain rate, $\mathbf{C}(t - \tilde{t}, \tilde{t})$ is the relaxation function, and the dependence in \tilde{t} accounts for material aging [10]. LVE may be applied for small deformations. However, the degree to which it is applicable depends on each specific material.

Both linear and nonlinear models have been proposed to model the viscoelastic behavior of the polymer matrix. The linear Maxwell model in combination with the time-temperature superposition principle³ were utilized in [4]. Pseudo-strains defined by R.A. Schapery [29] were applied by A. Barua and M. Zhou [15] to employ an LVE relation. A stress softening function was used by S. Ho [12] to capture NLVE effects through means of damage.

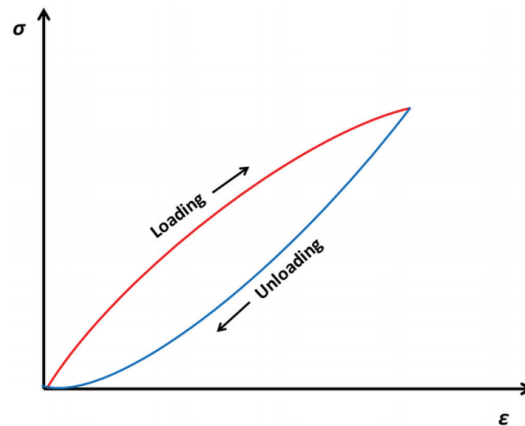


Figure 2.3: Loading-unloading viscoelastic behavior [24]

2.3. Continuum Damage

Damage is the result of bonds breaking at the molecular level. At larger length scales, damage manifests in the form of micro-cracks, macro-cracks, and other forms of degradation. Continuum damage mechanics uses continuous damage variables to characterize local material degradation [28]. In a FEM context, continuum damage represents material degradation in the IPs of regular continuum elements.

Continuum damage models based in a continuum damage mechanics framework may be either phenomenological or based in physics. Phenomenological models are based on empirical assumptions about material behavior and are calibrated experimentally or computationally. These models

²LVE implies nonlinear constitutive relations, so NR procedures are used even for linear PDEs.

³The time-temperature superposition principle states that in LVE viscoelastic properties can be mapped to different temperatures by a change in time scale [4]

are attractive for characterizing materials whose physical response is not fully understood or when experimental data is missing. Phenomenological models are usually easier to implement than physics-based models. Parameters introduced by phenomenological models usually have to be recalibrated for all different conditions where they are applied, because they are not inherent to general material response. Models based in physics are derived from fields such as thermodynamics, micromechanics, and fracture mechanics. They may or may not have empirical aspects, but they are not empirical in their entirety. Physics-based models have the advantage that they prescribe behavior directly related to the physics of the material. Therefore, the material parameters they introduce only need to be experimentally identified once.

Continuum damage models may produce premature crack initiation and instantaneous crack growth when damage becomes highly localized [28]. This is the consequence of the governing PDEs locally changing ellipticity and the damage rate becoming singular once the material is fully degraded, i.e. fractured. These issues arise because damage fields defined by damage variables are assumed to be continuous, but continuum damage models permit damage fields where damage discretely localizes. This leads to mesh sensitivity issues when applied in an FE context, because finer meshes can capture nonphysical discrete damage jumps better [28]. Figure 2.4 shows an example of loss of elasticity. The sample fails prematurely because a so-called localization band forms almost immediately after damage initiation.

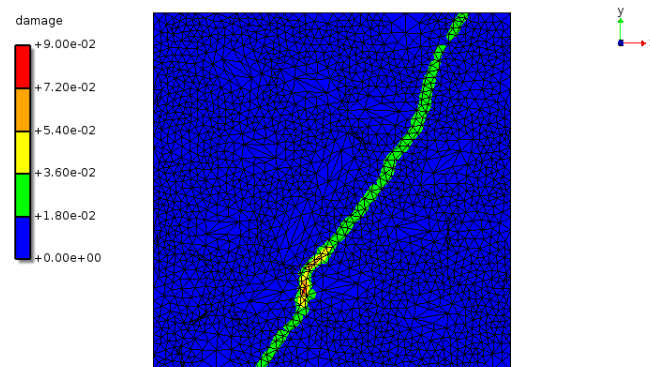


Figure 2.4: Localization band formed by loss of ellipticity

Nonlocal approaches to damage can prevent localization issues by modifying the damage models and/or the governing PDEs. For instance, the nonlocal approach considers a given region rather than a single IP. Another solution to localization is to introduce rate dependence in the constitutive formulation. This can be achieved, for instance, by considering viscoelasticity. Rate dependence stabilizes the rate boundary value problem (BVP). However, this is only the case when it is sufficiently significant [10].

Significant efforts have been made in developing and applying physics-based models to the matrix of solid propellants. Particular attention has been given to models derived from thermodynamics because they can be combined with other phenomena in a straightforward fashion. The strain softening function of Ho's NLVE model [12] is calibrated based on the recoverable strain energy density thermodynamic concept. Thermodynamic damage theory was utilized by X. Jingsheng [15] to formulate a damage-viscoelastic model. A model derived from fracture mechanics and micromechanics that combines brittle matrix damage and the inclusion of perfectly bonded elastic particles was proposed by H.K. Lee and D.K. Shin [20]. A non-viscous and a viscoelastic modified version of this model were applied in Chapter 4. Lee's and Shin's formulation and the non-viscous modified model do not include viscoelasticity, but do introduce rate dependence.

2.4. Cohesive Surface Modelling

Cohesive surface modelling is the application of a cohesive theory of fracture to model discontinuous damage as the formation of free surfaces in a continuum. A cohesive theory of fracture is a phenomenological framework closely related to fracture mechanics [25]. Free surface formation can represent a variety of damage phenomena, such as cracks, debonding, and delamination.

In cohesive surface modelling, the inelastic deformation ahead of the crack tip of newly formed

surfaces is governed by a phenomenological traction separation law (TSL), which relates cohesive force (i.e. traction) to displacement jump [25][26]. Three failure modes can be described by TSL's: normal (mode I), in-plane shear (mode II), and out-of-plane shear (mode III) decohesion. TSL's are formulated as

$$\mathbf{t} = g([\mathbf{u}], \beta) \quad (2.13)$$

Where $[\mathbf{u}]$ is the displacement jump, \mathbf{t} is the cohesive force and β represents the internal variables that account for the irreversibility of the free surface formation process [26]. Internal parameters such as cohesive strengths, energy release rates, and coupling parameters for the failure modes determine the character of the TSL and the state of the internal variables β . These parameters are identified either experimentally or computationally.

In FEM, Eq. (2.13) is usually employed in the rate form $\dot{\mathbf{t}} = \mathbf{T}[\dot{\mathbf{u}}]$ so that the quadratic convergence of the NR procedure is preserved [26]. The tensor \mathbf{T} is called the consistent cohesive tangent and it is formulated as $\mathbf{T} = \frac{\partial \mathbf{t}}{\partial [\mathbf{u}]}$.

There are two types of TSL's: initially elastic (or intrinsic) cohesive laws and initially rigid (or extrinsic) cohesive laws. Fig. 2.5 shows an example of both. Intrinsic laws govern constitutive behavior throughout the whole deformation process. Extrinsic laws are only applied after the failure criterion f_t is reached. A different constitutive law is in place before failure. Intrinsic TSLs require a high initial dummy stiffness prior to failure to avoid free surface formation, which can lead to ill-conditioning of the BVP. Extrinsic laws do not suffer from this shortcoming but their implementation is significantly more complex.

Various methods exist for cohesive surface modelling. Nowadays, XFEM is the most popular method. In XFEM, the displacement field of the solution is enriched with an additional term that generates a displacement jump between one side of a crack relative to the other side. The inclusion of zero-thickness cohesive interface elements (abbreviated as interface elements) is another widely used method. Interface elements are placed between the standard continuum elements of mesh, as shown in Fig. 2.6. This is done 'a priori' of numerical computations. Interface elements are infinitely thin and one dimension lower than the standard continuum elements that they connect [27]. They have a set of duplicate nodes for each of their nodal coordinate. Once failure is initiated, duplicate nodes move apart from each other forming a free surface.

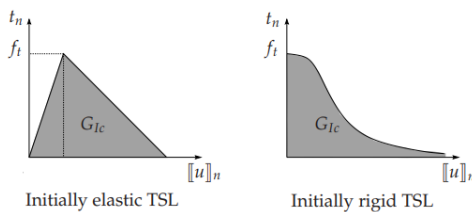


Figure 2.5: A intrinsic TSL (left) and an extrinsic TSL (right) [26]

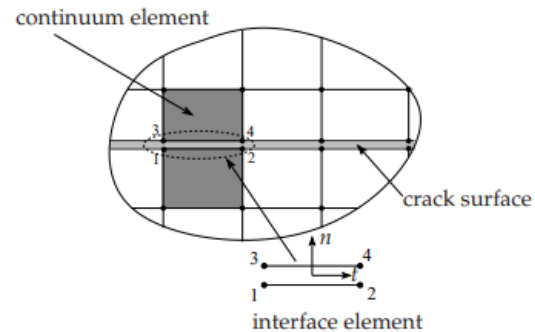


Figure 2.6: Four-noded interface element used to model a crack [26]

Applying interface elements in the matrix-particle interface is the most common method for characterizing debonding in solid propellants. They are conveniently placed in failure planes known 'a priori' and they have the advantage that they are decoupled from the viscoelastic and continuum damage models. Very similar bilinear mixed-mode TSLs were applied by Barua and Zhou [4] and by R. Hu [13] for modelling debonding in solid propellants. In Chapter 5 interface elements with a bilinear TSL, proposed by A. Turon et al [30], are utilized.

2.5. Homogenization

Homogenization methods provide a multiscale framework for capturing the properties and behavior of the micro-structure in the macro-structure. The idea is to construct an equivalent homogeneous macroscopic material based on microscopic heterogeneity. Homogenization theory is based on the

concept of a representative volume element (RVE), the principle of separation of scales, and averaging theorems [26]. An RVE is an idealized microscopic constituent which is assumed to be representative of the geometry and properties of the whole micro-structure. A view of deformed RVEs in the micro-structure is shown in Fig. 2.7. The principle of separation of scales states that the microscopic length scale is much smaller than the characteristic length scale over which the macroscopic loading varies [26]. Averaging theorems, such as the strain and stress averaging theorems, couple the macro- and the micro-structures in an energetically consistent manner [3]. They state that certain quantities can be extrapolated from the micro-structure to the macro-structure by taking their volume average over the undeformed RVE configuration. Mathematically, averaging theorems can be generalized as

$$\mathbf{A}_M = \frac{1}{V} \int_V \mathbf{A}_m dV \quad (2.14)$$

Where \mathbf{A} is the quantity to extrapolate and V is the volume of the undeformed RVE. The superscripts m and M refer to the micro-structure and the macro-structure, respectively.

Micro-structural fields can be additively decomposed in linear and perturbed contributions ⁴. The microscopic displacement field is given by

$$\mathbf{u}_m(\mathbf{x}_m) = \mathbf{E}_M(\mathbf{x}_M) \mathbf{x}_m + \mathbf{u}'_m(\mathbf{x}_m, t) \quad (2.15)$$

and the microscopic strain field is given by

$$\epsilon_m(\mathbf{x}) = \mathbf{S}^{el} \sigma_m(\mathbf{x}) + \epsilon'_m(\mathbf{x}) \quad (2.16)$$

Where \mathbf{E} is the second-order strain tensor, \mathbf{S}^{el} is the elastic compliance, and a prime denotes a perturbed field.

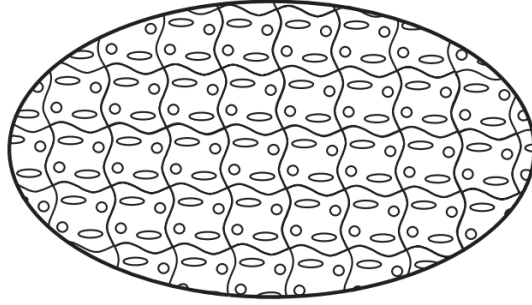


Figure 2.7: Deformed RVEs in the micro-structure [3]

Homogenization methods are divided in three broad categories: mathematical homogenization (MH), numerical homogenization (NH), and computational homogenization (CH). Exact analytical relations are obtained from MH, but they are often subject to many constraining assumptions and to simple geometries [3][26]. In NH, the parameters of a phenomenological effective macro-structural constitutive relation are determined by fitting the data obtained from numerical computations on a representative micro-structural sample (referred as cell or unit-cell in literature) [3][26]. Both choosing the macroscopic phenomenological model and performing the microscopic numerical computations, is done 'a priori' of macroscopic analyses. This is a relatively computationally efficient approach, but when the behavior becomes highly nonlinear the assumed macroscopic model may not be appropriate. In CH, computations on both the macro- and the micro-structure are performed concurrently to obtain the homogenized response and tangent stiffness of the macro-structure at each global time step. This accounts for the evolving state of the micro-structure. Consequently, CH is in general the most precise homogenization method, but also the most computationally demanding.

Homogenization frameworks are necessary to accurately describe materials where the micro-structure has a significant effect on the response of the macro-structure. MH was utilized by Lee and Shi [20] to derive a micromechanical model that accounts for matrix damage and the inclusion of perfectly bonded particles in particulate materials. Another micromechanical MH-based model was proposed by Yang

⁴Perturbed fields account for nonlinearities and heterogeneities in the micro-structure.

et al [36] to model matrix viscoelasticity and matrix-particle debonding for the same type of material. In Chapter 6, CH is utilized to capture micro-structures where viscoelasticity, continuum damage, and debonding are present.

3

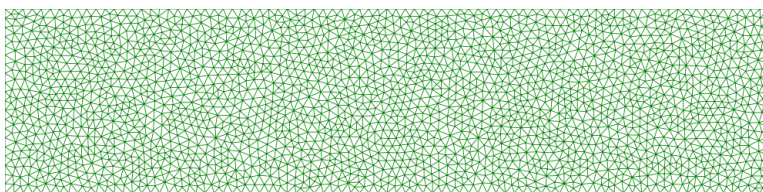
Linear Elasticity and Linear Viscoelasticity in the Matrix

The pre-failure behavior of the matrix material is assumed to be mainly governed by viscoelasticity. The motivation for this assumption is that the material experiences brittle damage, so damage probably initiates close to the ultimate strength. The elastic behaviour is investigated in this chapter; a material is said to behave elastically if it does not dissipate energy when it is subjected to loading. Viscoelasticity is of particular interest as the binder exhibits viscosity. A material exhibits viscosity when the stress depends on the strain and strain-rate. The preliminary tests shown in Fig .1.4 of Section 1.3 are employed for this purpose.

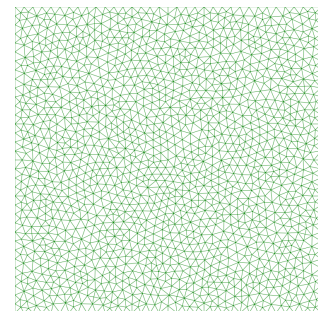
The identification of the (visco-)elastic behavior is done with the experiments performed by A.H. Lasschuit [19]. A Poisson ratio and the Young's modulus are identified from the experiments. These quantities are utilized for identifying the viscoelastic parameters and as inputs for the continuum damage model introduced in Chapter 4. Anisotropy and nonlinear elasticity are not considered because these topics are out of the scope of this thesis. However, their implications in the behavior of the matrix are briefly discussed.

The linear viscoelastic (LVE) Maxwell model is implemented to describe the elastic and viscous matrix behavior. This model captures the viscoelastic tension response reasonably well, and combining it with continuum damage is relatively straightforward.

For the simulations presented in this chapter, BCs and sample dimensions are always as prescribed by Fig. 3.2. The discretizations of the samples are always as prescribed by Fig. 3.1, unless otherwise stated.



(a) Tension mesh. 2310 nodes and 4410 elements



(b) Compression and shear mesh. 1567 nodes and 2996 elements

Figure 3.1: Meshes utilized for elastic and viscoelastic simulations

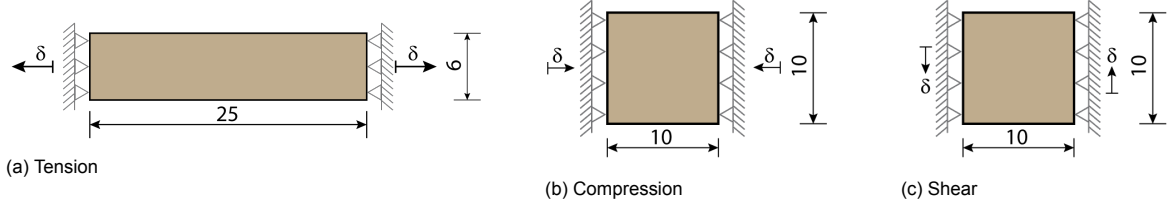


Figure 3.2: BCs and dimensions (dimensions in millimeters). Horizontal reactions are sampled for tension and compression and vertical reaction is sampled for shear

3.1. Theoretical Background

3.1.1. Linear Elasticity

In the theory of infinitesimal linear elasticity, the Cauchy stress tensor and the infinitesimal strain tensor are work-conjugates that define strain energy density. The constitutive relation between stress and strain is defined as linear, so it is characterized by the same tensorial relation for all states of deformation [5]. Consequently, the FEM formulation (2.8) only requires one global load step to solve linear elastic problems for any given loading conditions.

The constitutive equation (2.7) takes the following form in linear elasticity

$$\boldsymbol{\sigma}(\mathbf{x}) = \mathbf{C}^{el} \boldsymbol{\epsilon}(\mathbf{x}) \quad (3.1)$$

Where \mathbf{C}^{el} is the linear elastic stiffness, which is given by

$$\mathbf{C}^{el} = \begin{bmatrix} \lambda + 2\mu & \lambda & \lambda & 0 & 0 & 0 \\ \lambda & \lambda + 2\mu & \lambda & 0 & 0 & 0 \\ \lambda & \lambda & \lambda + 2\mu & 0 & 0 & 0 \\ 0 & 0 & 0 & \mu & 0 & 0 \\ 0 & 0 & 0 & 0 & \mu & 0 \\ 0 & 0 & 0 & 0 & 0 & \mu \end{bmatrix} \quad (3.2)$$

In which the Lamé constants λ and the μ are given by

$$\lambda = \frac{\nu E}{(1 + \nu)(1 - 2\nu)}, \quad \mu = \frac{E}{2(1 + \nu)} \quad (3.3)$$

Where E is the Young's modulus and ν is the Poisson ratio. The Lamé constant μ is the shear modulus, and it governs elastic response under pure deviatoric deformation. The bulk modulus κ governs elastic response under pure dilational deformation, and it is given by

$$\kappa = \frac{E}{3(1 - 2\nu)} \quad (3.4)$$

The linear elastic stiffness can be reduced by assuming plane strain conditions, this refers to a 2D state where there is no out-of-plane strain. The stiffness becomes:

$$\mathbf{C}^{el} = \frac{E}{(1 + \nu)(1 - 2\nu)} \begin{bmatrix} 1 - \nu & \nu & 0 \\ \nu & 1 - \nu & 0 \\ 0 & 0 & 1 - 2\nu \end{bmatrix} \quad (3.5)$$

3.1.2. The Generalised Maxwell Model

The Generalised Maxwell model is one of the most widely utilized LVE models. Its formulation stems from the premise that the viscoelastic response is determined by the system of linear springs and dashpots shown in Fig. 3.3, which is also called a Maxwell chain. This system consists of a spring connected in parallel with N so-called Maxwell elements, which are in-series arrangements of a spring and dashpot. More Maxwell elements can lead to better accuracy, but also to overfitting by numerical fitting methods. Overfitting can compromise the physical significance of viscoelastic parameters.

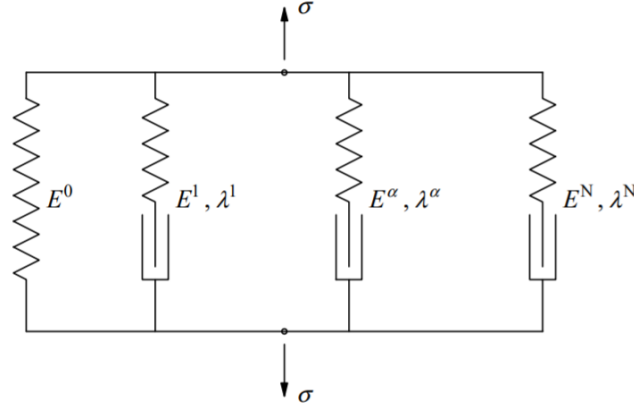


Figure 3.3: Maxwell chain [10].

When material aging is ignored, the Maxwell chain can be mathematically described with the following 1D relaxation function

$$E(t - \tilde{t}) = E^0 + \sum_{\alpha=1}^N E^{\alpha} \exp\left(-\frac{t - \tilde{t}}{\lambda^{\alpha}}\right) \quad (3.6)$$

Where λ^{α} is the relaxation time of a given Maxwell chain. The relaxation time is formulated as $\lambda^{\alpha} = \eta^{\alpha}/E^{\alpha}$, where E^{α} and η^{α} are the Young's modulus and the viscous resistance, respectively, of Maxwell element α . The 3D generalization of the relaxation function is given by

$$\mathbf{C}(t - \tilde{t}) = \bar{\mathbf{C}}E(t - \tilde{t}) \quad (3.7)$$

Where the dimensionless matrix $\bar{\mathbf{C}}$ is given by

$$\bar{\mathbf{C}} = \frac{1}{(1+v)(1-2v)} \begin{bmatrix} 1-v & v & v & 0 & 0 & 0 \\ v & 1-v & v & 0 & 0 & 0 \\ v & v & 1-v & 0 & 0 & 0 \\ 0 & 0 & 0 & \frac{1}{2}-v & 0 & 0 \\ 0 & 0 & 0 & 0 & \frac{1}{2}-v & 0 \\ 0 & 0 & 0 & 0 & 0 & \frac{1}{2}-v \end{bmatrix} \quad (3.8)$$

Introducing the relaxation function described by Eq.(3.7) into the relaxation constitutive relation described by Eq.(2.12) and expanding the result [10], the incremental stress-strain relation of a given IP becomes

$$\Delta\sigma = \bar{\mathbf{C}}E^0\Delta\epsilon + \sum_{\alpha=1}^N \left(1 - \exp\left(-\frac{\Delta t^{max}}{\lambda^{\alpha}}\right)\right) \left(\frac{E^{\alpha}}{\Delta t^{max}/\lambda^{\alpha}} \bar{\mathbf{C}}\Delta\epsilon - \sigma^{\alpha}(t - \Delta t^{max})\right) \quad (3.9)$$

Where $\Delta\sigma$ and $\Delta\epsilon$ are the differences in stress and strain between the current and the previous global time steps, respectively. A time difference parameter Δt^{max} is introduced by the model. This parameter alongside the global time discretization determines the loading rate. More specifically, if the BCs are applied in the form of displacement increments, the loading rate is given by $\dot{\epsilon} = \Delta t/\Delta t^{max}$. Where Δt is the displacement increment applied by the BCs at a given global time step. The loading rate $\dot{\epsilon}$ is usually referred to as the strain rate in this thesis.

3.2. Elastic Behavior

The matrix exhibits significantly different responses in tension and compression—see Fig. 1.4. This is a common macroscopic behavior of polymers which stems from their properties at a molecular level [32].

Polymers are composed of large molecules that form chain-like structures that are very long compared to their cross-sections [6]. These chains form random coils and are highly entangled with each other [32]. Consequently, the mechanical behavior of polymers is not exclusively determined by the molecular composition of the chains, but also by their local arrangements and interactions [5]. For instance, a region of a polymer that is being stretched may behave significantly differently than a region of the same polymer that is being compressed because the chains in these regions may undergo different motions. Furthermore, polymer materials can usually sustain very large deformations. As a consequence, the elastic behavior of polymers at a continuum level are generally anisotropic and nonlinear.

Many nonlinear elasticity continuum models have been proposed to characterize different materials, and various methods of implementing these models in a FEM context have been proposed under the framework of hyperelasticity. Nonlinear elasticity models can characterize the anisotropic and large deformation behavior of polymers. TNO's matrix behaves anisotropically and it can sustain large deformations in compression, but not in tension. Therefore, hyperelastic (or hyperviscoelastic, if viscoelasticity is considered) models should probably be considered for a complete computational characterization of the matrix. Choosing, implementing, and utilizing a hyperelastic model for characterizing a given material is a daunting task. Especially when the behavior of said material at a molecular level is not well understood and experimental data is limited, which is the case for TNO's matrix. This thesis does not focus in characterizing the anisotropic nature of the matrix and tension experiments are the main subject of analysis, so considering the effect of large deformations is not necessary. Therefore, hyperelastic models are not considered and the elastic behavior of the matrix is idealized as isotropic and linear elastic.

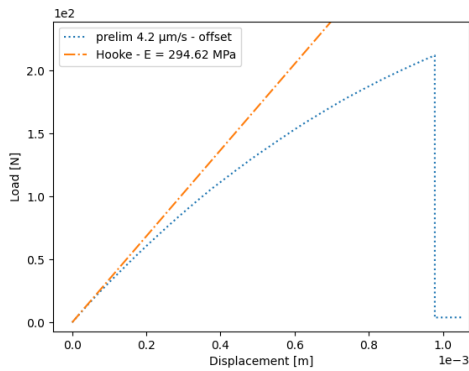
The tension Young's modulus for TNO's matrix material was identified through trial and error, the Young's modulus is $E = 294.62 \text{ MPa}$. This is the Young's modulus utilized throughout the thesis to characterize the idealized isotropic linear elastic behavior. The experiment with $\dot{\epsilon} = 4.2 \mu\text{m/s}$ is chosen for identifying the stiffness because it is the one where least experimental issues were observed. The line obtained from the simulation fitted to the experimental load-displacement curve is shown in Fig. 3.4a, and the corresponding maximum principal stress field is shown in Fig. 3.5a. Note that the experimental result shown is offsetted such that start-up effects (see Section 1.3 for definition) are not shown. That is, the earliest point of the original load-displacement curve where start-up effects are believed to become negligible is taken as the origin of the offsetted curve. Start-up effects are only present in a very short range of the original curve, so they are assumed to have little effect on the state of the experimental sample.

To understand the anisotropic and nonlinear elastic nature of the matrix, the compression experiments (Fig. 1.4b) are briefly discussed. In compression the matrix exhibits two long quasi-linear branches. This implies that the molecular structure of the matrix undergoes different processes during each branch. For example, in the first branch compressive action between the chains might be significant and then become negligible for the second branch, where inter-chain friction might be the main resisting action. Note, however, that this is just an example, and the exact processes that occur at each branch are unknown. Prior to the first branch it gradually gains stiffness over a small strain region, in between the two branches it gradually loses stiffness, and after the second branch it slowly builds stiffness again. It is not known how the matrix behaves after this because the experimental samples failed prematurely. It is assumed that damage in the matrix was negligible before failure because tension experiments show that damage occurs in a brittle manner. It is unclear whether the small initial region where the matrix gradually gains stiffness occurs because of start-up effects or because the matrix behaves like this in general. Overall, the response of the matrix is less stiff and it takes a different path in compression compared to tension. The Young's moduli for both compression quasi-linear branches were found with the same procedure as for tension. The results found for the first and the second quasi-linear branches are $E = 125.85 \text{ MPa}$ and $E = 66.00 \text{ MPa}$, respectively. The lines fitted to the compression experiment are shown in Fig.3.4b.

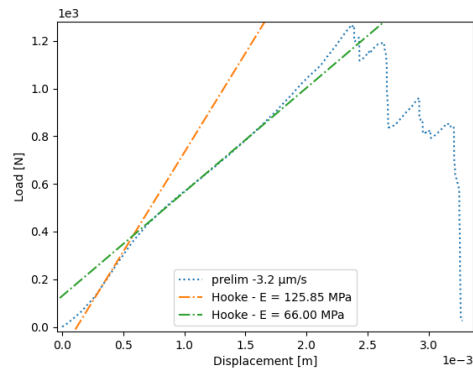
The general behavior of the matrix under arbitrary loading conditions and stress states is not known. Furthermore, the available experimental data is insufficient to construct a reliable hypothesis for general behavior. This poses a limitation for modelling the behavior of the matrix that binds solid propellants in Chapters 5 and 6. The micro-structure of solid propellants develops a variety of stress states for all types of macroscopic BCs. To see this, see the deviatoric and hydrostatic stress fields shown in Figures 5.9–5.10 of Chapter 5, which show that stress state varies significantly within RVEs subjected to simple BCs. This thesis is concerned with computationally reproducing the tension behavior of

solid propellants. The general anisotropic behavior of the matrix is not known, so going forward, it is idealized as isotropic. This, however, is a significant simplification. In reality, anisotropy probably has an important effect in the tension behavior of solid propellants because compression and shear stress states occur in the matrix of the micro-structure. The properties for the matrix and the particles that are used throughout the thesis are summarized in Table 3.1.

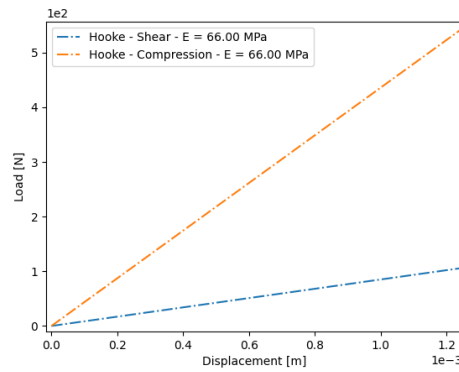
For reference for the following chapters, linear elastic results for compression and shear simulations are given here. The compression and shear responses of the matrix are compared in Fig.3.4c, where the Young's modulus of the second compression branch is utilized for both cases. The corresponding maximum principal stress fields are shown in Figures 3.5b and 3.5c.



(a) Tension stiffness identification



(b) Compression stiffness identification



(c) Compression and shear comparison

Figure 3.4: Experimental responses and linear elastic simulations

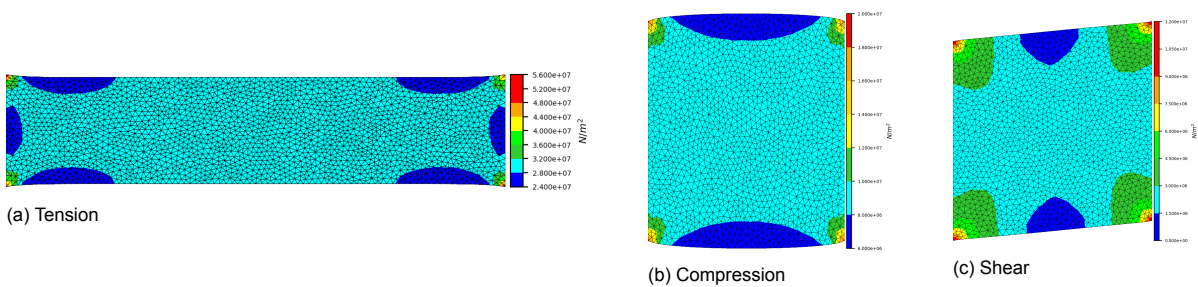


Figure 3.5: Maximum principal stress fields for 1mm displacement

E_0 (MPa)	ν_0	E_1 (MPa)	ν_1
249.62	0.39	15000	0.32

Table 3.1: Elastic properties of TNO's matrix (subscript 0) and particles [14] (subscript 1)

3.3. Viscoelastic Behavior

The Generalised Maxwell model is utilized for capturing the viscoelastic behavior of the matrix. Only one Maxwell element is considered for the Generalised Maxwell model. The viscoelastic parameters are identified by fitting the incremental stress relation described by Eq.(3.9) to the chosen tensile experiment with MATLAB's algorithm for nonlinear least squares fitting. The fitting is performed by considering the same Poisson ratio, dimensions, and BCs as in the experimental specimen. The output of this procedure is equivalent to the solution of a four-noded quadrilateral finite element because the stress and strain fields are uniform in both cases. Therefore, the fitting procedure is said to be performed with an equivalent single-element mesh, or just single-element mesh for simplicity. The simple configuration considered for the Generalised Maxwell model can accurately reproduce the region of the experimental load-displacement curve to which it was fitted, so there is no need for additional Maxwell elements.

The nonlinear least squares fitting start at the origin of the offsetted curve and the cutoff point is chosen at a displacement value that is assumed to be slightly smaller than the displacement necessary for damage initiation. This criterion is employed to avoid introducing damage effects into the identification of viscoelastic parameters, and to maximize the amount of data used for the fitting. Two cases are considered for identifying the viscoelastic parameters, a brittle and a ductile case, where the cutoffs are 80.0% and 7.37% of the displacement before rupture, respectively. Note that the terminology for the two cases comes from the criterion used for determining the cutoff points. The pre-damage regime is larger for the brittle case because the damage regime is smaller by definition. Note that damage is not treated in this chapter, but acknowledging its presence in the experiments is necessary. The purpose of investigating the two cases is that the *exact* moment of damage initiation in the experiments is not known, so it is useful to understand the role of viscoelasticity when damage is assumed to start early and when it is assumed to start late. The brittle case is a better *approximation* of reality because the experiments exhibit brittle failure. The ductile case is investigated for comparison.

The response of the single-element mesh utilized for parameter identification suffers from Poisson locking, so it is stiffer than the one of the multi-element mesh shown in Fig. 3.1a. Poisson locking implies that the single-element mesh stores more energy than the multi-element mesh for the same applied displacement because its deformation is limited to a uniform strain field. Therefore, the BCs applied in the horizontal direction inhibit the single element from releasing energy by deforming in the vertical direction. Conversely, the multi-element mesh is inhibited from deforming in the vertical direction only close to the vertical edges. The ratio between the energy stored by an element that is free to deform vertically to the energy stored by an element with inhibited vertical deformation is $a_{PL} = 1/(1 - \nu)$. For the case of the matrix there is $a_{PL} = 1.639$. The ratio of stored energy, and consequently of stiffness, between the single- and the multi-element meshes could be approximated with a_{PL} . However, a procedure that takes into account the effect that the undeformable vertical edges have on the multi-element mesh by considering its linear elastic stiffness is constructed instead. The procedure is described below and is accompanied with an example. The values given in the example correspond to the brittle case.

1. Obtain the parameters E_s^0 , E_s^1 and λ_s^1 for the single-element mesh from nonlinear least square fitting

$$E_s^0 = 39.59 \text{ MPa}, \quad E_s^1 = 134.5 \text{ MPa}, \quad \lambda_s^1 = 184.9 \text{ s}$$

2. Set the multi-element mesh quantities E_m^0/E_m^1 and $\lambda_{1,m}$ equal to those of the single-element mesh

$$\frac{E_m^0}{E_m^1} = \frac{E_s^0}{E_s^1}, \quad \lambda_m^1 = 184.9 \text{ s}$$

3. Find the scaling factor a that determines the ratio between the linear elastic stiffness of the multi-element mesh (which was obtained in the previous section) and the total stiffness of the single-

element mesh

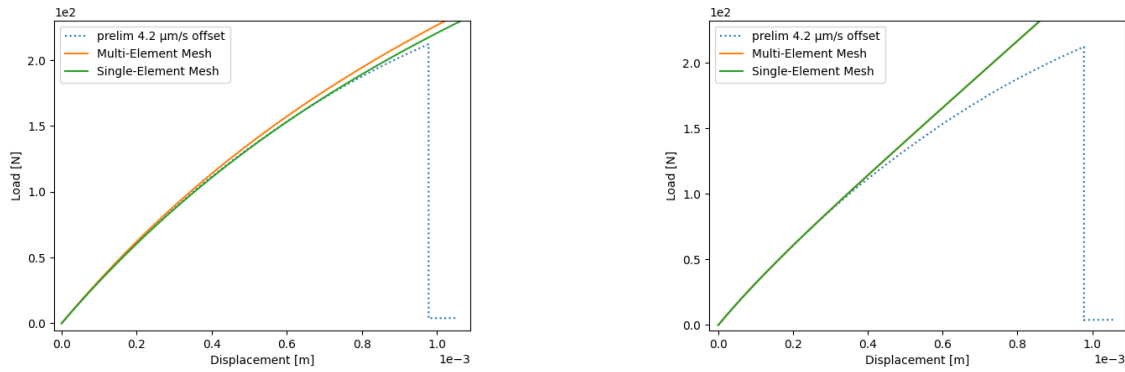
$$a = \frac{E_m^{el}}{E_s^0 + E_s^1} = 1.692$$

4. Obtain the stiffnesses for the multi-element mesh by scaling the single-element mesh stiffnesses by the scaling factor a

$$E_m^0 = aE_s^0 = 67.00 \text{ MPa}, \quad E_m^1 = aE_s^1 = 227.6 \text{ MPa}$$

Note that the relaxation times are the same for the single- and the multi-element meshes. This is because Poisson locking does not affect the time scale over which the material experiences relaxation. Also note that $a \approx a_{PL}$, which implies that the undeformable vertical edges have a relatively small effect on the accumulation of strain energy.

The parameters identified for both the brittle and the ductile cases are shown in Table 3.2. The single-element mesh and the multi-element mesh responses are compared in Fig. 3.6 for both the brittle and the ductile case. The figure shows that the procedure used to extrapolate the Maxwell parameters only induces a small deviation from the original approximation. The deviation is visible for the brittle case but not for the ductile case. The deviation is larger for the brittle case because the cutoff point is higher, so the parameter identification involves greater complexity.



(a) Brittle case

(b) Ductile case

Figure 3.6: Single-element mesh and multi-element mesh approximations

E^0 (MPa)	E^1 (MPa)	λ^1 (s)
218.2	76.43	37.03

(a) Brittle case

E^0 (MPa)	E^1 (MPa)	λ^1 (s)
39.59	134.5	184.9

(b) Ductile case

Table 3.2: Viscoelastic parameters for TNO's matrix material

Utilizing the parameters identified for both the brittle and the ductile cases, the response of the simulations is compared to the experiments for different strain rates in Figures 3.7 and 3.8. These comparisons show that the approximation of the experiments with different strain-rates deviate more. This discrepancy can be attributed to limitations of the Generalised Maxwell model, the parameter identification, and to experiments.

The brittle case parameters approximate the response of the experiment employed for the fitting better because the cutoff point is higher. Both cases approximate the $\dot{\epsilon} = 17.7 \mu\text{m/s}$ experiment similarly. The brittle case under-predicts the load for the $\dot{\epsilon} = 1.8 \mu\text{m/s}$ experiment, but the ductile case does not. Thus, the ductile case can still replicate this curve if damage is considered, but the brittle case cannot.

The responses of the brittle and the ductile cases are shown in Fig. 3.9 for different strain rates. The brittle case is more sensitive to strain rate than the ductile case. This is because for the ductile case damage significantly affects pre-failure behavior, so the influence of viscoelasticity is smaller. The

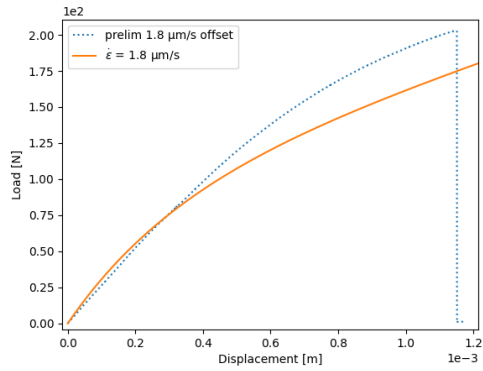
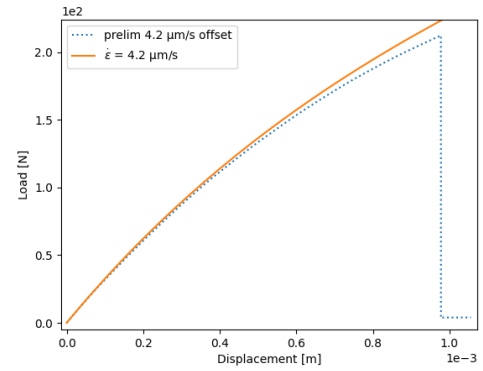
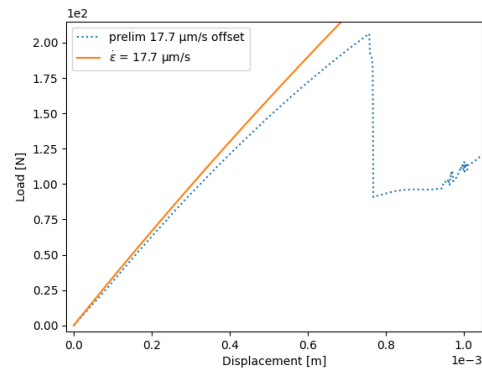
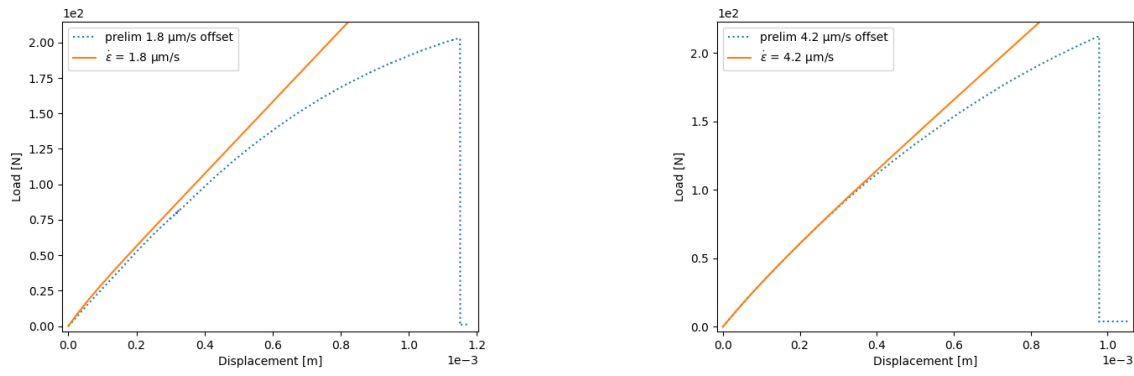
(a) 1.8 $\mu\text{m/s}$ strain rate(b) 4.2 $\mu\text{m/s}$ strain rate(c) 17.7 $\mu\text{m/s}$ strain rate

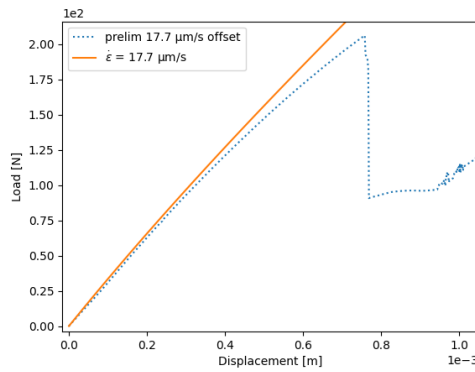
Figure 3.7: Brittle case approximations for different experiments

fields for the maximum principal stress are shown in Fig. 3.10 for both the brittle and the ductile cases. Both fields have similar distributions, but different magnitudes, as the elastic field shown in Fig. 3.5a because the strain rates within the specimens are relatively homogeneous.



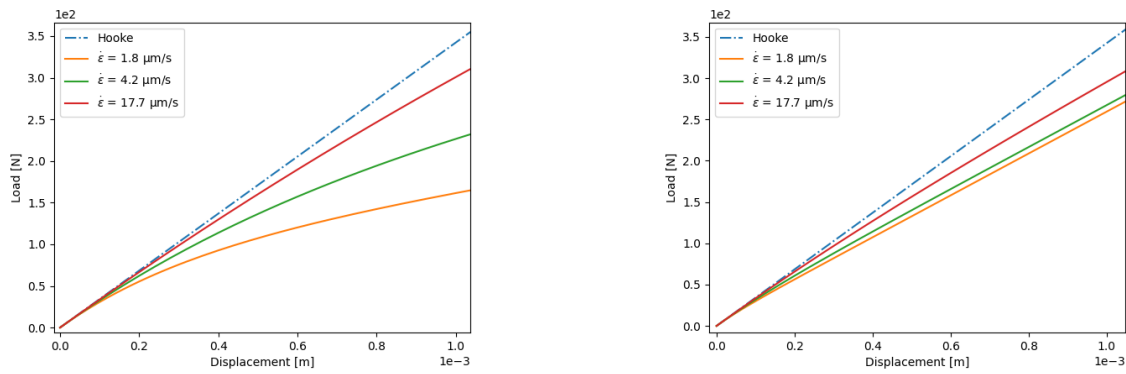
(a) 1.8 $\mu\text{m/s}$ strain rate

(b) 4.2 $\mu\text{m/s}$ strain rate



(c) 17.7 $\mu\text{m/s}$ strain rate

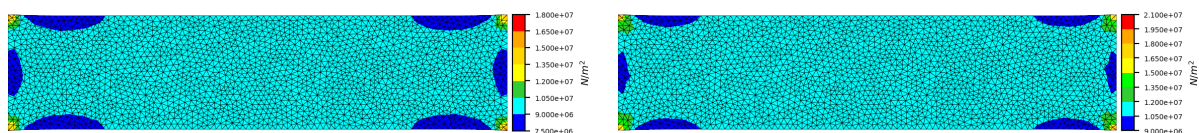
Figure 3.8: Ductile case approximations for different experiments



(a) Brittle case

(b) Ductile case

Figure 3.9: Comparison between the brittle and the ductile case for different strain rates



(a) Brittle case

(b) Ductile case

Figure 3.10: Maximum principal stress fields for $\dot{\epsilon} = 4.2\mu\text{m/s}$ and 1mm displacement

3.4. Conclusion

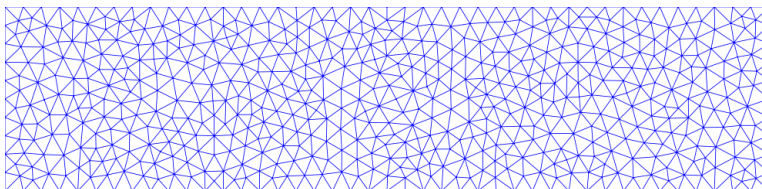
The elastic and viscoelastic behaviors of the matrix material were investigated in this chapter employing isotropic linear elasticity and the Maxwell model for LVE. The Young's modulus of a material is easy to identify and carries substantial information. Therefore, the first step to characterize the material was to identify its tension Young's modulus from the preliminary tension experiment of strain rate $\dot{\epsilon} = 4.2\mu\text{m}/\text{s}$. The matrix exhibits viscoelastic properties, and viscoelastic parameters must be known to characterize the damage properties of the matrix and the solid propellants in the following chapters. Therefore, the tension viscoelastic parameters were identified from the same $\dot{\epsilon} = 4.2\mu\text{m}/\text{s}$ experiment for a so-called single-element mesh utilizing nonlinear least squares fitting. These parameters were extrapolated to the case of a multi-element mesh employing a procedure that corrects the Poisson locking experienced by the single-element mesh. The region of the experiment for which the parameters were fitted was accurately reproduced. However, the accuracy of the approximations for experiments with different strain rates was significantly lower for the same parameters. Loss of accuracy occurs because of discrepancies between the experimental samples and because of the isotropy and LVE simplifications. To improve the quality of the parameters obtained from nonlinear least squares fitting data from relaxation experiments is necessary. To improve the characterization of the elastic and viscoelastic behaviors of TNO's matrix material anisotropy and state-dependency should be considered. Experimental data from DMA, creep, and loading-reloading experiments would be useful for this purpose.

Damage in the Matrix and in Perfectly Bonded Solid Propellants

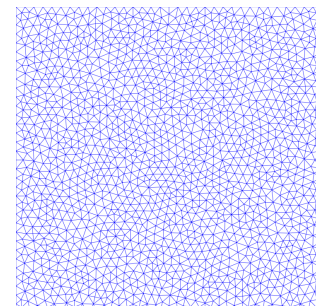
The damage-viscoelastic behavior of the matrix is investigated by combining the Generalised Maxwell model and a modified version of the physics-based continuum damage model proposed by H.K. Lee and D.K. Shin [20]. Lee's and Shin's model was specifically developed for modelling damage in particle reinforced composites with a brittle matrix and perfectly bonded stiff particles. Solid propellants fit into this category, except that the particles are not perfectly bonded. Nonetheless, the special case of perfectly bonded particles is relevant for understanding the material and may be of interest in preliminary stages of design. Furthermore, the damage model can also be utilized for the matrix-only. The modified version of Lee's and Shin's model is applicable to any class of linear elastic isotropic material, so it is a non-viscous model. The viscoelastic version of the modified model is applicable to any class of isotropic LVE material. The matrix is assumed to be isotropic and LVE.

The modified damage model and its extension to viscoelasticity are introduced. A numerical comparison between the modified model and Lee's and Shin's original implementation is presented. This comparison also serves as a verification that the model was correctly implemented into the FEM program. The behavior of the non-viscous modified model is investigated. Parameters are identified in order to replicate the matrix-only tension experiments (Fig. 1.4a) with the viscoelastic version of the model. The special case of perfectly bonded particles is also considered and computational results are compared to the solid propellant tension experiments, Fig. 1.5a. Finally, the suitability of utilizing the damage-viscoelastic model for the matrix and for the matrix within a computational homogenization (CH) framework is discussed.

BCs and sample dimensions in this chapter are as prescribed by Fig. 4.2. The meshes for the corresponding computational samples are shown in Fig. 4.1. These are always utilized unless noted otherwise. In general, the global time step magnitude is $1.0 \times 10^{-5} m$ and the maximum total displacement is $1.98 \times 10^{-3} m$. These values always apply unless stated otherwise.



(a) Tension mesh. 601 nodes and 1096 elements



(b) Compression and shear mesh. 1567 nodes and 2996 elements

Figure 4.1: Meshes utilized for the damage model simulations

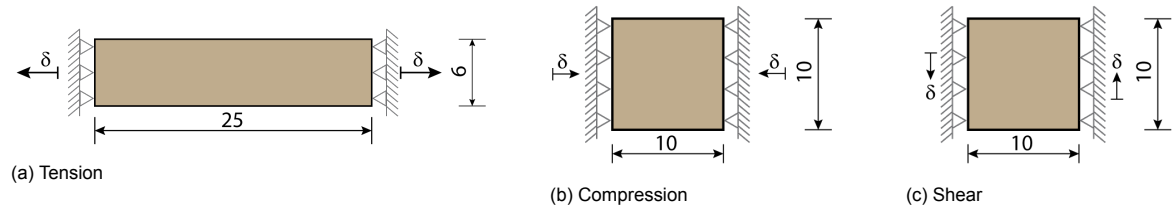


Figure 4.2: BCs and dimensions (dimensions in millimeters). Horizontal reactions are sampled for tension and compression and vertical reaction is sampled for shear.

4.1. Particle Reinforced Brittle Composite Model

Lee and Shin construct their model [20] by combining the constitutive model for embedded particles presented by J.W. Ju and T.M. Chen [16], the constitutive model for micro-crack damage presented by J.W. Ju and K.H. Teng [18], the damage evolution model for micro-crack growth presented by F. Addessio and J. Johnson [2], and the damage evolution model for micro-crack nucleation presented by D.R. Curran, D.A. Shockey and L. Seaman [8]. Both constitutive models and the micro-crack growth model are based in micromechanical fracture mechanics. Mathematical homogenization (MH) is also employed in the constitutive models to define the macroscopic constitutive relations. The micro-crack nucleation model is based on observation, but it resembles the rate of nucleation equation from classical nucleation theory (CNT). This is the most common model to quantify nucleation, where nucleation marks the transition of one thermodynamic phase to another. The model for embedded particles incorporates the stiffening effect of perfectly bonded particles into the undamaged homogenized material. It is completely decoupled from the formulation of the constitutive model for micro-crack damage. Both damage evolution models are given in rate form, so they introduce a damage rate dependence into the composite damage model. The Generalised Maxwell model introduces a viscoelastic rate dependence to the viscoelastic extension of the modified damage model. The formulations that give rise to the damage and the viscoelastic rate dependencies are completely decoupled, and are motivated by different physical phenomena.

This section describes the modified version of the damage model and its extension to viscoelasticity. Lee's and Shin's original implementation is modified by extending its constitutive damage formulation to three orthogonal directions (rather than the originally proposed unidirectional formulation), by introducing a parameter called the threshold micro-crack density, and by considering a different rate of crack growth equation, i.e. a different damage evolution law.

4.1.1. Constitutive Behavior

The constitutive models utilized by Lee and Shin define the macroscopic constitutive behavior in terms of the elastic compliance of the matrix $\mathbf{s}^{el} = \mathbf{s}^0$ and so-called perturbed compliances $\langle \mathbf{s}^{*i} \rangle$. The perturbed compliances are obtained by taking the ensemble average¹ of the perturbed part of the microscopic strain decomposition equation Eq. (2.16), and extrapolating it to the macro-structure by means of averaging theorems Eq. (2.14). The resulting governing macroscopic compliance is given by

$$\mathbf{s} = \mathbf{s}^0 + \langle \mathbf{s}^* \rangle \quad (4.1)$$

Where the perturbed part can be additively decomposed as

$$\langle \mathbf{s}^* \rangle = \left(\langle \mathbf{s}^{*1} \rangle + \langle \mathbf{s}^{*2} \rangle + \langle \mathbf{s}^{*3} \rangle + \langle \mathbf{s}^{*4} \rangle \right) \quad (4.2)$$

The superscripts represent the phases of the material. Where (1) is the phase of the first-order contribution due to the existence of particles, (2) is the phase of the first-order contribution due to existence of micro-cracks, (3) is the phase of the second-order contribution due to pairwise particle interaction, and (4) is the phase of the second-order contribution due to pairwise interaction of micro-cracks.

The perturbed compliance due to noninteracting particles $\langle \mathbf{s}^{*1} \rangle$ is obtained by assuming that particles do not intersect one another, that they are perfectly bonded to the matrix and *statistical homo-*

¹The average over the ensemble of all statistical realizations of randomly distributed micro-cracks and particles in the RVE.

ogeneity² [16]. Furthermore, it is assumed that particles are spherical, of uniform size and randomly distributed [16]. The definition of the phase 1 compliance is

$$\langle \bar{\mathbf{s}}^{*1} \rangle = \begin{bmatrix} \mathcal{S}_1^1 + 2\mathcal{S}_2^1 & \mathcal{S}_1^1 & \mathcal{S}_1^1 & 0 & 0 & 0 \\ \mathcal{S}_1^1 & \mathcal{S}_1^1 + 2\mathcal{S}_2^1 & \mathcal{S}_1^1 & 0 & 0 & 0 \\ \mathcal{S}_1^1 & \mathcal{S}_1^1 & \mathcal{S}_1^1 + 2\mathcal{S}_2^1 & 0 & 0 & 0 \\ 0 & 0 & 0 & \mathcal{S}_2^1 & 0 & 0 \\ 0 & 0 & 0 & 0 & \mathcal{S}_2^1 & 0 \\ 0 & 0 & 0 & 0 & 0 & \mathcal{S}_2^1 \end{bmatrix} \quad (4.3)$$

where

$$\mathcal{S}_1^1 = -2\phi (5\psi_1 + 5v_0\psi_1 - 2\psi_2 + 10v_0\psi_2) \quad (4.4)$$

$$\mathcal{S}_2^1 = -4\phi (4 - 5v_0) \psi_2 \quad (4.5)$$

in which ψ_1 and ψ_2 are given by

$$\psi_1 = \frac{-9\alpha\kappa_0 - 6\beta\kappa_0 + 4\beta\mu_0}{36\beta(3\alpha + 2\beta)\kappa_0\mu_0} \quad (4.6)$$

$$\psi_2 = \frac{1}{8\beta\mu_0} \quad (4.7)$$

and where α and β are

$$\alpha = 2(5v_0 - 1) + 10(1 - v_0) \left(\frac{\kappa_0}{\kappa_1 - \kappa_0} - \frac{\mu_0}{\mu_1 - \mu_0} \right) \quad (4.8)$$

$$\beta = 2(4 - 5v_0) + 15(1 - v_0) \frac{\mu_0}{\mu_1 - \mu_0} \quad (4.9)$$

Note that the elastic properties of the matrix and the particles have subscripts (0) and (1), respectively. Also note that the radius of the particles is not an explicit variable in the definition of this compliance. Instead, the volume fraction of particles ϕ is present to account for the relative amount of particles present.

The perturbed compliance due to non-interacting micro-cracks $\langle \bar{\mathbf{s}}^{*2} \rangle$ is obtained by assuming that micro-cracks do not intersect one another and that *local homogeneity*³ holds [18]. Furthermore, it is assumed that the faces of all micro-cracks have an normal outward normal vector in the same direction, meaning micro-cracks lie in parallel planes. The micro-cracks are assumed penny-shaped, of uniform size and randomly distributed [18]. The definition of the phase 2 compliance for microcracks orthogonal to the local z-axis is

$$\langle \bar{\mathbf{s}}^{*2} \rangle = \frac{16(1 - v_0^2)}{3E_0(2 - v_0)} \omega \begin{bmatrix} 0 & 0 & 0 & 0 & 0 & 0 \\ 0 & 0 & 0 & 0 & 0 & 0 \\ 0 & 0 & 2 - v_0 & 0 & 0 & 0 \\ 0 & 0 & 0 & 2 & 0 & 0 \\ 0 & 0 & 0 & 0 & 2 & 0 \\ 0 & 0 & 0 & 0 & 0 & 0 \end{bmatrix} \quad (4.10)$$

Where ω is the volume-averaged micro-crack density

$$\omega \equiv \frac{N\bar{c}^3}{V} \quad (4.11)$$

For which \bar{c} is the mean crack radius, N is the number of cracks per unit volume, and V is the RVE averaging volume [20].

Micro-crack alignment can be extended to the three local Cartesian axes (x, y and z) by changing the probability density function (PDF) that describes micro-crack location from $f(\mathbf{n}) = f(\mathbf{e}_z)$ to $f(\mathbf{n}) =$

²In a statistically homogeneous material the averaged material properties are independent of the averaging domain.

³A locally homogeneous material is one where the spatial gradient of the probability density functions of the geometry and the distribution of micro-cracks are small.

$f(\mathbf{e}_x) + f(\mathbf{e}_y) + f(\mathbf{e}_z)$, for which $f(\mathbf{e}_x) = f(\mathbf{e}_y) = f(\mathbf{e}_z)$. Where \mathbf{n} is the outward normal of a micro-crack and \mathbf{e}_i (with $i = x, y, z$) are the unit basis vectors of the Cartesian coordinate system. The modified phase 2 compliance for this micro-crack configuration is given by

$$\langle \bar{\mathbf{S}}^{*2} \rangle = \frac{16(1-v_0^2)}{3E_0(2-v_0)} \omega \begin{bmatrix} 2-v_0 & 0 & 0 & 0 & 0 & 0 \\ 0 & 2-v_0 & 0 & 0 & 0 & 0 \\ 0 & 0 & 2-v_0 & 0 & 0 & 0 \\ 0 & 0 & 0 & 4 & 0 & 0 \\ 0 & 0 & 0 & 0 & 4 & 0 \\ 0 & 0 & 0 & 0 & 0 & 4 \end{bmatrix} \quad (4.12)$$

This formulation accounts for damage that occurs in orthogonal planes and evolves isotropically. It is appropriate for the damage evolution model that will be introduced in Section 4.1.2 because deviatoric and hydrostatic stresses generate damage in said model. For a similar constitutive formulation that accounts for orthotropic damage evolution, the crack-radius should be assumed to be uniform only for aligned micro-cracks. Unaligned micro-cracks (i.e. micro-cracks with different \mathbf{n}) may have different crack size. Thus, the PDF that describes micro-crack location, and now also radius, should be written as $f(\mathbf{n}, c) = f(\mathbf{e}_x, c_x) + f(\mathbf{e}_y, c_y) + f(\mathbf{e}_z, c_z)$, for which $f(\mathbf{e}_x, c_x) = f(\mathbf{e}_y, c_y) = f(\mathbf{e}_z, c_z)$. Where c is crack radius and c_i are the (uniform) crack radii for specific orthogonal directions. Consequently, there would be separate damage variables \bar{c}_i , N_i , and ω_i for each orthogonal plane. For guidance on how to construct more complex damage constitutive relations see J.W. Ju and K.H. Teng [18].

The perturbed compliance due to the pairwise interaction of particles $\langle \bar{\mathbf{S}}^{*3} \rangle$ is derived based on the same assumptions as $\langle \bar{\mathbf{S}}^{*1} \rangle$ [16]. The definition of the phase 3 compliance is

$$\langle \bar{\mathbf{S}}^{*3} \rangle = \begin{bmatrix} \mathcal{S}_1^3 + 2\mathcal{S}_2^3 & \mathcal{S}_1^3 & \mathcal{S}_1^3 & 0 & 0 & 0 \\ \mathcal{S}_1^3 & \mathcal{S}_1^3 + 2\mathcal{S}_2^3 & \mathcal{S}_1^3 & 0 & 0 & 0 \\ \mathcal{S}_1^3 & \mathcal{S}_1^3 & \mathcal{S}_1^3 + 2\mathcal{S}_2^3 & 0 & 0 & 0 \\ 0 & 0 & 0 & \mathcal{S}_2^3 & 0 & 0 \\ 0 & 0 & 0 & 0 & \mathcal{S}_2^3 & 0 \\ 0 & 0 & 0 & 0 & 0 & \mathcal{S}_2^3 \end{bmatrix} \quad (4.13)$$

where

$$\mathcal{S}_1^3 = -2\phi^2 (15\bar{\gamma}_1\psi_1 + 10\bar{\gamma}_2\psi_1 + 15v_0\bar{\gamma}_1\psi_1 + 10v_0\bar{\gamma}_2\psi_1 + 10\bar{\gamma}_1\psi_2 - 4\bar{\gamma}_2\psi_2 + 10v_0\bar{\gamma}_1\psi_2 + 20v_0\bar{\gamma}_2\psi_2) \quad (4.14)$$

$$\mathcal{S}_2^3 = -8\phi^2 (4 - 5v_0) \bar{\gamma}_2\psi_2 \quad (4.15)$$

in which

$$\bar{\gamma}_1 = \frac{5}{4\beta^2} \left[-2(1-v_0) - 5v_0^2 - \frac{4\alpha}{3\alpha+2\beta} (1+v_0)(1-2v_0) \right] \quad (4.16)$$

$$\bar{\gamma}_2 = \frac{5}{8\beta^2} \left[11(1-v_0) + 5v_0^2 - \frac{3\alpha}{3\alpha+2\beta} (1+v_0)(1-2v_0) \right] \quad (4.17)$$

The perturbed compliance due to the pairwise interaction of particles $\langle \bar{\mathbf{S}}^{*4} \rangle$ is derived based on the same assumptions as $\langle \bar{\mathbf{S}}^{*2} \rangle$ [18]. The definition of the phase 4 compliance is

$$\langle \bar{\mathbf{S}}^{*4} \rangle = \frac{16(1-v_0^2)}{3E_0(2-v_0)} \omega^2 \begin{bmatrix} 0 & 0 & 0 & 0 & 0 & 0 \\ 0 & 0 & 0 & 0 & 0 & 0 \\ 0 & 0 & (2-v_0)\hat{k}_1 & 0 & 0 & 0 \\ 0 & 0 & 0 & 2\hat{k}_2 & 0 & 0 \\ 0 & 0 & 0 & 0 & 2\hat{k}_2 & 0 \\ 0 & 0 & 0 & 0 & 0 & 0 \end{bmatrix} \quad (4.18)$$

Where \hat{k}_1 and \hat{k}_2 depend on the radius of the integration used for the ensemble-averaging operation [18].

For the case where micro-cracks are aligned to the three Cartesian axes, the modified phase 4 compliance is obtained by utilizing the same PDF $f(\mathbf{n})$ that was utilized to obtain the modified phase 2 compliance. For simplification, interactions between unaligned micro-cracks are ignored. The modified phase 4 compliance is given by

$$\langle \mathbf{s}^{*4} \rangle = \frac{16(1-v_0^2)}{3E_0(2-v_0)} \omega^2 \begin{bmatrix} (2-v_0)\hat{k}_1 & 0 & 0 & 0 & 0 & 0 \\ 0 & (2-v_0)\hat{k}_1 & 0 & 0 & 0 & 0 \\ 0 & 0 & (2-v_0)\hat{k}_1 & 0 & 0 & 0 \\ 0 & 0 & 0 & 4\hat{k}_2 & 0 & 0 \\ 0 & 0 & 0 & 0 & 4\hat{k}_2 & 0 \\ 0 & 0 & 0 & 0 & 0 & 4\hat{k}_2 \end{bmatrix} \quad (4.19)$$

Similarly to the modified phase 2 compliance, this expression only allows isotropic damage evolution. The same modifications as mentioned for the phase 2 compliance should be made to the PDF $f(\mathbf{n}, c)$ to permit orthotropic damage evolution.

4.1.2. Damage Evolution: Nucleation and Growth of Micro-Cracks

Damage is assumed to evolve as the consequence of both crack nucleation and growth, which are assumed to be independent and sequential processes [20]. It is important to note that the quantities corresponding to the number and size of micro-cracks; N and \bar{c} , respectively, are statistical quantities [2]. Their purpose is to provide values that result in a globally accurate macroscopic micro-crack density ω .

The rate of micro-cracks nucleation \dot{N} is given by

$$\dot{N} = \begin{cases} \dot{N}_0 \exp\left[\frac{\sigma - \sigma_{n0}}{\sigma_1}\right] & \sigma > \sigma_{n0} \\ 0, & \sigma < \sigma_{n0} \end{cases} \quad (4.20)$$

where σ_{n0} is the nucleation threshold stress, σ is the hydrostatic stress, and \dot{N} and σ_1 are parameters which can be identified from impact experiments [8]. Curran, Shockley and Seaman [8] do not mention how they derived Eq. (4.20), but it is implied that it comes from experimental observation. The authors claim that all the parameters present in the rate equation are material properties, not phenomenological parameters. This claim could be justified if the rate equation is indeed a reformulation of CNT for the specific case of micro-crack nucleation.

Adessio and Johnson [2] describe micro-crack growth utilizing so-called damage surfaces. A micro-crack is assumed to become unstable (i.e. grow) when its energy state lies outside its damage surface, which is defined by the energy balance of the micro-crack. Microscopic damage surfaces are transformed into a single macroscopic damage surface by averaging the strain in the macroscopic region under consideration. Micro-cracks within this region are assumed to become unstable when the stress state of the region lies outside the macroscopic damage surface [2].

Lee and Shin utilize a macroscopic damage surface that assumes exponential crack-size distribution. This is at odds with the damage constitutive relations that they employ (Eqs. (4.10) and (4.18)), which assume uniform crack-size distribution. Nevertheless, the results obtained in the following sections show that the behavior of the damage model is reasonable in spite of the inconsistent formulation. The macroscopic damage surface for an isotropic material with exponential crack-size distribution is defined by

$$F^n(p, q, \bar{c}) = \begin{cases} q^2 + \frac{45}{4(5-v_0)} \left[(2-v_0)p^2 - \frac{2K}{\bar{c}} \right] = 0, & p < 0 \\ q^2 - \frac{45}{2(3-2v_0^2)} \left[(\mu_{fr}p + \sigma_0) \left(\mu_{fr}p + \sigma_0 + \sqrt{\frac{\pi K}{c}} \right) + \frac{K}{c} \right], & p > 0 \end{cases} \quad (4.21)$$

In which σ_0 is the cohesive stress and μ_{fr} is the coefficient of friction. The pressure p , the deviatoric stress q and K are given by

$$p = -\frac{1}{3}\sigma_{ii}, \quad q = \sqrt{\frac{3}{2}q_{ij}q_{ij}}, \quad K \equiv \frac{\pi}{2} \frac{2-v_0}{1-v_0} \gamma G \quad (4.22)$$

Where $q_{ij} = \sigma_{ij} + p\delta_{ij}$. And γ and G are the crack surface energy and the shear modulus, respectively.

The crack-tip speed in a homogeneous isotropic continuum approaches the Rayleigh speed as it propagates [2]. The Rayleigh wave speed is approximated by the shear wave speed. Therefore, the rate of crack growth is defined as

$$\dot{c} = \beta \dot{c}_{\max} \tanh(d_s) \quad (4.23)$$

Where d_s quantifies the distance by which the stress state exceeds the damage surface, \dot{c}_{\max} is the shear wave speed, and β is a constant control parameter.

The shear wave speed is given by

$$\dot{c}_{\max} = \sqrt{\frac{\hat{G}}{\rho^*}} \quad (4.24)$$

Where \hat{G} is the degraded shear modulus. The expression for this parameter is

$$\hat{G} = \frac{G}{1 + 2G\beta^e \bar{c}^3} \quad (4.25)$$

in which

$$\beta^e = \begin{cases} \frac{128\pi}{320\pi} \frac{(5-\nu)(1-\nu)}{15} \frac{N_0}{G}, & p \leq 0 \\ \frac{128\pi}{320\pi} \frac{(5-\nu)(1-\nu)}{15} \frac{N_0}{G}, & p > 0 \end{cases} \quad (4.26)$$

Equation (4.25) for the degraded shear modulus was defined by Addessio and Johnson [2], and it is utilized in this thesis. Instead of a degraded shear modulus, Lee and Shin utilized a degraded Young's modulus E^* that was defined by H.K. Lee and S. Simunović [21]. The behaviors resulting from the different rate of crack growth relations are compared in Section 4.2.

Lee and Shin defined the parameter d_s as

$$d_s = q^2 - F^n \quad (4.27)$$

This definition is inappropriate for quantifying the overstress because it is the argument of a hyperbolic tangent function. The magnitude of d_s depends on the units system utilized, so the value returned from the hyperbolic tangent will be different for different unit systems. Calculations are performed in SI units, so $|d_s| \gg 10$ and consequently, $\tanh(d_s) \approx 1$ and $\frac{d(\tanh(d_s))}{d\dot{c}} \approx 0$. This means that the rate of crack growth equation Eq.(4.23) and its algorithmic implementation become independent of overstress. The distance between the damage surface and the stress state d_s is defined with Eq.(4.27). This makes the description of crack growth the weakest aspect of the damage model. The consequences of having a crack growth equation that is independent of state are discussed later in this chapter, when the damage model is applied. Exploring overstress measures is a complex task that is not in the scope of this study.

4.1.3. Finite Element Implementation and Extension to Viscoelasticity

The constitutive relation proposed by Lee and Shin for their model takes the usual form of damage formulations. A secant stress-strain relation is given by

$$\sigma = \mathbf{C}(N, \bar{c})\epsilon \quad (4.28)$$

Where $\mathbf{C}(N, \bar{c})$ is the secant stiffness, the inverse of the governing macroscopic compliance defined by Eq. (4.1).

The rate form of the constitutive equation Eq. (4.28) is the starting point for the FE implementation of Lee's and Shin's model. Using the chain rule for derivatives, it is given by

$$\dot{\sigma} = \mathbf{C}\dot{\epsilon} + \frac{\partial \mathbf{C}}{\partial N} \dot{N}\epsilon + \frac{\partial \mathbf{C}}{\partial \bar{c}} \dot{\bar{c}}\epsilon \quad (4.29)$$

Linearizing the the stress rate $\dot{\sigma}$ and the strain rate $\dot{\epsilon}$ within a global time step as $\Delta\sigma$ and $\Delta\epsilon$, respectively, the constitutive rate equation Eq. (4.29) can be discretized as

$$\sigma_{n+1} = \sigma_n + \mathbf{C}\Delta\epsilon_{n+1} + \frac{\partial \mathbf{C}}{\partial N} \Delta N_{n+1} \Delta\epsilon_{n+1} + \frac{\partial \mathbf{C}}{\partial \bar{c}} \Delta \bar{c}_{n+1} \epsilon_{n+1} \quad (4.30)$$

Note that the notation t and $t + \Delta t$ introduced in Section 2.1 for describing the previous and the current global time steps was changed to n and $n + 1$, respectively. This equation is solved sequentially. That is, first the second term of the right-hand side is solved and summed with the first term, then the third term is solved and summed with the other terms, and then the same follows for the fourth term. The third and the fourth terms are called the softening terms because only they can make the incremental relation lose positive-definiteness. More specifically, the third term is called the crack-growth softening term and the fourth term is called the nucleation softening term. It is important to note that despite their name, these terms may be active even before the material exhibits softening. The softening terms are proportional to the gradient of the secant stiffness with respect to the damage variables, so they are large when damage grows abruptly.

The nucleation rate Eq. (4.20) and growth rate Eq. (4.23) equations can be solved by applying the incremental form of the backward Euler method [20]. Their discretization is given by

$$N_{n+1} = N_n + \Delta t_{n+1}^{loc} \dot{N}_0 \cdot \exp \left[\frac{(\sigma)_{n+1} - \sigma_{no}}{\sigma_1} \right] \quad (4.31)$$

$$\bar{c}_{n+1} = \bar{c}_n + \beta \Delta t_{n+1}^{loc} \sqrt{\frac{(\hat{G})_{n+1}}{(\rho^*)_{n+1}}} \tanh(d_s) \quad (4.32)$$

Where t^{loc} is a time difference parameter and is interchangeable with the parameters \dot{N}_0 and β . These three parameters alongside the global time discretization determine the loading rate. Equations (4.31) and (4.32) are solved locally within the global time step of interest using the NR method. The local NR procedure takes the form $x_{n+1}^{(l+1)} = x_{n+1}^{(l)} - \frac{r(x_{n+1}^{(l)})}{r'(x_{n+1}^{(l)})}$, where $r(x)$ is the residual obtained at a local time step l from solving the discretized form of damage variable x at a global time step $n + 1$.

Discretized incremental equation Eq. (4.30) can lead to highly unstable numerical behavior for the implemented version of the damage model. Instabilities occur when after a time step of inelastic deformation the response of the following time step becomes elastic again because the stress state goes back into the damage surface. This can produce oscillations between elastic and inelastic deformations at the IPs. This process is clearly shown in Fig. 4.3a for a four-noded single-element mesh and for a three-noded multi-element mesh⁴. The parameters and dimension of the single-element mesh are the same as for the multi-element mesh. The local behavior of the multi-element mesh is more stable because neighboring elements stabilize each other.

Instabilities are caused by large values of the crack-growth softening term. Micro-cracks grow abruptly at damage initiation because micro-crack size as a function of deformation is not smooth and not differentiable at this point, see the micro-crack evolution figures in Appendix A and in Lee and Shin [20]. Therefore, the numerical behavior of a given IP usually becomes unstable at the time step of crack-growth initiation. Micro-cracks grow at a large rate, even if the stress state is barely outside the damage surface. Therefore, instabilities also take place when the material is highly degraded, because the state of stress falls deep into the damage surface. The instabilities are a consequence of the rate of crack growth equation being independent of state.

A new parameter called the *threshold micro-crack density* ω_{n0} is introduced with the purpose of reducing numerical instabilities. This parameter specifies a threshold after which the softening terms are activated. Below this threshold damage may evolve but the softening terms are set to zero. Thus, the initial non-differentiable part of the crack growth function can be bypassed. Utilizing the threshold micro-crack density, the discretized incremental constitutive equation is given by

$$\sigma_{n+1} = \begin{cases} \sigma_n + \mathbf{C} \Delta \epsilon_{n+1} & \omega < \omega_{n0} \\ \sigma_n + \mathbf{C} \Delta \epsilon_{n+1} + \frac{\partial \mathbf{C}}{\partial N} \Delta N_{n+1} \Delta \epsilon_{n+1} + \frac{\partial \mathbf{C}}{\partial \bar{c}} \Delta \bar{c}_{n+1} \epsilon_{n+1} & \omega \geq \omega_{n0} \end{cases} \quad (4.33)$$

This formulation cannot avoid instabilities when the material is highly degraded.

Lee and Shin suggest to use the following expression as the tangent stiffness \mathbf{C}^{tan} for the global NR procedure

$$\frac{\partial \Delta \sigma}{\partial \Delta \epsilon} = \mathbf{C} + \frac{\partial \mathbf{C}}{\partial \bar{c}} \Delta \bar{c} + \frac{\partial \mathbf{C}}{\partial N} \Delta N \quad (4.34)$$

⁴The multi-element mesh simulation corresponds to the case of Fig. 4.8a in which $\beta = 6.33 \times 10^{-7}$.

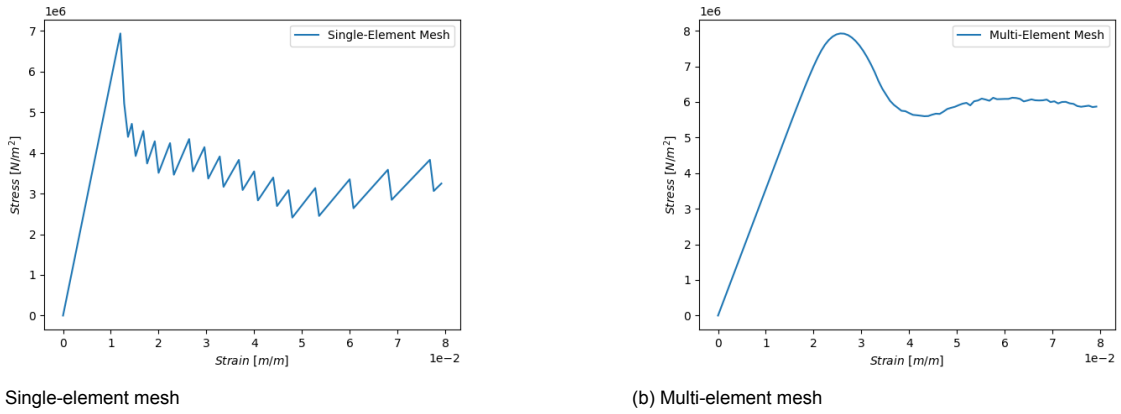


Figure 4.3: Comparison of unstable behavior for different meshes

Note that $\frac{\partial \Delta \sigma}{\partial \Delta \epsilon} \neq \frac{\partial \sigma}{\partial \epsilon}$, so Eq. (4.34) is a pseudo-tangent stiffness rather than a consistent tangent stiffness.

Computational efficiency is crucial for CH, which is employed in Chapter 6. Lee's and Shin's pseudo-tangent stiffness is not a good choice for efficiently carrying out the NR procedure. In fact, it has been observed that utilizing it generally delivers worse computational performance than utilizing the secant stiffness. Figure 4.4⁵ illustrates this for a concrete example. The secant stiffness is not a good choice for carrying out the NR procedure either because it is always positive-definite, and the tangential relation loses positive-definiteness during softening. The rate constitutive equation Eq. (4.29) cannot analytically relate the strain rate $\dot{\epsilon}$ to the stress rate $\dot{\sigma}$ with a linear system of equations, so a consistent tangent stiffness is not possible. It is hypothesized that Quasi-NR methods (also called Secant-Newton methods) can characterize the tangential relation better than the secant or the pseudo-tangent stiffnesses, and deliver good computational performance. Choosing which Quasi-NR method to use must be a judicious decision. The secant stiffness is utilized for the NR procedure in this thesis for simplicity. But investigating and employing Quasi-NR methods is recommended for future research.

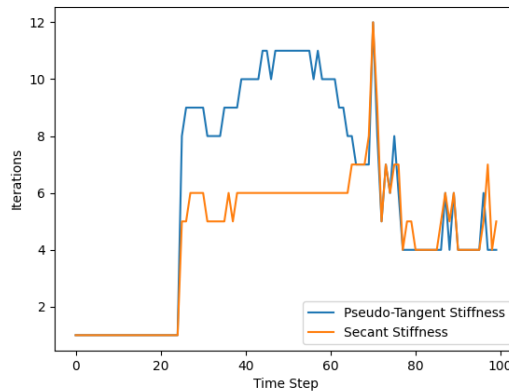


Figure 4.4: NR global iterations per time step for different choices of tangent stiffness

To extend the implemented damage model to viscoelasticity, a relaxation function must be found and placed into the relaxation constitutive relation described by Eq.(2.12). The resulting integral expression must be transformed to a close form expression. For this purpose it was attempted to employ the method utilized by B.J. Yang et al [36], who rigorously extend the same embedded particle constitutive model utilized here and a statistical debonding damage evolution equation to viscoelasticity. Yang transforms the relaxation constitutive relation to the Laplace domain. There he replaces the elas-

⁵The simulation corresponds to the case of Fig. 4.38 in which $\dot{\epsilon} = 4.2 \mu\text{m/s}$.

tic parameters with transformed viscoelastic parameters and then transforms the so-called equivalent elastic problem back to the time domain. It was not possible to apply this method to the damage model implemented here because the resulting inverse Laplace transformation cannot be solved analytically.

Since Yang's method could not be applied, the damage model was extended to viscoelasticity in an approximate manner. The second term of the elastic incremental relation (Eq.(4.33)), which is the first of the sequential loading process and accounts for the positive-definite part, was replaced by the viscoelastic incremental relation of the Maxwell model (Eq.(3.9)). The softening terms remain elastic. The resulting viscoelastic version of the damage model is given by

$$\sigma_{n+1} = \begin{cases} \sigma_n + \mathbf{C}^0 \Delta \epsilon + \sum_{\alpha=1}^N \left(1 - \exp\left(-\frac{\Delta t^{max}}{\lambda^\alpha}\right)\right) \left(\frac{1}{\Delta t^{max}/\lambda^\alpha} \mathbf{C}^\alpha \Delta \epsilon - \sigma^\alpha(t - \Delta t^{max})\right) & \omega < \omega_{n0} \\ \sigma_n + \bar{\mathbf{C}} E^0 \Delta \epsilon + \sum_{\alpha=1}^N \left(1 - \exp\left(-\frac{\Delta t^{max}}{\lambda^\alpha}\right)\right) \left(\frac{E^\alpha}{\Delta t^{max}/\lambda^\alpha} \bar{\mathbf{C}} \Delta \epsilon - \sigma^\alpha(t - \Delta t^{max})\right) + \\ \frac{\partial \mathbf{C}}{\partial N} \Delta N_{n+1} \Delta \epsilon_{n+1} + \frac{\partial \mathbf{C}}{\partial \bar{c}} \Delta \bar{c}_{n+1} \epsilon_{n+1} & \omega \geq \omega_{n0} \end{cases} \quad (4.35)$$

Where the stiffnesses \mathbf{C}^0 and \mathbf{C}^α are obtained from the Young's moduli E^0 and E^α , respectively. The method used for obtaining this expression is not rigorous, as this expression is derived from a linear elastic basis and not from a viscoelastic basis. Furthermore, the damage evolution equations are not extended to viscoelasticity, as only brittle damage is of concern. The physics encapsulated by the elastic model are lost in the pre-failure damage regime of the viscoelastic model. The equation for the damage surface is not extended to viscoelasticity either, because it is assumed that elastic damage surfaces can predict viscoelastic damage initiation sufficiently well.

For a step-by-step description of the algorithmic implementation of the particle reinforced brittle composite model, see Lee and Shin [20]. It is easy to see how viscoelasticity and ω_{n0} fit in their algorithmic description. Note that their description contains a few errors.

4.2. Numerical Comparison

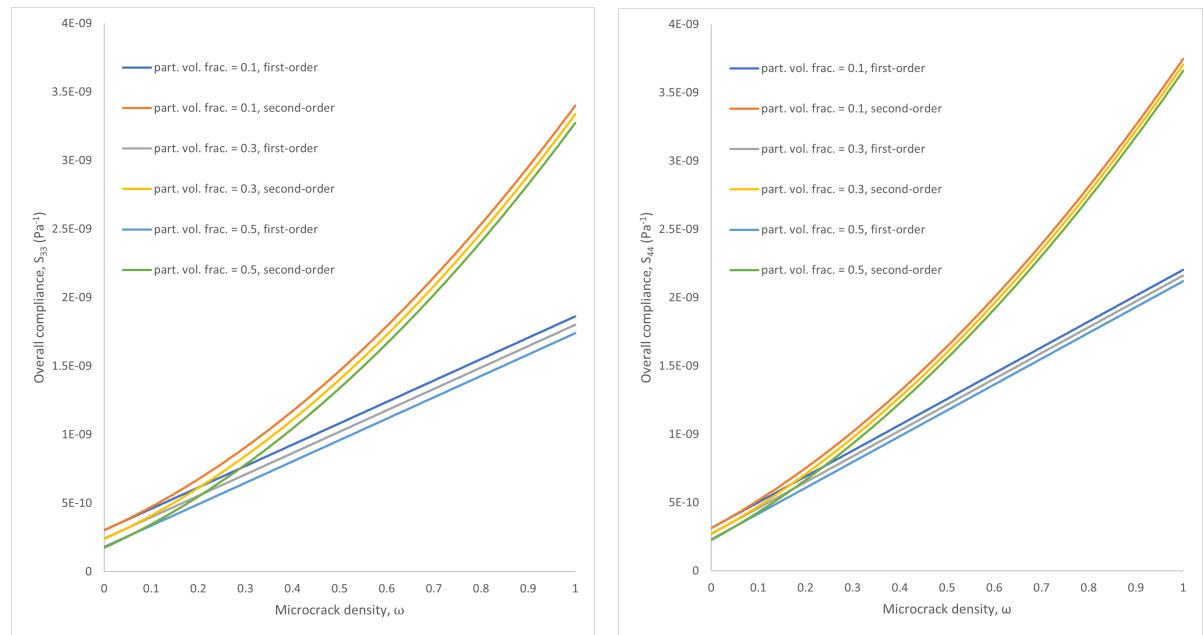
The non-viscous version of the damage model implemented in this thesis is a modified version of Lee's and Shin's model [20]. The numerical behaviors of this model and of Lee's and Shin's original implementation are compared here. The threshold crack density is set to $\omega_{n0} = 0.00$ for ignoring the effect of this parameter in the comparison. For the BCs and mesh employed, the behavior of the model is identical for unidirectional and for orthogonal micro-crack configurations. Therefore, the effect of different micro-crack configurations is not considered in the comparison either. The only difference between the formulations of both models that can be appreciated in this comparison is that they employ different rate of crack growth equations.

The figures from Lee and Shin [20] are recreated in Appendix A with the modified model. Some of these figures are also shown here for specific comparisons. The same parameters, mesh, and BCs are employed. The behaviors shown in Lee's and Shin's figures are not in accordance with the reported input. This can easily be seen by realizing that the observed linear elastic stiffnesses are not consistent with the input. Additionally, the strain rate imposed on the BCs is not specified, which is an important parameter because the model is rate dependent. Their figures suggest that they used different strain increments for each global time step based on the locations of the sampled data on the strain axis. The value assigned to the time difference parameter Δt^{loc} is not mentioned. Thus, it is not possible to determine if the strain rate is constant or variable. Finally, Lee and Shin do not specify the size of the RVE averaging volume V . Since Lee and Shin report a part of their input erroneously and do not report another part of it, the figures obtained from both models cannot be rigorously compared. However, coarse comparisons regarding the general behaviors of both models are some times possible.

A constant strain increment of $\Delta \epsilon = 2.5 \times 10^{-4}$ is utilized, this value is within the range of strain increments observed in Lee and Shin [20]. For simplicity, it is assumed that $\Delta t^{loc} = 1.0$ s and $V = 1.0$ m³. Note that even though this value of V does not obey the principle of separation of scales, it does not cause issues because it simply scales the number of micro-cracks per unit volume N . The formulations of the modified and the original models only require the ratio N/V to be characteristic of the material.

Different combinations of perturbed compliances as a function of micro-crack density ω are shown in Fig. 4.5. These combinations exhibit similar behavior as in Lee and Shin [20]. Their values are slightly different, because Lee and Shin utilized different parameters. The figure shows that first-order

perturbed compliances grow linearly and second-order perturbed compliances grow quadratically with ω . It also shows that for high ω second-order effects (i.e. crack interaction effects) are significant.



(a) Longitudinal compliances

(b) Shear compliances

Figure 4.5: First-order-only compliances and combination of first-order and second-order compliances for $\phi = 0.1$ and $\phi = 0.3$

The results of most simulations show similar patterns for the modified model and for Lee's and Shin's model. The effects of second order compliances $\langle \mathbf{S}^{-*3} \rangle$ and $\langle \mathbf{S}^{-*4} \rangle$ become more noticeable as the volume fraction ϕ and the micro-crack density ω increase, respectively. Increasing ϕ makes the response stiffer, reduces the deformation necessary for damage initiation, and does not affect the rate of crack growth or of modulus degradation. Increasing the control parameter β increases the rate of crack growth and of modulus degradation. For the modified model the effect of the control parameter β is small, due to the modulus becoming completely degraded almost immediately. Decreasing ω postpones damage initiation, decreases the initial micro-crack size, and does not affect the rate crack growth or of modulus degradation.

Although the two versions of the damage model exhibit similar patterns, the numerical values that they output are different. This suggests that the two crack growth equations predict damage differently. In Lee and Shin's model [20] crack growth is (quasi-) linear with deformation, and in the modified model crack growth is highly nonlinear. Therefore, the modified model reacts brittler than Lee and Shin's model. However, it is unknown if this is due to the crack growth equation, different input parameters, or different strain rates. It is possible that Lee and Shin utilized an adaptive strain rate to avoid excessive brittleness. This is inferred as it is not mentioned whether Δt^{loc} is a constant.

For the modified model faster crack growth sometimes leads to marginally reduced brittleness, e.g. Fig. 4.6. Also, loading in one direction can lead to development of stress in the other direction, (e.g. Fig. 4.7. This occurs because the parameters utilized produce excessively brittle behavior for which failure occurs immediately after damage initiation. This suggests that extreme brittle post-failure softening is inaccurate, as the crack-growth softening term acts spuriously. The modified model predicts physically sound behavior when the response of the material is not extremely brittle. For example, Fig. 4.8 shows that the material becomes more brittle when β increases, which is in accordance with Lee and Shin's results.

Even though the parameters used by Lee and Shin are unknown, a comparison between the modified model and Lee and Shin's model was made. The modified model exhibits similar patterns, therefore the model is implemented correctly.

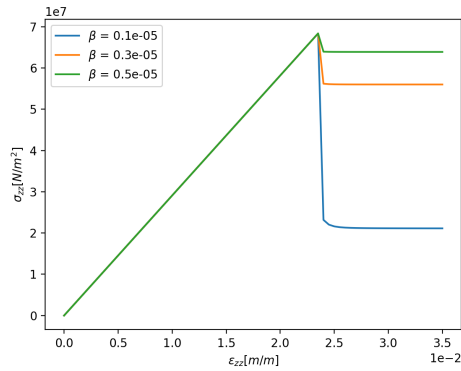


Figure 4.6: Stress-strain curve for different values of control parameter β

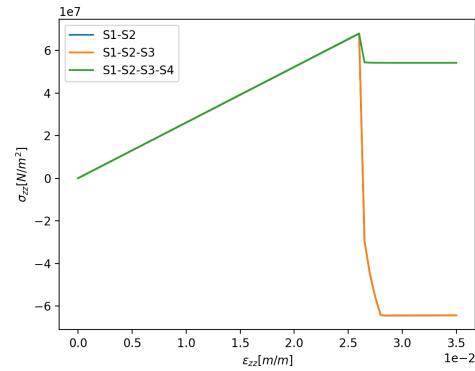


Figure 4.7: Stress-strain curve for first- and second-order contributions and $\phi = 0.1$

4.3. Non-Viscous Damage of the Matrix

The behavior of the modified model is investigated with the purpose of understanding non-viscous damage. The model's behavior is investigated with tension, compression and shear simulations. The effect of inclusions is also investigated, but only with tension simulations. Furthermore, the effects of mesh discretization and strain rate are explored with tension simulations. Simulations where damage is caused by crack growth-only and by both crack growth and crack nucleation together are performed.

The influence of most parameters are explored with tension simulations, in order to stay consistent with Lee and Shin [20]. The only parameters explored in other load states are the cohesive stress σ_0 , the friction coefficient μ , and the threshold micro-crack density ω_{n0} because their effects are better appreciated in other load states. The time difference parameter is taken as $\Delta t^{loc} = 1.0 s$. This allows the rates of crack growth and crack nucleation to be defined only by β and \dot{N}_0 , respectively. The ratio N_0/V is considered as a single parameter, this ratio is called the initial micro-crack distribution. The motivation for this is that when crack nucleation does not occur the ratio N/V is always constant and equal to the initial micro-crack distribution.

All simulations presented in this section are performed using the elastic parameters in Table 3.1 and the damage parameters in Table 4.1, unless otherwise stated. Table 4.1 contains two different sets of values, the brittle case and the ductile case. The two cases are investigated to understand how the modified model behaves for different types of damage, and to compare the behaviors of a brittle and a ductile matrix. Crack growth for negative hydrostatic stress and nucleation are inhibited, unless otherwise stated or implied. If the type of BCs applied to a simulation are not explicitly stated, tension BCs are applied. Micro-cracks are simply referred to as cracks for brevity.

The modified damage model is not susceptible to neither early failure from loss of ellipticity nor to mesh sensitivity, as will be shown in Sections 4.3.5 and 4.3.6, respectively. This is mentioned now because it is important to take it into consideration when reading the results presented before the aforementioned sections.

Parameter	Brittle Case	Ductile Case	Units
β	4.33×10^{-7}	1.0×10^{-8}	-
γ	11.8	0.0406	$Pa \cdot m$
N_0/V	1.0×10^8	1.0×10^{10}	m^{-6}
ω_0	0.10	0.01	%
σ_{n0}	1.0×10^{999}	1.0×10^{999}	N/m^2
σ_{n0}	5.0×10^5	1.0×10^6	N/m^2
\dot{N}_0	1.0×10^8	1.0×10^8	$m^{-3}s^{-1}$
σ_1	2.0×10^9	2.0×10^9	N/m^2
σ_0	1.0×10^{999}	1.0×10^{999}	N/m^2
σ_0	2.0×10^7	2.0×10^7	N/m^2
μ_{fr}	0.26	0.26	-
ρ^*	1169.5	1169.5	kg/m^3
\hat{k}_1	0.987125	0.987125	-
\hat{k}_2	0.816686	0.816686	-
Δt^{loc}	1.0	1.0	s
ω_{n0}	0.0	0.0	%
ϕ	0.0	0.0	-

Table 4.1: Default damage parameters. Blue value is used by default when nucleation is allowed. Green value is used by default when crack growth for negative hydrostatic stress is allowed

4.3.1. Tension

The effect of the control parameter β on the load-displacement response of a tension specimen is shown in Fig. 4.8. The parameter affects the magnitude of the ultimate strength, displacement at ultimate strength, and the rate of softening. Thus, the control parameter determines the overall brittleness of the material. Where higher values of β result in a more brittle response. This occurs because the parameter directly scales the strain rate, and consequently the rate of crack growth. The effect of the control parameter on the specimen's response is greater for the ductile case, because it acts over a larger loading region. Strain rate dependence is further investigated in Section 4.3.5.

Numerical instabilities are observed for all the curves of the brittle case and for the curve with $\beta = 5.0 \times 10^{-8}$ of the ductile case. The unstable behavior is not an issue as it arises after failure. In the tensile experiments TNO's matrix fails immediately after the ultimate strength. Therefore, this thesis does not focus in modelling softening behavior. Note that numerical instabilities can occur locally before their effect is noticeable in the global load-displacement response.

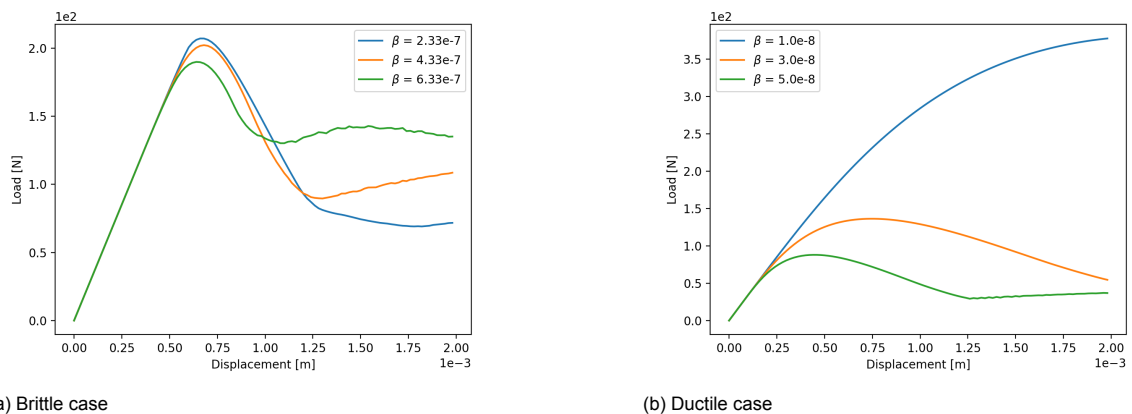
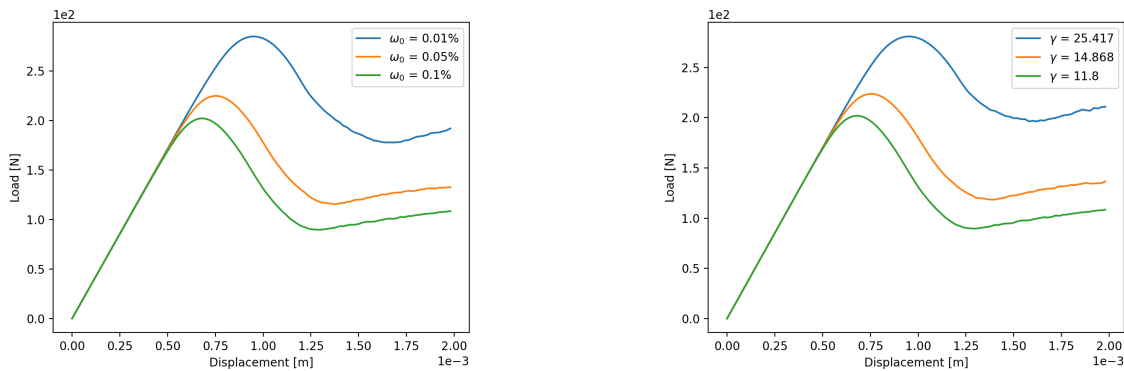


Figure 4.8: Response of specimen for different values of control parameter β

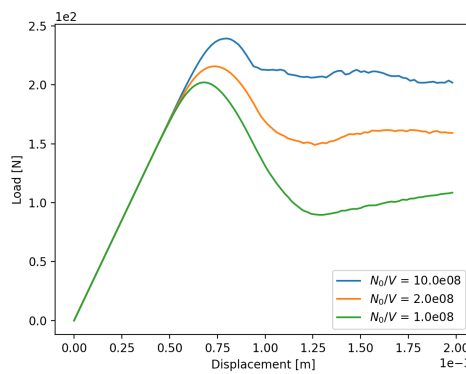
The effect of varying the initial crack density ω_0 , crack surface energy γ , and initial crack distribution N_0/V are shown for the brittle and ductile cases in Figures 4.9 and 4.10, respectively. These three parameters have the common characteristic that they directly scale the ratio γ/\bar{c} in the damage surface

equation Eq. (4.21). The values of ω_0 , γ , and N_0/V were chosen such that they scale the ratio γ/\bar{c} equally. For example, the orange curve in Fig. 4.9c scales the ratio γ/\bar{c} in the same manner as the orange curves in Fig. 4.9a and Fig. 4.9b. The consequence of these three parameters all scaling γ/\bar{c} is that they have the same or very similar effect in determining the yield strength and displacement. The crack surface energy and the initial crack distribution affect the yield values in the same manner. The initial crack density affects the yield values slightly differently because it degrades the compliances $\bar{\mathbf{S}}^{*2}$ and $\bar{\mathbf{S}}^{*4}$, and consequently the stiffness \mathbf{C} , even in the elastic regime. However, the initial degradation should always be negligible. The physical interpretation of why γ/\bar{c} determines the moment of damage initiation is straightforward. If more work is needed to generate cracks and if initial cracks are smaller, then a larger stress is needed to initiate crack growth. The post-damage behavior that ω_0 , γ and N_0/V trigger are different. This is due to the gradient that scales the crack-growth softening term, which directly depends on the damage quantities ω , N , and \bar{c} . This simply means that the number and size of cracks affects the rate of crack growth. The parameter ω_0 directly affects ω and \bar{c} ; the parameter N_0/V directly affects ω , \bar{c} and N ; and the parameter γ does not directly affect any damage quantity. Increasing ω_0 marginally increases the rate of crack growth, as larger cracks are less stable. Increasing N_0/V reduces the rate of crack growth, because more energy is necessary for more cracks to grow the same amount. Furthermore, increasing N_0/V increases the ultimate strength in the brittle case and reduces the ultimate strength in the ductile case, because the post-damage effect is greater for the ductile case. Note that variations of N_0/V affect the post-damage regime significantly more than variations of the other parameters. This suggests that the number of cracks per unit volume N has a large impact on the scaling gradient.



(a) Initial crack density ω_0

(b) Crack surface energy γ



(c) Initial crack distribution N_0/V

Figure 4.9: Response of brittle specimen for different values of ω_0 , γ , and N_0/V

The effect of the nucleation threshold stress σ_{n0} is shown in Fig. 4.11. This threshold determines when nucleation damage initiates in the same manner as γ determines the initiation of crack growth damage. This threshold does not have a direct impact on the softening terms. Variations of σ_{n0} affect

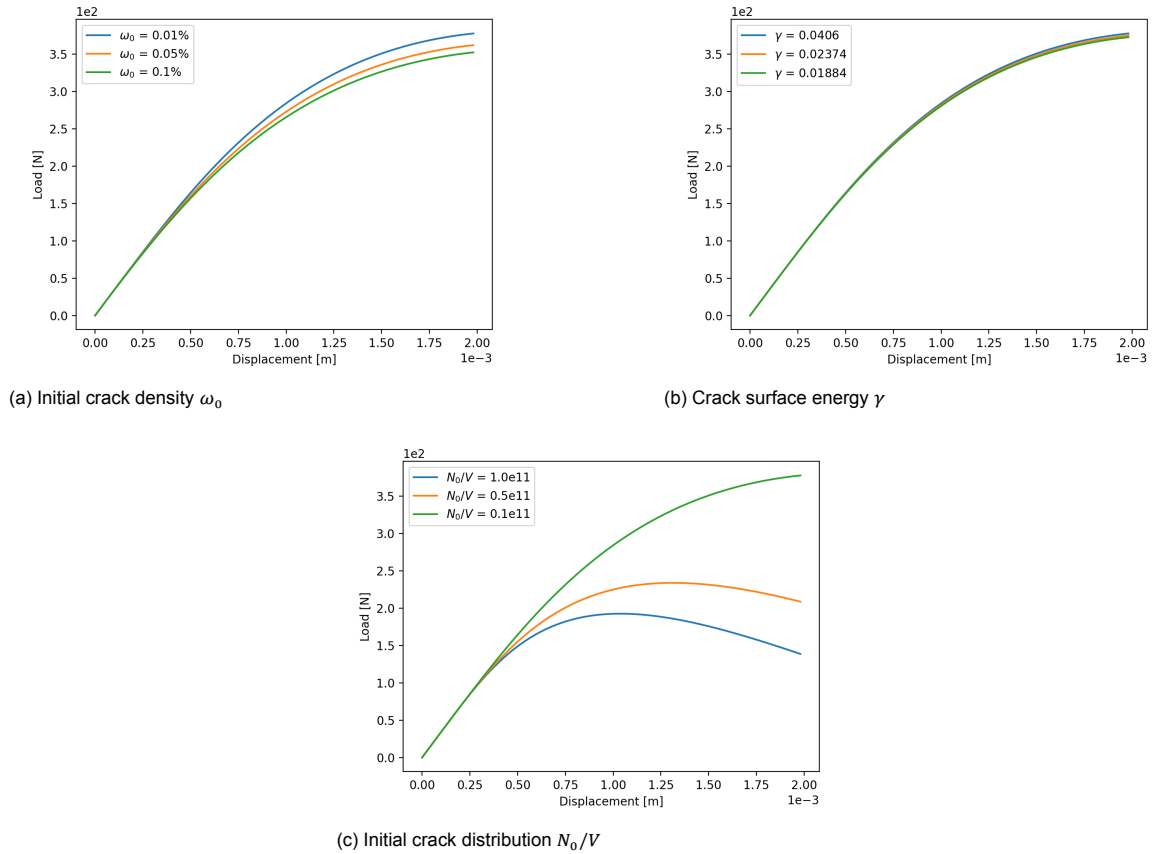


Figure 4.10: Response of ductile specimen for different values of ω_0 , γ , and N_0/V

the computational responses differently than variations of γ . There are two reasons for this. The first reason is that when σ_{n0} is investigated crack growth and crack nucleation take place concurrently. This results in crack growth before nucleation, prohibiting the hydrostatic stress from surpassing the threshold. The second reason is that crack nucleation produces a different behavior than crack growth. The damage compliances $\langle \bar{\mathbf{S}}^{*2} \rangle$ and $\langle \bar{\mathbf{S}}^{*4} \rangle$ are scaled by \bar{c} and N differently, and the evolution equations for the two damage mechanisms are also different. In fact, the rate of nucleation equation Eq. (4.20) depends on state while the rate of crack growth equation Eq. (4.23) does not.

The effect of the crack nucleation rate \dot{N}_0 is shown in Fig. 4.12. This rate determines brittleness associated to crack nucleation in the same manner that β determines brittleness associated to crack growth. The large differences observed in Fig. 4.8 between the brittle and ductile case for varying β are not observed here, because for both cases \dot{N}_0 acts over a similar portion of the loading range.

The effect of the constant parameter σ_1 is shown in Fig. 4.13. No physical justification was given for σ_1 by Curran, Shockley, and Seaman [8] or by Lee and Shin [20]. Therefore, σ_1 is assumed to be completely empirical. This parameter determines the importance of overstress on the rate of nucleation. This is clearly shown for the ductile case, where the effect of overstress is reduced for higher σ_1 until it becomes negligible. The overstress does not have a significant impact for the brittle case, except when σ is low enough such that it accelerates crack nucleation to the extent where crack growth never occurs. This is the case for $\sigma_1 = 2.0 \times 10^6$ in the figure. This special case exhibits negligible softening, suggesting that the nucleation softening term is small. The nucleation softening term is generally smaller than the crack-growth softening term because materials experience rupture when cracks grow, not when they nucleate. This suggests that for brittle damage predicting damage initiation is more important than describing damage evolution. As a side note, this means that if numerical instabilities are not an issue, the rate of crack growth equation Eq. (4.23) may be acceptable even though it is independent of state. Consequently, Lee's and Shin's original model [20] is applicable for very brittle

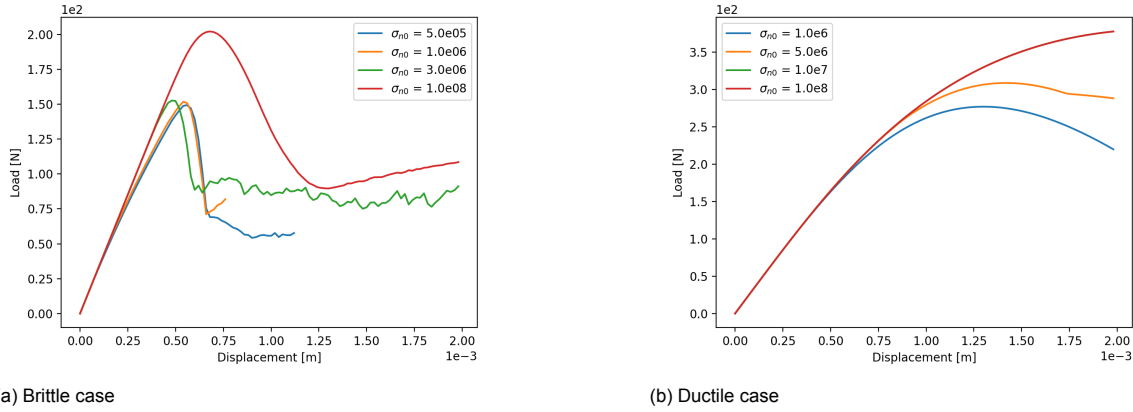


Figure 4.11: Response of specimen for different values of threshold stress σ_{n0}

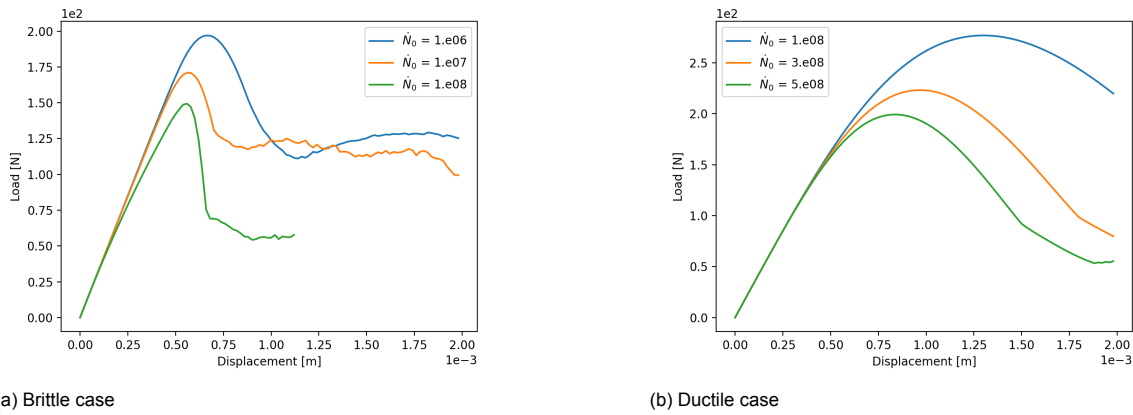
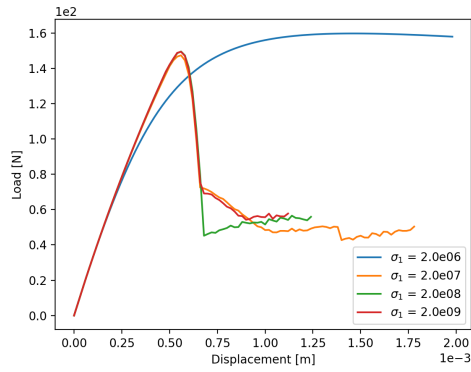


Figure 4.12: Response of specimen for different values of initial rate of nucleation N_0

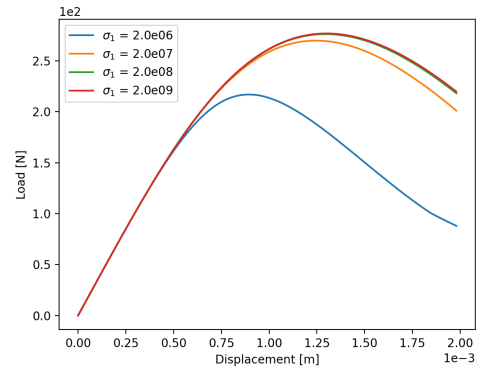
materials, provided that numerical instabilities do not compromise results.

The damage and the stress fields at ultimate strength are shown in Figures 4.14 and 4.15, respectively, for simulations with both crack growth and nucleation. Damage and stress distributions are similar to each other for the ductile case. This is not the case for the brittle case, where spurious non-symmetrical distributions are observed. Spurious distributions imply that local behavior is numerically unstable, even though local instabilities are not yet reflected in the global load-displacement response. This implies that local instabilities do not necessarily compromise global behavior when brittle damage is considered. Damage concentrates at the vertical edges of the specimen for numerically unstable behavior because the strain rate attains its lowest magnitude in those regions. For a detailed investigation of rate dependence see Section 4.3.5.

The crack nucleation damage mechanism will not be considered in the following sections of this thesis. The main motivation for this is that the rate of nucleation equation Eq. (4.20) introduces many material parameters that must be identified with complex experimental techniques. These experiments are not available for the matrix. Considering crack nucleation would increase the complexity of the parameter identification and it would reduce the generality of the damage model. Furthermore, it is not known if the nucleation parameters are phenomenological or material properties. In contrast, the only parameter that the rate of crack growth equation Eq. (4.23) introduces is the crack surface energy γ , which is a material property. Finally, it was shown in this section that crack growth is a more relevant mechanism than crack nucleation for capturing brittle material rupture.

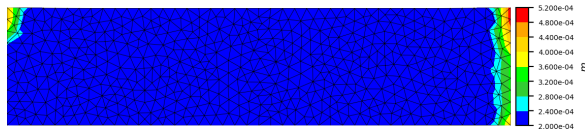


(a) Brittle case

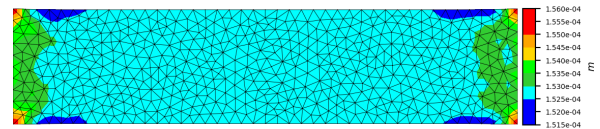


(b) Ductile case

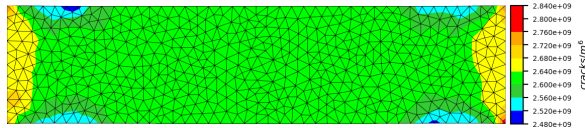
Figure 4.13: Response of specimen for different values of σ_1



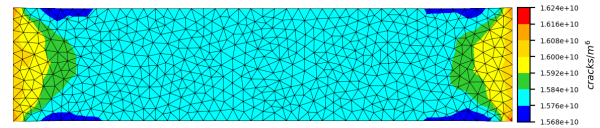
(a) Crack size \bar{c} for brittle case



(b) Crack size \bar{c} for ductile case

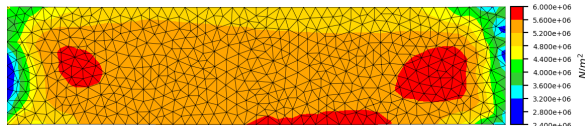


(c) Crack distribution N/V for brittle case

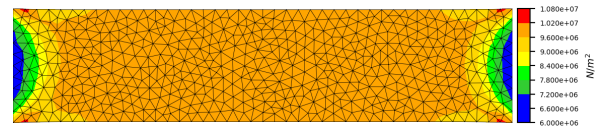


(d) Crack distribution N/V for ductile case

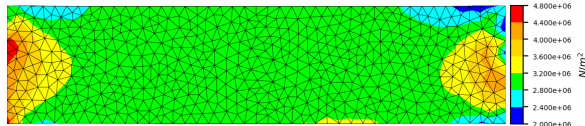
Figure 4.14: Damage fields



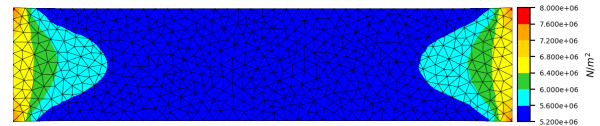
(a) Deviatoric stress for brittle case



(b) Deviatoric stress for ductile case



(c) Hydrostatic stress for brittle case

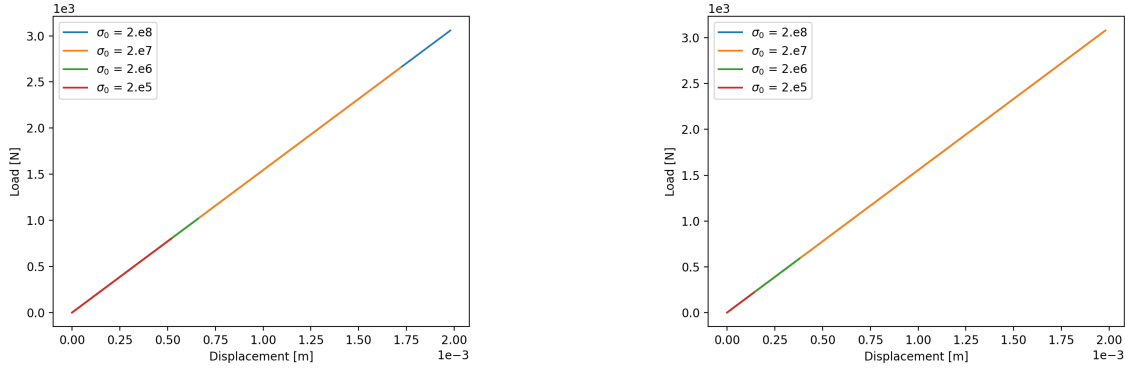


(d) Hydrostatic stress for ductile case

Figure 4.15: Stress fields

4.3.2. Compression

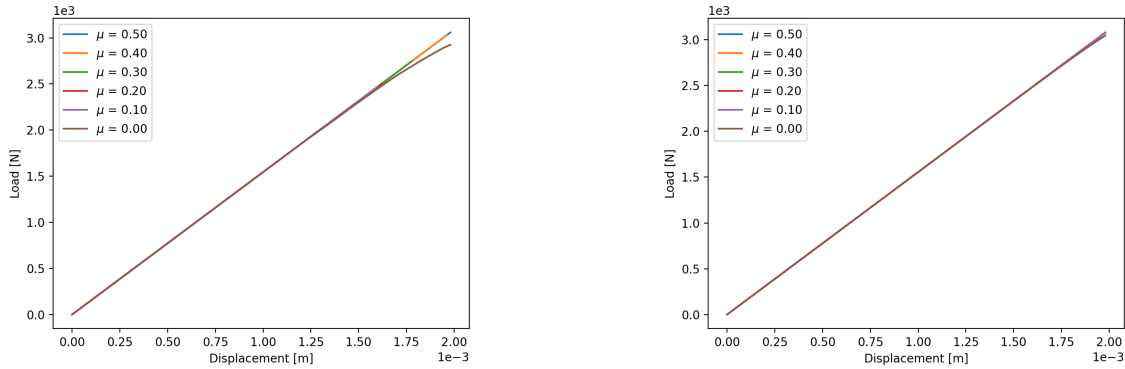
The crack growth evolution model proposed by Addessio and Johnson [2] allows damage to occur in a pure compression stress state, in contrast to most continuum damage models. The damage surface proposed by Addessio and Johnson for a negative hydrostatic stress depends on two additional material properties: the cohesive stress σ_0 and the coefficient of friction μ_{fr} . The effects of both these properties are shown in Figures 4.16 and 4.17 for compression simulations. The responses of both the brittle and the ductile cases appear to be either linear or quasi-linear for any choice of σ_0 and μ_{fr} . The two parameters only seem to affect the convergence behavior of the numerical solution.



(a) Brittle case

(b) Ductile case

Figure 4.16: Response of specimen for different values of cohesive stress σ_0



(a) Brittle case

(b) Ductile case

Figure 4.17: Response of specimen for different values of friction coefficient μ

In general, the modified model appears to exhibit early unconvergence for compression behavior before significant nonlinearities are apparent in the global load-displacement curves. Early unconvergence is a consequence of numerical instabilities. These instabilities are often local, and not visible in global load-displacement curves. The threshold crack density ω_{n0} is employed for the case where $\sigma = 2.0 \times 10^6$, which is different than the default $\omega_{n0} = 2.0 \times 10^7$, to improve numerical stability. The results are shown in Fig.4.18, which shows that ω_{n0} can improve convergence in the presence of nonlinearities. Figures 4.19a and 4.20a show the damage fields at peak load for different values of ω_{n0} . Damage is ubiquitous in the samples where $\omega_{n0} \neq 0.00$. In contrast, cracks do not coalesce when $\omega_{n0} = 0.00$, which explains why softening is not exhibited before unconvergence of the numerical solution. The effect that the magnitude of ω_{n0} has on the manifestation of damage depends on brittleness. Figure 4.18 shows that increasing ω_{n0} by 0.10 in the brittle case has a similar effect as increasing it by 0.01 in the ductile case. This occurs because the rate of crack growth is slower in the ductile case, so instabilities are less severe.

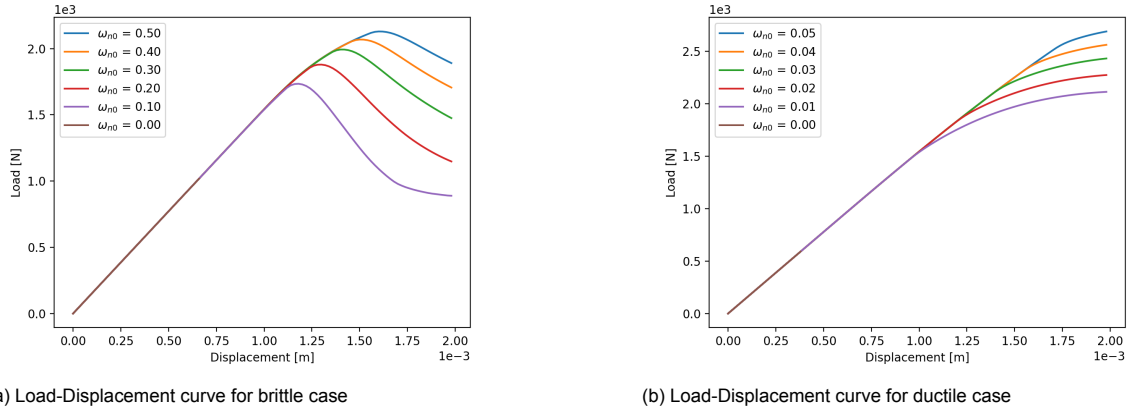


Figure 4.18: Response of specimen for different values of threshold crack density ω_{n0}

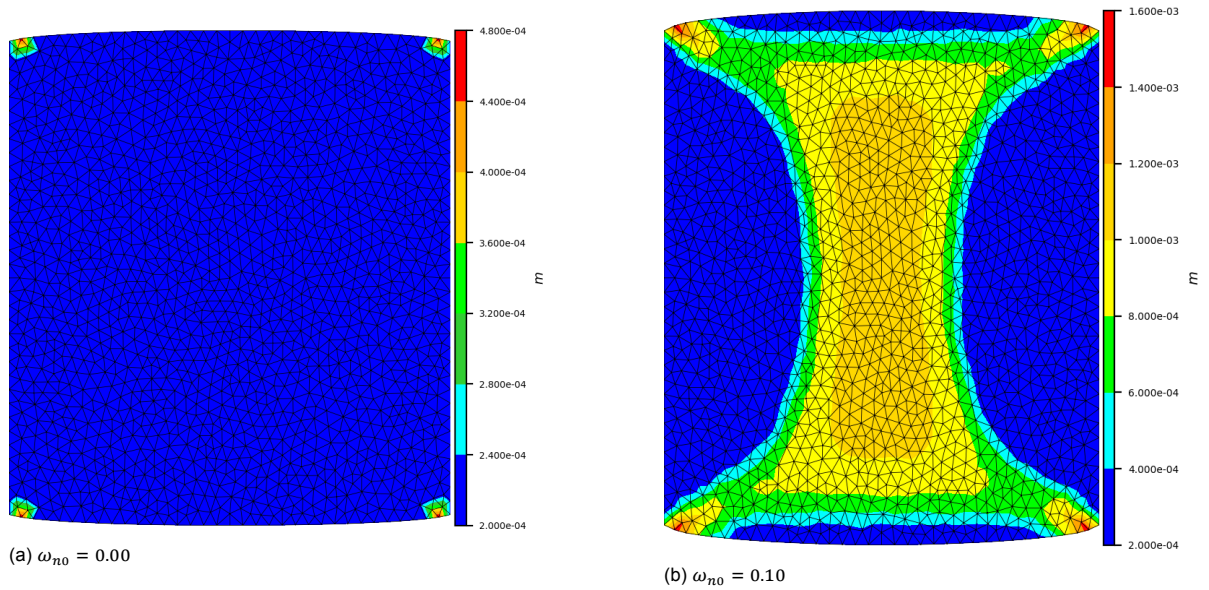


Figure 4.19: Brittle case damage fields at peak load for different values of threshold crack density ω_{n0} . Peak load corresponds to ultimate strength when $\omega_{n0} \neq 0.00$ and to the time step before nonconvergence when $\omega_{n0} = 0.00$.

Crack growth for negative hydrostatic stresses will not be considered in any other section of this thesis. The compression yield and ultimate strengths of TNO's matrix are not known with sufficient confidence. The compression experiments (Fig. 1.4b) always failed as soon as the samples became larger than the clamps, so experimental errors may have been significant. Therefore, the parameters σ_0 and μ_{fr} cannot be estimated by fitting to the experiments. The drawback of not considering damage for negative hydrostatic stresses is that shear damage is restricted and underestimated.

Since damage for negative hydrostatic stresses will not be considered, the effects of σ_0 and μ_{fr} are not investigated for varying values of ω_{n0} .

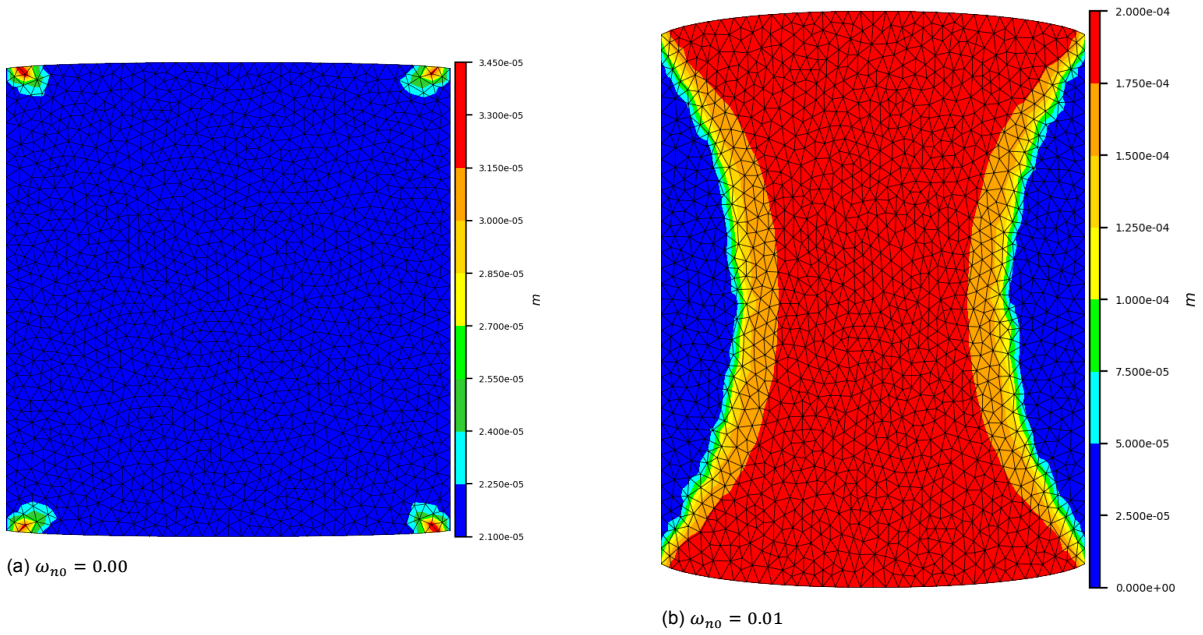


Figure 4.20: Ductile case damage fields at peak load for different values of threshold crack density ω_{n0} . Peak load corresponds to ultimate strength when $\omega_{n0} \neq 0.00$ and to the time step before unconvergence when $\omega_{n0} = 0.00$.

4.3.3. Shear

Like compression simulations, shear simulations also suffer from numerical instability. Therefore, the effect of the threshold crack density ω_{n0} is investigated in Fig 4.21. The results show that increasing ω_{n0} can stabilize shear behavior. However, the stabilizing effect is smaller than in compression. For all values of ω_{n0} the solution becomes unstable before softening. This is because cracks do not coalesce to form a failure plane, as shown in Fig. 4.22. Failure planes cannot form because damage is inhibited in regions of negative hydrostatic stress. The hydrostatic and deviatoric stresses for $\omega_{n0} = 0.00$ are shown in Fig. 4.23. The regions with negative hydrostatic stress coincide with the regions of highest deviatoric stress. Therefore, it is expected that damage would occur in these regions in reality.

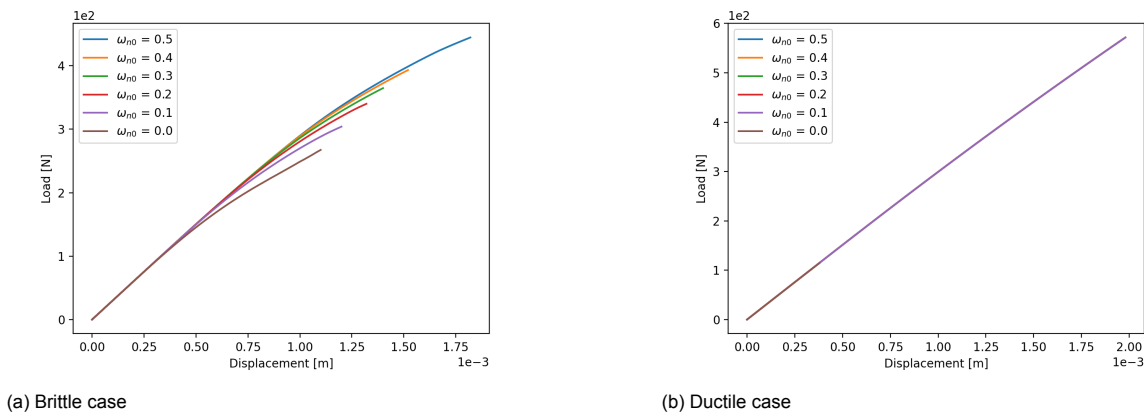


Figure 4.21: Response of specimen for different values of threshold crack density ω_{n0}

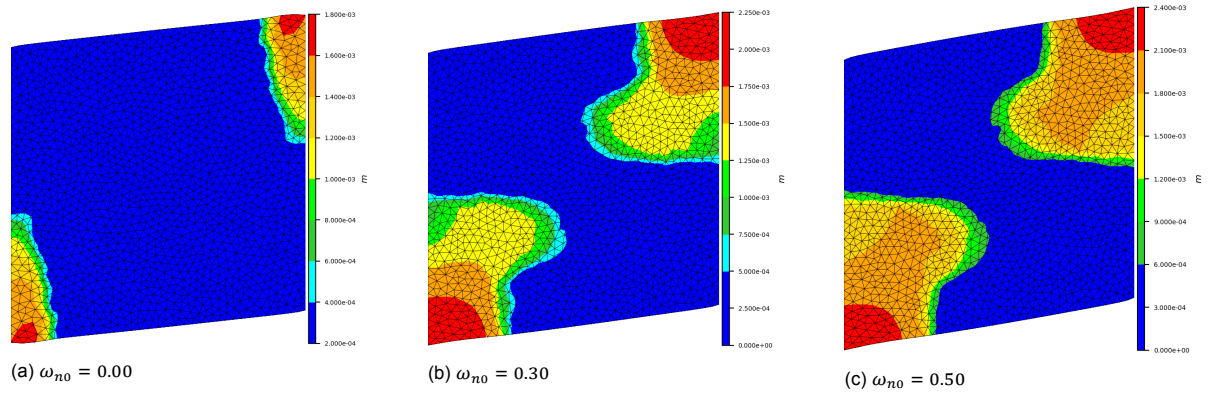


Figure 4.22: Brittle case damage fields for different values of ω_{n0} . At time step before unconvergence

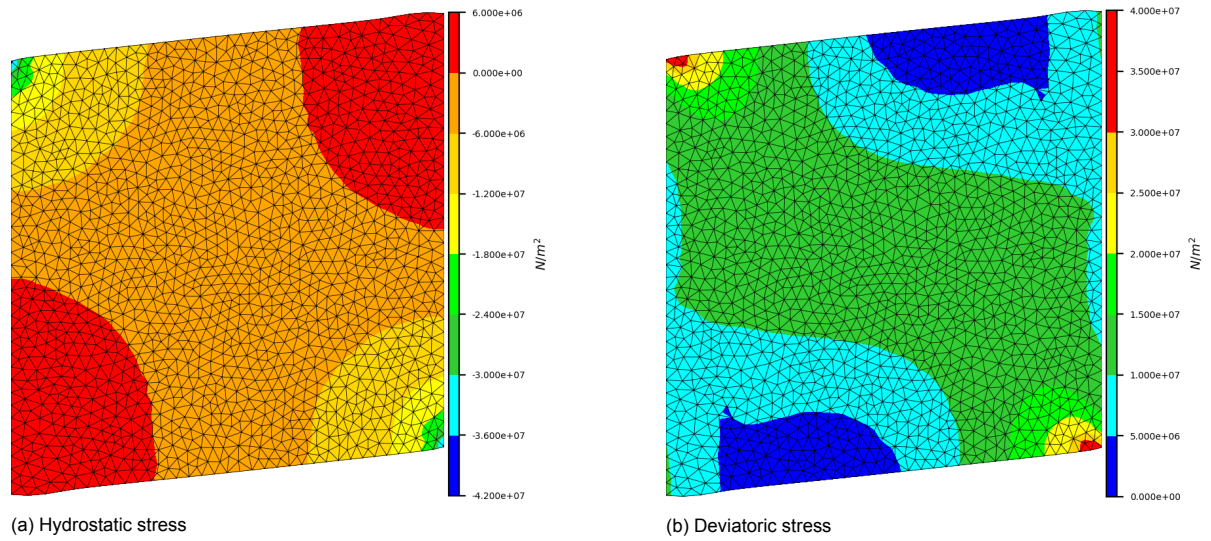
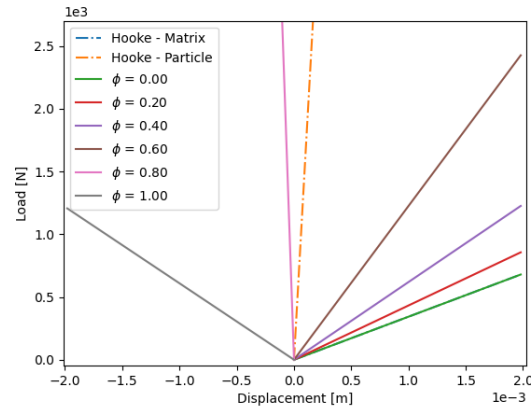


Figure 4.23: Brittle case stress fields for $\omega_{n0} = 0.00$. At time step before unconvergence

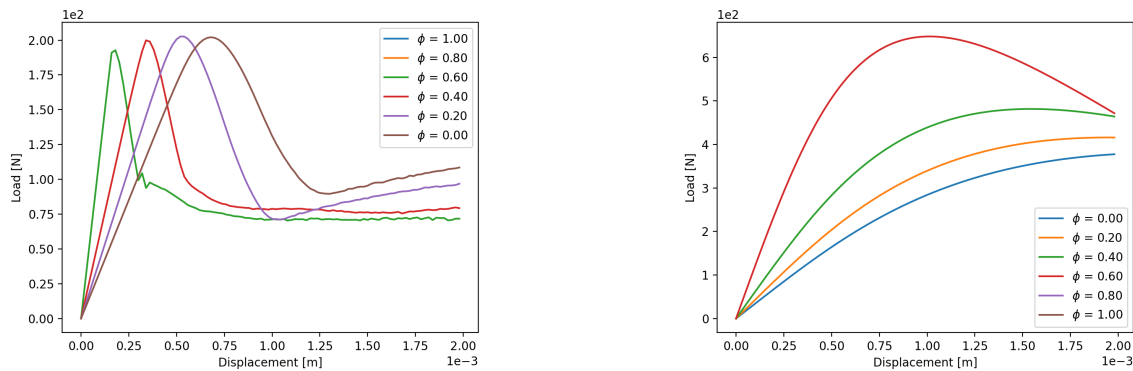
4.3.4. Effects of Inclusion of Particles

The compliances $\langle \bar{\mathbf{S}}^{*1} \rangle$ and $\langle \bar{\mathbf{S}}^{*3} \rangle$ that account for the presence of perfectly bonded particles are completely decoupled from the damage formulation of the model. They act as constant elastic additions to the secant compliance \mathbf{S} . Therefore, microscopic stress concentrations do not affect damage evolution. Additional ensemble averaged perturbed compliances that account for crack-particle interactions are necessary for this purpose [20]. The effect of the compliances $\langle \bar{\mathbf{S}}^{*1} \rangle$ and $\langle \bar{\mathbf{S}}^{*3} \rangle$ is shown in Fig. 4.24 for different volume fractions ϕ and without damage. For a volume fraction of $\phi = 0.00$ the result coincides with the elastic behavior of the matrix. For volume fractions up to $\phi = 0.60$ the stiffness increases monotonically with increasing ϕ , which is expected as the particles are stiffer than the matrix. For $\phi > 0.80$ the stiffness becomes negative, which is physically impossible. This suggests that the compliances $\langle \bar{\mathbf{S}}^{*1} \rangle$ and $\langle \bar{\mathbf{S}}^{*3} \rangle$ are only valid within the range of volume fractions $0.0 \leq \phi \leq \phi_c \leq 1.0$. That is, the compliances remain positive-definite for values of ϕ below a critical volume fraction ϕ_c , which is generally less than 1.0. The specific value of ϕ_c varies in a case-by-case basis; and depends on the elastic properties of the matrix, the elastic properties of the particles, and on how the properties of both constituents compare to each other.

The effect of ϕ in the presence of damage is shown in Fig. 4.25. Brittleness and ultimate strength increase with increasing ϕ . Until $\phi > \phi_c$, in which case the solution becomes unconverged in the first time step. This behavior is consistent with the real behavior of the matrix, for which brittleness and ultimate strength increase with stiffness. The effect of ϕ on ultimate strength is much greater for the

Figure 4.24: Response of specimen for different values of particle volume fraction ϕ without damage

ductile case than for the brittle case. In the brittle case failure occurs almost immediately after damage initiation, which occurs for the same stress state for all ϕ . Therefore, the elastic stiffness has little effect in the post-damage regime of the brittle case.



(a) Brittle case

(b) Ductile case

Figure 4.25: Response of specimen for different values of particle volume fraction ϕ with damage

4.3.5. Effect of Time Discretization

The rate of crack growth equation Eq. (4.23) is a dynamic relation. Consequently, the modified damage model is strain rate dependent. Strain rate is determined by the the global time step Δt , the time difference parameter Δt^{loc} , and the control parameter β . More precisely, $\dot{\epsilon} \sim \frac{\Delta t}{\Delta t^{loc} \beta}$. Figure 4.26 shows that Δt and β influence the load-displacement and crack evolution responses similarly, in the absence of numerical instabilities. Note that cracks do not grow for the smallest strain rate, as the response becomes locally unstable early in the deformation process. So the damage field is similar to that of Fig. 4.14a.

The effect of strain rate in the presence of numerical instabilities is shown in Fig. 4.27. The default strain rate of the ductile case is scaled down by a factor of 100, by either decreasing Δt or by increasing β . The figure shows that the global load-displacement and the local stress-strain responses obtained with the different scaling methods are very different. The stability of the crack-growth softening term depends on time step size. The term is unstable for both scaling methods, but it is less unstable when Δt is reduced. Finer time discretizations are generally more stable for the same strain rate, because the scaling gradient ($\partial \mathbf{C} / \partial \bar{\epsilon}$) of the softening term is more stable. This can be inferred from Fig. 4.27c, which shows that crack growth is smoother when Δt is reduced. The magnitude of crack growth is similar for both scaling methods despite the stress states being different. This is because the rate of

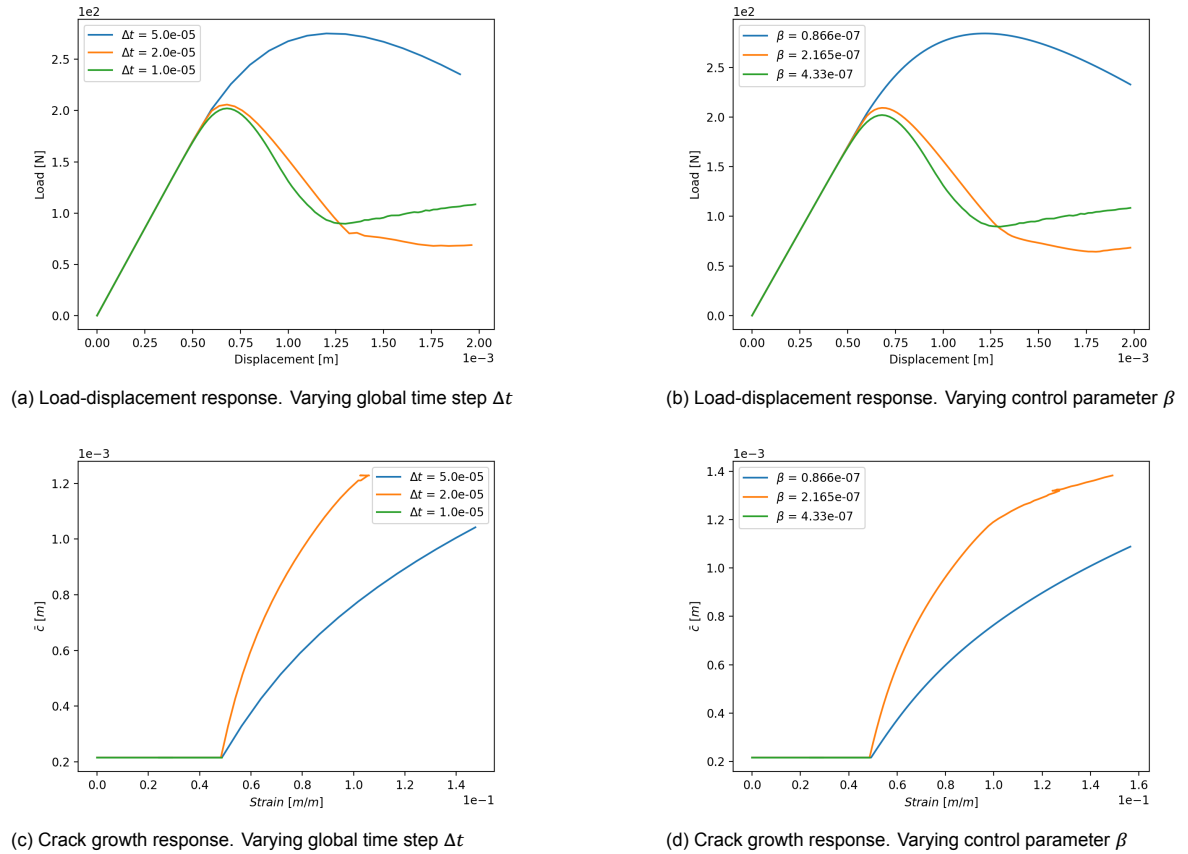


Figure 4.26: Comparison of the brittle case response for varying values of the global time step Δt and of the control parameter β . Where the strain rate is scaled equally by both parameters

crack growth equation Eq. (4.23) is independent of state.

The strain rate dependence of the model has important consequences regarding damage localization. In order to investigate localization, an RVE with 20 particles that represents the micro-structure of solid propellants is considered. The mesh for this RVE is shown in Fig. D.15 and its specific details are given in Table D.1. The set 2 parameters shown in Table 4.3 for $\dot{\epsilon} = 4.2 \mu\text{m}/\text{s}$ are the parameters employed for the simulations performed with this mesh. Figure 4.28 shows the global stress-strain behavior of the RVE for different strain rates and for different values of the threshold crack density ω_{n0} . Figure 4.29 shows the damage fields at ultimate stress and at maximum displacement for the curves of Fig. 4.28. The figures show that damage is more localized for lower strain rates, consequently the ultimate stress is smaller. These results are in agreement with the behavior of TNO's matrix, which exhibits higher ultimate strengths for higher strain rates.

The same patterns are observed for $\omega_{n0} = 0.00$ and $\omega_{n0} = 0.10$. Cracks grow bigger for $\omega_{n0} = 0.10$, but localization still occurs for low strain rates. This means that the ω_{n0} parameter, introduced in this thesis, does not reduce the model's ability to capture localization. Localization takes place for non-zero values of ω_{n0} because damage localizes even in the absence of the softening terms.

Figure 4.30 compares the localization behavior of the modified damage model to the localization behavior of an isotropic phenomenological damage model of the form $\sigma = (1 - \omega_{dam})\mathbf{C}\epsilon$. Where ω_{dam} is a damage variable that ranges from zero to one. The phenomenological model is rate-independent and no non-local technique is applied. Therefore, the phenomenological model predicts failure across a localization band for a very small applied deformation, as shown in Figures 4.30a–4.30c. This occurs for all possible sets of model parameters, so early failure is caused by loss of ellipticity. Figures 4.30d–4.30f show that the modified damage model behaves significantly different for the same strain rate. Damage concentrates in several locations and numerical instabilities occur. Damage concentrates in several locations as the damage surface depends on the deviatoric stress, whereas the initiation criterion for the

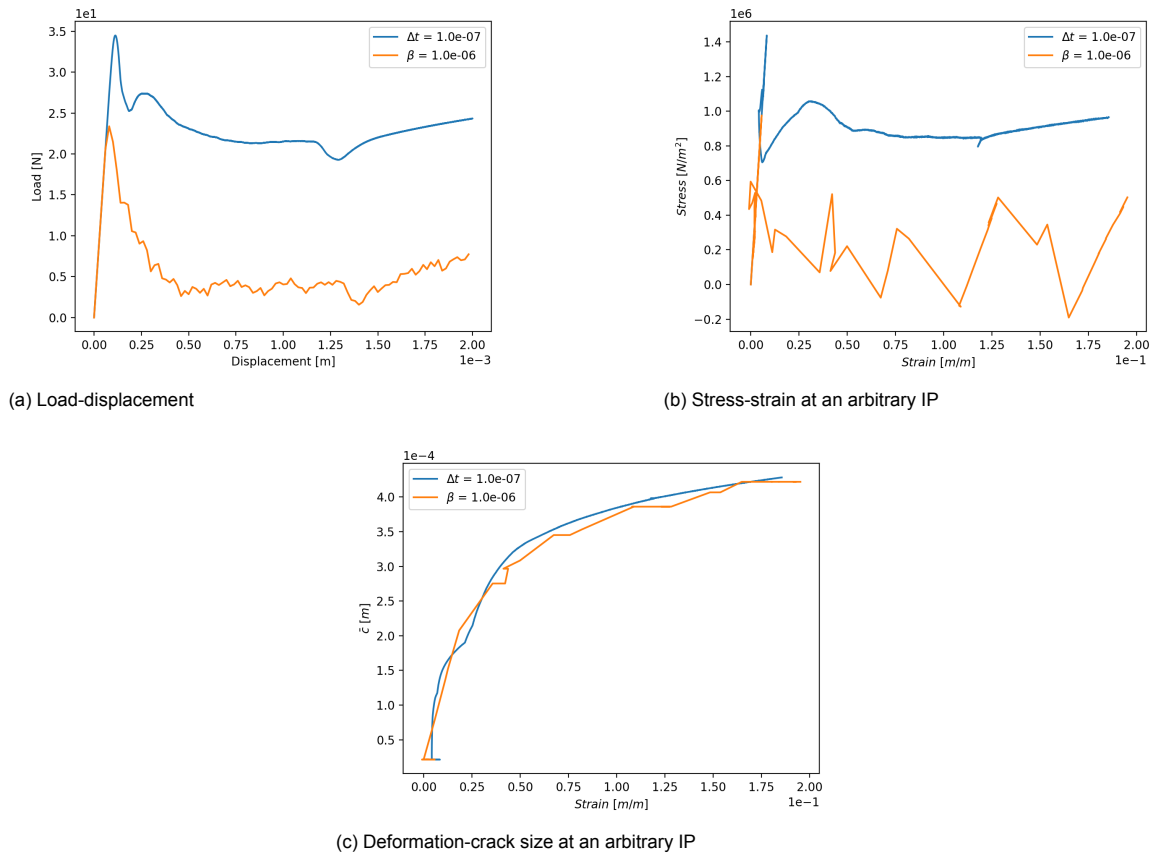


Figure 4.27: Unstable response of the ductile case. Where both Δt and β scale the original strain rate by 10^{-2} .

phenomenological model depends on the L2 norm of the principal strains. Furthermore, the modified model inhibits damage in regions of negative hydrostatic stress. A localization band is not observed due to the significant rate dependence, the inhibition of damage for negative hydrostatic stresses, and the distorting effect of numerical instabilities on the damage field. Numerical instabilities occur as the response is excessively brittle for the low strain rate considered. The modified model always generates numerical instabilities for strain rates that approximate quasi-static loading. This occurs because the crack-growth softening term initiates abruptly, causing a large discrete drop in stress. This is shown in Fig. 4.31 for a single-element mesh, where the smallest time step corresponds to a time discretization of one million steps.

Lee and Shin [20] employed a different rate of crack growth equation than the one employed for the modified damage model. Their implementation is rate dependent as well. Lee and Simunovic [21] implemented the same rate of crack growth equation as Lee and Shin [20] for a different constitutive model. Figure 4.32 shows the rate dependence found by Lee and Simunovic for a single-element mesh. Their results exhibit a similar rate dependent behavior as the one found in this section with the modified damage model. Their results do not exhibit numerical stability issues, which might be the case because they use a different constitutive formulation.

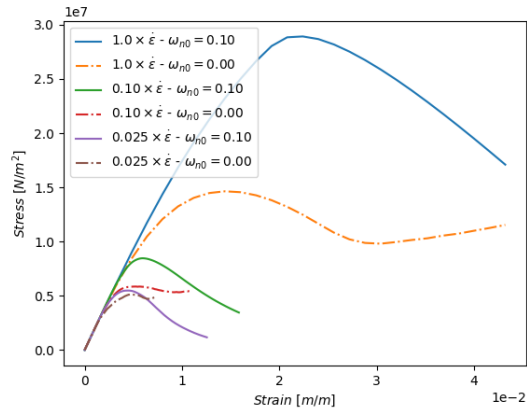


Figure 4.28: Response of RVE for different strain rates, where $\dot{\epsilon} = 4.2 \mu\text{m/s}$.

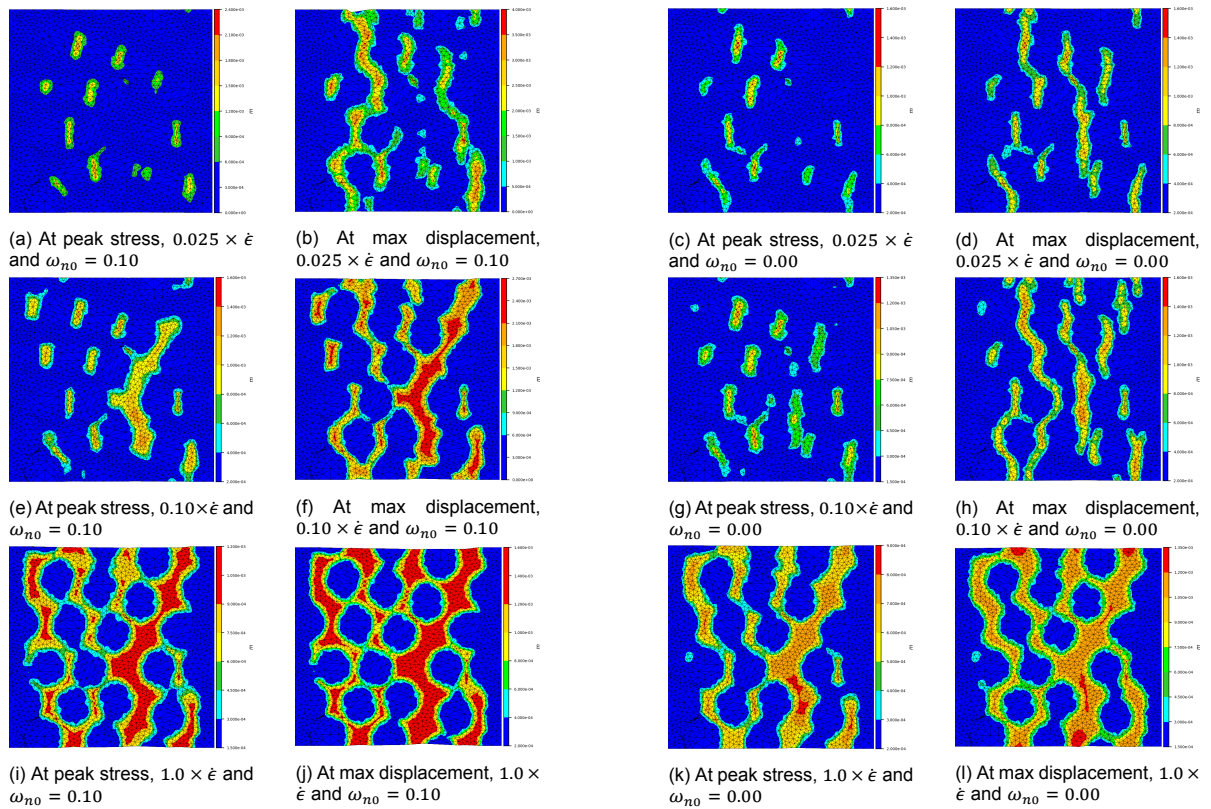


Figure 4.29: Damage fields for simulations of Fig. 4.28

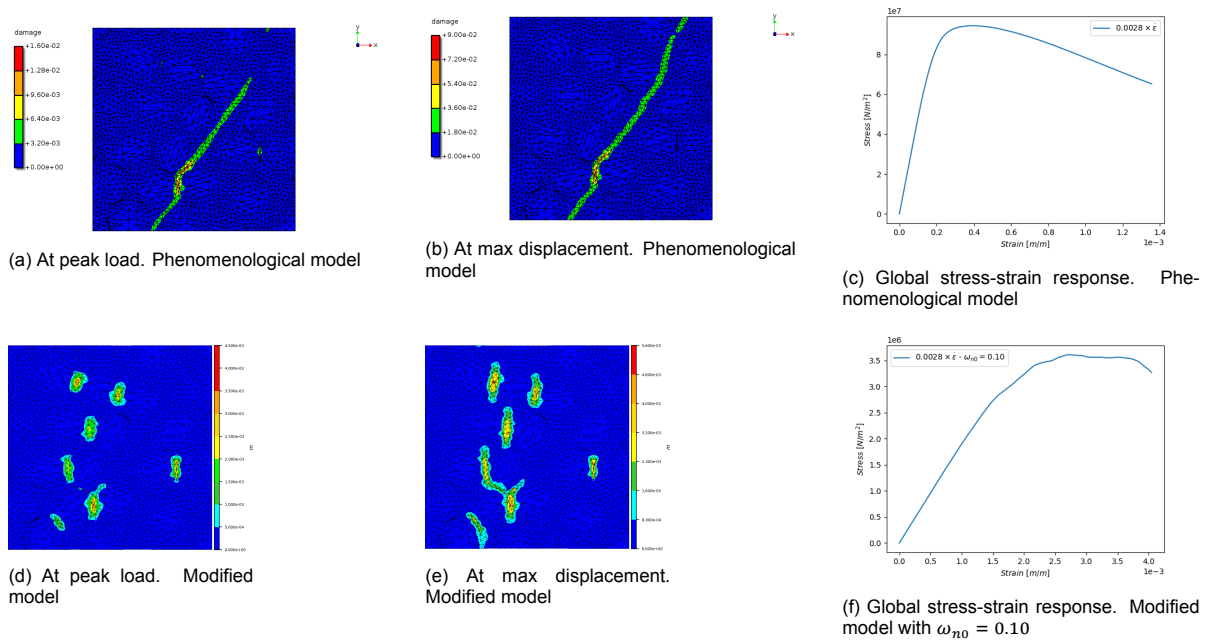


Figure 4.30: Comparison between the modified damage model and a phenomenological continuum model of the form $\sigma = (1 - \omega_{dam})\mathbf{C}\epsilon$

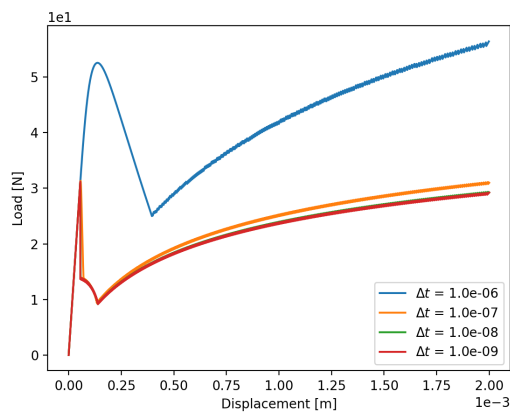
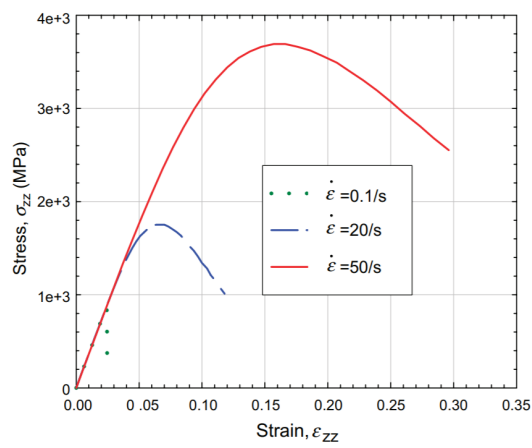
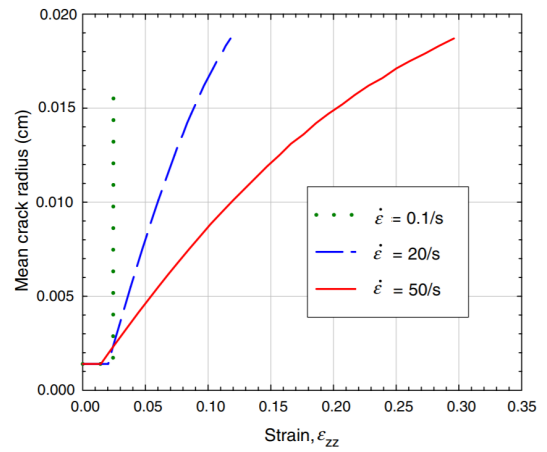


Figure 4.31: Convergence to quasi-static loading for a single-element mesh. The ductile case parameters are employed



(a) Stress-strain behavior



(b) Crack growth behavior

Figure 4.32: Stress-strain and crack growth rate dependence in tension observed by Lee and Simunovic [21] for a single-element mesh. The element has different dimensions as the tension specimen investigated in this chapter

4.3.6. Effect of Mesh Discretization

The modified damage model is strongly rate dependent, so it is not susceptible to loss of ellipticity. Recall from the literature review (Section 2.3) that loss of ellipticity produces singular rates of damage. Therefore, it causes mesh sensitivity because finer meshes approximate singularities better. Since the modified model does not suffer from loss of ellipticity and does not have any other source of mesh sensitivity, it is not mesh sensitive. Figure 4.33 shows that the response of the RVE from the previous section is very similar for three different mesh refinements. Meshes 1, 2, and 3 are shown in Figures D.13–D.15, and their details are given in Table D.1. The set 2 parameters shown in Table 4.3 for $\dot{\epsilon} = 4.2 \mu\text{m}/\text{s}$ and for elasticity are employed for the simulations. Except, the global time step is changed to $\Delta t = 2.045 \times 10^{-9}$, meaning the strain rate changes to $\dot{\epsilon} = 8.589 \times 10^{-4} \mu\text{m}/\text{s}$. Since the particulate RVE does not suffer from mesh sensitivity, it directly follows that the macroscopic matrix-only meshes (Fig. 4.1) are not mesh sensitive either. This is because localization bands form more easily in the RVE, so the RVE would be more prone to loss of ellipticity than the macroscopic meshes.

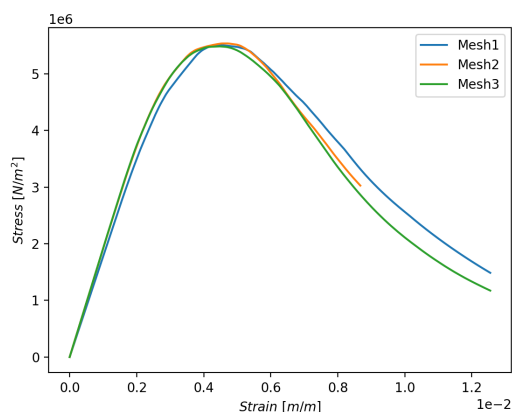


Figure 4.33: Response of RVE for different mesh refinements. Strain rate is $\dot{\epsilon} = 8.589 \times 10^{-4} \mu\text{m}/\text{s}$.

Throughout this chapter, the initial crack distribution N_0/V has been defined as uniform for all the IPs within a mesh. Alternatively, one might argue that N_0/V should be a function of element size because the RVE averaging volume V should scale accordingly to the macroscopic region that it represents. However, this approach would result in a poorly defined BVP, because the damage initiation criteria would not be homogeneous for the whole mesh. Recall from Section 4.3.1 that scaling N_0/V scales the ratio γ/\bar{c} , which determines the magnitude of the damage surface. Figure 4.35a shows that if $V = 0.10V_e$, where V_e is the volume of a finite element, then the initial damage field is heterogeneous. Figure 4.35b shows that numerical instabilities take place immediately after the stress state of any IP leaves its the damage surface. The figure exhibits the same spurious damage distribution discussed in Section 4.3.1 for Fig. 4.14a. The damage field shifts from heterogeneous to evenly (and spuriously) distributed in only one time step, 120 NR iterations were necessary for convergence. Figures 4.35c and 4.35d show that the spurious damage distribution persists throughout the entire simulation. The load-displacement responses of this simulation and two other simulations performed with different meshes of the same dimensions are shown in Fig. 4.34. The details of the meshes are shown in Table 4.2.

Mesh	Nodes	Elements
1	601	1096
2	2297	4384
3	8977	17536

Table 4.2: Details for meshes 1, 2, and 3

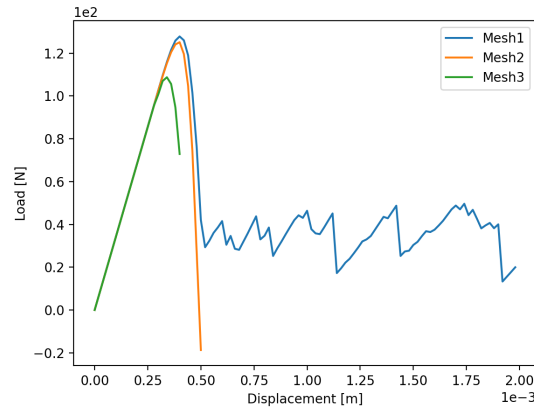


Figure 4.34: Ductile case response for different meshes when the initial crack distribution N_0/V depends on element size

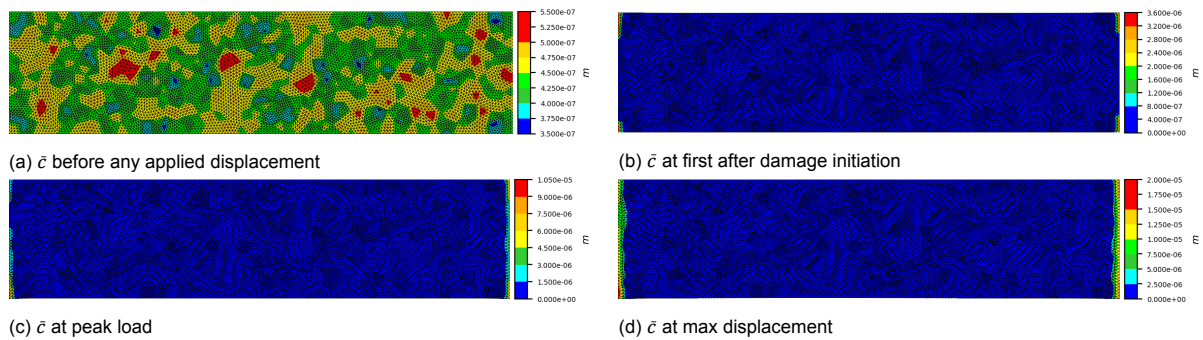


Figure 4.35: Damage fields for Mesh 3 at different stages of the loading process. N_0/V dependent on element size

4.4. Viscoelastic Damage of the Matrix

4.4.1. Behavior of the Matrix and Parameter Identification

Two different sets of damage parameters that can reproduce the results of the matrix-only preliminary experiment with strain rate $\dot{\epsilon} = 4.2 \mu\text{m/s}$ are shown in Table 4.3. Chapters 5–6 utilize these parameters to investigate the behavior of the solid propellants. The brittle viscoelastic parameters given in Table 3.2a were employed for identifying the damage parameters. Nucleation and crack-growth in regions of negative hydrostatic stress are not considered, because the available experimental data is insufficient for investigating these damage mechanisms.

The two sets of parameters correspond to $\omega_{n0} = 0.00$ (set 1) and to $\omega_{n0} = 0.10$ (set 2). The values for the parameters were found by simple trial and error. The only predefined condition was that the crack surface energy γ must be within 1–100 Pa m, which is a range where the surface energies of glassy polymers generally lie [11]. Sets 1 and 2 are non-unique in the sense that other parameter combinations can also reproduce the response of TNO's matrix for the values of ω_{n0} considered. The damage initiation criteria, the ultimate strength, and the overall brittleness can be controlled in multiple ways, as was shown in Section 4.3. Conversely, if the crack surface energy γ would be known from the manufacturer, the initial damage surface would be uniquely defined by a unique initial crack size \bar{c}_0 . The values for the initial crack density ω_0 , the initial crack distribution N_0/V , and the control parameter β would still be indeterminate. However, the bounds over which they yield good approximations to the experiments would be small. Alternatively, the initial crack density ω_0 could be set to a predefined value, in which case N_0/V would be uniquely defined by Eq. (4.11) and a unique β would yield the best approximation to the experiments.

The motivation for identifying set of parameters for $\omega_{n0} = 0$ and for $\omega_{n0} \neq 0$ is to determine the best balance between numerical stability and accuracy of the experimental approximations. Figures 4.36 and 4.37 show the approximations to the experiments for sets 1 and 2, respectively. Figure 4.38 compares the behavior for different strain rates for each set. The ultimate strength of the experiment

Parameter	Set 1	Set 2	Units
β	7.07×10^{-7}	1.01×10^{-6}	-
β	3.03×10^{-7}	4.33×10^{-7}	-
β	7.19×10^{-8}	1.03×10^{-7}	-
γ	11.8	11.8	Pa m
N_0/V	1.0×10^9	1.0×10^8	m^{-6}
ω_0	0.10	0.10	%
σ_{n0}	1.0×10^{999}	1.0×10^{999}	N/m^2
σ_0	1.0×10^{999}	1.0×10^{999}	N/m^2
ρ^*	1169.5	1169.5	kg/m^3
\hat{k}_1	0.987125	0.987125	-
\hat{k}_2	0.816686	0.816686	-
Δt^{loc}	1.0	1.0	s
ω_{n0}	0.0	0.10	%
ϕ	0.0	0.0	-
Δt	1.0×10^{-5}	1.0×10^{-5}	m

Table 4.3: Damage parameters for the matrix. Blue value is used when $\dot{\epsilon} = 1.8\mu m/s$, green value is used when $\dot{\epsilon} = 4.2\mu m/s$, red value is used when $\dot{\epsilon} = 17.7\mu m/s$. Nucleation is inhibited, so the parameters N and σ_1 are not shown

with strain rate $\dot{\epsilon} = 1.8\mu m/s$ is approximated better with set 1. The experiment with $\dot{\epsilon} = 17.7\mu m/s$ broke prematurely and therefore the ultimate strength is not representative of the material. However, set 1 most likely approximated the experiment with $\dot{\epsilon} = 17.7\mu m/s$ better, as higher strain rates produce more brittle responses. The shortcoming of set 1 is that it produces numerical instabilities, which are clearly visible in the load-displacement curves with $\dot{\epsilon} = 1.8\mu m/s$ and $\dot{\epsilon} = 4.2\mu m/s$ immediately after ultimate load. Consequently, the damage fields are spuriously distributed, as shown in Fig. 4.39. Conversely, instabilities are not visible in the load-displacement curves of set 2, and the damage fields (Fig. 4.40) are physically feasible. Set 1 approximates the global load-displacement behavior of the experiments better, but it predicts physically unreasonable local behavior. Set 2 deviates more from the experiments, but predicts physically sound local behavior. This thesis employs CH to analyze solid propellants. Therefore, set 2 is utilized in Chapters 5–6 because averaging theorems consider local behavior for transmitting information between different length scales.

The load-displacement response of the matrix for compression BCs is shown in Fig. 4.41a. The response is identical for set 1 and set 2, because there is no damage. The observed behavior is purely viscoelastic. Damage does not occur because the hydrostatic stress is negative everywhere, as shown in Fig. 4.41b. This poses a limitation for capturing the tensile behavior of solid propellants, because negative hydrostatic stresses occur in their micro-structure due to the presence of particles. As mentioned before, damage for negative hydrostatic stresses is not explored because of limitations of the experimental data.

The load-displacement response of the matrix for shear BCs is shown in Fig. 4.42. Both sets 1 and 2 show numerical instabilities. For set 2 these numerical instabilities are small and only visible for the strain rate of $\dot{\epsilon} = 1.8\mu m/s$. These instabilities are not a major issue for reproducing the tensile behavior of the propellants in Chapter 6, because shear is not the dominant load state in the micro-structure. However, set 2 is not ideal for capturing the behavior of the propellants for any arbitrary load state. A higher ω_{n0} would be required for this purpose. The drawback of increasing ω_{n0} is that the ability to capture the general strain rate dependent behavior may be compromised. An alternative to increasing ω_{n0} is to explore and apply rate of crack growth equations that depend on the state of the material. For recommendations on how to achieve this see Chapter 7.

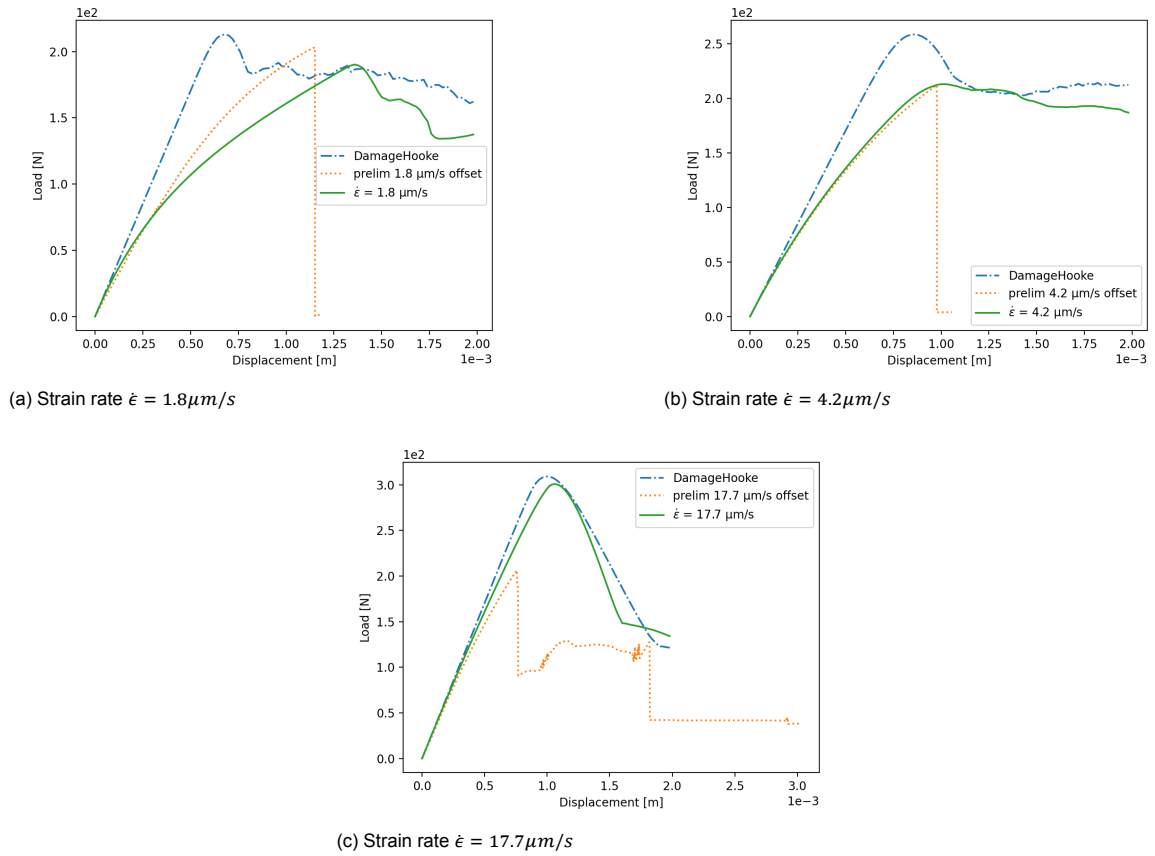
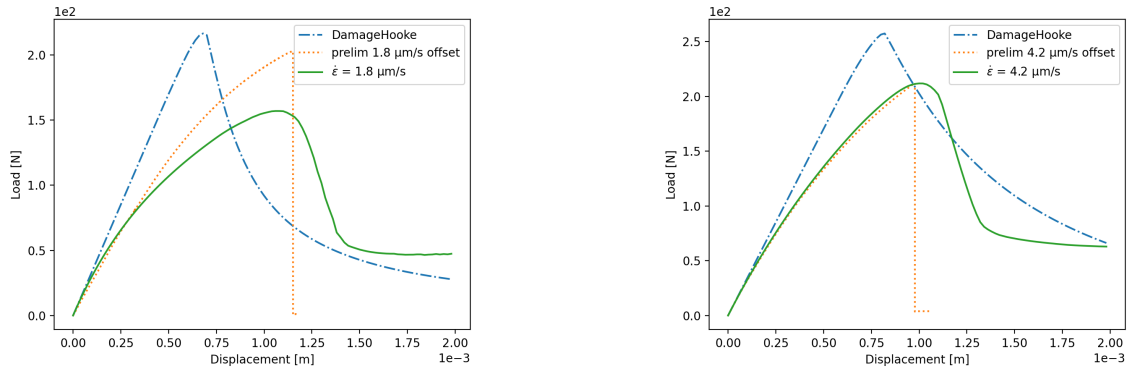
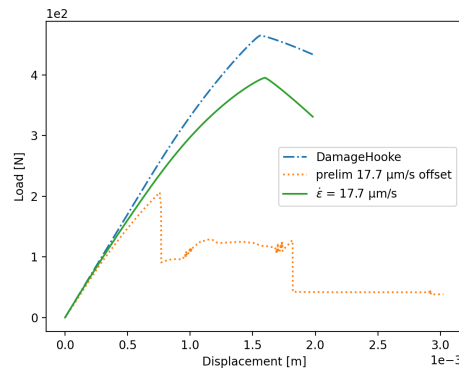


Figure 4.36: Tension response of specimen for set 1 parameters and different strain rates



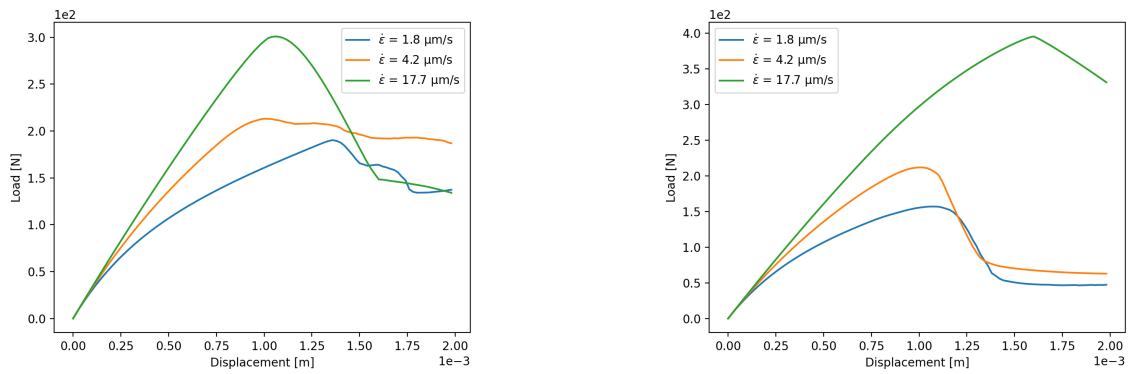
(a) Strain rate $\dot{\epsilon} = 1.8 \mu\text{m/s}$

(b) Strain rate $\dot{\epsilon} = 4.2 \mu\text{m/s}$



(c) Strain rate $\dot{\epsilon} = 17.7 \mu\text{m/s}$

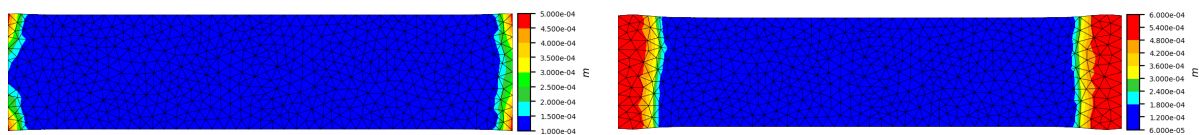
Figure 4.37: Tension response of specimen for set 2 parameters and different strain rates



(a) Set 1 parameters

(b) Set 2 parameters

Figure 4.38: Tension response of specimen for both sets of parameters and different strain rates



(a) Crack size \bar{c} at peak load.

(b) Crack size \bar{c} at maximum displacement.

Figure 4.39: Crack-size damage field for tension response. Set 1 parameters

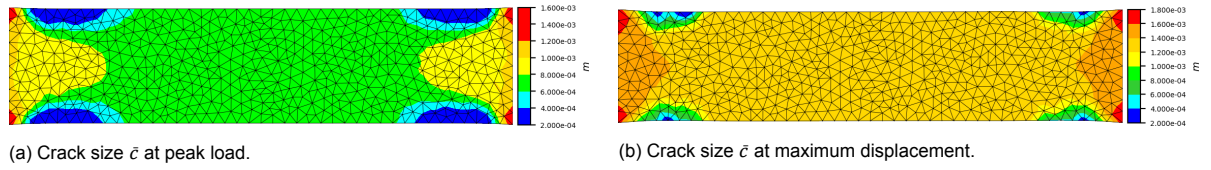
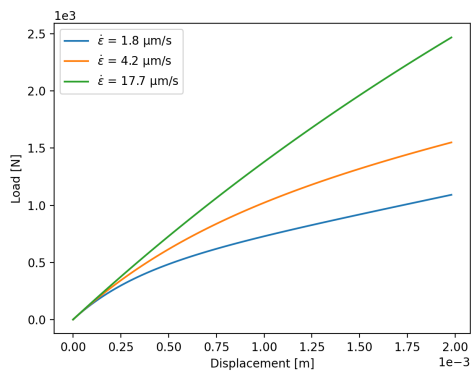
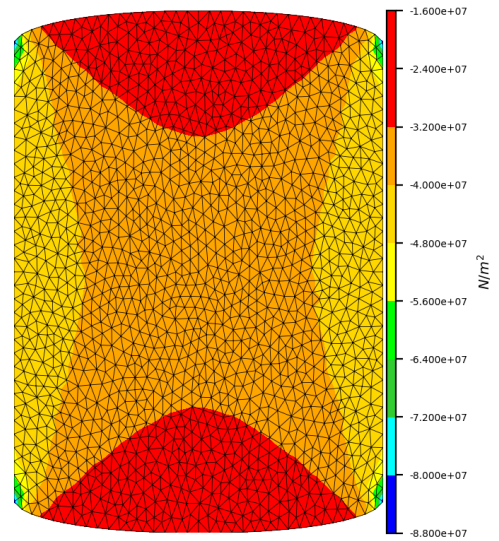


Figure 4.40: Crack-size damage field for tension response. Set 2 parameters

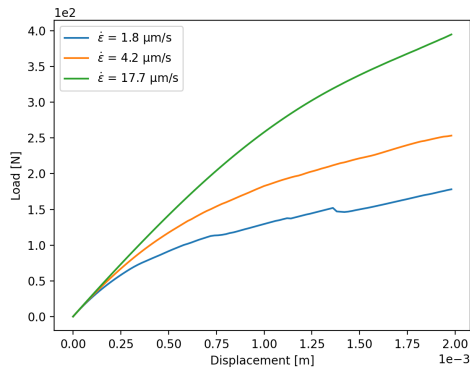


(a) Load-Displacement curves for different strain rates

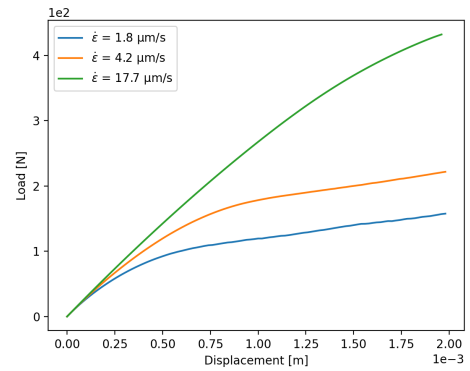


(b) Hydrostatic stress at max displacement for $\dot{\epsilon} = 17.7 \mu/s$

Figure 4.41: Compression response of specimen. Same response for both sets of parameters



(a) Set 1 parameters



(b) Set 2 parameters

Figure 4.42: Shear response of specimen for both sets of parameters and different strain rates

4.4.2. Viscoelastic vs. Non-Viscous Damage for Matrix Characterization

TNO's matrix-only tension experiments were successfully reproduced with the viscoelastic modified damage model. The experiments and their brittle failure can only be reproduced when viscoelasticity is considered. The non-viscous modified damage model cannot reproduce the experiments for brittle behavior because it behaves linear elastically before failure. In contrast, TNO's load-displacement curves exhibit significant nonlinearity prior to failure. Figures 4.36 and 4.37 show that the viscoelastic model can and that the non-viscous model cannot capture pre-failure nonlinearities. They also show that differences in response between both models become larger for lower strain rates because viscous effects become more significant. It is possible to capture the complete nonlinear behavior of the experiments with the non-viscous model if damage initiates early in the loading process. But then, ductile failure is assumed by definition. The matrix is known to exhibit brittle and viscoelastic behavior, so it necessarily has to be modelled with the viscoelastic modified damage model. The only additional properties that the viscoelastic damage model introduces in comparison to the non-viscous damage model are the elastic stiffnesses and the relaxation times of the Generalised Maxwell model. These properties can be identified from nonlinear least squares fitting and by accounting for Poisson locking, as was done in Chapter 3.

4.4.3. Behavior of Perfectly Bonded Solid Propellants

The parameters given in Table 4.3, with $\phi = 0.60$, are employed with the purpose of understanding the viscoelastic damage of TNO's solid propellants for the special case of perfectly bonded particles. Figures 4.43a and 4.43b compare the computationally predicted load-displacement behavior to the experiments. Note that the computational behavior was predicted for perfectly bonded particles, whereas debonding took place in the experiments. Also recall from Section 4.3.4 that the implemented model does not account for the effects of stress concentrations in the micro-structure.

The model captures the linear elastic regime remarkably well for both sets of parameters and for both strain rates. Evidently, the spurious behavior observed for high volume fractions ϕ in Section 4.3.4 does not occur for TNO's solid propellants when $\phi = 0.60$. The computational results exhibit significantly greater ultimate strengths and brittle responses than the experiments for both sets of parameters. This suggests that particle debonding and stress concentrations have an important influence on the behavior of the solid propellants. Note that the difference in behavior between the strain rates of $\dot{\epsilon} = 4.2 \mu\text{m}/\text{s}$ and $\dot{\epsilon} = 4.5 \mu\text{m}/\text{s}$ is larger for the experimental data than for the computational results. It is hypothesized that this is the case because the experimental specimens may have suffered from manufacturing flaws. It is also hypothesized that the source of the flaws was either poor interfacial bonding or clumping of the particles. The quality of the matrix was probably similar for both specimens because they both exhibit similar linear elastic regimes.

The damage fields in Fig. 4.44 show that local numerical instabilities are present for both sets of parameters at ultimate strength. The damage field for set 1 is significantly more distorted by these instabilities than the damage field for set 2. The set 2 load-displacement results are compared to CH results obtained for perfectly bonded propellants in Chapter 6. This is possible because local numerical instabilities do not imply that global load-displacement behavior is compromised, as was shown in the previous section. The results obtained with set 2 are in good agreement with the results of Chapter 6.

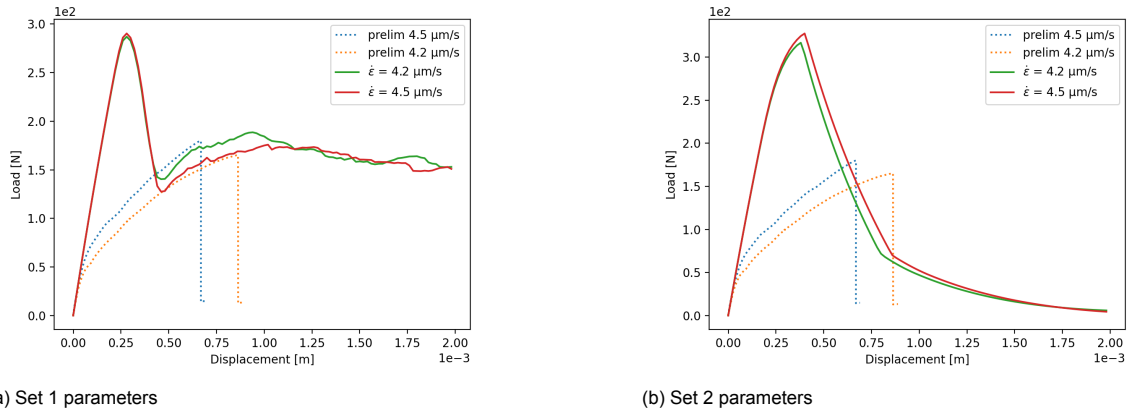
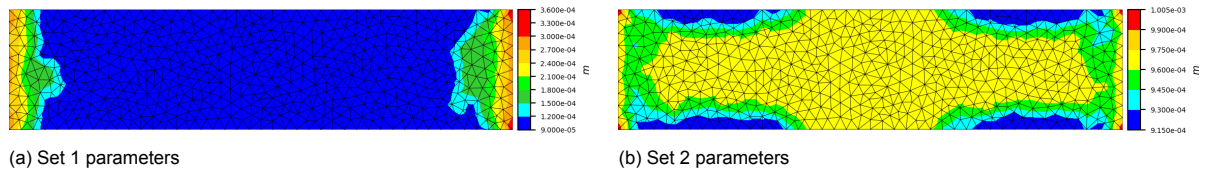


Figure 4.43: Tension response of specimen for both sets of parameters and different strain rates

Figure 4.44: Crack-size \bar{c} damage fields at peak load for both sets of parameters

4.5. Conclusion

Two modified versions of Lee's and Shin's damage model [20] were introduced in this chapter for investigating the effect of matrix damage in matrix-only and perfectly bonded solid propellant macroscopic samples. One version considers non-viscous damage and the other considers viscoelastic damage by applying the Generalised Maxwell model to the positive-definite term. In contrast to Lee's and Shin's original implementation, the both modified versions consider micro-crack growth in three orthogonal planes, a new parameter called the threshold micro-crack density ω_{n0} , and a different rate of crack growth equation. The direction of micro-crack growth was modified for better approximating the matrix and ω_{n0} was introduced for reducing numerical instabilities.

Tension, compression, and shear simulations were performed for the investigation. The modified models generally exhibit numerical instabilities in compression and shear, and also in tension when the input parameters describe highly brittle responses. Therefore, the effect of the newly introduced ω_{n0} was investigated for these cases. The parameter was found to greatly reduce numerical instabilities as its value increases, thereby fulfilling its intended purpose. The effect of the volume fraction ϕ was investigated for understanding its effect in perfectly bonded solid propellants. The constitutive terms $\langle \bar{\mathbf{s}}^{*1} \rangle$ and $\langle \bar{\mathbf{s}}^{*3} \rangle$ that account for perfectly bonded elastic particles were found to have a limited range of validity $0 \leq \phi \leq \phi_c \leq 1$. When ϕ exceeds the critical volume fraction ϕ_c , physically unfeasible behavior takes place. This negative result suggests that the model cannot be used to characterize some particulate composites. Strain rate dependence was investigated to understand its effect and to determine the extent to which it prevents early failure from loss of ellipticity. The observed dependence was significant and brittleness was observed as inversely proportional to strain rate (i.e. $\epsilon_u \propto \dot{\epsilon}^{-1}$). Both observations are encouraging because rate dependence was always sufficient to prevent loss of ellipticity and because the experiments exhibit the same brittleness trend. However, the results also show that numerical instabilities occur as quasi-static loading conditions are approached. This negative result suggests that the models cannot be employed for very low strain rates.

The viscoelastic damage model was employed for reproducing TNO's matrix-only experiments. Nucleation and crack-growth in regions of negative hydrostatic stress were not considered due to limitations in the experimental data. This was not a limitation for reproducing the matrix-only experiments because negative hydrostatic stresses do not take place. The damage parameters were identified by trial and error by fitting them to the experiment with strain rate $\dot{\epsilon} = 4.2 \mu\text{m/s}$. Identifications were per-

formed for the cases where $\omega_{n0} = 0.00$ and $\omega_{n0} = 0.10$ to determine if zero or non-zero ω_{n0} is better for continuing the investigation in the following chapters. The global behavior of the experiments with different strain rates were approximated better with $\omega_{n0} = 0.00$ than with $\omega_{n0} = 0.10$, however local behavior was significantly distorted. Therefore the parameters found for $\omega_{n0} = 0.10$ are more appropriate for a CH context, because averaging theorems transmit averaged local information between different scales. Mixed results were obtained for the effect of ω_{n0} in the matrix. The parameter permits to use CH in Chapter 6, but at the cost of some accuracy. Perfectly bonded solid propellants were investigated by considering a volume fraction of $\phi = 0.60$. In this case, the local behavior is distorted even with $\omega_{n0} = 0.10$. This, however, is not a major drawback because $\phi = 0.00$ in all the CH computations of Chapter 6 and because local instabilities do not necessarily compromise global behavior. Therefore, it will be possible to compare these results to the CH results of perfectly bonded solid propellants of Chapter 6.

The modified models generally exhibit favorable characteristics for modelling the matrix and perfectly bonded solid propellants, and are capable of providing insight about the effect of matrix damage in these materials. In particular, the models confirm that matrix micro-crack damage produces brittle failure. The main shortcoming of the modified models is that they exhibit numerical instabilities and that the technique employed for reducing them also reduces accuracy. Instabilities arise because the rate of crack growth equation is independent of state, which makes it questionable from a physics standpoint. The best way to improve these models is to find a suitable state dependent rate of crack growth equation. Shifting to such equation would drastically reduce numerical instabilities and improve the characterization of the matrix.

5

Micro-Structural Behavior and Debonding in the RVE

The micro-structural behavior of solid propellants is investigated by employing the continuum damage-viscoelastic model presented in Chapter 4 to the matrix and the Turon model for interface elements [30] to the matrix-particle interfaces. The response of the micro-structure is explored when all constituents are linear elastic, when only matrix viscoelastic damage is considered, when only interfacial damage is considered, and when both damage mechanisms act together. For each of these cases, the micro-structure is idealized utilizing various RVEs in which particles are pseudo-randomly distributed and which differ in number of particles, particle size, and mesh refinement. The particles are always treated as linear elastic. The goal of this investigation procedure is to understand how the different damage mechanisms and micro-structural geometric components affect the behavior of the micro-structure.

The behavior of the Turon model is explored in order to understand the effects of interfacial damage in solid propellants. The theoretical background for this model and for the FEM formulation of interface elements is given in this chapter. The Turon model was identified as a suitable model for characterizing particle debonding because it is thermodynamically consistent for mixed mode loading. This characteristic is essential for modelling the micro-structure because a variety of loading modes take place within it as a consequence of its particulate nature. This is true for all types of loading conditions (i.e. BCs).

Tension, compression, and shear BCs are applied to all the RVEs utilized in this chapter. Schematic representations of the generalized BCs and of the generalized RVE geometry are shown in Fig. 5.1. The elastic parameters identified in Chapter 3 (Table 3.1) are always employed for the particles, and also for the matrix when viscoelastic damage is not considered. The brittle viscoelastic parameters identified in Chapter 3 (Table 3.2a) and the set 2 damage parameters identified in Chapter 4 (Table 4.3) are employed for all cases where viscoelastic matrix damage is considered. A strain rate of $\dot{\epsilon} = 1.68 \times 10^{-4} \text{ s}^{-1}$ was applied to all simulations presented in this chapter. This is equivalent to the strain rate (which strictly speaking is a loading velocity, not a strain rate) of $\dot{\epsilon} = 4.2 \text{ } \mu\text{m/s}$ applied to the experiment utilized for identifying the damage-viscoelastic parameters.

The RVE meshes considered in this chapter are shown in Appendix D. The number of particles $nfx1$ in the RVEs varies from 10 to 100 and the particle size Df varies from $10 \text{ } \mu\text{m}$ to $40 \text{ } \mu\text{m}$. RVEs with uniform and normal particle size distribution are considered. RVEs with normally distributed particle size are assigned the label v1, v2, or v3, depending on the input utilized for pseudo-random sampling from the particle size PDF. See Appendix D for a more detailed description of the RVEs and the associated terminology. As default for meshes with uniform particle size, the number of mesh refinements is $n_m = 1$, the particle size is $Df = 30 \text{ } \mu\text{m}$, and the number of particles is $nfx1 = 50$. And for meshes with normally distributed particle size, the number of mesh refinements is $n_m = 0$, the input version for particle size generation is v2, and the number of particles is $nfx1 = 50$. If the type of particle size distribution (i.e. uniform or normal) within an RVE is not explicitly stated, assume a normal distribution.

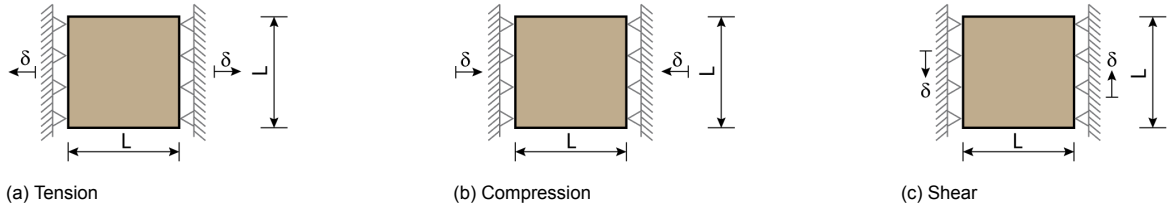


Figure 5.1: BCs applied to the RVEs

5.1. Theoretical Background

5.1.1. The Turon Model for Interface Elements

Turon et al [30] developed a model for interface elements which guarantees a smooth transition between free surface initiation and free surface propagation for all combinations of failure modes. Free surfaces are initiated after the cohesive strength τ^0 is exhausted, or equivalently, when the displacement jump exceeds the initiation criterion Δ^0 . For terminology clarification, note that in the context of this thesis free surface initiation refers to debonding damage initiation, since debonding is represented by free surfaces. Free surfaces propagate freely (i.e. without cohesive resistance) after the critical energy release rate G_c is exhausted, or equivalently, when the displacement jump exceeds the free surface propagation criterion Δ^f . The free surface formation process for the bilinear TSL proposed in the model is shown in Fig. 5.2. The smooth transition between free surface initiation and propagation ensures that energy dissipation in loading-unloading-reloading cycles is always positive, satisfying thermodynamic laws.

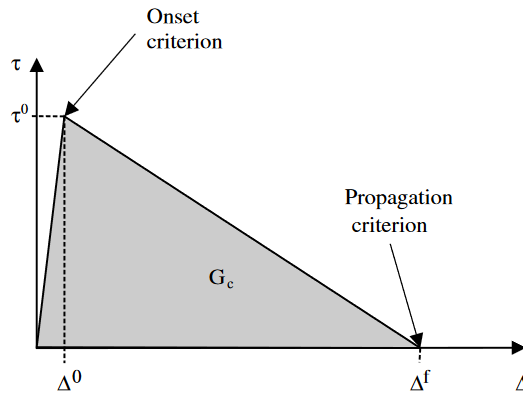


Figure 5.2: Bilinear TSL proposed in Turon [30]

The Turon et al [30] model describes a bilinear TSL based on a displacement jump and cohesive traction. The following notations are utilized in the description of the model. Operations within angle brackets are defined as $\langle x \rangle = \frac{1}{2}(x + |x|)$. Cohesive tractions and displacement jumps are represented by τ_j and Δ_j , respectively. Where the subscript j indicates the loading and/or failure mode. Normal mode I is denoted by $j = 3$ and tangential modes II and III are denoted by $j = 1$ and $j = 2$, respectively. The so-called shear cohesive traction and shear displacement jump are defined as

$$\tau_{\text{shear}} = \sqrt{(\tau_2)^2 + (\tau_3)^2}, \quad \Delta_{\text{shear}} = \sqrt{(\Delta_2)^2 + (\Delta_3)^2}, \quad (5.1)$$

The norm of the displacement jump λ and the damage threshold r determine when free surfaces may form and grow. More specifically, free surfaces evolve when $\lambda > r$. The damage threshold enforces the Kuhn-Tucker relations, so it is defined as

$$r = \max\{r^0, \lambda_{old}^{max}\} \quad (5.2)$$

Where r^0 is equal to the initiation displacement jump and λ_{old}^{max} is the largest value of the norm of the

displacement jump that has being achieved. The norm of the displacement jump is defined as

$$\lambda = \sqrt{(\Delta_3)^2 + (\Delta_{\text{shear}})^2} \quad (5.3)$$

The energy release rates for the different modes are given by G_I , G_{II} , and G_{III} . And the so-called shear energy release rate is defined as

$$G_{\text{shear}} = G_{II} + G_{III} \quad (5.4)$$

The proposed free surface initiation criterion $r^0 = \Delta^0$ (5.5) and free surface propagation criterion $r^f = \Delta^f$ (5.6) are given by

$$(\Delta^0)^2 = (\Delta_3^0)^2 + ((\Delta_{\text{shear}}^0)^2 - (\Delta_3^0)^2) B^\eta \quad (5.5)$$

$$\Delta^f = \frac{\Delta_3^0 \Delta_3^f + (\Delta_{\text{shear}}^0 \Delta_{\text{shear}}^f - \Delta_3^0 \Delta_3^f) B^\eta}{\Delta^0} \quad (5.6)$$

Where η is an experimental parameter which determines the size of the effect on the damage evolution by the difference between mode I and mode II debonding properties and the difference between the shear and the total damage states. The quantity B is given by

$$B = \frac{\beta^2}{1 + 2\beta^2 - 2\beta} \quad (5.7)$$

In which the mixed-mode ratio β is defined as

$$\beta = \frac{\Delta_{\text{shear}}}{\Delta_{\text{shear}} + \langle \Delta_3 \rangle} \quad (5.8)$$

Since the TSL is bilinear, the initiation (5.9) and propagation (5.10) criteria in pure normal and pure shear deformation are given by

$$\Delta_3^0 = \frac{\tau_3^0}{K}, \quad \Delta_{\text{shear}}^0 = \frac{\tau_{\text{shear}}^0}{K} \quad (5.9)$$

$$\Delta_3^f = \frac{2G_{I,c}}{\tau_3^0}, \quad \Delta_{\text{shear}}^f = \frac{2G_{\text{shear},c}}{\tau_{\text{shear}}^0} \quad (5.10)$$

Where τ_3^0 is the normal cohesive strength, τ_{shear}^0 is the shear cohesive strength, $G_{I,c}$ is the normal critical energy release rate, $G_{\text{shear},c}$ is the shear critical energy release rate, and K is the dummy stiffness. All these quantities are input material parameters.

The proposed constitutive relation is

$$\tau_i = (1 - d)C_{ij}^0 \Delta_j - dC_{ij}^0 \bar{\delta}_{3j} \langle -\Delta_3 \rangle \quad \text{with} \quad C_{ij}^0 = \bar{\delta}_{ij} K \quad (5.11)$$

Where C_{ij}^0 is the undamaged tangent stiffness, $\bar{\delta}_{ij}$ is the Kronecker delta, and d is a scalar damage variable given by

$$d = \begin{cases} 0, & \lambda \leq \Delta^0 \quad \& \quad r^0 \leq \Delta^0 \\ \frac{\lambda - \Delta^0}{\lambda} \frac{\Delta^f}{\Delta^f - \Delta^0}, & \Delta^0 < \lambda \quad \& \quad r < \lambda \leq \Delta^f \\ \frac{\Delta^f - \Delta^0}{\Delta^f - \Delta^0} \frac{\Delta^f}{[\Delta^0 + \Delta^f(\lambda - \Delta^0)]}, & \Delta^0 < r \quad \& \quad \lambda \leq r \leq \Delta^f \\ 1, & \Delta^f < \lambda \end{cases} \quad (5.12)$$

The tangent stiffness at a given moment of the loading process is obtained from the rate form of the constitutive relation, namely $\dot{\tau}_i = C_{ij}^{\text{tan}} \dot{\Delta}_j$. It is given by

$$C_{ij}^{\text{tan}} = \begin{cases} C_{ij} - K \left(1 + \bar{\delta}_{3i} \frac{\langle -\Delta_i \rangle}{\Delta_i} \right) \left(1 + \bar{\delta}_{3j} \frac{\langle -\Delta_j \rangle}{\Delta_j} \right) H \Delta_i \Delta_j & \Delta^0 < \lambda \quad \& \quad r < \lambda \leq \Delta^f \\ C_{ij} & \text{Otherwise} \end{cases} \quad (5.13)$$

Where C_{ij} is the secant stiffness and is given by

$$C_{ij} = \bar{\delta}_{ij} K \left[1 - d \left(1 + \bar{\delta}_{3j} \frac{\langle -\Delta_j \rangle}{\Delta_j} \right) \right] \quad (5.14)$$

And the quantity H is expressed as

$$H = \frac{\Delta^f \Delta^0}{\Delta^f - \Delta^0} \frac{1}{\lambda^3} \quad (5.15)$$

5.1.2. Finite Element Formulation of Interface Elements

Turon model's is implemented for interface elements within the FEM framework. The formulation for four-noded 1D interface elements is described here.

Suppose that the two faces of an interface element ie are called the positive and the negative face. Then, the displacement jump experienced by this element is given by

$$[\mathbf{u}_{ie}(\mathbf{x})] = \mathbf{u}_{ie}^+ - \mathbf{u}_{ie}^- = \mathbf{N}_{int} (\mathbf{a}_{ie}^+ - \mathbf{a}_{ie}^-) \quad (5.16)$$

Where the element's shape function matrix is formulated as

$$\mathbf{N}_{int} = \begin{bmatrix} N_1 & 0 & N_2 & 0 \\ 0 & N_1 & 0 & N_2 \end{bmatrix} \quad (5.17)$$

The contribution of the element towards the internal force vector \mathbf{f}_{int} is given by

$$\mathbf{f}_{ie,+}^{coh} = + \int_{\Gamma_d} \mathbf{N}_{int}^T \mathbf{t} d\Gamma, \quad \mathbf{f}_{ie,-}^{coh} = - \int_{\Gamma_d} \mathbf{N}_{int}^T \mathbf{t} d\Gamma \quad (5.18)$$

And the stiffness matrix of the element is given by

$$\mathbf{K}_{ie}^{int} = \begin{bmatrix} \int_{\Gamma_d} \mathbf{N}_{int}^T \mathbf{T} \mathbf{N}_{int} d\Gamma & - \int_{\Gamma_d} \mathbf{N}_{int}^T \mathbf{T} \mathbf{N}_{int} d\Gamma \\ - \int_{\Gamma_d} \mathbf{N}_{int}^T \mathbf{T} \mathbf{N}_{int} d\Gamma & \int_{\Gamma_d} \mathbf{N}_{int}^T \mathbf{T} \mathbf{N}_{int} d\Gamma \end{bmatrix} \quad (5.19)$$

5.2. Linear Elastic Behavior

The linear elastic behavior of the micro-structure of solid propellants is investigated by considering both the matrix and the particles in the RVEs as linear elastic.

The effect of mesh refinement on the stress-strain behavior is shown in Fig. 5.3. Mesh refinement affects the results for tension/compression¹ and shear BCs similarly. Mesh refinements 1 and 2 are closer to each other than mesh refinements 0 and 1. This occurs because in elasticity the order of convergence of nodal displacements is $O(h^2)$ for elements with linear shape functions, where h is a measure of element size [34]. The figure shows that as mesh refinement increases the response becomes stiffer. This is counter-intuitive because for homogeneous materials coarser meshes are generally stiffer, however the RVE represents a heterogeneous material. Where stress concentrations are in regions where particles are close to each other. Figure 5.4 shows that for the finer mesh the magnitudes of the highest stress are generally higher, and that stress concentrations are less spread out. Conversely, for the coarser mesh stress concentrations occupy larger regions, significantly extending into the particles, so they are said to change location. Since stresses at regions of stress concentrations are larger and more localized in the soft matrix for the finer mesh, strains are also larger in these regions (see the strain fields). Larger strains translate to more strain energy, and more strain energy translates to more external work done by the BCs. Therefore, the change in magnitude and location of stress concentrations explains why the RVE becomes stiffer for finer meshes. This also explains why the change in stiffness upon refinement is relatively large compared to a linear elastic BVP.

The effect of particle distribution and particle size Df on the stress-strain behavior is shown in Figures 5.5 and 5.6 for RVEs with particles of uniform and varying size, respectively. Figure 5.5 shows that for both tension/compression and shear BCs the responses of different RVEs with uniform particle size are very similar. This occurs because the solutions of linear elastic BVPs are size-independent, when BCs are scaled accordingly to specimen size. The linear elastic constitutive relation is formulated in terms of strains and stresses, which are length scale-independent relative measures of force and deformation. The small differences in response observed in Figure 5.5 are purely a consequence of the different spatial distributions of particles. The effect of particle distribution is small because the number of particles considered (i.e. $nfx1 = 50$) is high enough such that the different RVEs have similar averaged responses. That is, stress concentrations appear with similar frequency in all RVEs, so in order to achieve the prescribed strains the BCs apply similar amounts of external work to all the RVEs. Figure 5.6 shows that when Df varies within the RVEs the responses of the different RVEs are also very similar. This is because the number of particles is high enough such that the Gaussian PDF from which Df is sampled manifests similarly in the different RVEs. Therefore, even though particle size distribution is not the same for all RVEs, it is very similar.

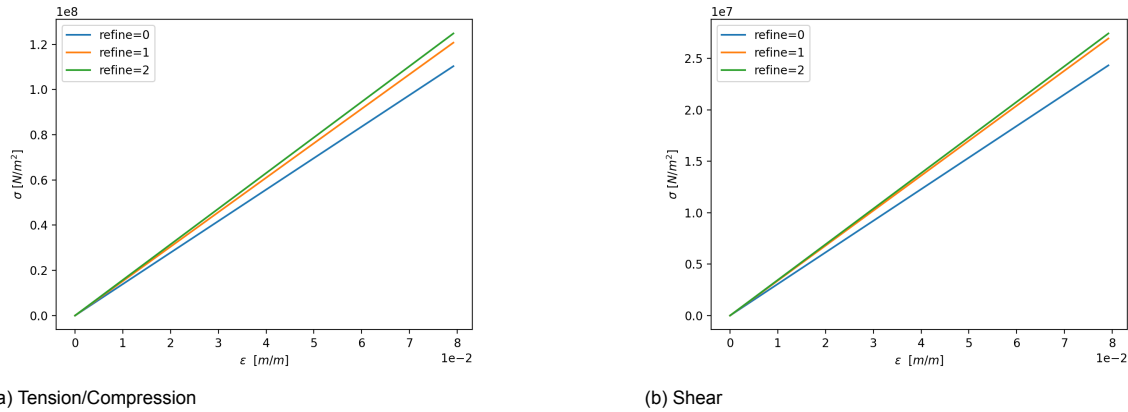


Figure 5.3: Effect of mesh refinement for v2 RVE with 50 particles

The effect of the number of particles $nfx1$ on the stress-strain behavior is shown in Figures 5.7 and 5.8 for RVEs with particles of uniform and varying size, respectively. The figures show that when outlier responses exist they correspond to RVEs with relatively low $nfx1$ for both types of particle size distribution and for both tension/compression and shear BCs. RVEs with low $nfx1$ can have significantly different responses than RVEs with high $nfx1$ because stress concentrations, or the lack of them, affect their response more acutely. As $nfx1$ increases responses show less sensitivity to it, because the overall (or homogenized) properties of the RVE approach statistical homogeneity. Recall that in order to formulate the constitutive relations that account for microscopic particles (Eqs. (4.3) and (4.13)), the model presented in Chapter 4 assumed that particulate composites achieve statistical homogeneity when separation of scales holds. Therefore, the validity of this assumption is confirmed by the results shown here. Note that the responses of the RVEs subjected to shear BCs show greater scatter than the responses of the RVEs subjected to tension BCs for both types of particle size distribution. This suggests that dilational material properties converge faster than distortional material properties, because dilational behavior affects stress-strain response more for tension/compression than for shear BCs. Therefore, the following relation is implied $CR(\mu_h) < CR(K_h) < CR(\lambda_h)$; where $CR(\cdot)$ denotes convergence rate towards statistical homogeneity and μ_h , λ_h , and K_h are the homogenized Lamé parameters and the homogenized bulk modulus, respectively. Note that the bulk modulus K_h converges faster than the Lamé parameter λ_h , as K_h is defined in terms of both Lamé parameters. Figures 5.9 and 5.10 show that hydrostatic pressure fields vary less with respect to $nfx1$ in magnitude and distribution than deviatoric stress fields for both types of BCs, as expected from comparing the tension and shear responses.

¹In linear elasticity BCs that differ only in sign, produce solutions that also differ only in sign. Therefore, when sign is omitted, tension and compression BCs yield the same result.

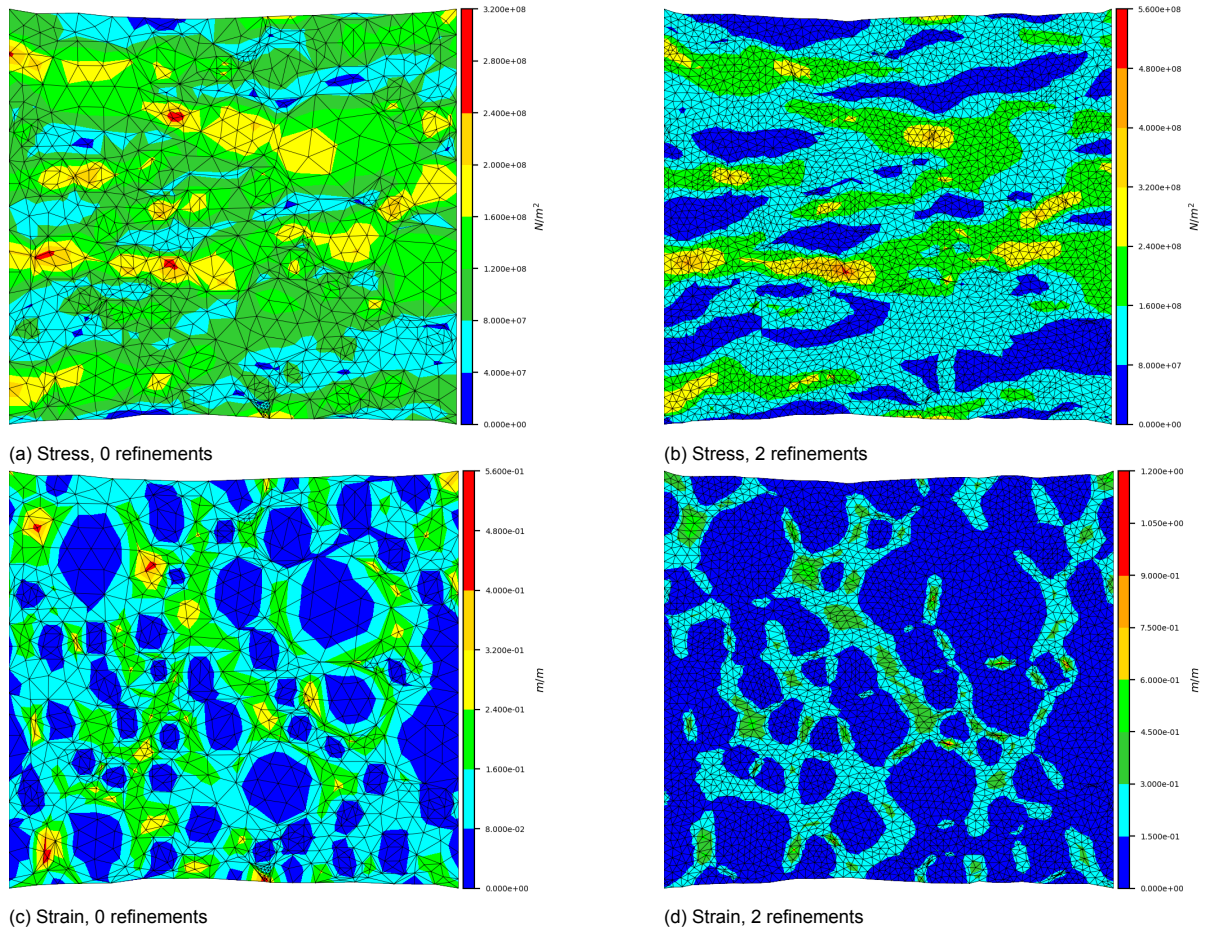


Figure 5.4: Maximum principal stress and strain fields for v2 RVE with 50 particles when subjected to tension BCs for different mesh refinements

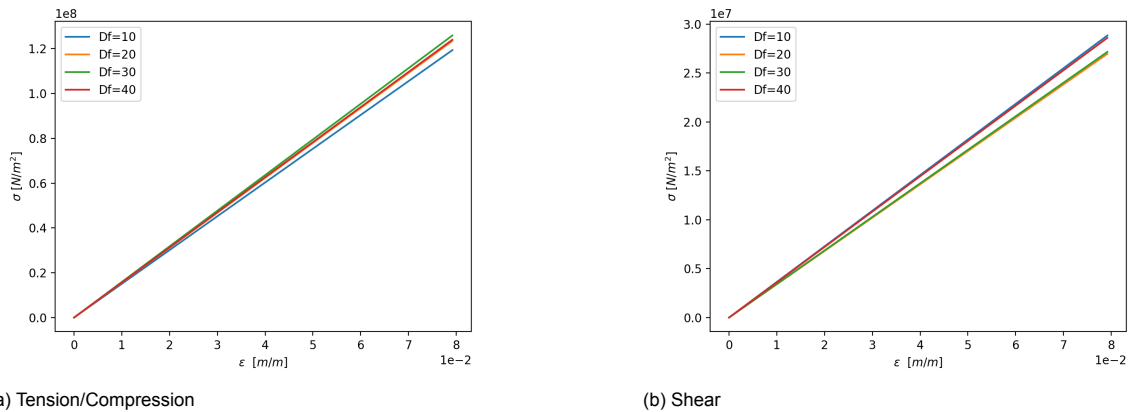
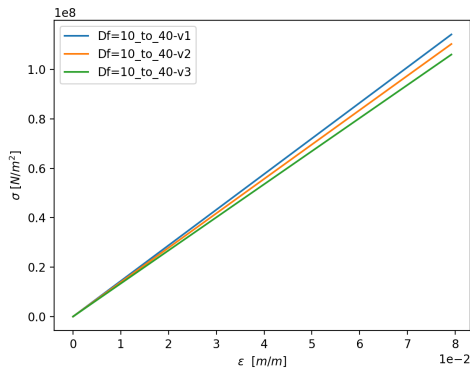
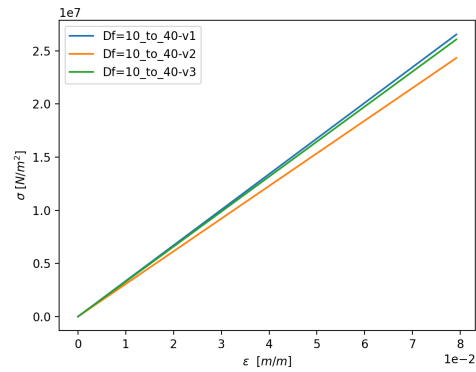


Figure 5.5: Effect of particle distribution and particle size Df for RVEs with uniformly distributed particle size

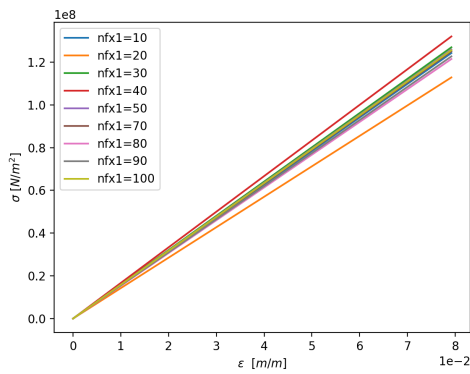


(a) Tension/Compression

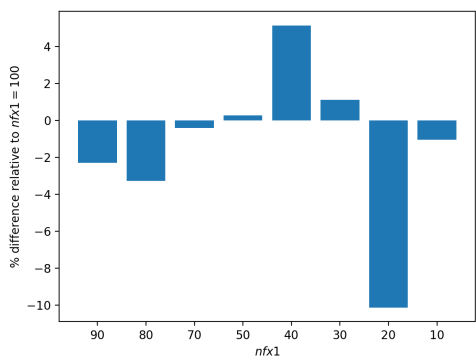


(b) Shear

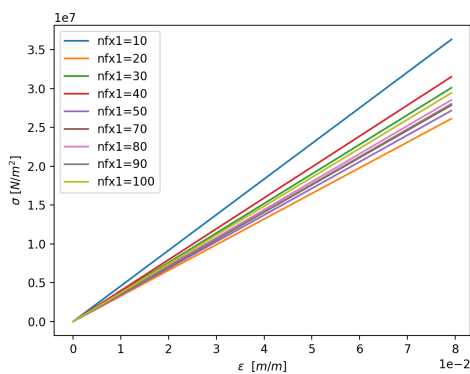
Figure 5.6: Effect of particle distribution and particle size distribution for RVEs with normally distributed particle size Df



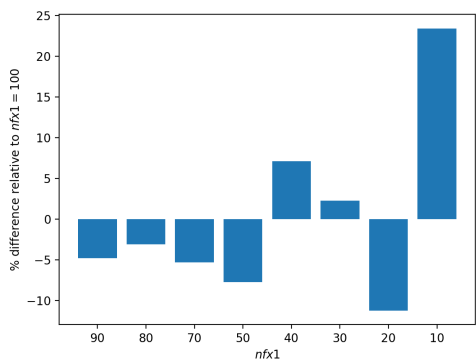
(a) Tension/Compression



(b) Relative differences in ultimate stress between the curves in Fig. 5.7a



(c) Shear



(d) Relative differences in ultimate stress between the curves in Fig. 5.7c

Figure 5.7: Effect of number of particles $nfx1$ for RVEs with particle size $Df = 30\mu m$

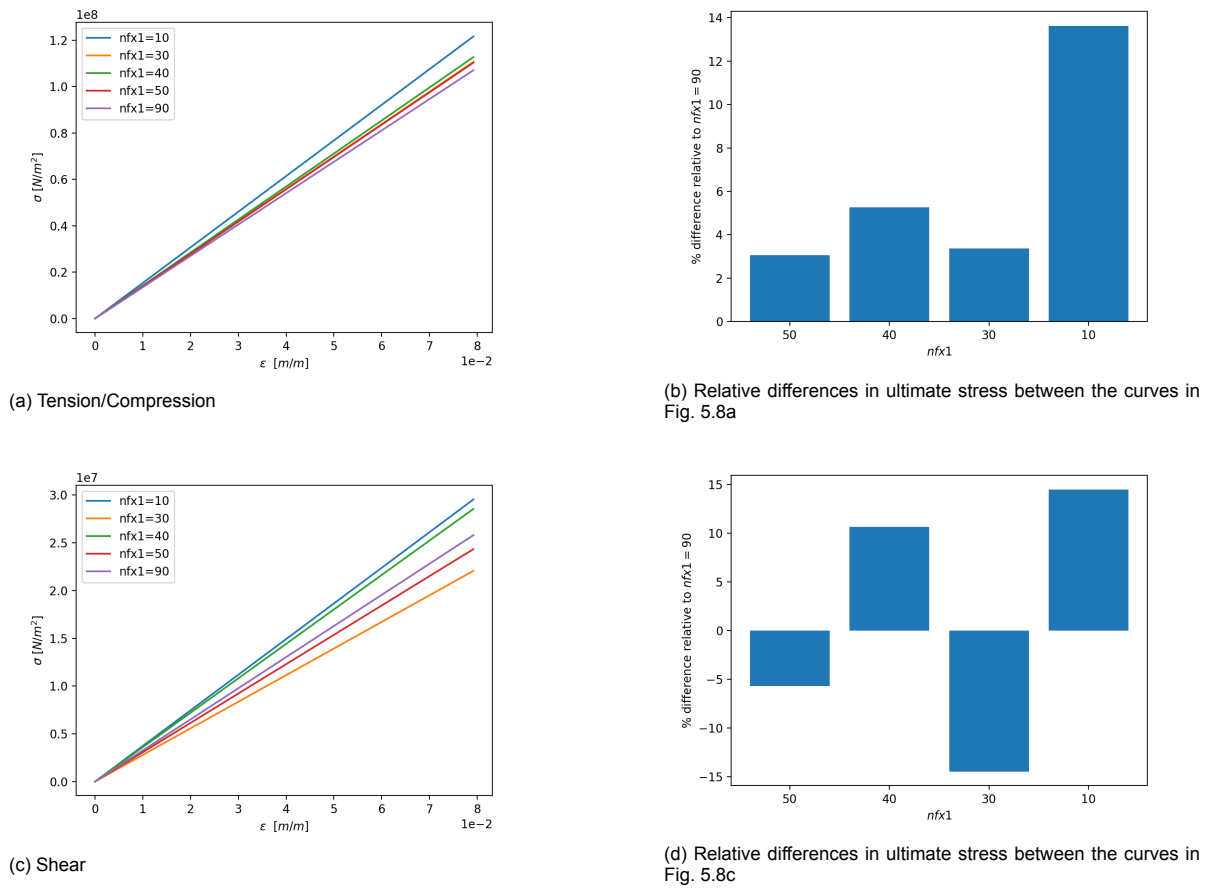


Figure 5.8: Effect of number of particles $nfx1$ for v2 RVEs

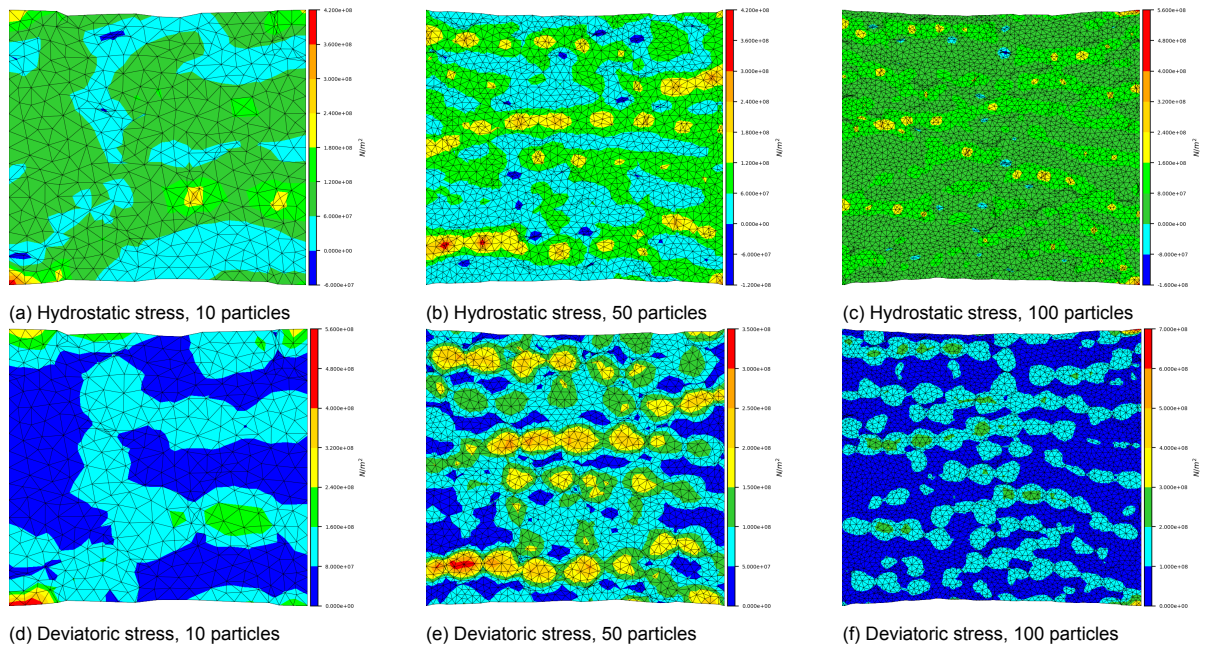


Figure 5.9: Hydrostatic and deviatoric stress fields for RVE with $Df = 30$ when subjected to tension BCs. Different refinements and number of particles $nfx1$ are considered

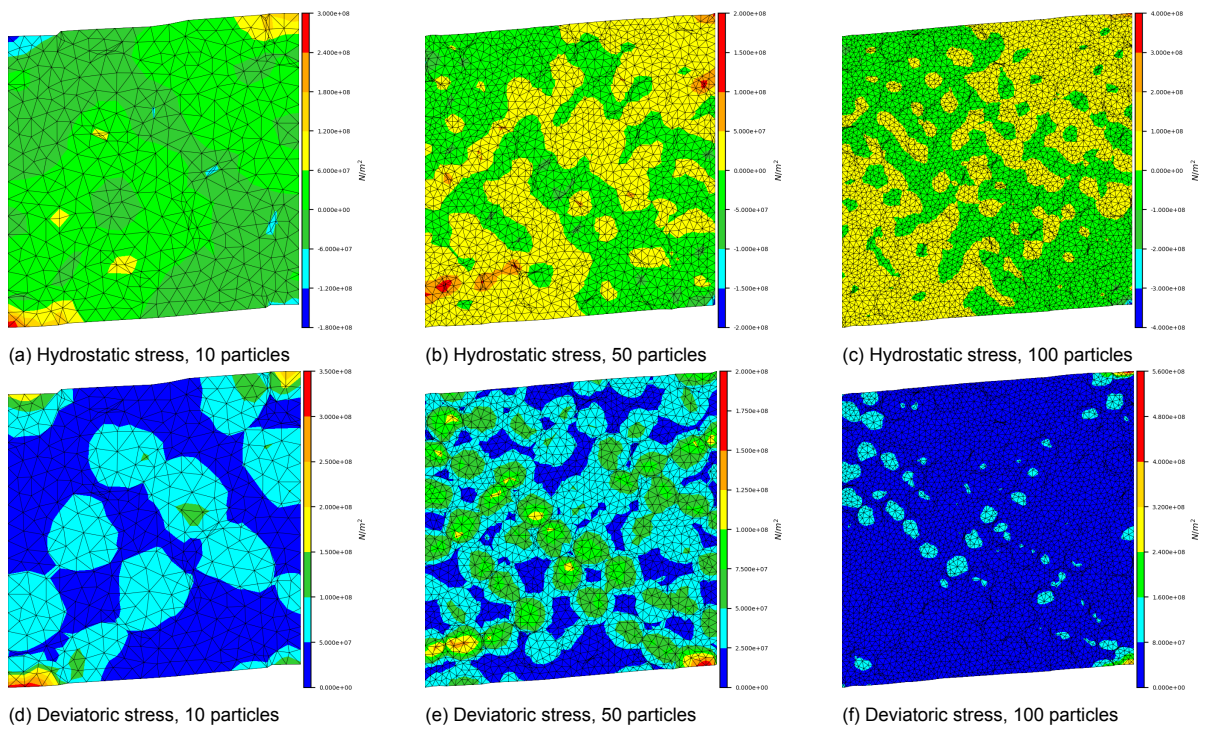


Figure 5.10: Hydrostatic and deviatoric stress fields for RVE with $Df = 30$ when subjected to shear BCs. Different refinements and number of particles n_{fx1} are considered

5.3. Damage-Viscoelastic Behavior

The viscoelastic damage behavior of the micro-structure of solid propellants is investigated by applying the damage-viscoelastic model to the matrix of the RVEs.

The effect of mesh refinement on the stress-strain behavior is shown in Fig. 5.11. The observations and conclusions from the previous section regarding mesh refinement apply here as well. Stress concentrations change in magnitude and location upon mesh refinement, as shown in Fig. 5.12. This implies that damage fields also change in magnitude and location upon mesh refinement, as damage surfaces (Eq.(4.21)) are defined in terms of stresses. Indeed, Fig. 5.12 shows that the magnitude of the damage field is generally greater for the finer mesh than for the coarser mesh. Consequently, the global stiffness of the finer mesh degrades faster. This is shown in Fig. 5.11a, where finer meshes exhibit a greater softening rate. The figures also show that mesh refinement affects numerical stability and convergence behavior, which occurs because damage evolves differently for different meshes. Note that the RVE exhibits similar converging behavior upon mesh refinement as in the previous section, which implies that loss of ellipticity and singular rates of damage are not an issue.

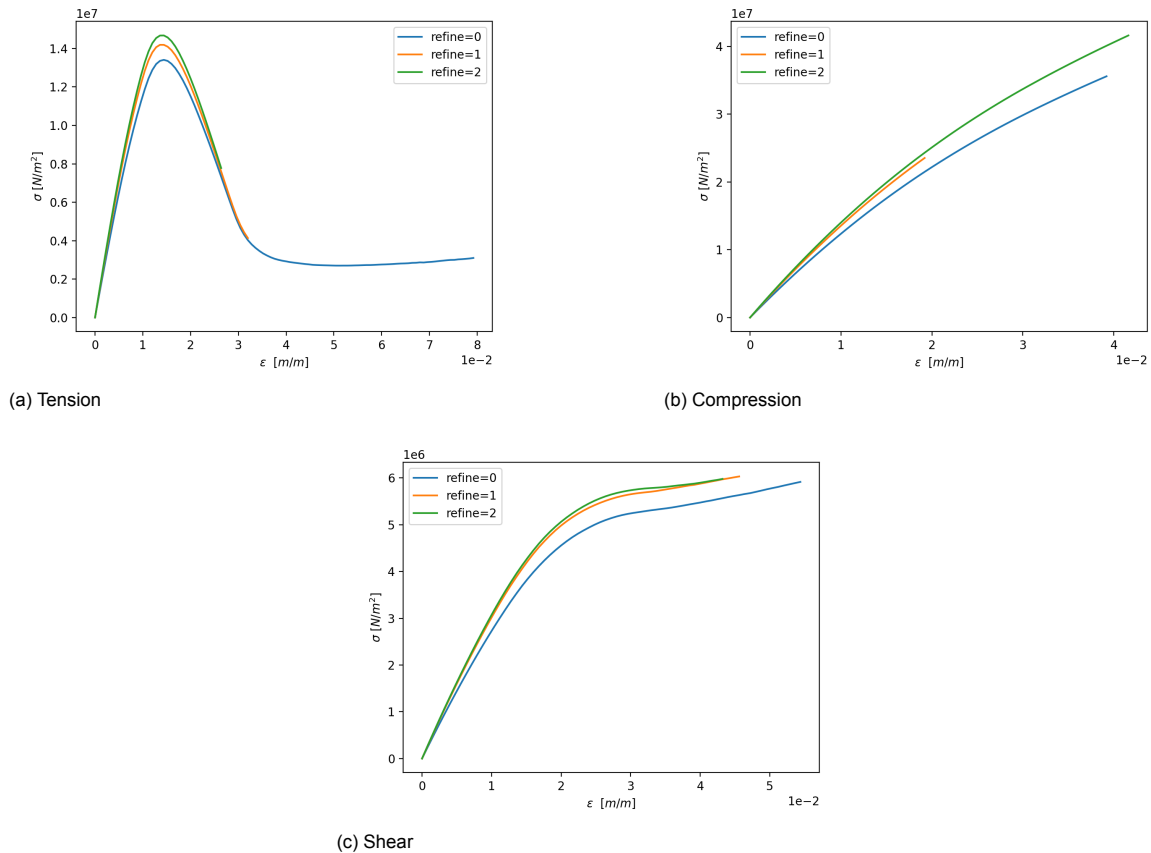


Figure 5.11: Effect of mesh refinement for v2 RVE with 50 particles

The effect of particle distribution and particle size Df on the stress-strain behavior is shown in Figures 5.13 and 5.14 for RVEs with particles of uniform and varying size, respectively. The responses are unaffected by variations of Df , because the damage-viscoelastic model is formulated in terms of stress and strain. The responses are not sensitive to particle distribution, because the number of particles considered (i.e. $nfx1 = 50$) is high enough such that the different RVEs have similar averaged responses. Figures 5.13a and 5.14a show that RVEs subjected to tension BCs are the least sensitive to variations in Df and particle distribution. Tension BCs trigger more damage than other BCs because the RVEs are mostly covered by regions of positive hydrostatic stress. This damage degrades the matrix in regions of stress concentrations and inhibits the matrix from accumulating strain energy. Figures 5.13c and 5.14c show that RVEs subjected to shear BCs are the most sensitive to variations in Df and particle distribution. This is because more particles are necessary to achieve statistical homogeneity

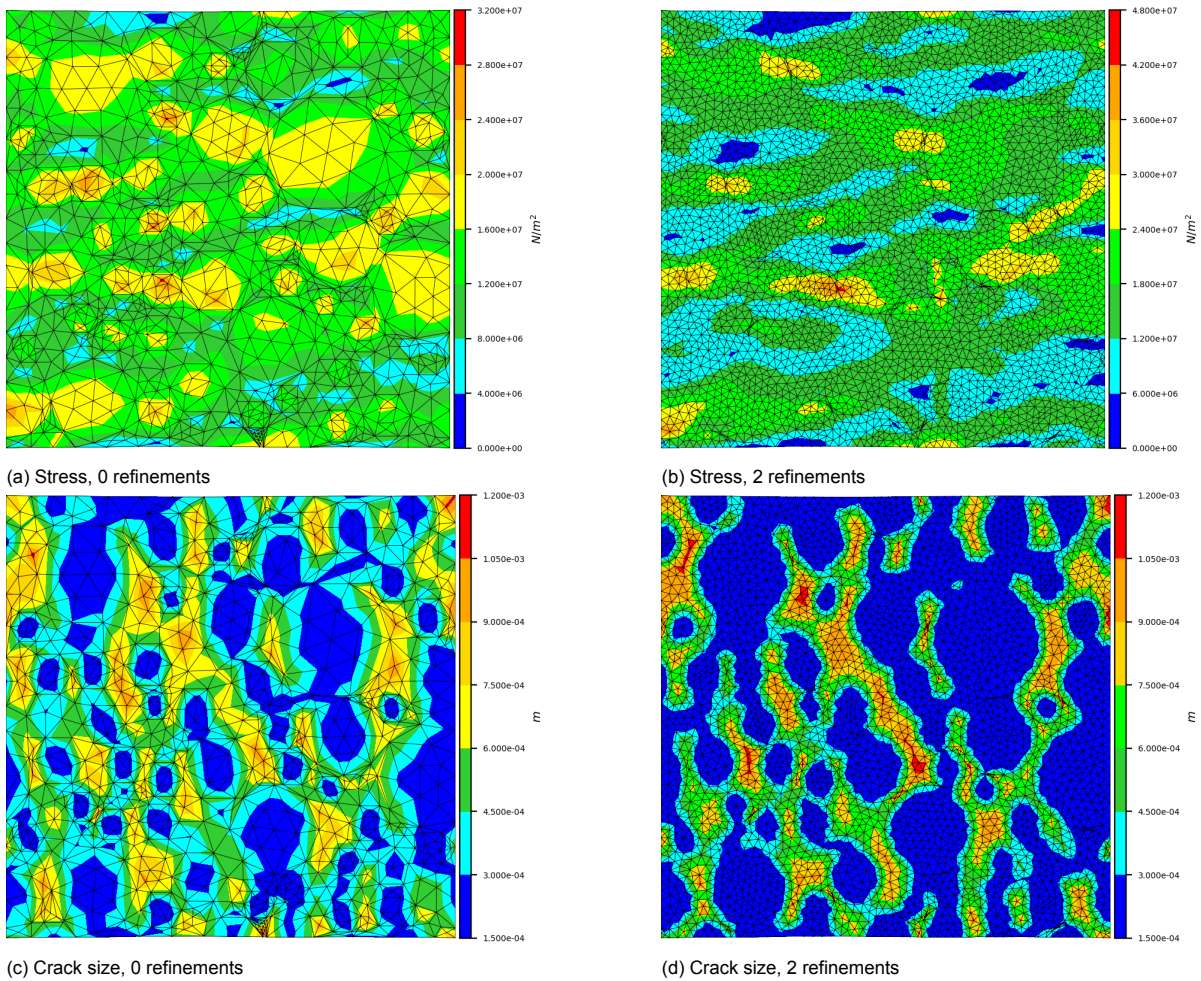


Figure 5.12: Maximum principal stress and mean crack size \bar{c} fields for v2 RVE with 50 particles when subjected to tension BCs for different mesh refinements

and because numerical instabilities take place. Recall from Chapter 4 that a linear recovery of the stress-strain curve implies numerical instabilities.

The effect of the number of particles $nfx1$ on the stress-strain behavior is shown in Figures 5.15 and 5.16 for RVEs with particles of uniform and varying size, respectively. Compared to the linear elastic results of the previous section, viscoelastic damage reduces stress-strain sensitivity to variations of $nfx1$ for tension BCs, it barely affects sensitivity for compression BCs, and it has mixed effect on the sensitivity for shear BCs. For tension BCs, damage inhibits regions of stress concentrations from accumulating strain energy. Therefore, the strain energies that different RVEs store are similar. Figures 5.17a–5.17c and 5.18a–5.18c show that RVEs subjected to tension BCs indeed experience significant matrix damage at ultimate strength. In contrast, damage has a relatively small influence in the stress-strain responses of RVEs subjected to compression BCs, as shown in Figures 5.17d–5.17f and 5.18d–5.18f. Damage also reduces the scatter of the responses for shear BCs by reducing stress concentrations. For instance, the $nfx1 = 10$ curve of Fig. 5.15e is less of an outlier here compared to the previous section, with the only difference being the matrix model. Conversely, damage can also increase sensitivity with respect to $nfx1$ for shear BCs. Damage occurs in a preferential direction when RVEs are subjected to shear BCs, because hydrostatic stresses tend to be positive in the diagonal from the lower left to the upper right corner and negative in the other diagonal, as shown Figures 5.10a–5.10c. Consequently, damage introduces an additional dependence on the convergence rate towards statistical homogeneity of the homogenized shear modulus $CR(\mu_h)$, the spatial distribution of particles across the diagonals. Having an additional dependence decreases $CR(\mu_h)$, which is reflected in the responses of the RVEs with normally distributed Df , as sensitivity increases with respect to $nfx1$.

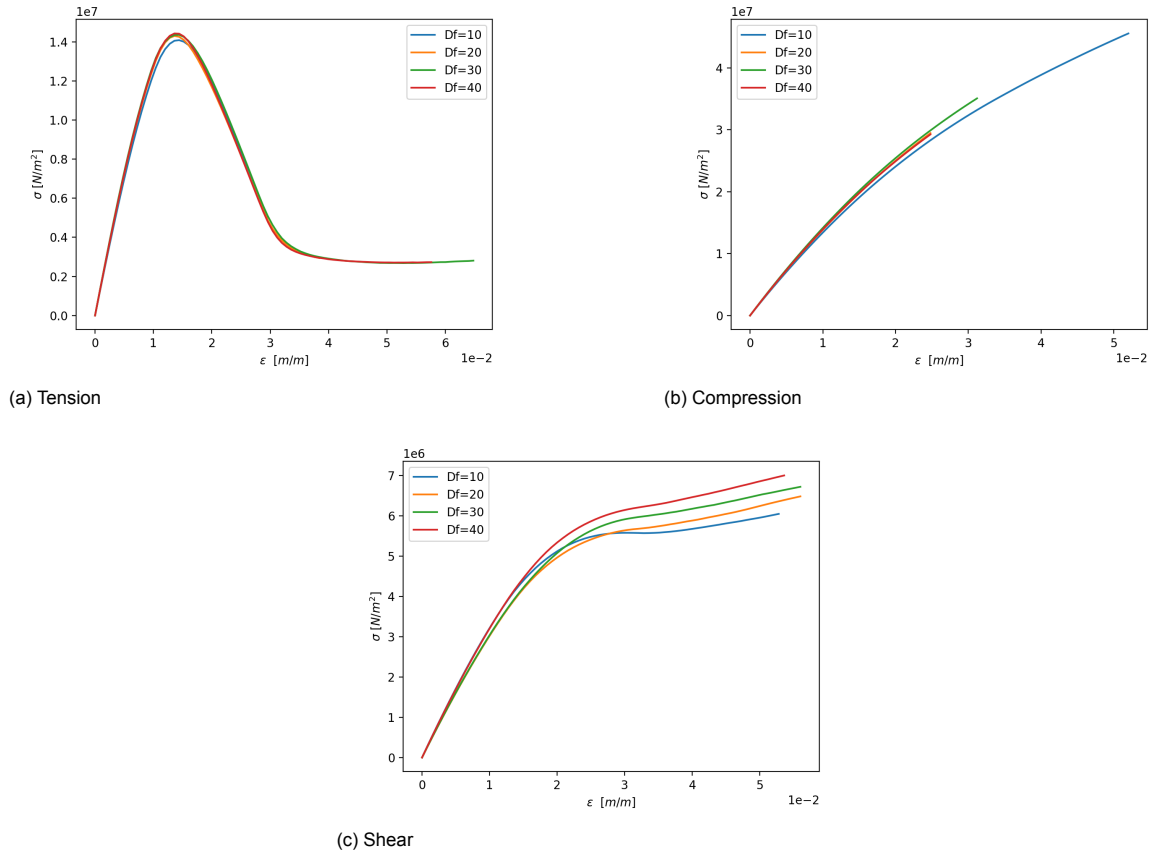
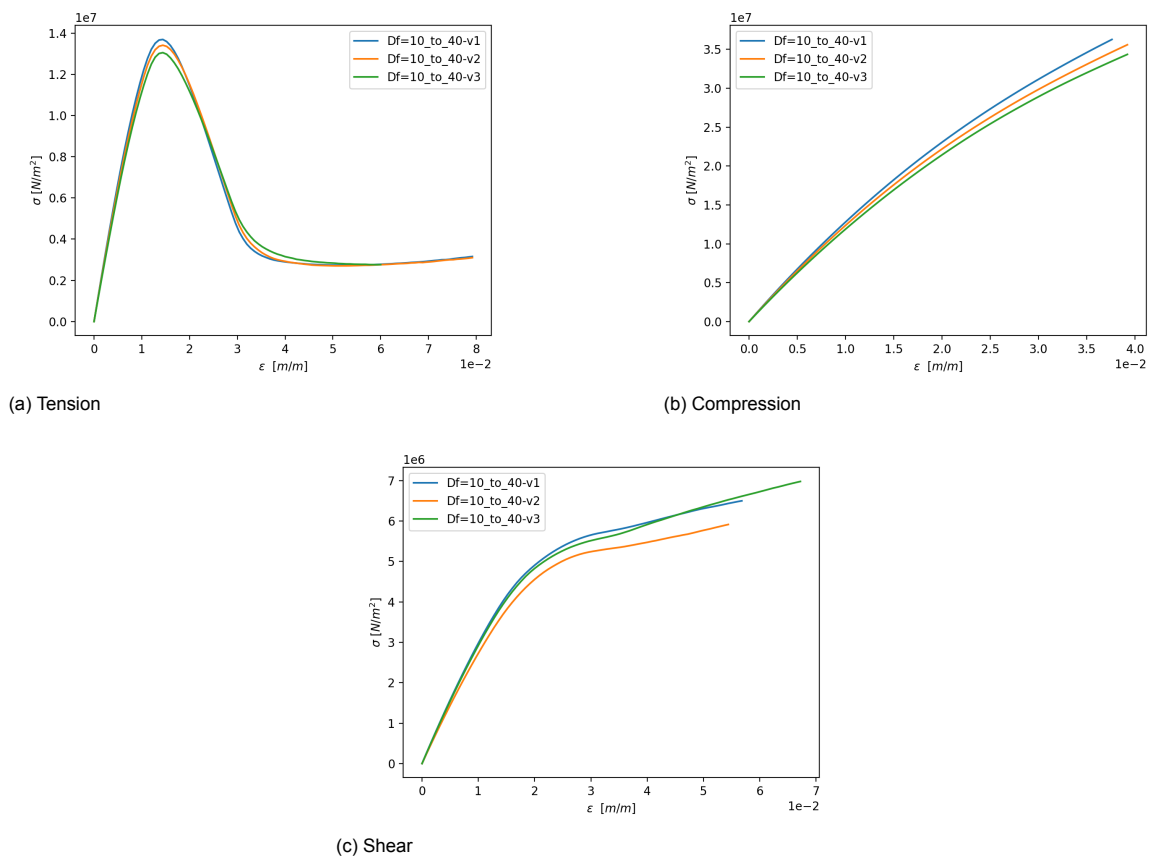
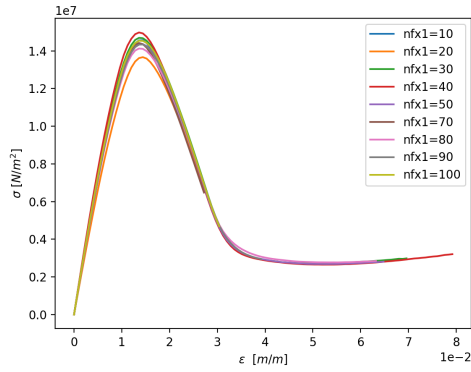


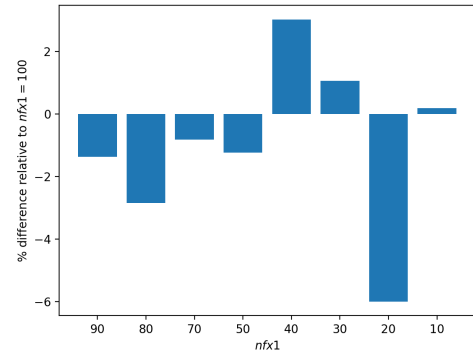
Figure 5.13: Effect of particle distribution and particle size Df for RVEs with uniformly distributed particle size

Figures 5.17g–5.17i and 5.18g–5.18i show the damage fields for shear BCs before global numerical instabilities take place. The figures show that indeed damage occurs in a preferential direction, and that this preferential direction is more uniformly and clearly marked for RVEs with uniform than for normal Df distribution. This implies that statistical homogeneity is achieved faster when the distribution of Df is uniform, which explains why the responses of RVEs with uniform Df exhibit less scatter than the responses of RVEs with varying Df .

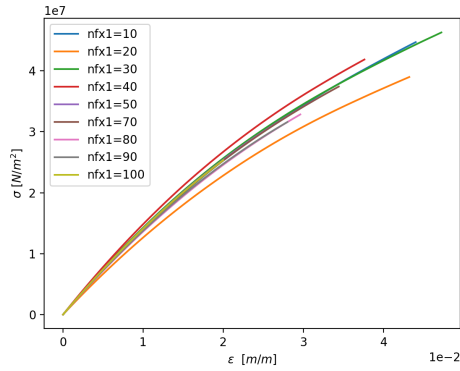
Figure 5.14: Effect of particle distribution and particle size distribution for RVEs with normally distributed particle size Df



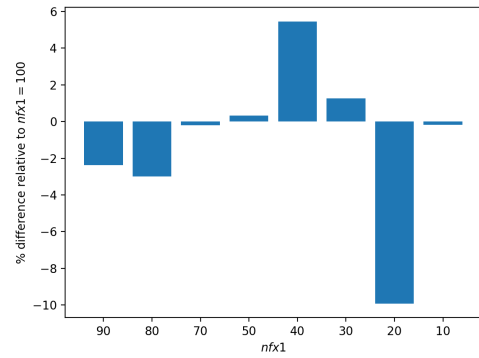
(a) Tension



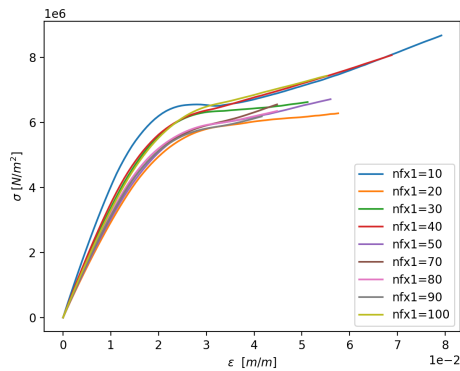
(b) Relative differences in ultimate stress between the curves in Fig. 5.15a



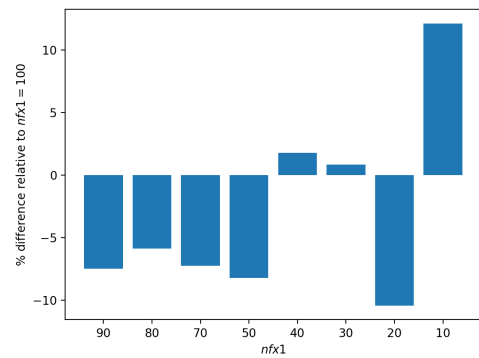
(c) Compression



(d) Relative differences in stress between the curves in Fig. 5.15c for a strain of $\epsilon = 0.0200$

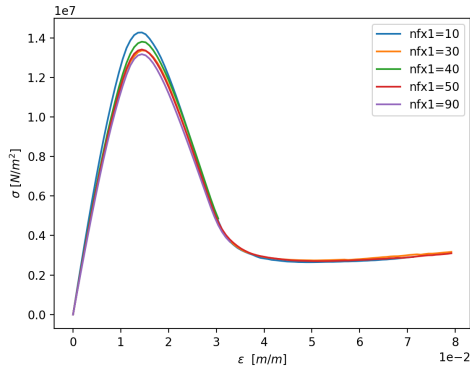


(e) Shear

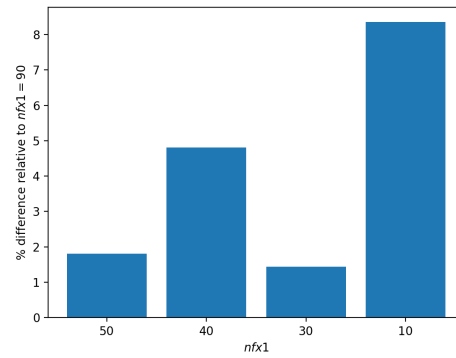


(f) Relative differences in stress between the curves in Fig. 5.15e for a strain of $\epsilon = 0.0200$

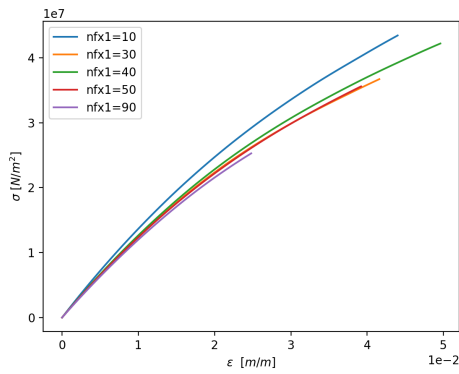
Figure 5.15: Effect of number of particles $nfx1$ for RVEs with particle size $Df = 30\mu m$



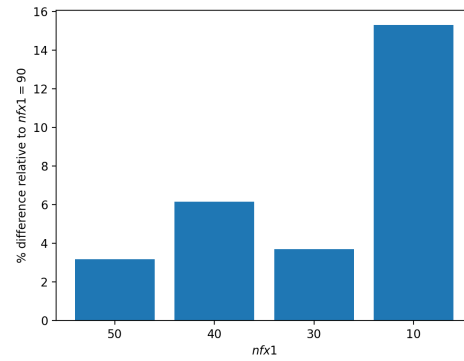
(a) Tension



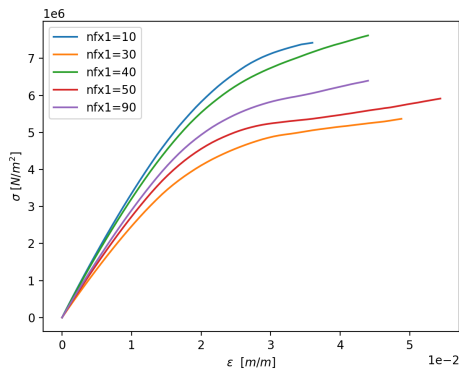
(b) Relative differences in ultimate stress between the curves in Fig. 5.16a



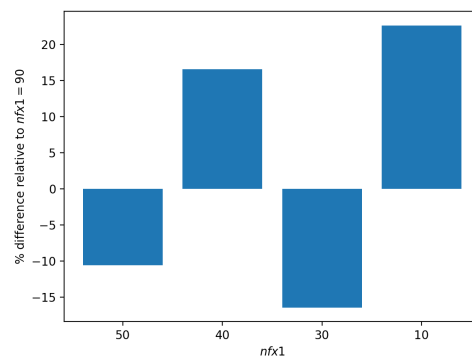
(c) Compression



(d) Relative differences in stress between the curves in Fig. 5.16c for a strain of $\epsilon = 0.0240$



(e) Shear



(f) Relative differences in stress between the curves in Fig. 5.16e for a strain of $\epsilon = 0.0320$

Figure 5.16: Effect of number of particles $nfx1$ for v2 RVEs

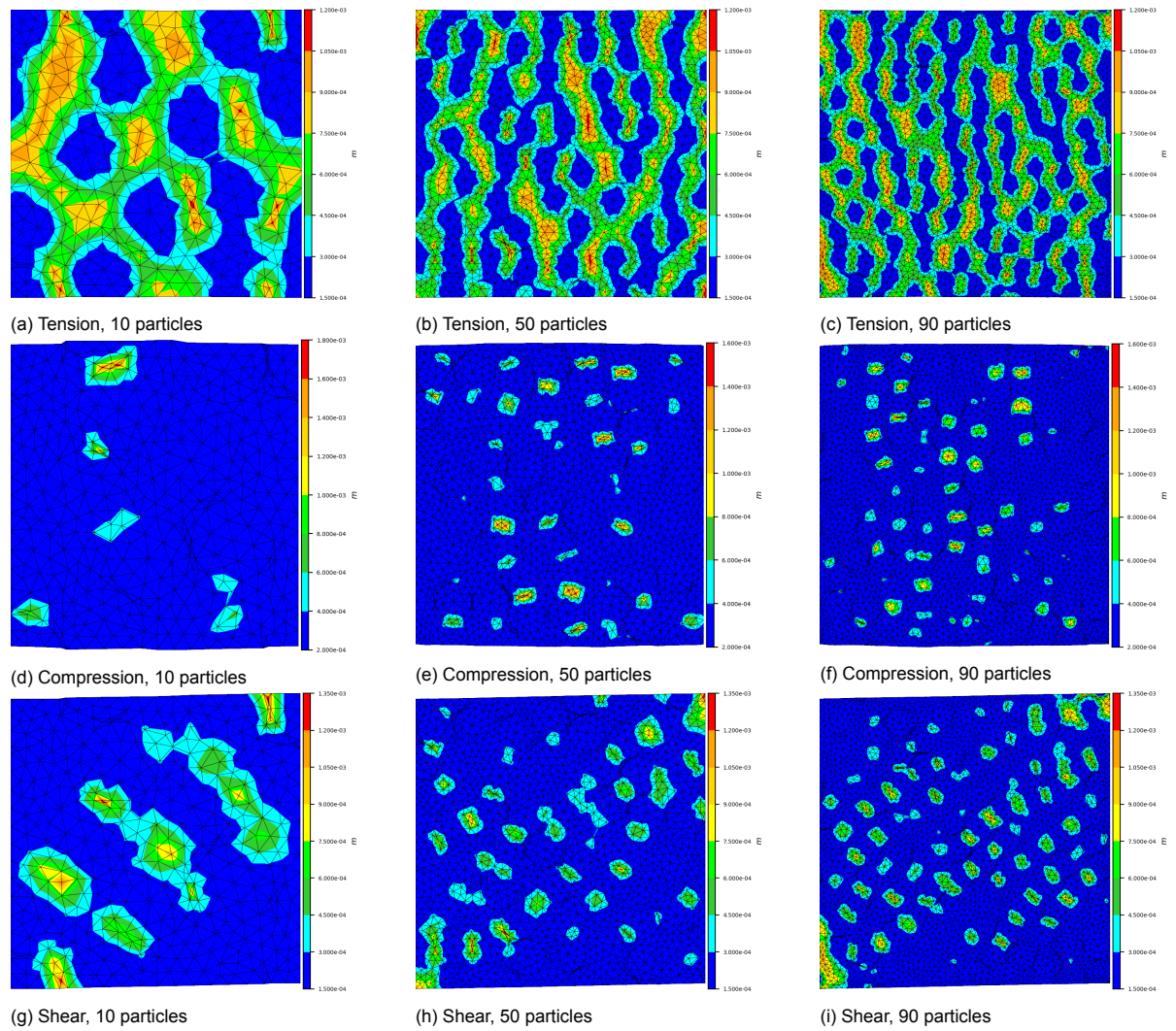


Figure 5.17: Mean crack size \bar{c} fields for RVE with $Df = 30$ when subjected to tension, compression, and shear BCs. For tension the fields are given at ultimate stress, for compression at the step before unconvergence (the strain is given in the subfigures), and for shear at $\epsilon = 0.0200$. Different number of particles $n_{f \times 1}$ are considered

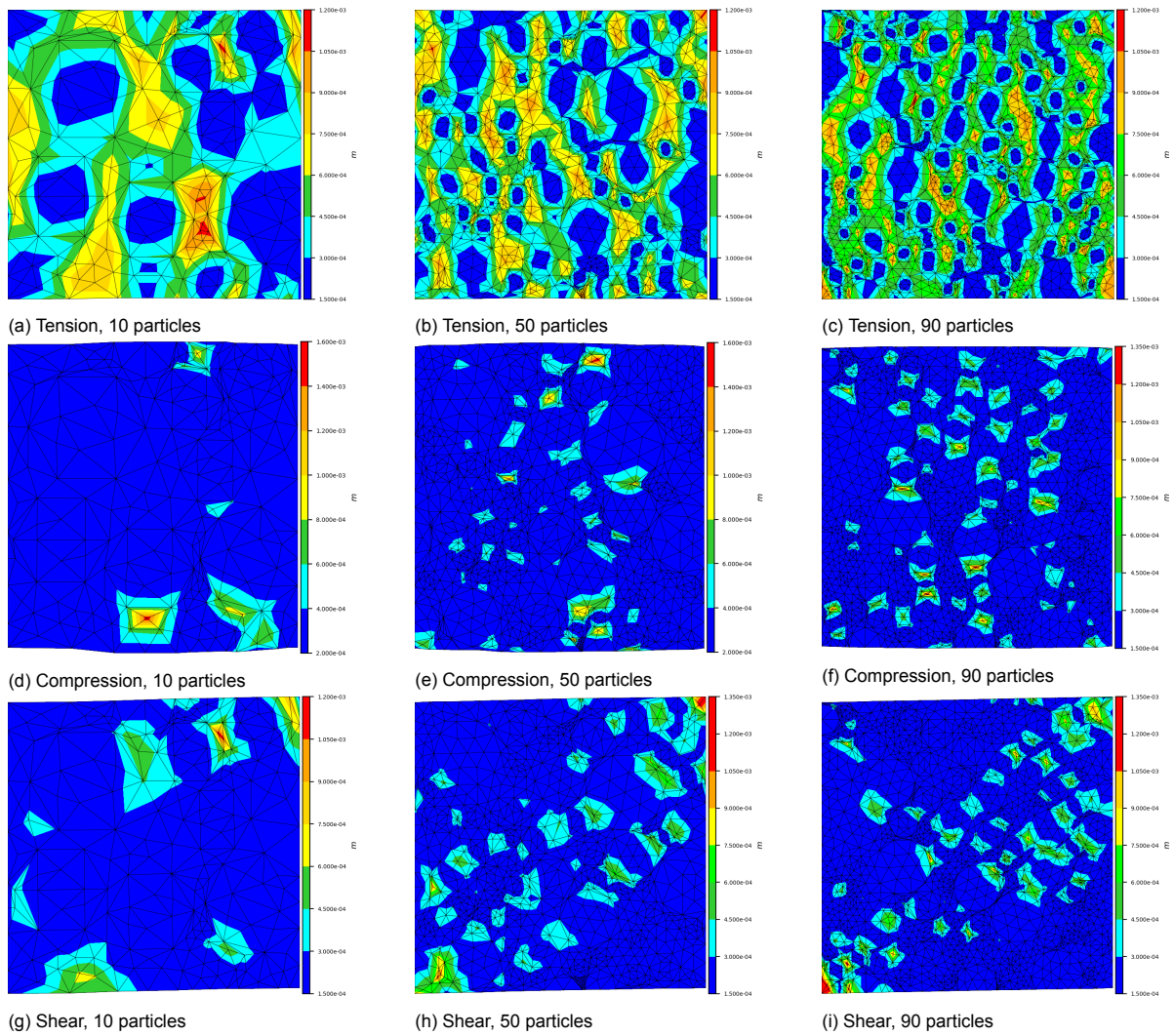


Figure 5.18: Mean crack size \bar{c} fields for v2 RVE when subjected to tension, compression, and shear BCs. For tension the fields are given at ultimate stress, for compression at the step before un convergence (the strain is given in the subfigures), and for shear at $\epsilon = 0.0200$. Different number of particles n_{fx1} are considered

5.4. Debonding Behavior

5.4.1. Behavior of the Debonding Model

The behavior of the Turon model for interface elements is investigated with the purpose of understanding debonding damage in the micro-structure of the solid propellants. The matrix is treated as linear elastic so that nonlinearities introduced by the Turon model can be explored in isolation of nonlinearities introduced by other constitutive models. The default mesh employed in this section has v2 normally distributed particle size, 50 particles, and no mesh refinements (Fig. D.20). This mesh and the default debonding parameters of Table 6.1 are employed for all simulations within this section unless stated otherwise. The cohesive strengths τ are referred to as the strengths and the energy release rates G are referred to as the energies for simplicity.

Parameter	Value	Units
K	4.0×10^{13}	N/m^3
τ_I	5.0×10^6	N/m^2
τ_{II}	5.0×10^6	N/m^2
τ_{II}	2.5×10^6	N/m^2
G_{Ic}	1.125×10^2	J/m^2
G_{Ic}	1.125×10^3	J/m^2
G_{IIc}	1.125×10^2	J/m^2
G_{IIc}	1.125×10^1	J/m^2
η	0.5	-

Table 5.1: Default debonding parameters. Blue value is used when both energies are equal to each other but the strengths are different. Green values are used when both strengths are equal to each other but the energies are different.

The global stress-strain behavior of the RVE when subjected to tension BCs, when the default mesh is subjected to four refinements (Fig. D.26), and when the energies are $G_{Ic} = G_{IIc} = 1.125 \times 10^1 J/m^2$ is shown in Fig.5.19a. The stress-strain response can be divided into five regimes; the linear elastic regime and four debonding damage regimes. The debonding damage regimes are defined for describing and understanding how the RVE behaves locally at specific moments of the loading process. The linearity or nonlinearity of global response is the criterion used for defining each regime because it is an indicator of local behavior. According to the theory of differential equations, global behavior is linear only when local behavior is locally linear everywhere. Turon's TSL is bilinear, so local nonlinearities only occur when local behavior shifts from linear elastic to softening, from softening to decohesive, or from softening to unloading. That is, when the slope of the TSL changes. Debonding regime I takes place while some IPs shift from linear elasticity to softening. Debonding regime II starts when no new IPs shift to softening, but damage continues to evolve in the IPs that already started softening. Debonding regime III takes place while softening IPs shift to free surface propagation and/or unloading. Debonding regime IV starts when no new IPs shift to free surface propagation. Damage continues evolving in the remaining softening IPs and free surfaces propagate freely in the IPs whose energies were exhausted. Stress redistribution occurs in regimes I and III, therefore their stress-strain responses are nonlinear. The softening branch of Turon's TSL is linear and free surface propagation requires no energy. Therefore, the stress-strain responses of regimes II and IV are linear. In other words, the governing PDE is nonlinear in regimes I and III because the constitutive laws act nonlinearly in some (but not all) IPs, and linear in regimes II and IV because the constitutive laws act linearly in all IPs. In reality different debonding regimes interact with each other, with one regime generally dominating over the others. Therefore, when either regime II or IV dominates, the response is generally not perfectly linear, it is quasi-linear.

Figures 5.19b and 5.19c show the stress fields of the RVE at peak load (early regime III) and at maximum displacement (late regime IV), respectively. Figure 5.19b shows that stresses concentrate between slightly damaged interfaces of closely located particles. The overall stiffnesses of regions located between severely damaged interfaces has been degraded, so stresses have redistributed away from them. The color contour of Fig. 5.19c is almost uniform. This implies that at regime IV damaged interfaces have significantly degraded the local stiffness of most of the RVE and stress concentrates in very small spatial regions.

The global stress-strain responses of the RVE for varying values of the mode I energy G_{Ic} , of the

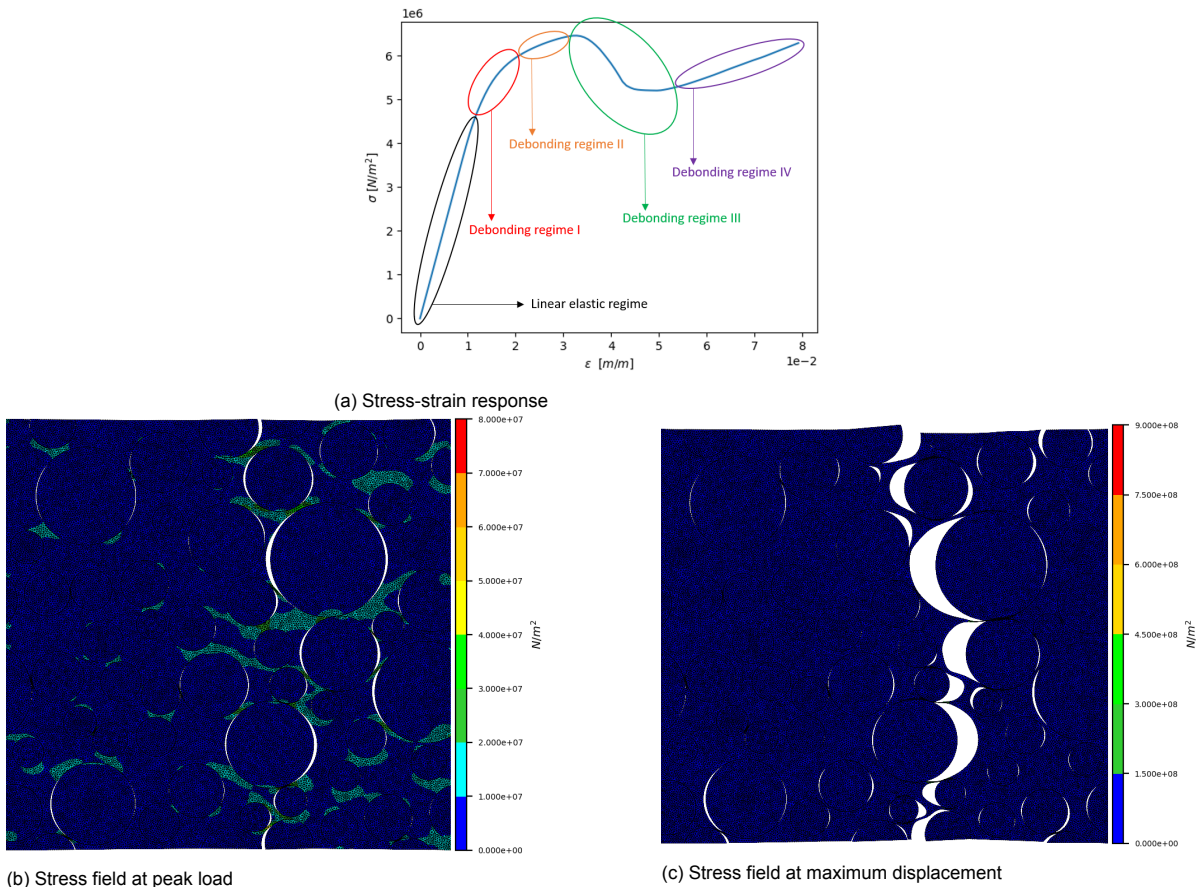


Figure 5.19: Global stress-strain response and maximum principal stress fields of the specimen when subjected to tension BCs. Default mesh and parameters are used, except mesh is subjected to 4 refinements and $G_{IC} = G_{IIC} = 4.5 \times 10^{-2} \text{ J/m}^2$.

mode II energy G_{IIC} , and of both energies are shown in Figures 5.20, 5.21, and 5.22, respectively. All the responses only exhibit debonding regimes I and II, free surface propagation is not initiated at any IP. In fact, it has been observed that free surface propagation cannot take place in the mesh and BCs under consideration for any possible set of input debonding parameters. The response of the mesh is very insensitive to changes in the energies, which determine the local softening stiffness and the displacement jump for free surface propagation. Lower energies result in marginally softer global responses, but early unconvergence occurs when the energies are too low. This suggests that in order to capture debonding regimes III–IV highly refined meshes are necessary. This thesis investigates solid propellants under various conditions using CH. Therefore, utilizing highly refined meshes would be computationally unfeasible. Consequently, this thesis only investigates the debonding behavior of the micro- and the macro-structures of the solid propellants under the context of debonding regimes I–II.

The responses of the RVE for varying values of the mode I strength τ_I and of the mode II strength τ_{II} are shown in Figures 5.23 and 5.24, respectively. The strengths determine the criteria for damage initiation. Therefore, they directly affect the magnitude of the local softening stiffness, the slope of debonding regime II, and the lengths of the linear elastic regime and of debonding regime I. The figures show that indeed the linear elastic regimes and debonding regimes I are extended for larger strengths. However, the strengths appear to have a negligible effect on the slopes of debonding regimes II. This occurs because the default energies are very large relative to the other debonding parameters. Therefore softening is negligible, even for relatively large deformations. Instead, the stresses at the IPs remain almost constant once debonding is initiated.

The responses are more sensitive to changes in the mode II strength, especially for compression and shear. In fact, compression simulations seem almost unaffected by variations of the mode

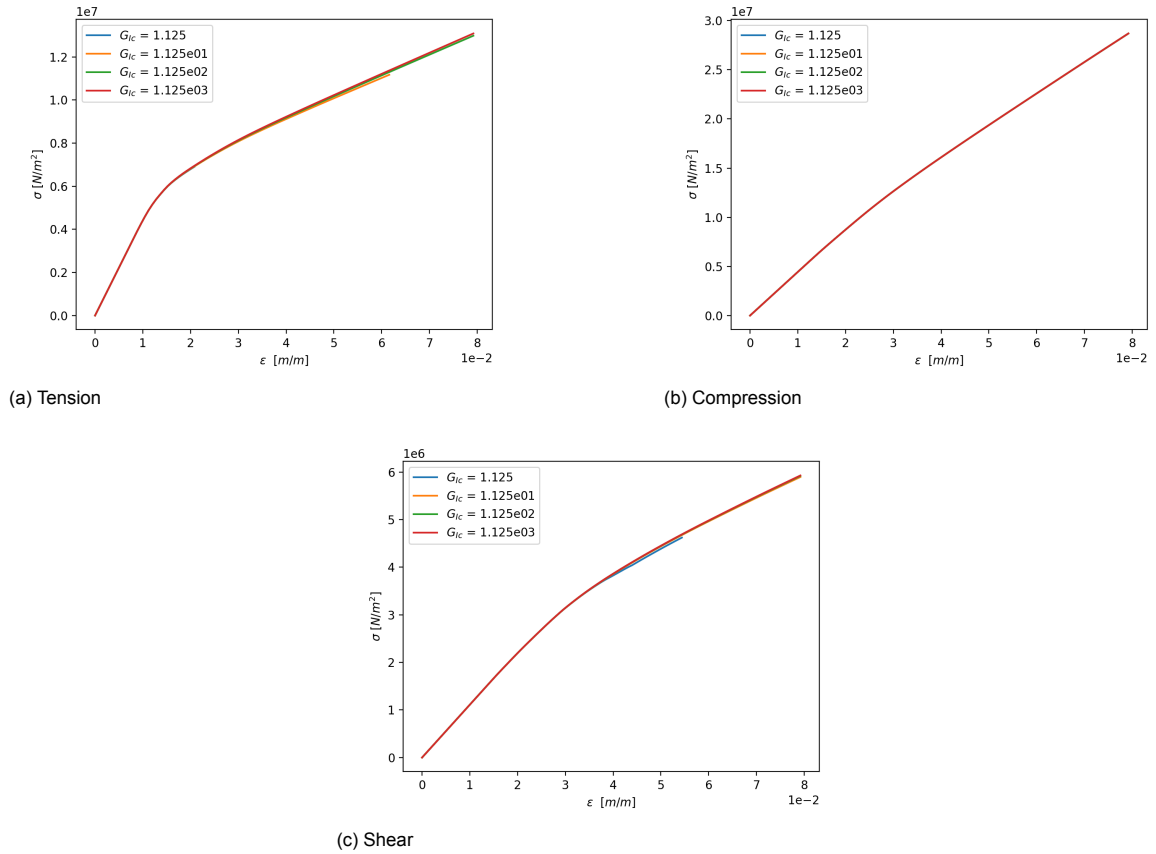


Figure 5.20: Response of specimen for different values of mode I energy G_{Ic}

I strength. The mode II strength has a larger effect because shear stress states are more ubiquitous than tension stress states in the RVE for all the BCs applied. Tension stress states cannot occur at the same time and in the same location as compression stress states, and compression stress states occupy regions of the RVE for all types of BCs. The extent of these regions, and consequently of the importance of the mode I strength, depends on the applied BCs. In contrast, shear stress states can coexist with both compression and tension stress states.

The responses of the RVE for varying values of the experimental parameter η are shown in Figures 5.25–5.27. The experimental parameter η determines how much the difference between mode I and mode II debonding properties and the difference between mode II and total damage evolution affect the response. When debonding properties are the same for both modes (i.e. $\tau_I = \tau_{II}$ and $G_{Ic} = G_{IIc}$), the value of η has no effect on the response by definition. This can be observed in Fig. 5.25. The strengths have a greater influence than the energies on the response for the input values considered. Therefore, the value of η has a much greater influence on the response when the strengths are not equal to each other (i.e. $\tau_I \neq \tau_{II}$ and $G_{Ic} = G_{IIc}$) than when the energies are not equal to each other (i.e. $\tau_I = \tau_{II}$ and $G_{Ic} \neq G_{IIc}$), as shown in Figures 5.27 and 5.26, respectively. In fact, when the energies are not equal to each other η has a negligible effect on the response, but it does affect numerical stability. Notice that when the strengths are not equal to each other the effect of η is also negligible for compression BCs, as shown in Fig. 5.27b. This occurs because mode II debonding damage and total debonding damage are almost the same. In this case mode I debonding damage is negligible, because the vast majority of the RVE is in a compression stress state.

The responses of the RVE for varying values of the dummy stiffness K are shown in Fig. 5.28. Relatively high values of K lead to early unconvergence of the numerical solution, as shown in Fig. 5.28a. Therefore, a value of K for which the linear elastic regime accurately approximates the linear elastic BVPs (i.e. when there are no interface elements) for all BCs under consideration does not exist for the default mesh. Furthermore, the BVPs are highly conditioned with respect to K , when the stiffnesses

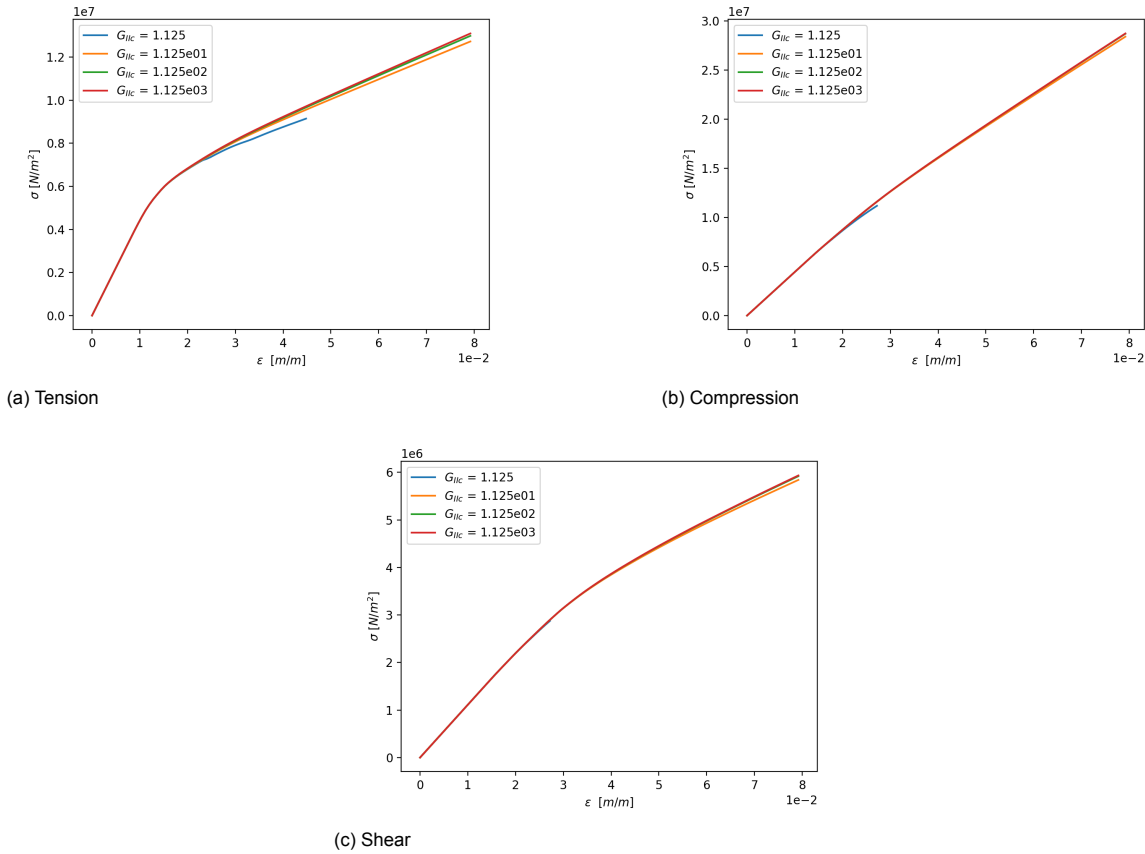


Figure 5.21: Response of specimen for different values of mode II energy G_{IIc}

of the linear elastic regimes are significantly lower than the stiffnesses of the linear elastic BVPs. As a consequence, working with a K that does not cause early unconvergence entails working with an ill-conditioned BVP. Values of K that are not sufficiently large to approximate the linear elastic BVPs allow non-negligible displacement jumps to occur even before debonding damage is initiated. The consequences of working with BVPs that suffer from these issues are explored in the next section.

All the figures presented in this section for the default mesh are recreated in Appendix B.1 for the case where the modified damage model is applied to the matrix. These figures are not discussed because the debonding parameters generally affect the responses of the BVPs considered in the Appendix and the BVPs considered here similarly. The only difference worth noting is that free surface propagation can sometimes take place in the default mesh when matrix damage is considered. Consequently, the BVPs can be more sensitive to changes in the energies—see Fig. B.3a.

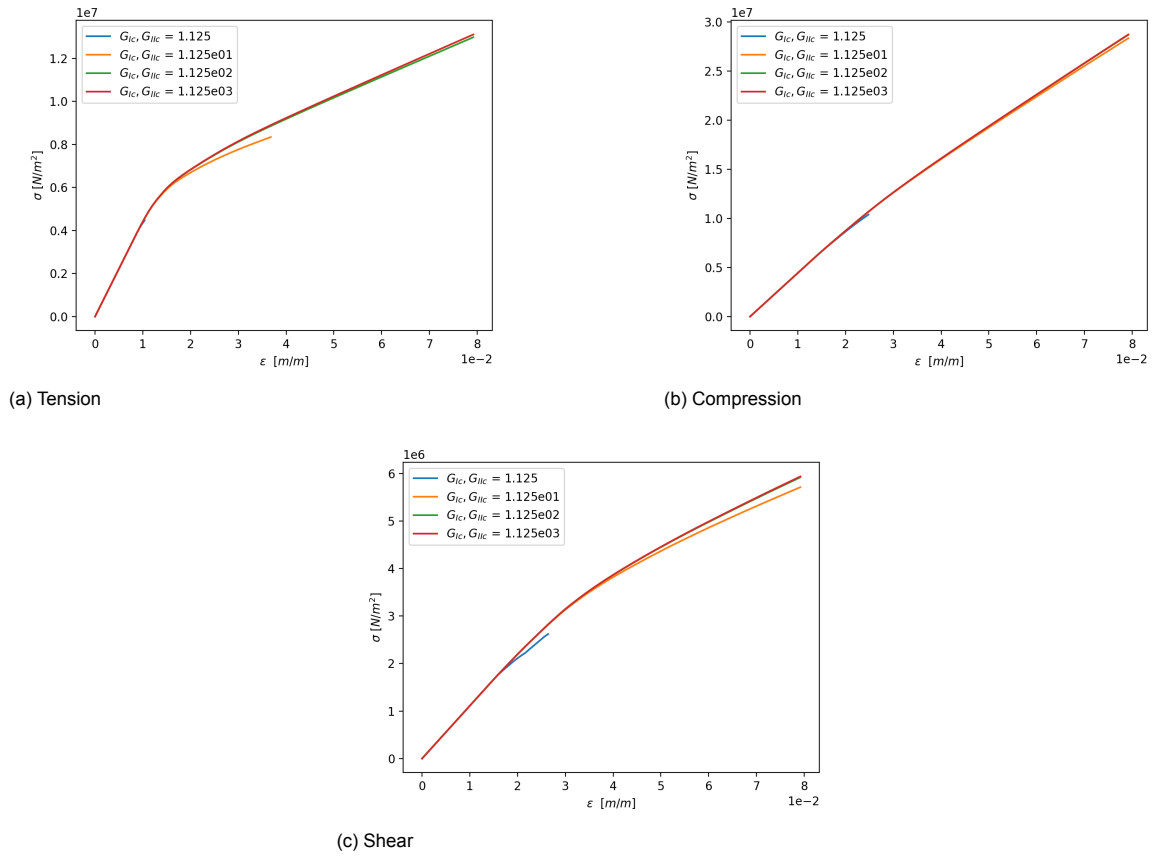
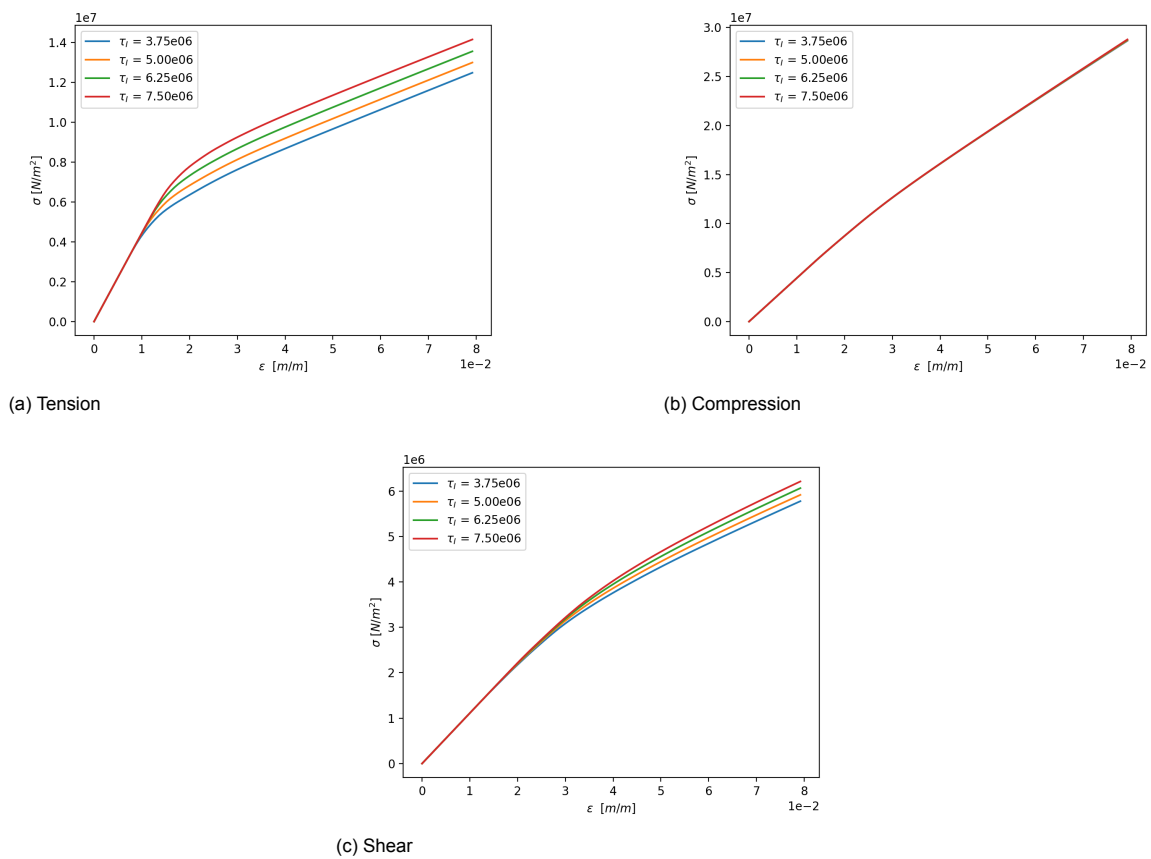


Figure 5.22: Response of specimen for different values of mode I and mode II energies G_{IC} and G_{IIC}

Figure 5.23: Response of specimen for different values of mode I strength τ_I

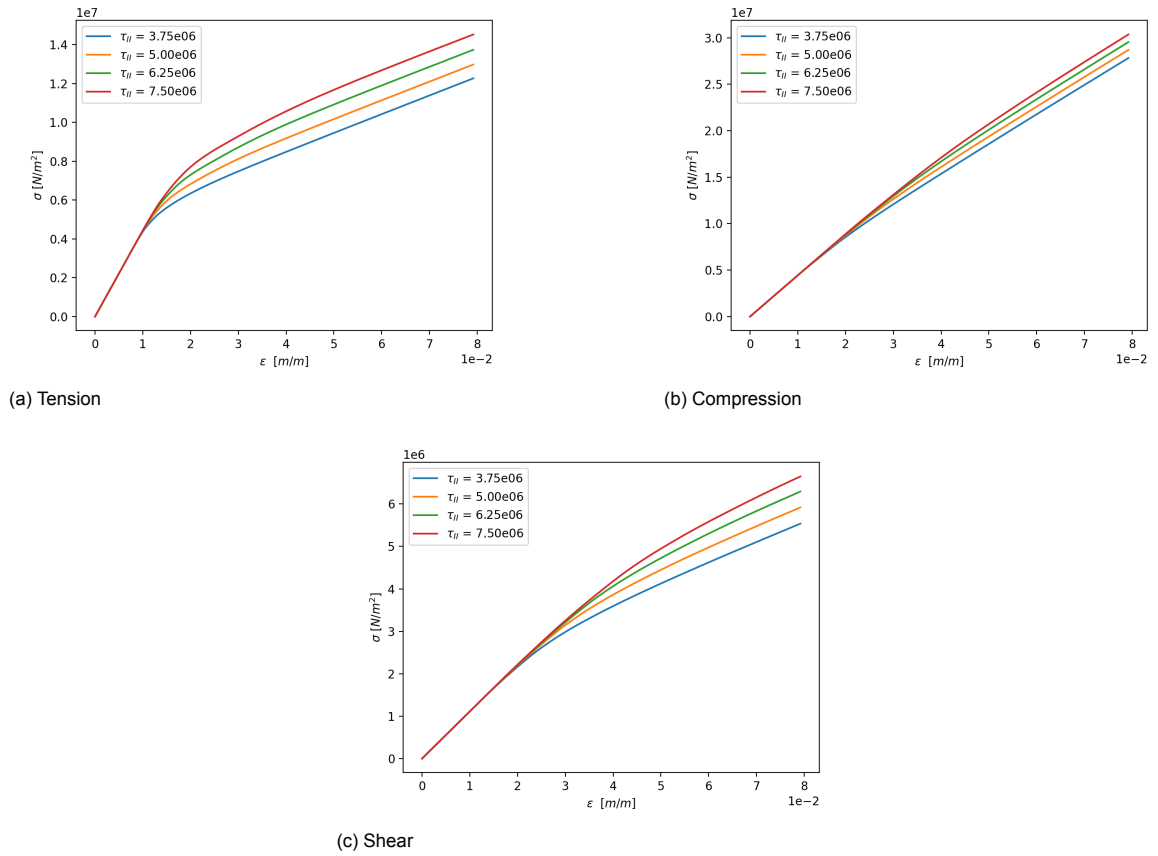


Figure 5.24: Response of specimen for different values of mode II strength τ_{II}

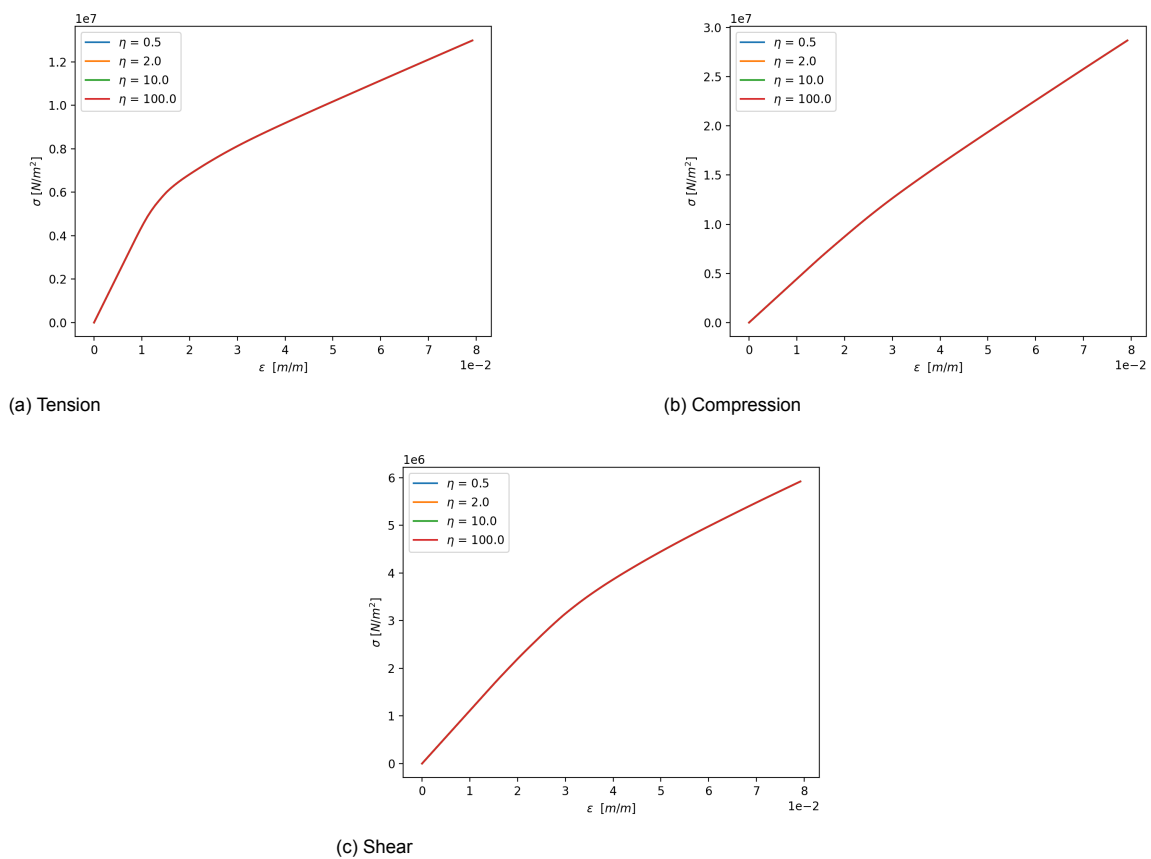


Figure 5.25: Response of specimen for different values of experimental parameter η when both strengths and both energies are equal to each other

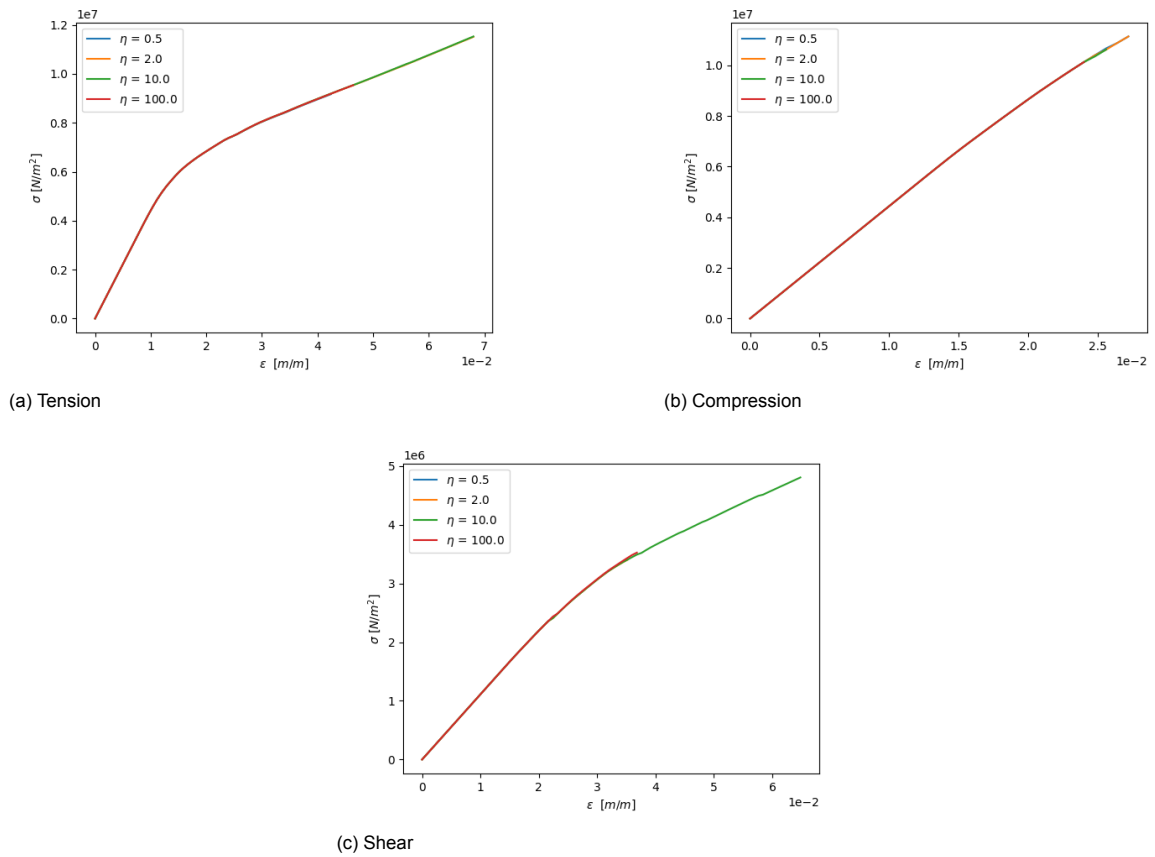


Figure 5.26: Response of specimen for different values of experimental parameter η when both strengths are equal to each other but the energies are different

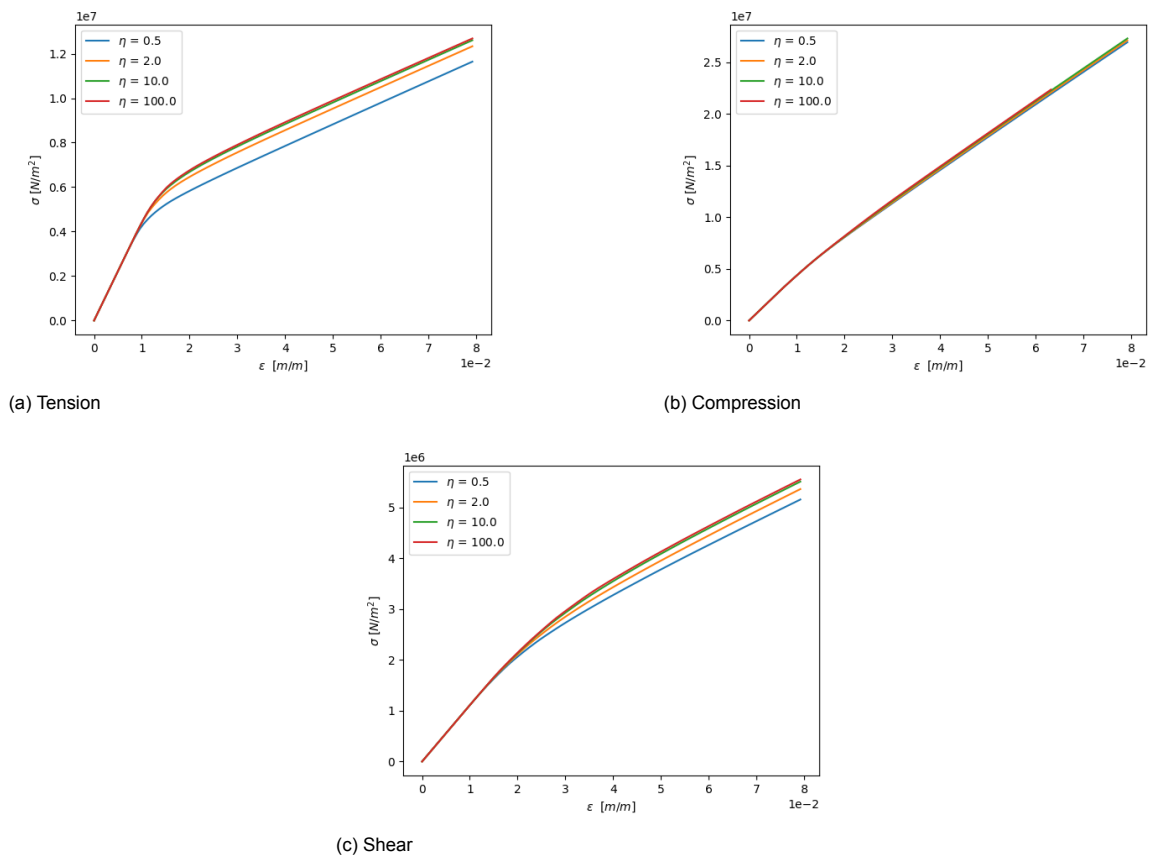


Figure 5.27: Response of specimen for different values of experimental parameter η when both energies are equal to each other but the strengths are different

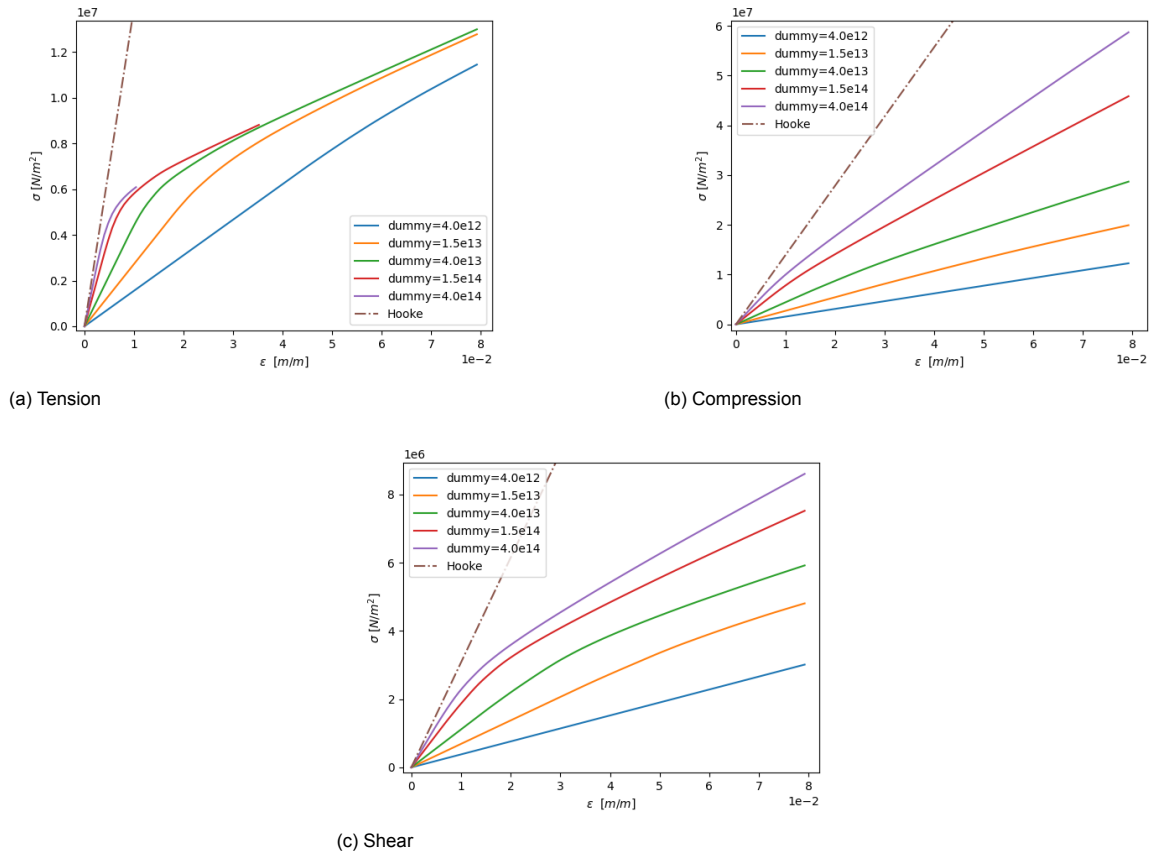


Figure 5.28: Response of specimen for different values of dummy stiffness K

5.4.2. Mesh Refinement, Particle Size, and Particle Distribution

The debonding damage behavior of the micro-structure of solid propellants is investigated by applying the Turon model to the matrix-particle interfaces of the RVEs.

The effect of mesh refinement on the stress-strain behavior is shown in Fig. 5.29. Very fine meshes are necessary for the solution to converge upon refinement, especially compared to the linear elastic and the continuum damage cases investigated in the previous sections. This occurs because stress concentrations and particle geometry are highly sensitive to mesh refinement, as shown in Fig. 5.30. In turn, the solution of the BVP is highly sensitive to stress concentrations and particle geometry. Stress concentrations are important because they are located close to the interface elements. Particle geometry is important because the total energy necessary for damage to evolve depends on the length of matrix-particle boundaries and because the outward normal of these boundaries determines the direction of damage evolution in the failure mode space, i.e. the mode I–mode II space. Mesh refinement has a larger effect for tension BCs than for compression and shear BCs because the RVE experiences greater debonding damage when subjected to tension. Coarser meshes produce stiffer stress-strain responses than finer meshes because stress concentrations become more acute upon refinement.

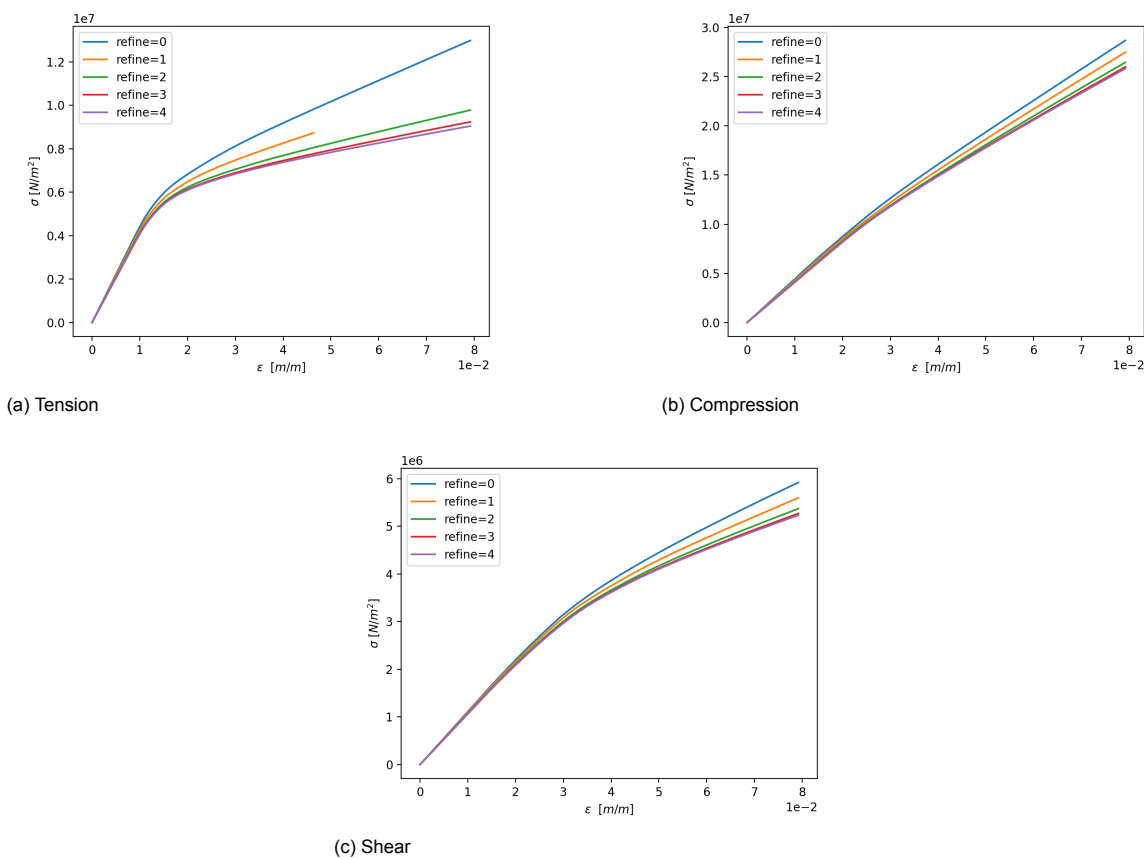


Figure 5.29: Effect of mesh refinement for v2 RVE with 50 particles

The effect of particle distribution and particle size Df on the stress-strain behavior is shown in Figures 5.31 and 5.32 for RVEs with particles of uniform and varying size, respectively. The responses of RVEs with uniform particle size distribution are highly sensitive to variations in Df . RVEs with larger Df are stiffer in the linear elastic regime and experience a greater damage rate in the debonding damage regimes. This occurs because the Turon model relates traction, which is a relative measure of force, to displacement jump, which is an absolute measure of material translation. Larger RVEs are subjected to larger total displacements by the BCs, so their interface elements experience larger displacement jumps. Consequently, the dummy stiffness K prescribes larger tractions and the energy release rates G_I, G_{II} are exhausted faster. This means that if an RVE and its corresponding BCs are scaled by a factor a , then K must be scaled by a^{-1} and G_I and G_{II} must be scaled by a to obtain the same

response of the unscaled RVE. The responses of different RVEs with normal particle size distribution are similar because the number of particles considered (i.e. $n_{fx1} = 50$) is high enough such that the Gaussian PDF from which particle size is sampled manifests similarly in the different RVEs. Since the Turon model introduces a size effect, it would be sensible to make K , G_I , and G_{II} functions of Df . This was not done in this thesis, but is recommended for future work.

The effect of the number of particles n_{fx1} on the stress-strain behavior is shown in Figures 5.33 and 5.34 for RVEs with particles of uniform and varying size, respectively. Debonding damage reduces the sensitivity of the responses with respect to n_{fx1} for both types of particle size distribution relative to the linear elastic case (Section 5.3). This is particularly true in the linear elastic regime, where the responses of RVEs with different n_{fx1} are practically indistinguishable when subjected to tension and compression BCs and are similar when subjected to shear BCs. This implies that for the choice of dummy stiffness K , stress concentrations are reduced because stress concentrations are the main cause for variations in response in the absence of damage. Comparing the stress fields of Section 5.2 to the linear elastic fields in Figures 5.35 and 5.36, it is clear that indeed stress concentrations are smaller here. The K employed reduces stress concentrations because it significantly softens the elastic response of the material along the interfaces. This is a spurious effect caused by the value of K being too low compared to the stiffness of the constituents of the solid propellants. The value of K , however, cannot be increased much without causing early nonconvergence of the numerical solution, as was shown in Section 5.4. The responses of different RVEs exhibit greater variation in the debonding regime than in the linear elastic regime. The regime II stiffnesses clearly differ more when particle size is normally distributed than when it is uniformly distributed. This occurs because the size effect introduced by the Turon is only relevant when particle size distribution is non-uniform. The responses of RVEs subjected to compression BCs are very similar even in the debonding damage regime because damage evolves very slowly.

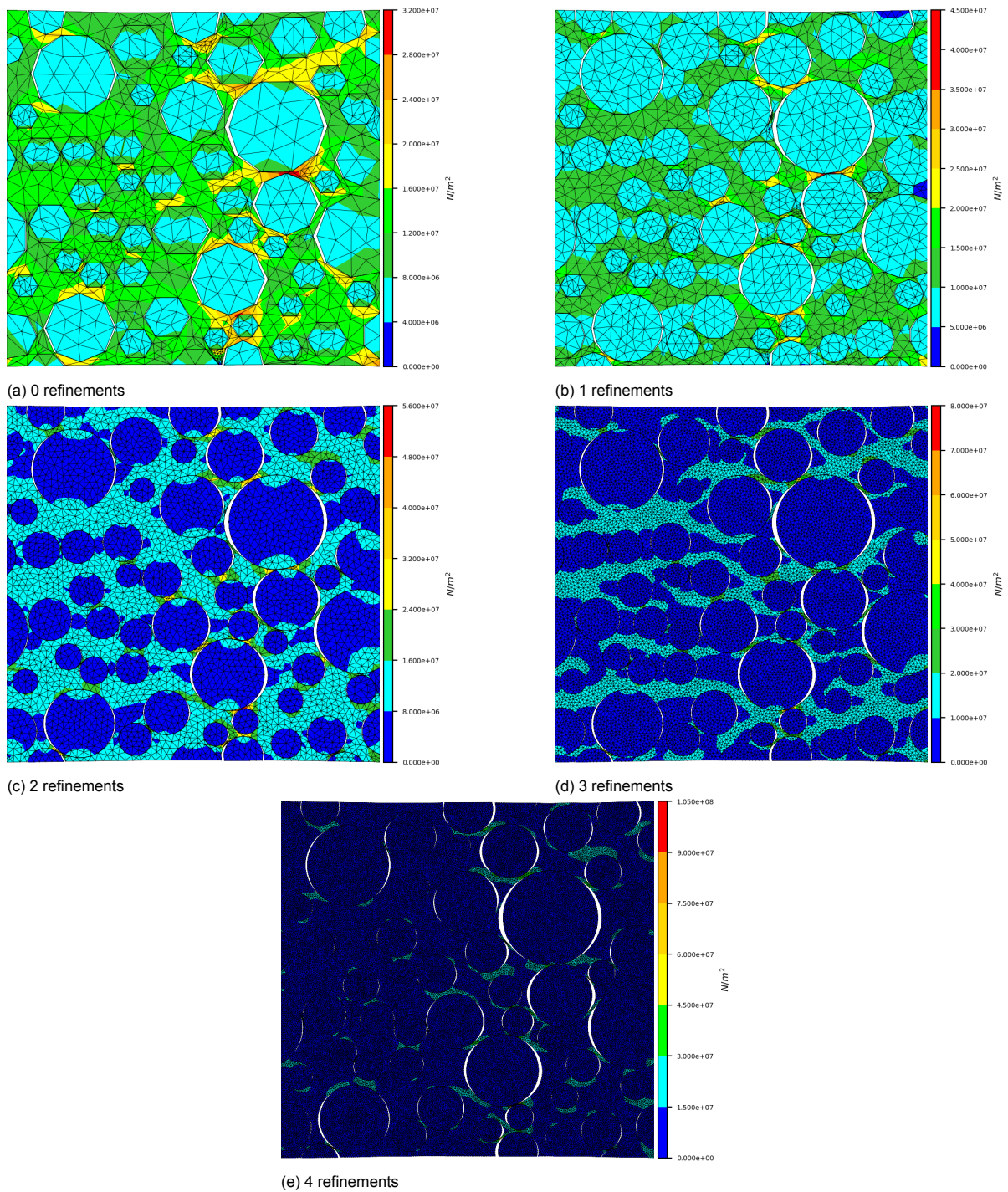


Figure 5.30: Maximum principal stress fields for v2 RVE with 50 particles when subjected to tension BCs for different mesh refinements. Fields given for an imposed strain of $\epsilon = 0.0472$.

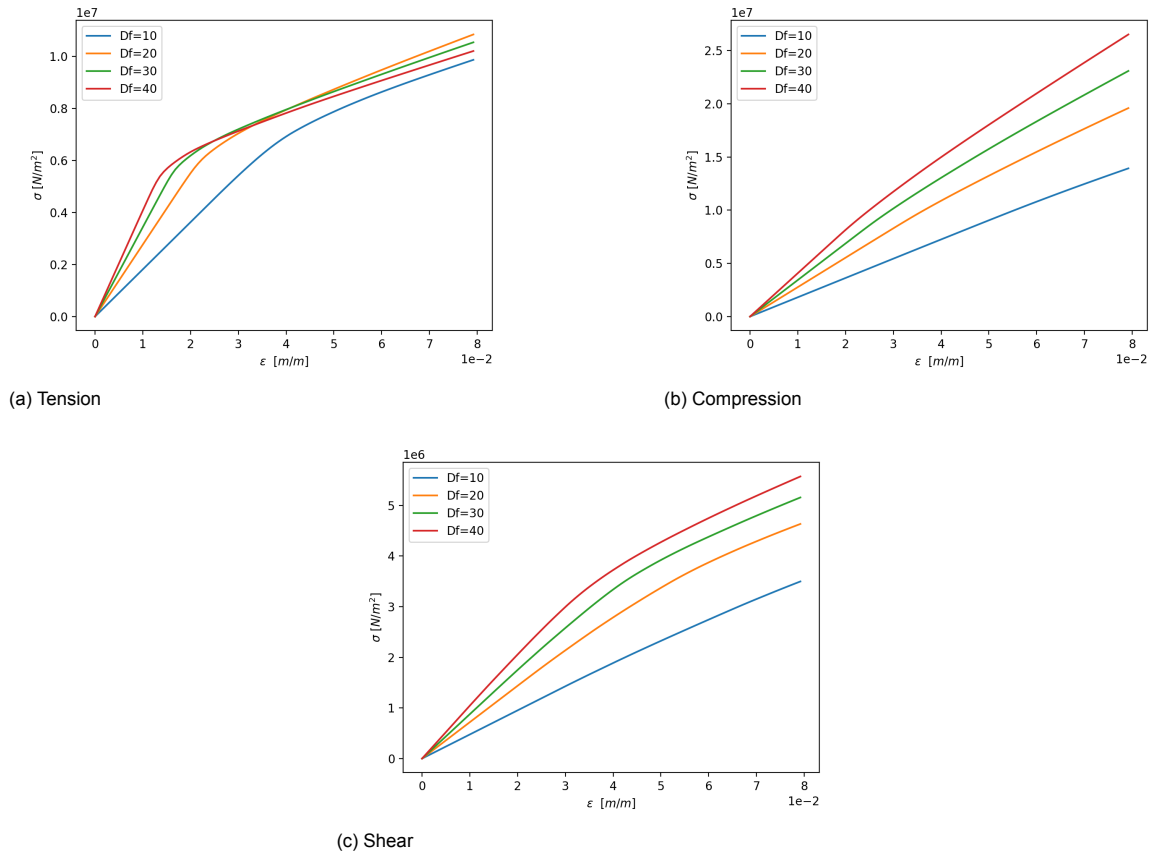


Figure 5.31: Effect of particle distribution and particle size Df for RVEs with uniformly distributed particle size

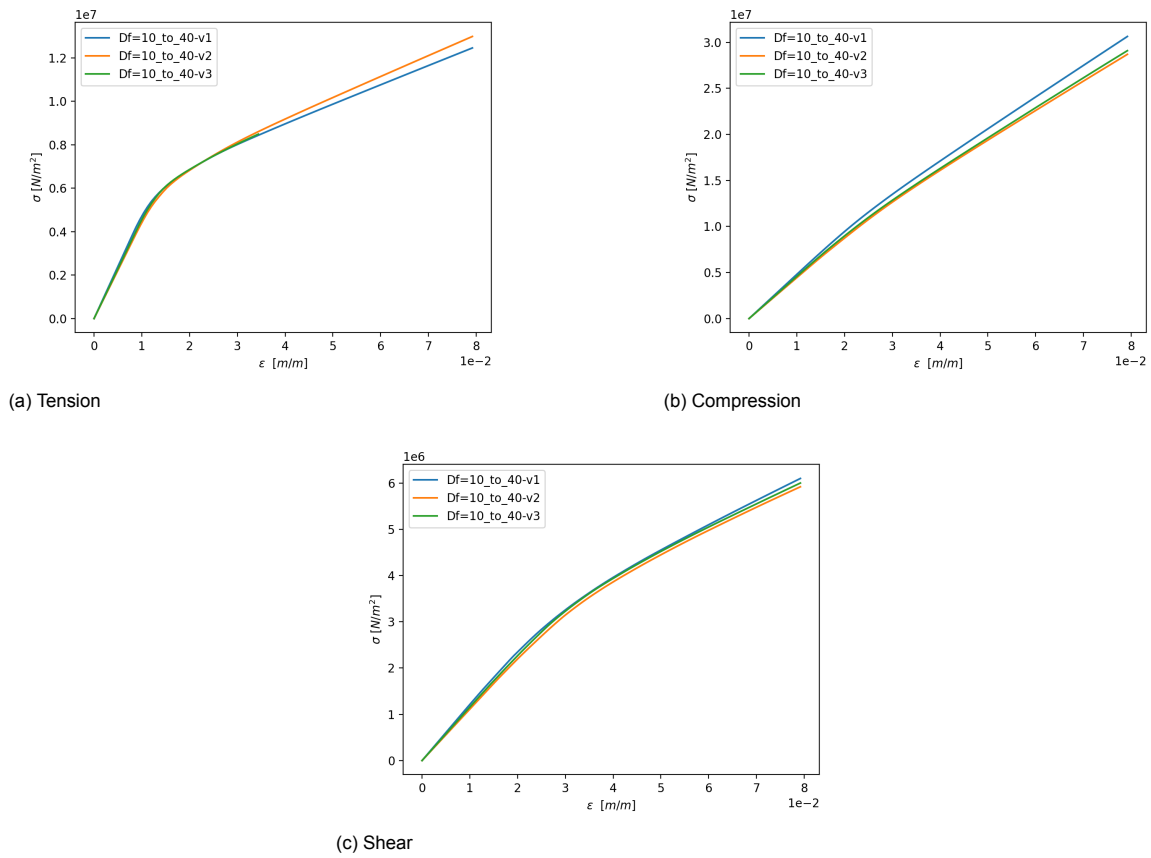
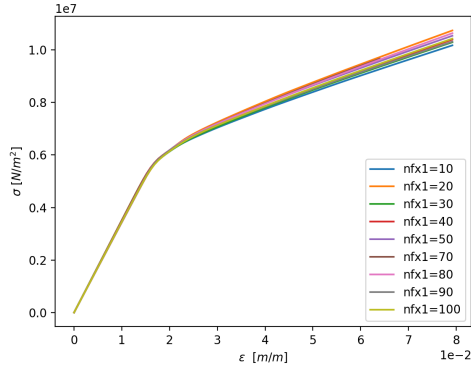
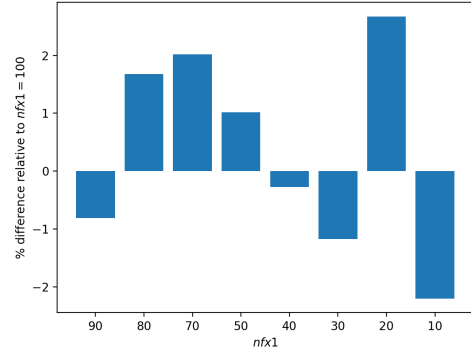


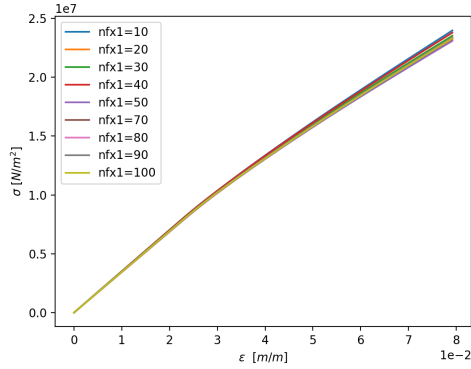
Figure 5.32: Effect of particle distribution and particle size distribution for RVEs with normally distributed particle size Df



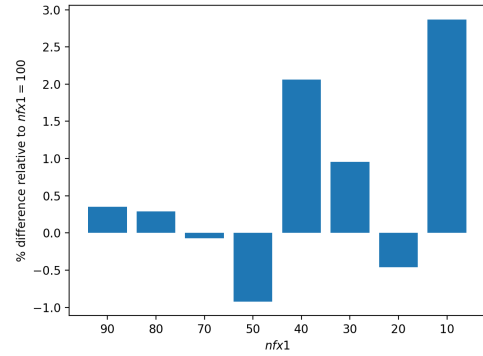
(a) Tension



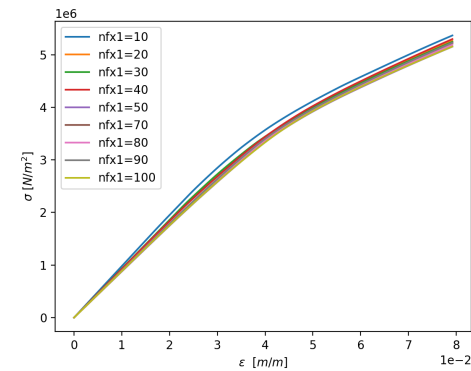
(b) Relative differences in stress between the curves in Fig. 5.33a for a strain of $\epsilon = 0.0640$



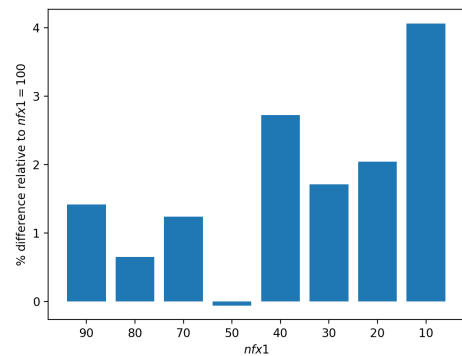
(c) Compression



(d) Relative differences in ultimate stress between the curves in Fig. 5.33c

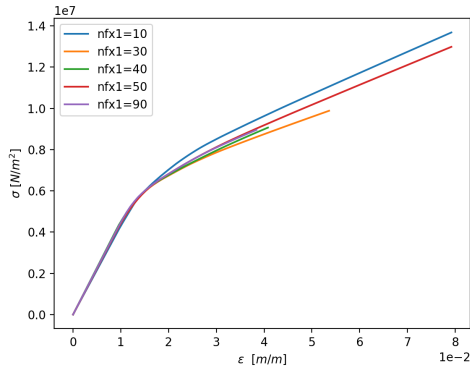


(e) Shear

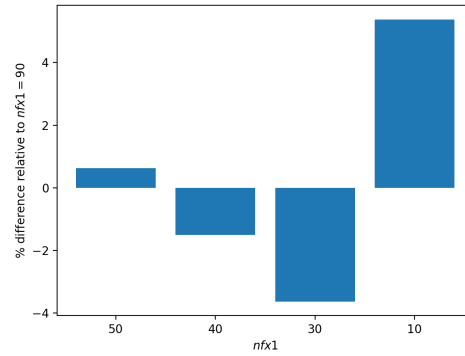


(f) Relative differences in ultimate stress between the curves in Fig. 5.33e

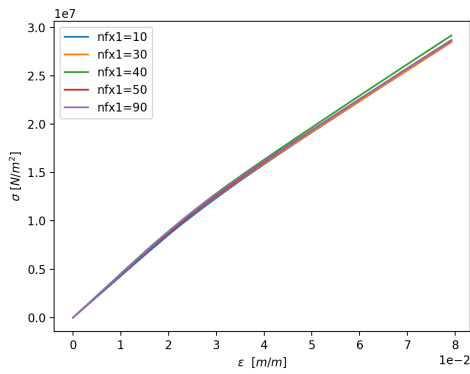
Figure 5.33: Effect of number of particles $nfx1$ for RVEs with particle size $Df = 30\mu m$



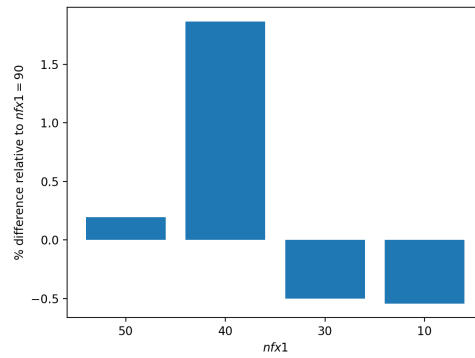
(a) Tension



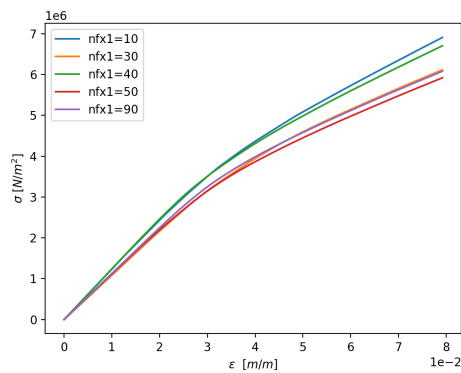
(b) Relative differences in stress between the curves in Fig. 5.34a for a strain of $\epsilon = 0.0360$



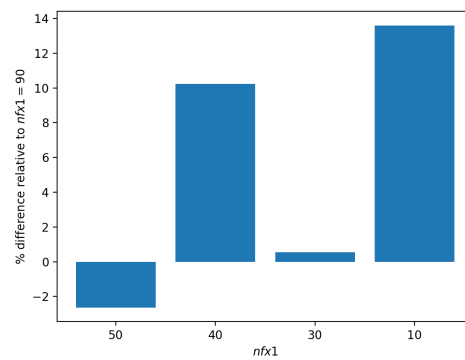
(c) Compression



(d) Relative differences in ultimate stress between the curves in Fig. 5.34c

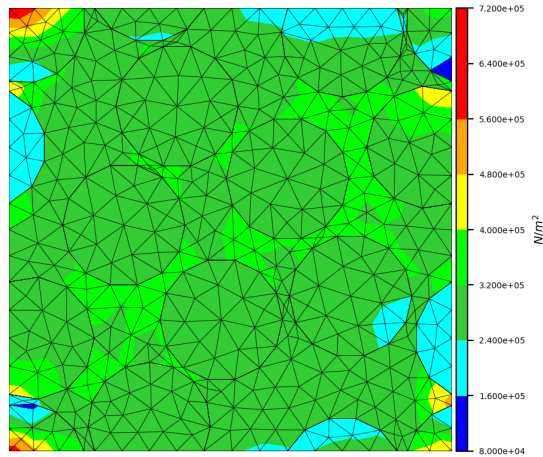


(e) Shear

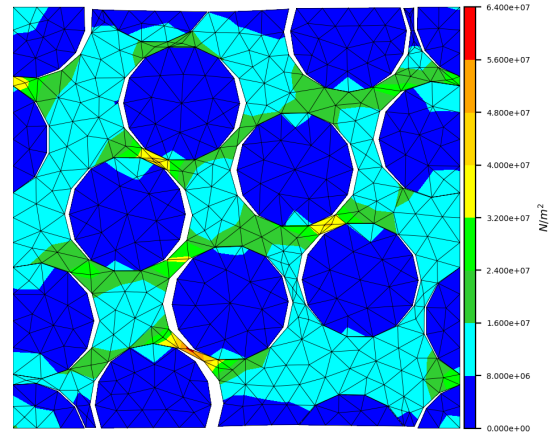


(f) Relative differences in ultimate stress between the curves in Fig. 5.34e

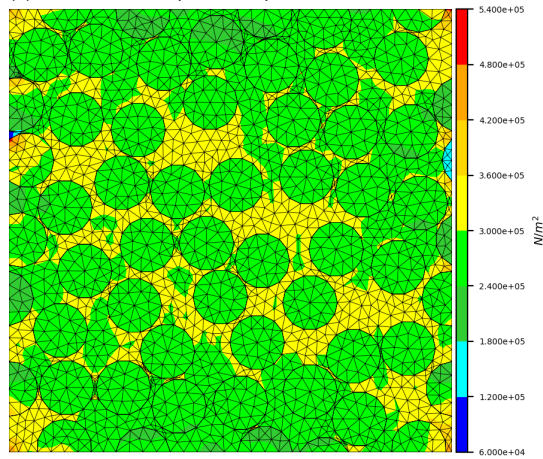
Figure 5.34: Effect of number of particles $nfx1$ for v2 RVEs



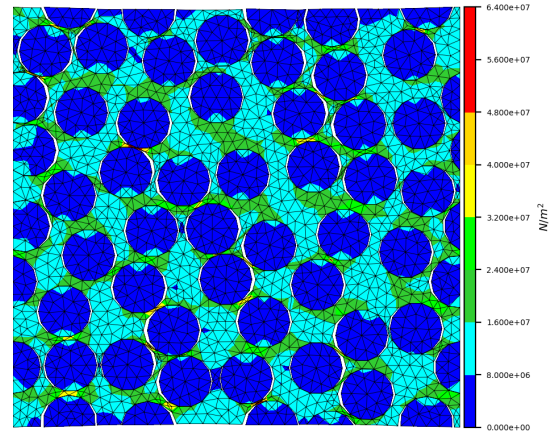
(a) Linear elastic response, 10 particles



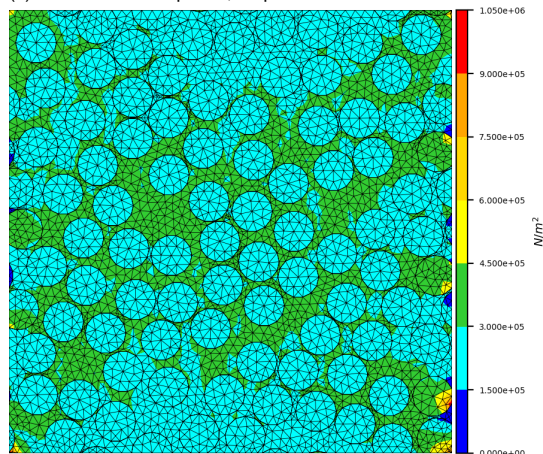
(b) Debonding response, 10 particles



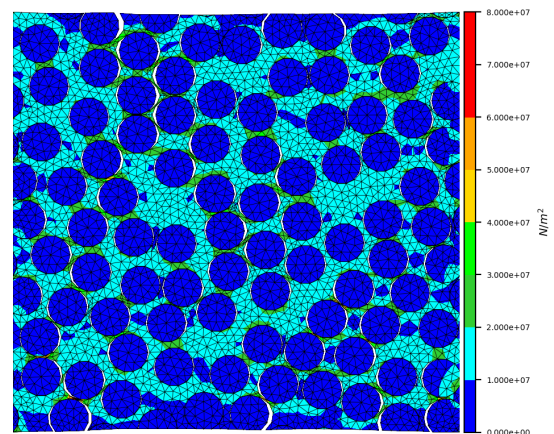
(c) Linear elastic response, 50 particles



(d) Debonding response, 50 particles



(e) Linear elastic response, 90 particles



(f) Debonding response, 90 particles

Figure 5.35: Maximum principal stress fields for RVE with $Df = 30$ when subjected to tension BCs. The fields are given for the linear elastic and debonding regimes of the response and for different number of particles $nfx1$. The linear elastic fields correspond to an imposed strain of $\epsilon = 0.00080$ and the debonding fields correspond to an imposed strain of $\epsilon = 0.0640$.

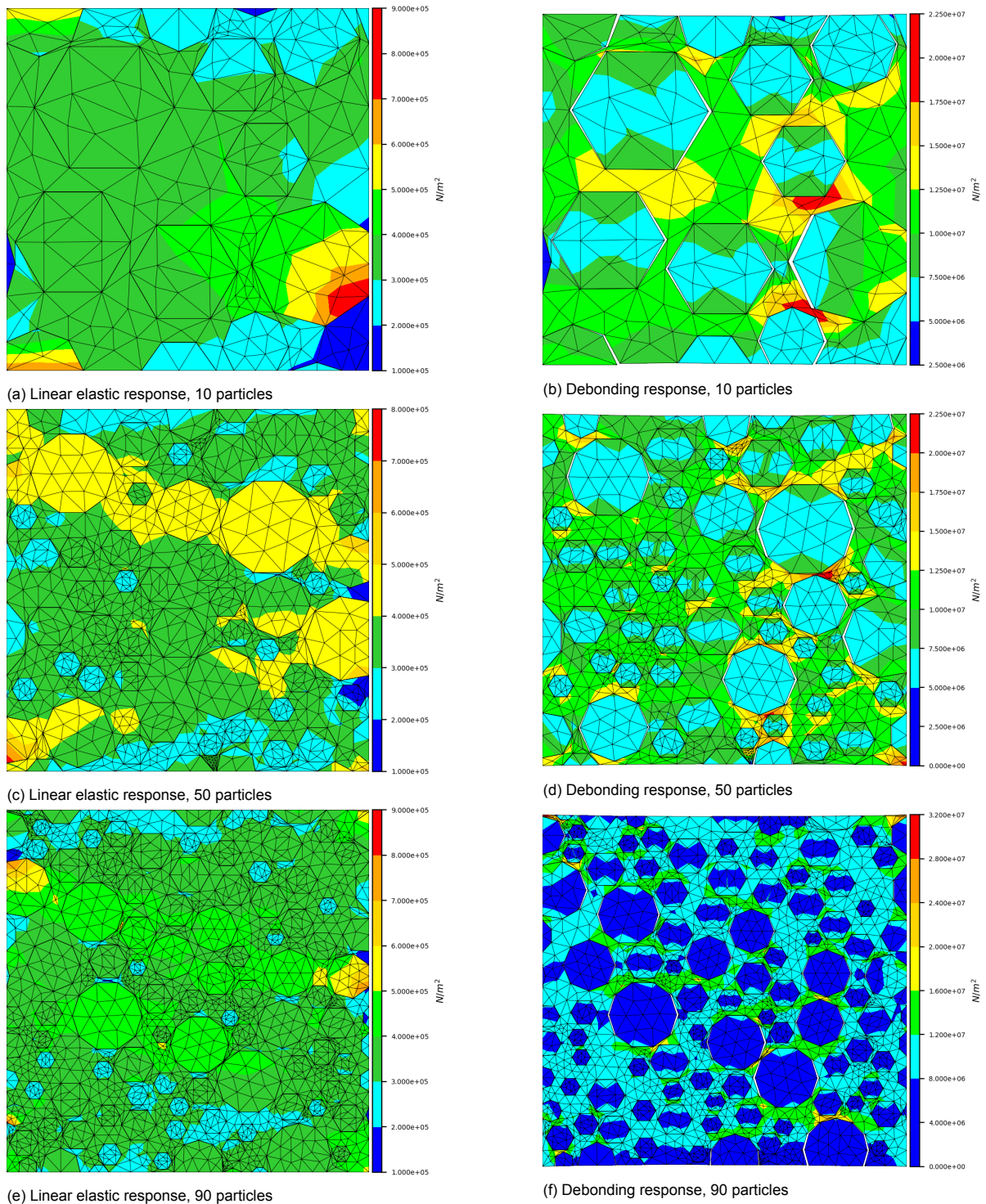


Figure 5.36: Maximum principal stress fields for v2 RVE when subjected to tension BCs. The fields are given for the linear elastic and debonding regimes of the response and for different number of particles $nfx1$. The linear elastic fields correspond to an imposed strain of $\epsilon = 0.00080$ and the debonding fields correspond to an imposed strain of $\epsilon = 0.0640$.

5.5. Damage-Debonding-Viscoelastic Behavior

The overall behavior of the micro-structure of solid propellants is investigated by applying the damage-viscoelastic model to the matrix and the Turon model to the matrix-particle interfaces of the RVEs.

The effect of mesh refinement on the stress-strain behavior is shown in Fig. 5.37. Recall from Sections 5.2, 5.3, and 5.4.2 that stress concentrations increase in magnitude upon mesh refinement and stiffen the stress-strain response. Stress concentrations also increase matrix and debonding damage in the RVE, which in turn reduce stress concentrations. Therefore, competing mechanisms determine the evolution of stress concentrations, and consequently, of the RVE's stiffness. When only matrix damage is considered the mechanism that increases stiffness dominates, and when only debonding damage is considered the mechanism that decreases stiffness dominates. The figure shows that when both forms of damage are considered the net effect is a decrease in stiffness. Mesh refinement has a near negligible effect on stress-strain response for compression and shear BCs because the competing mechanisms partially counteract each other. Mesh refinement has a larger effect for tension BCs because the RVE experiences greater matrix and debonding damage when subjected to tension. Figure 5.38 shows the stress and damage fields of the RVE for different meshes at ultimate load. Changes in stress concentrations upon mesh refinement are less evident here than in previous sections because both matrix and debonding damage work together in reducing stress concentrations. For this reason, damage fields provide a clearer depiction of the stress history of the matrix. Coarser meshes exhibit a greater rate of softening than finer meshes because coarser meshes experience more overall (i.e. volume averaged) matrix damage. This is contrary to the results of Section 5.3, where only matrix damage is considered and finer meshes experience more matrix damage. This discrepancy occurs because when debonding damage is also considered it significantly reduces the magnitude and volume occupied by stress concentrations. Debonding damage increases for finer meshes, thereby reducing stress concentrations and overall matrix damage.

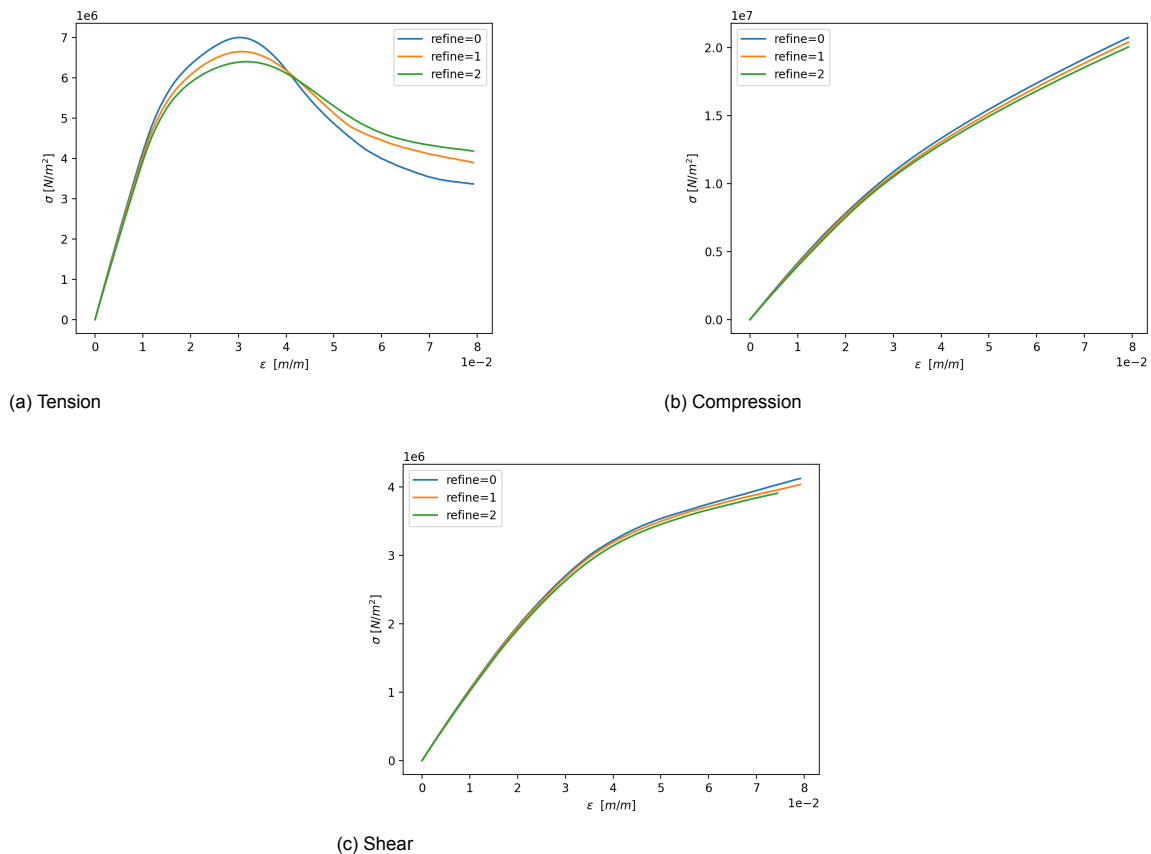


Figure 5.37: Effect of mesh refinement for v2 RVE with 50 particles

The effect of particle distribution and particle size D_f on the stress-strain behavior is shown in

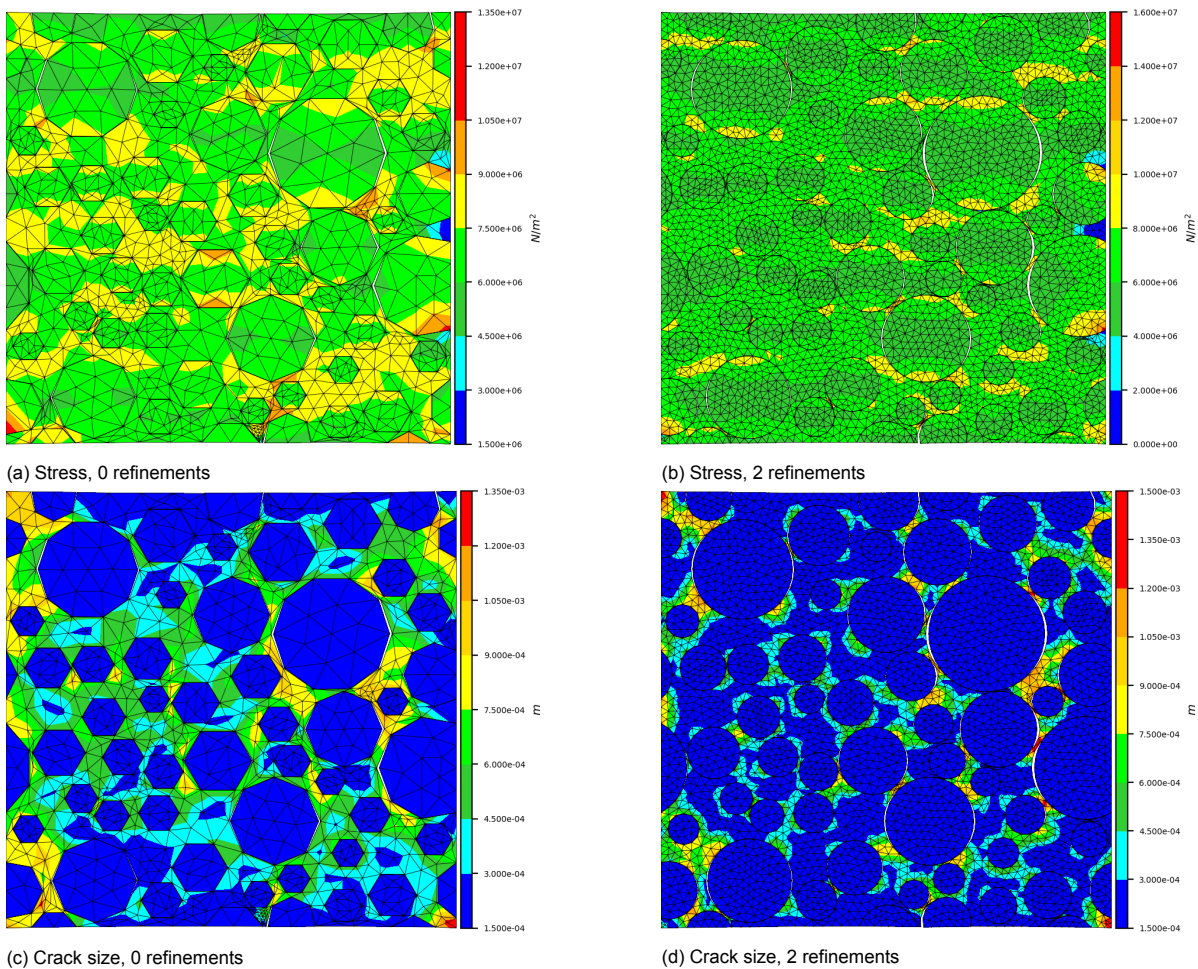


Figure 5.38: Maximum principal stress and mean crack size \bar{c} fields for v2 RVE with 50 particles when subjected to tension BCs for different mesh refinements.

Figures 5.39 and 5.40 for RVEs with particles of uniform and varying size, respectively. The responses of RVEs with uniform particle size distribution are highly sensitive to variations in Df . This occurs because the Turon model introduces a size effect which was discussed in Section 5.4.2. Recall from Section 5.3 that the damage-viscoelastic model is unaffected by variations of Df . Therefore, the Turon model is the unique source of size sensitivity. Also recall that both the Turon model and the damage-viscoelastic model are not sensitive to particle distribution for the number of particles considered (i.e. $nfx1 = 50$). This explains why the different RVEs with normally distributed particle size exhibit very similar responses.

The effect of the number of particles $nfx1$ on the stress-strain behavior is shown in Figures 5.41 and 5.42 for RVEs with particles of uniform and varying size, respectively. In the undamaged regime, where the response is purely viscoelastic, the responses of RVEs with different number of particles are almost identical for all BCs considered and for both types of particle size distribution. This occurs because the value assigned to the dummy stiffness K has a significant influence in the local and the global stiffnesses of the RVEs. For a detailed explanation on why a low value of K makes the responses insensitive with respect to $nfx1$ in the undamaged regime see Section 5.4.2. Compared to the case where only debonding damage is considered, we see that when viscoelastic damage is also considered the stress-strain responses exhibit less scatter when subjected to tension BCs, similar scatter when subjected to compression BCs, and more scatter when subjected to shear BCs. This is the same pattern observed in Section 5.3 when the matrix is modelled with the damage viscoelastic model instead of linear elasticity. Figures 5.43–5.44 show that when both debonding and matrix damage are considered, matrix damage evolves at a lower rate than when only matrix damage is considered (compare to Figures 5.17–5.18). The main reason for this is that the matrix experiences lower stresses, because

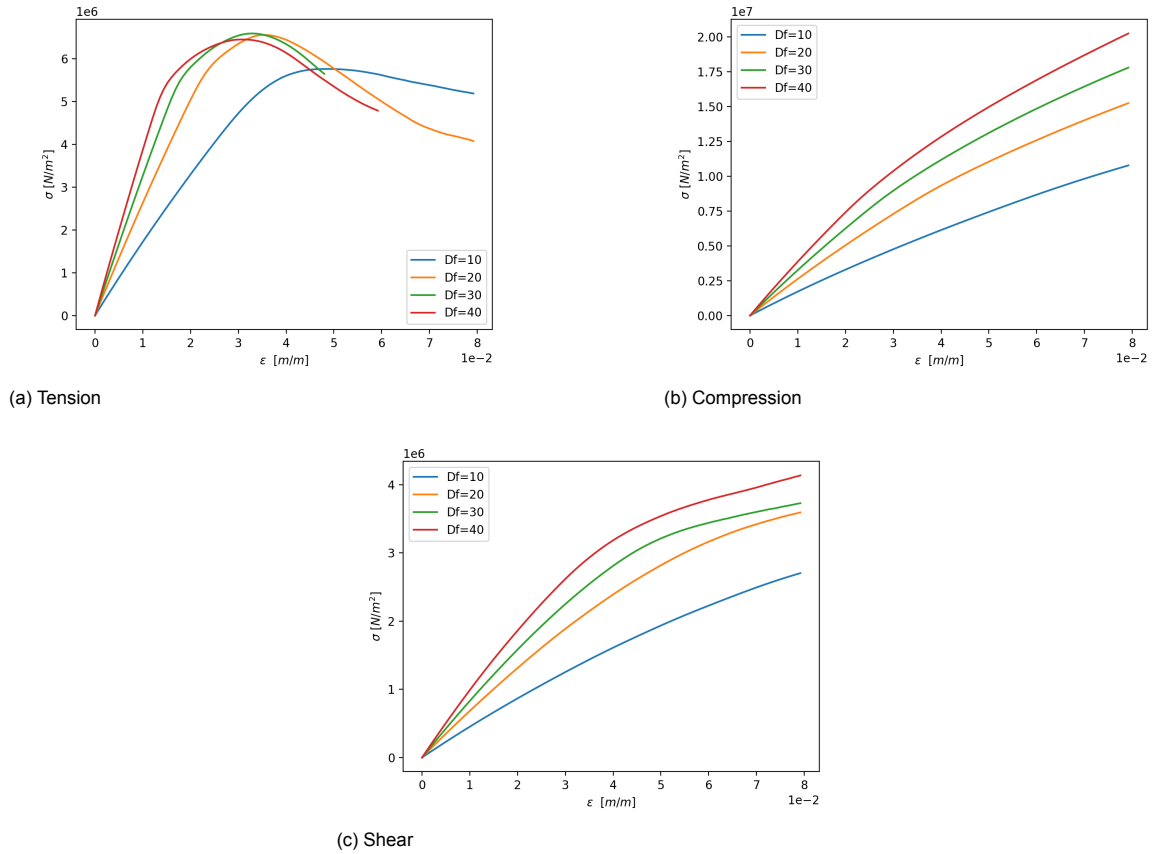
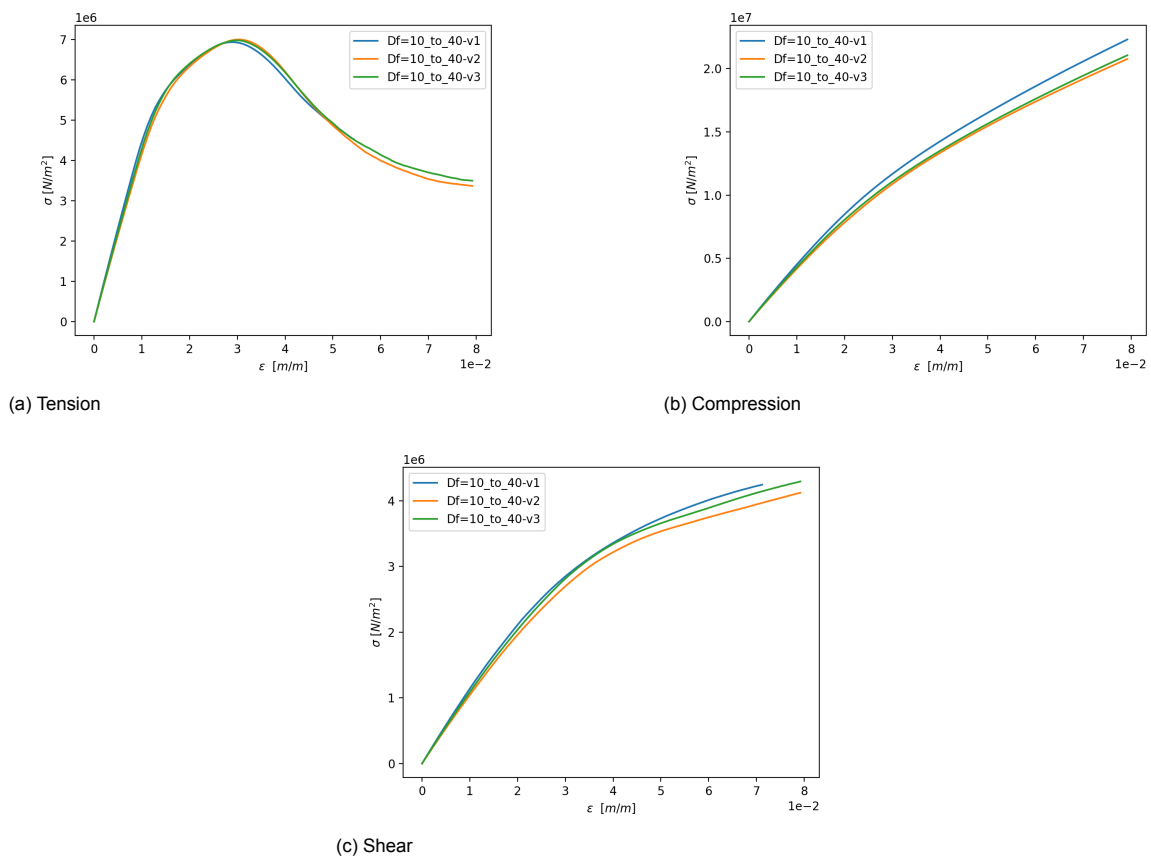
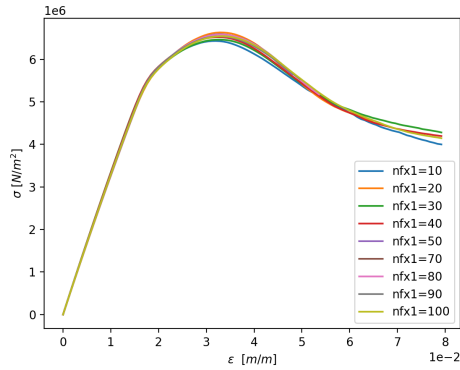


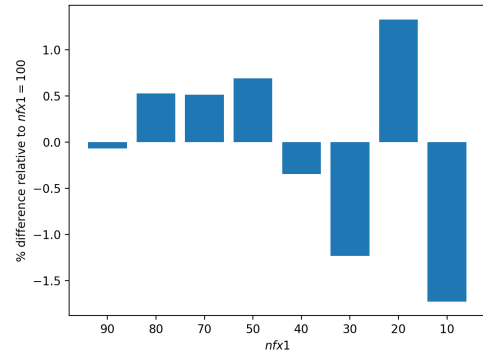
Figure 5.39: Effect of particle distribution and particle size Df for RVEs with uniformly distributed particle size

K reduces local stiffness. Energy dissipation caused by debonding damage is only a secondary cause for the reduction of matrix damage. In fact, debonding damage dissipates much less energy when matrix damage is considered compared to when it is not. To see this, compare the displacement jumps shown in this section to the ones shown in Figures 5.35-5.36 of Section 5.4.2. The effect of debonding damage is greatly reduced by the effect of matrix damage because matrix damage reduces stress concentrations occurring near the interfaces.

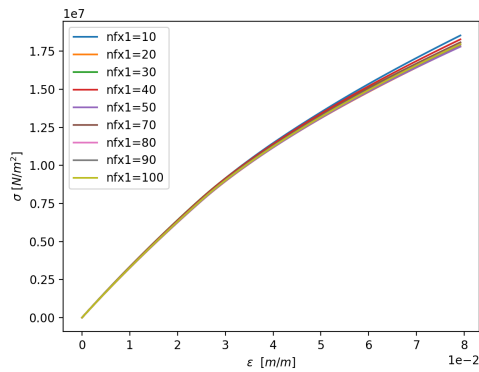
Figure 5.40: Effect of particle distribution and particle size for RVEs with normally distributed particle size Df



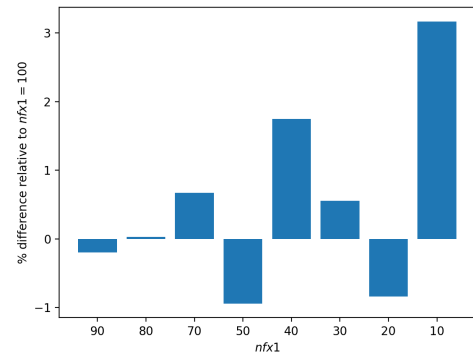
(a) Tension



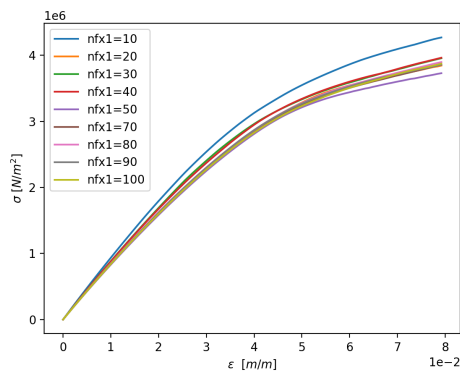
(b) Relative differences in ultimate stress between the curves in Fig. 5.41a



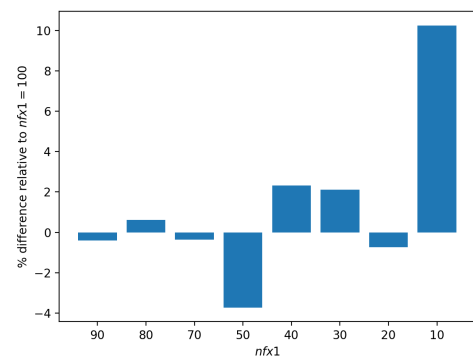
(c) Compression



(d) Relative differences in ultimate stress between the curves in Fig. 5.41c

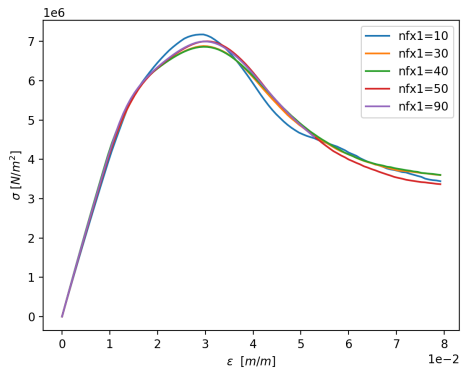


(e) Shear

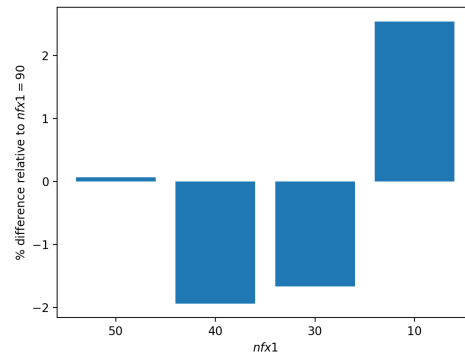


(f) Relative differences in ultimate stress between the curves in Fig. 5.41e

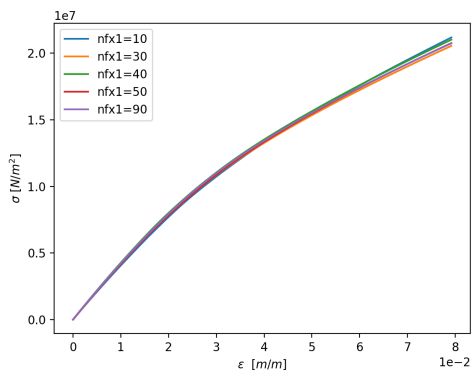
Figure 5.41: Effect of number of particles $nfx1$ for RVEs with particle size $Df = 30\mu m$



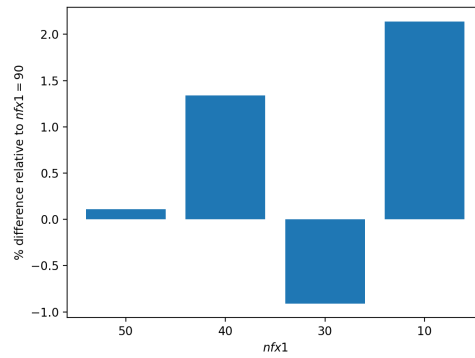
(a) Tension



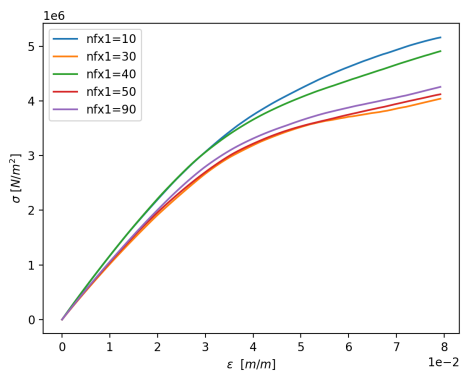
(b) Relative differences in ultimate stress between the curves in Fig. 5.42a



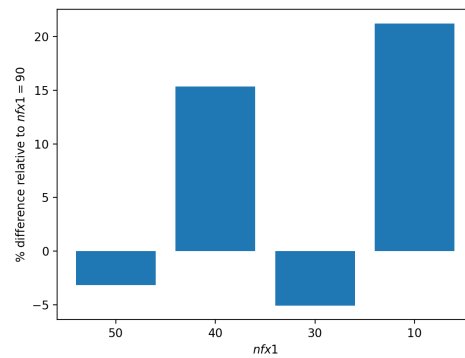
(c) Compression



(d) Relative differences in ultimate stress between the curves in Fig. 5.42c



(e) Shear



(f) Relative differences in ultimate stress between the curves in Fig. 5.42e

Figure 5.42: Effect of number of particles $nfx1$ for v2 RVEs

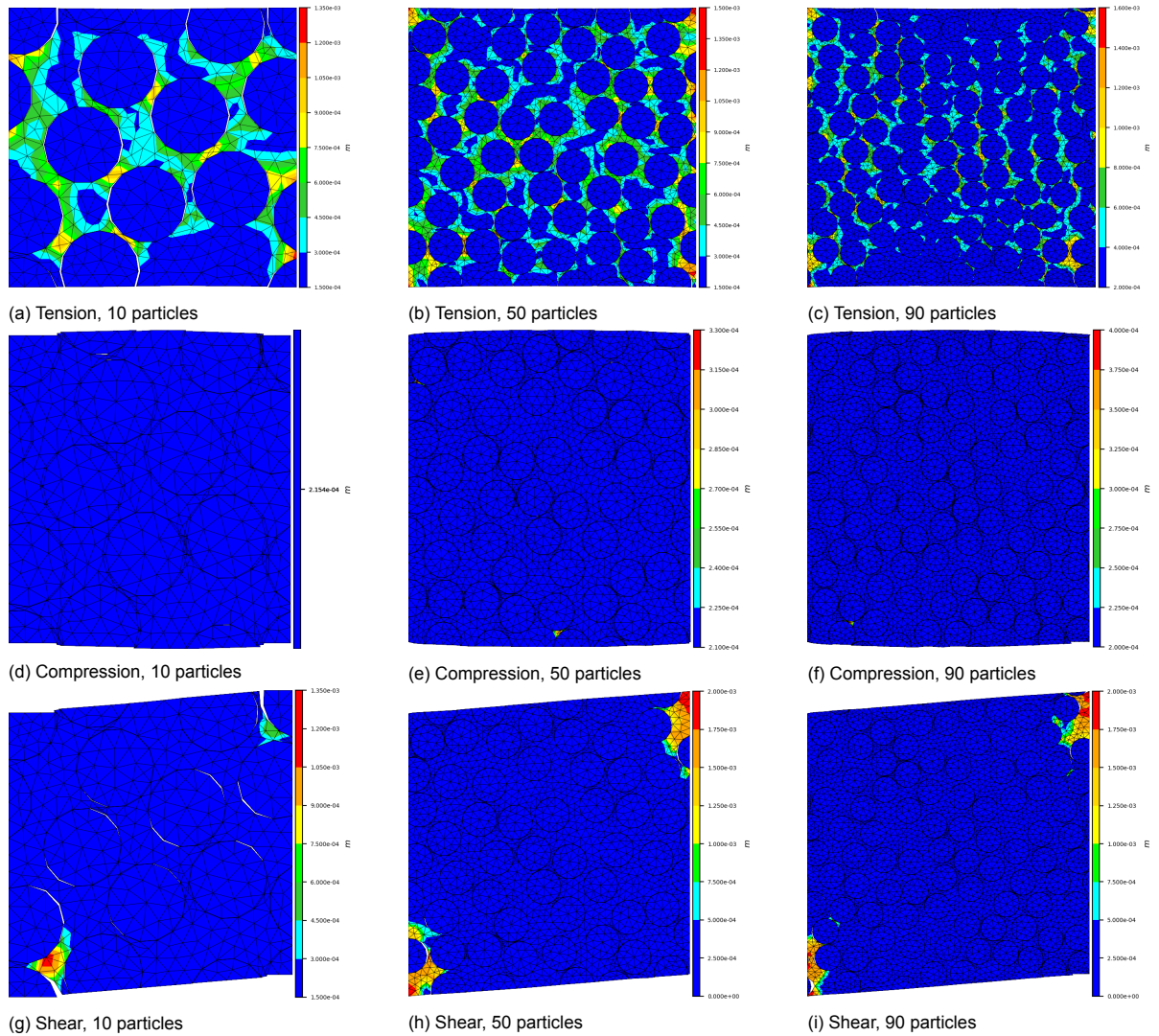


Figure 5.43: Mean crack size \bar{c} fields for RVE with $Df = 30$ when subjected to tension, compression, and shear BCs. The fields are given at maximum load. Different number of particles $nfx1$ are considered.

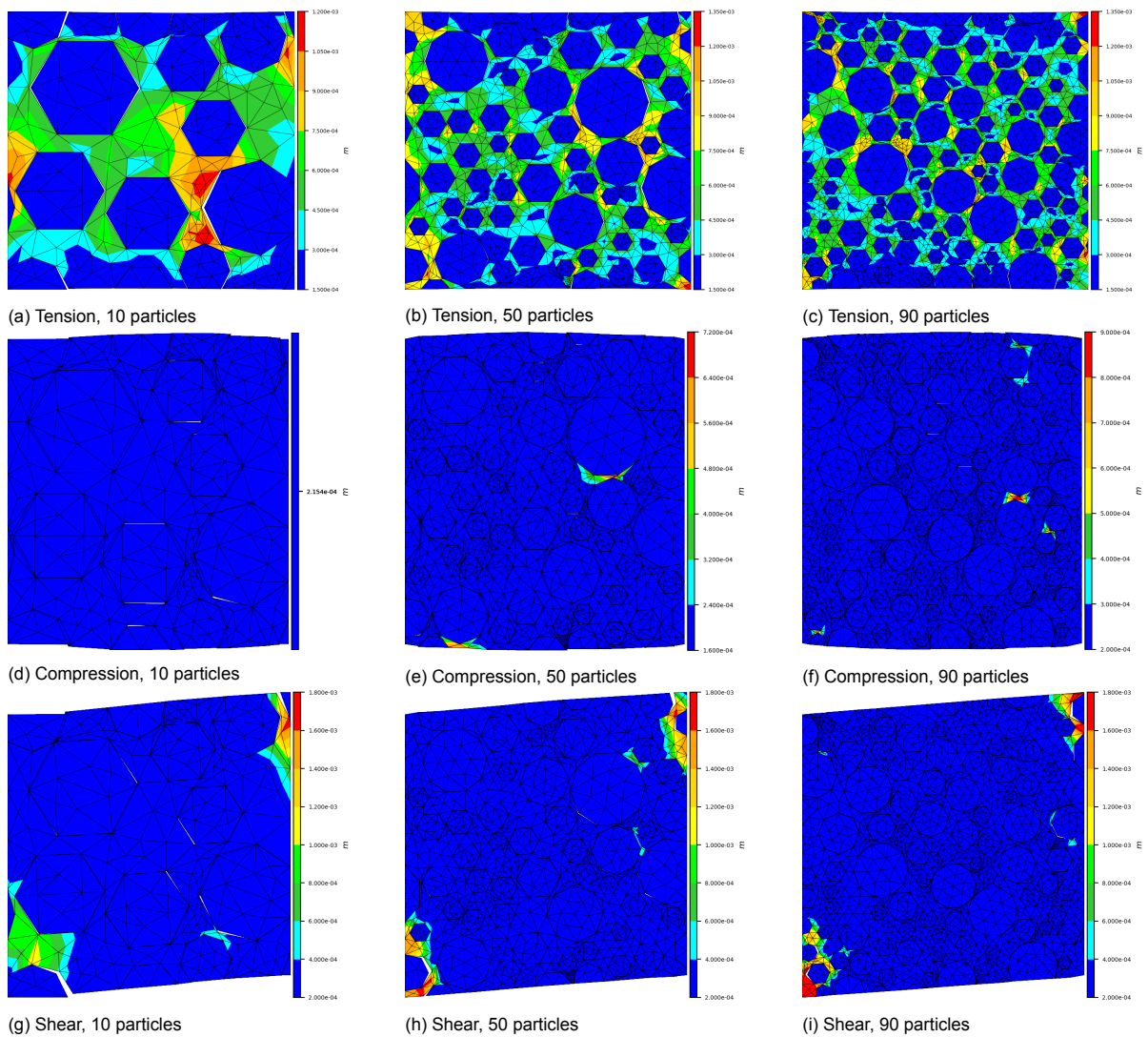


Figure 5.44: Mean crack size \bar{c} fields for v2 RVE when subjected to tension, compression, and shear BCs. The fields are given at maximum load. Different number of particles n_{fx1} are considered.

5.6. Conclusion

The micro-structural behavior of solid propellants was investigated in this chapter by considering different combinations of constitutive relations and RVE mesh geometries. Tension, compression, and shear BCs were considered for all analyses. Stress concentrations were shown to be the main source of sensitivity with respect to particle distribution, number of particles $nfx1$, and mesh refinement. Continuum matrix damage reduced the magnitude of stress concentrations. As a consequence it reduced the sensitivity of the RVEs with respect to particle distribution and $nfx1$.

The Turon model for interface elements was introduced and investigated to understand and apply debonding damage. It was shown that the debonding behavior of the RVEs can be decomposed into four regimes. With unrefined meshes only the first two regimes can manifest before the numerical solution becomes unconverged. This shows that the debonding behavior described by the Turon model is highly sensitive to mesh refinement, and very fine meshes are necessary to achieve convergence. Unconvergence can also be caused by high values of the dummy stiffness K . Due to this, the K of the interface elements cannot be set sufficiently high enough to properly approximate the linear elastic BVPs (where no interface elements are present) with the linear elastic regimes. Furthermore, conditioning of the numerical solutions with respect to K increases as the approximations of the linear elastic BVPs worsen. In general, the numerical solutions are ill-conditioned for permissible values of K . Since a relatively low K is utilized, the responses of the RVEs lose sensitivity with respect to particle distribution and $nfx1$. This is due to significant displacement jumps in the linear elastic regime, so stress concentrations become weaker. Additionally, debonding also contributes to reducing stress concentrations in the debonding regime. The Turon model is formulated in terms of tractions and displacement jumps, so it introduces a size dependency on Df . When matrix and debonding damage are both considered, the RVEs exhibit the same behaviors previously mentioned for each form of damage. Stress concentrations become weaker when both damage mechanisms act together than when only one is considered as more overall damage takes place.

Within the context of this thesis, the most limiting factor for characterizing the micro-structural behavior of solid propellants is the difficulty in capturing debonding damage. The Turon model requires highly refined RVE meshes for good behavior, which is not feasible within a CH context. In contrast, the modified viscoelastic damage model generally exhibits good numerical behavior.

6

Macro-Structural Behavior and Debonding in the Experimental Samples

The macro-structural behavior of solid propellants is investigated by employing the damage-viscoelastic model presented in Chapter 4 to the matrix, the Turon model for interface elements presented in Chapter 5 to the matrix-particle interfaces, and computational homogenization (CH). The investigation procedure of this chapter is similar to the procedure of Chapter 5, but for the macro-structure instead of the micro-structure. The effects that geometric and constitutive aspects of the RVEs have on macroscopic response are investigated. The behavior of the Turon model is investigated to understand how the problematic aspects of its behavior identified in Chapter 5 extend to a CH context. In this chapter only tension BCs are applied, with only one compression and one shear exception.

The macroscopic meshes are shown in Fig. 6.1. Three different mesh refinements are considered for tension simulations. Mesh refinements define element size by applying *Gmsh* characteristic lengths defined by $L_M = 0.005/(n_M + 1)$. Where n_M is the number of times that a mesh has been refined relative to the base case $n_M = 0$. The characteristic length for the compression/shear mesh is $L_M = 0.0025$. The BCs applied to the meshes are shown in Fig. 6.2. The BCs always apply a strain rate of $\dot{\epsilon} = 4.2 \mu\text{m/s}$ and the $n_M = 0$ mesh is always utilized for tension simulations, unless otherwise noted.

The RVE meshes considered in this chapter are shown in Appendix D. The number of particles $nfx1$ in the RVEs varies from 10 to 100 and the particle size Df varies from $10 \mu\text{m}$ to $40 \mu\text{m}$. RVEs with uniform and normal particle size distribution are considered. RVEs with normally distributed particle size are assigned the label $v1$, $v2$, or $v3$, depending on the input utilized for pseudo-random sampling from the particle size PDF. See Appendix D for a more detailed description of the RVEs and the associated terminology. As default for meshes with uniform particle size, the number of mesh refinements is $n_m = 1$, the particle size is $Df = 30 \mu\text{m}$, and the number of particles is $nfx1 = 50$. And for meshes with normally distributed particle size, the number of mesh refinements is $n_m = 0$, the input version for particle size generation is $v2$, and the number of particles is $nfx1 = 50$. If the type of particle size distribution (i.e. uniform or normal) within an RVE is not explicitly stated, assume a normal distribution. The mesh with $nfx1 = 50$, $v2$ size generation input, and $n_m = 0$ is sometimes referred to as the "default mesh".

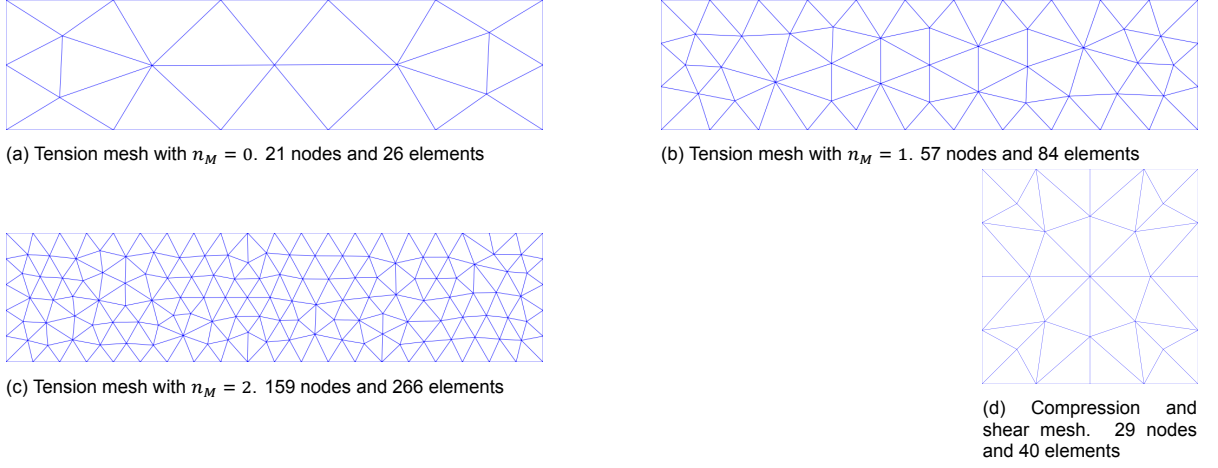


Figure 6.1: Macroscopic meshes utilized for CH simulations. For tension meshes, n_M is the number of mesh refinements

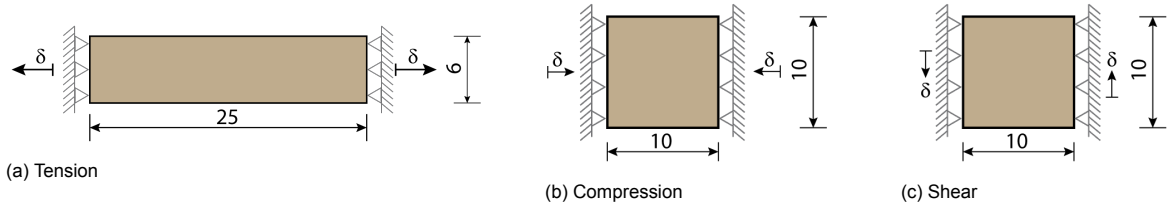


Figure 6.2: Macroscopic BCs and dimensions (dimensions in millimeters). Horizontal reactions are sampled for tension and compression and vertical reaction is sampled for shear.

6.1. First-Order Computational Homogenization

First-order computational homogenization (CH) owes its name to the homogenized response that it describes, which only depends on the first-order macroscopic deformation gradient [3]. It is the simplest variation of CH and it lays the foundations for more intricate forms of this framework. In CH the macro- and the micro-structures are evaluated concurrently. A brief description of first-order CH is given here. For more detail the reader is referred to Phu [26].

The procedure for first-order CH can be broken down in four steps [3]:

1. Defining the geometry and constitutive behavior of the RVE.
2. Prescribing the BCs for the micro-structural BVPs (i.e. imposed on the RVE) from macro-structural input.
3. Solving the micro-structural BVPs. From which the solutions are extrapolate the macro-structural stresses and material tangents.
4. Solving the macro-structural BVP.

Steps 2 and 3 are performed for each macroscopic IP at each global time step.

Step 1 is performed only once, before numerical computations. The principle of separation of scales, computational efficiency, and the minimum RVE size required to adequately capture homogenized micro-structural behavior must be considered.

The BCs prescribed in Step 2 must fit within the framework imposed by averaging theorems (Eq.(2.14)). So-called periodic boundary conditions satisfy this requirement and provide more accurate results than other widely employed BCs, such as prescribed displacement BCs [3][26]. Periodic BCs are always utilized in this chapter. Therefore, the description of CH given in this section continues within the context of periodic BCs, as prescribed in Fig. 6.3. Periodic BCs state that imposed displacements in opposite RVE boundaries $\Gamma_{m,i}^+$ are periodic and that the outward normal vectors (and consequently, tractions) are anti-periodic [26]. Mathematically, these conditions are formulated as

$$\mathbf{u}'(\mathbf{x}_m^+) = \mathbf{u}'(\mathbf{x}_m^-), \quad \mathbf{t}(\mathbf{x}_m^+) = -\mathbf{t}(\mathbf{x}_m^-) \quad (6.1)$$

Periodic BCs map strains at a macroscopic IP to the displacements of the microscopic controlling nodes $b = 1, 2, 4$ of Fig. 6.3 with

$$\mathbf{u}_b = [\mathbf{u}_1 \quad \mathbf{u}_2 \quad \mathbf{u}_4] = \mathbf{H}^T \epsilon_M \quad (6.2)$$

Where ϵ_M is the macroscopic strain vector at a given IP, and \mathbf{H} is a function of micro-structural coordinates given by

$$\mathbf{H} = \frac{1}{2} \begin{bmatrix} 2x & 0 & 2x & 0 & 2x & 0 \\ 0 & 2y & 0 & 2y & 0 & 2y \\ y & x & y & x & y & x \end{bmatrix} \quad (6.3)$$

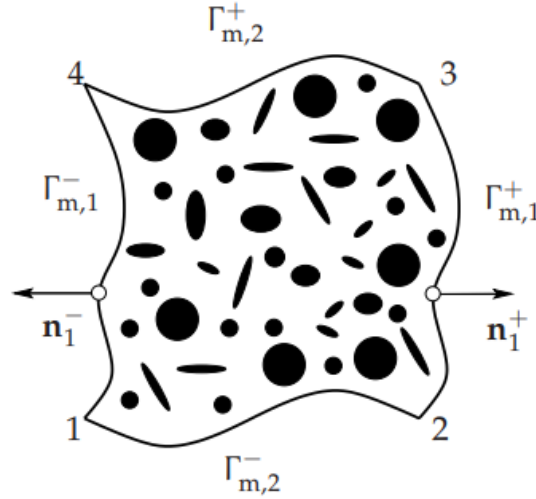


Figure 6.3: RVE subjected to periodic BCs

In Step 3, the macroscopic stress is extrapolated with the following simplification of the stress-averaging theorem

$$\sigma_M = \frac{1}{V} \mathbf{H} \mathbf{f}_b \quad (6.4)$$

Where the vector \mathbf{f}_b is obtained from solving the micro-structural BVP and it contains the external forces at nodes b . The macroscopic material tangent is derived from the variation of microscopic displacements and forces $\mathbf{K} \delta \mathbf{u} = \delta \mathbf{f}$. It is given by

$$\mathbf{C}_M = \frac{1}{V} \mathbf{H} \bar{\mathbf{K}}_{bb} \mathbf{H}^T \quad (6.5)$$

In which $\bar{\mathbf{K}}_{bb}$ is obtained from static condensation and is given by

$$\bar{\mathbf{K}}_{bb} = \mathbf{K}_{bb} - \mathbf{K}_{ba} \mathbf{K}_{aa}^{-1} \mathbf{K}_{ab} \quad (6.6)$$

Where a denotes the nodes in the RVE that do not belong to the set of controlling nodes.

Finally, The FEM continuum formulation for nonlinear problems in solid mechanics Eq. (2.8) solves the macro-structural BVP in Step 4.

6.2. Linear Elastic Behavior

The linear elastic behavior of the macro-structure of solid propellants is investigated by considering both the matrix and the particles in the RVEs as linear elastic.

The effect of mesh refinement on the load-displacement behavior is shown in Fig. 6.4. When finer microscopic meshes are utilized for the same macroscopic mesh, the response becomes stiffer. This occurs because stress concentrations in the micro-structure change in magnitude and location upon microscopic mesh refinement. For a detailed explanation about how mesh refinement affects the response of the micro-structure see Section 5.2. Comparing the tension response of the macro-structure given in Fig. 6.4a to the tension response of the micro-structure given in Fig. 5.3a, it is clear that convergence upon refinement is faster for the latter. This implies that when only the micro-structure is refined,

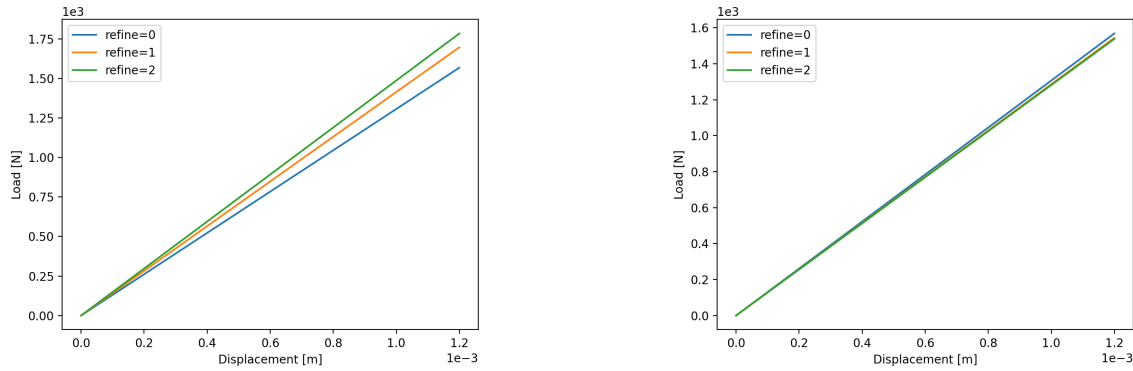
the order of convergence of the macro-structure is smaller than $O(h^2)$. Where h is a measure of microscopic element size. Refining only the micro-structure is equivalent to improving the homogenized constitutive relations without improving the structure of the system of equations utilized to characterize the macro-structural problem. Therefore, only the order of convergence of the constitutive relations is $O(h^2)$. Consequently, Figures 6.5a and 6.5b show that when only the micro-structure is refined, macro-structural stress fields vary negligibly with respect to their distribution but they vary significantly with respect to their magnitude. Note that the fields are not symmetric. This will be discussed later.

When finer macroscopic meshes are utilized for the same microscopic mesh, the response becomes softer, as shown in Fig. 6.4b. This is in line with the well known fact in FEM that coarser meshes produce stiffer responses for homogeneous materials. Solid propellants are not homogeneous materials, but their macro-structure is treated as such in the context of CH. The responses are much less sensitive to variations in macroscopic mesh refinement than to variations in microscopic mesh refinement. This is the case because contrary to refining the micro-structure, refining the macro-structure does not improve the characterization of stress concentrations. Refining the macro-structure simply improves the characterization of the homogenized macro-structure, where stress gradients are smaller. When only the macro-structure is refined, the order of convergence of the macro-structural problem is $O(H^2)$. Where H is a measure of macroscopic element size. This order of convergence is identical to that of classic FEM, because refining the macro-structure is equivalent to improving the solution of the macro-structural problem for the given homogenized constitutive relations. However, if the micro-structure is not refined, the accuracy of the homogenized constitutive relations is not improved. Consequently, Figures 6.5a and 6.5c show that when only the macro-structure is refined, macro-structural stress fields vary significantly with respect to their distribution but vary very little with respect to their magnitude.

When both the micro- and macro-structures are refined the response becomes stiffer, because micro-structural mesh refinement has a greater effect than macro-structural mesh refinement. Comparing the tension response of the macro-structure given in Fig. 6.4c to the tension response of the micro-structure given in Fig. 5.3a, we see that convergence rate upon refinement is almost identical for both cases. This suggests that when both the micro- and macro-structures are refined, the order of convergence is very close to $O(a^2)$. Where a is a measure of both micro- and macro-structural element size. That is, for a to be scaled by a number n , the characteristic element sizes at both length scales have to be scaled by n . It makes sense that the order of convergence is close to $O(a^2)$ because when both length scales are refined at the same rate, the order of convergence of the constitutive relations is $O(h^2)$ and the system of equations utilized to characterize the macro-structure improves with order $O(H^2)$. Figures 6.5a and 6.5d show that when both length scales are refined, macro-structural stress fields exhibit significant variation in both distribution and magnitude.

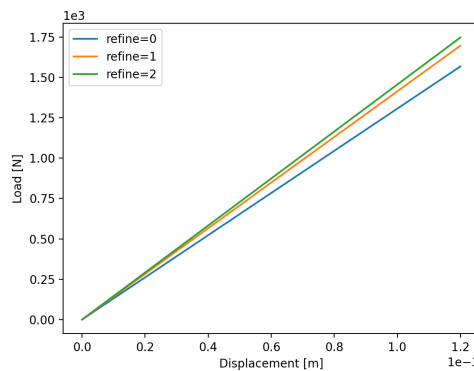
Recall from Chapter 4 that multi-scale homogenisation with perfectly bonded particles can also be considered through mathematical homogenization (MH). Figure 6.6 shows the effect of mesh refinement on the load-displacement response when MH (i.e. Eqs. 4.3 and 4.13) is utilized. The same meshes considered for the macro-structure throughout this chapter are considered for this analysis plus the mesh utilized for characterizing the tension samples in Chapter 4 (Fig. 4.1a), which corresponds to the third refinement. Mesh refinement does not affect the constitutive relations in MH, it only affects the system of equations utilized for describing the macro-structure. This is exactly the same as when only the macroscopic mesh is refined in CH. Consequently, both these cases exhibit similarly low sensitivity to variations in mesh refinement. Note that the MH responses shown in Fig. 6.6 are similar, but not identical, in magnitude to the CH responses shown in Fig. 6.4. Differences between the CH and the MH responses occur because the CH and the MH formulations apply different simplifications to their formulation. Namely, the MH formulation assumes that constitutive behavior is the same in all IPs, that particle size is uniformly distributed, and that statistical homogeneity is achieved. The CH formulation assumes that the constitutive behavior at each IP is given by the solution of a micro-structural BVP, and that the BCs imposed on this BVP are different for each IP. Furthermore, the RVE utilized for the CH computations is not perfectly statistically homogeneous and it has normally distributed particle size.

The stress fields for the MH load-displacement responses are shown in Fig. 6.7. These are clearly more symmetric than than the stress fields of Fig. 6.5 obtained from CH. The small asymmetries in the MH stress fields are exclusively caused by small mesh asymmetries. Conversely, the primary cause for the strong asymmetries observed in the CH stress fields is that the BCs applied to the micro-structure are different at each IP. The BCs are different at each IP because they depend on the macroscopic deformation gradient, which has the same magnitude but different direction at mirror points of the



(a) Micro-structure only

(b) Macro-structure only



(c) Both micro-structure and macro-structure

Figure 6.4: Effect of mesh refinement when v2 RVE with 50 particles is utilized. The subfigures show the number of refinements utilized for the specified length scales

macro-structure. Periodic BCs are asymmetric by definition, and asymmetric domains have different microscopic averaged stresses (as defined in Eq.(6.4)) at mirror points of the macro-structure. Note that for finer macro-structural discretizations CH stress fields become more symmetric. This occurs because the vertical component of the deformation gradient becomes less pronounced throughout the macro-structure upon mesh refinement. Which means that the vertical components of the microscopic BCs generally becomes less significant compared to the horizontal components, so the microscopic BCs become more symmetric.

The effects of particle distribution, of particle size D_f , and of the number of particles n_{fx1} on the load-displacement behavior are shown in Figures 6.8 and 6.9. The responses are unaffected by variations of D_f because linear elasticity is formulated in terms of stress and strain and because CH returns averaged stresses from the micro-structure to the macro-structure. The responses in Fig. 6.8 are not sensitive to particle distribution, because the number of particles considered (i.e. $n_{fx1} = 50$) is high enough such that the different RVEs have similar averaged responses. When outliers exist in Fig. 6.9 they correspond to macro-structures for which their RVEs have relatively low n_{fx1} . These same behaviors regarding variations in particle distribution, in D_f , and in n_{fx1} were observed in Section 5.2, where only micro-structural responses were considered. Note that different specimens exhibit similar, but not identical, variations in this section and in Section 5.2 because the macroscopic and microscopic BVPs are intrinsically different.

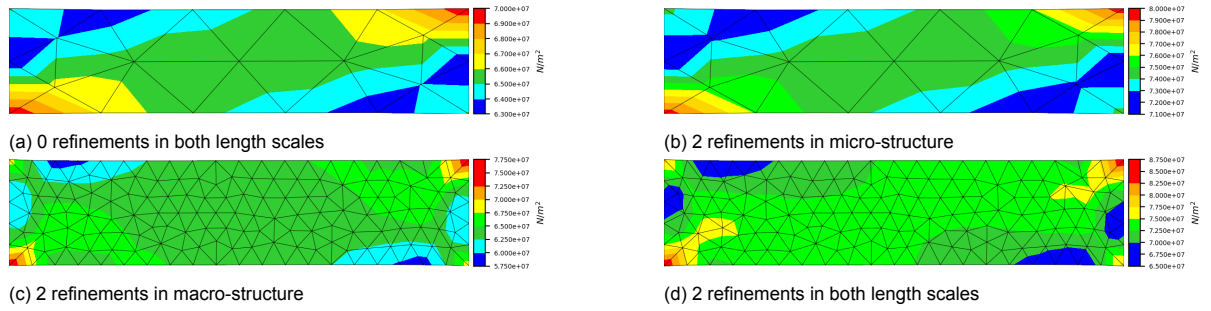


Figure 6.5: Maximum principal stress fields at maximum displacement for v2 RVE with 50 particles when subjected to tension BCs. Different mesh refinements are considered

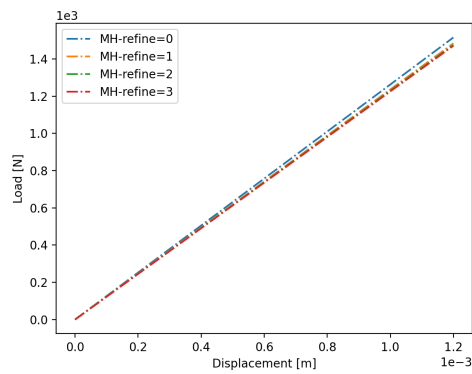


Figure 6.6: Effect of mesh refinement when MH is utilized for accounting for particles

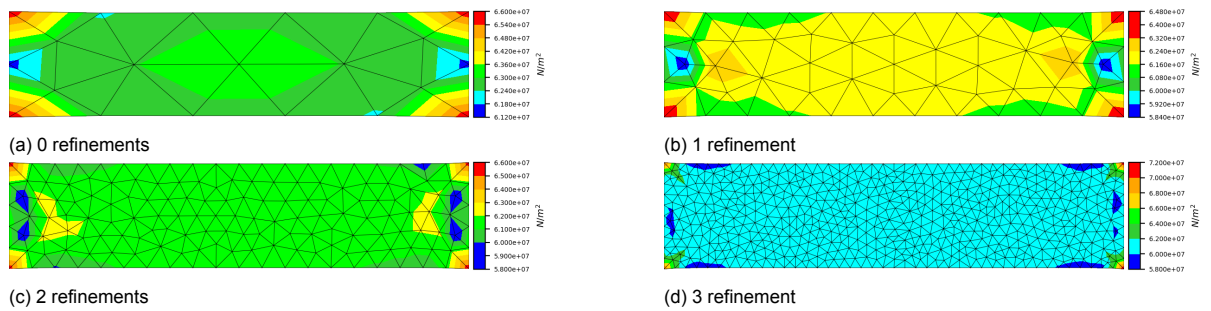
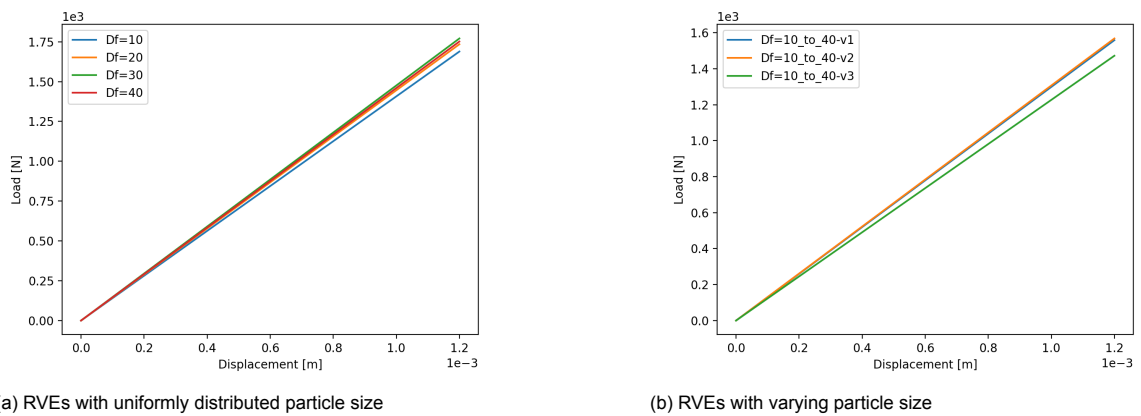


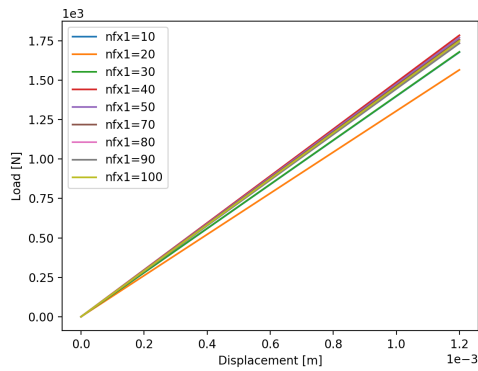
Figure 6.7: Maximum principal stress fields when MH is utilized for different mesh refinements



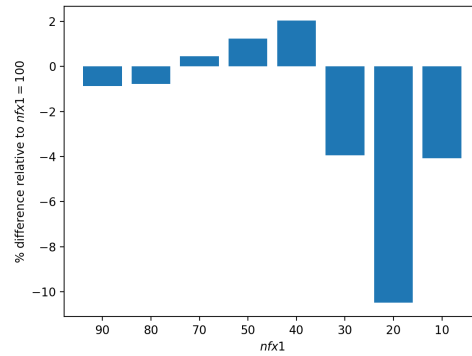
(a) RVEs with uniformly distributed particle size

(b) RVEs with varying particle size

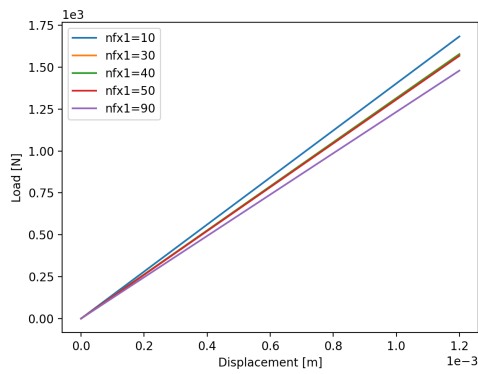
Figure 6.8: Effect of particle distribution and particle size Df



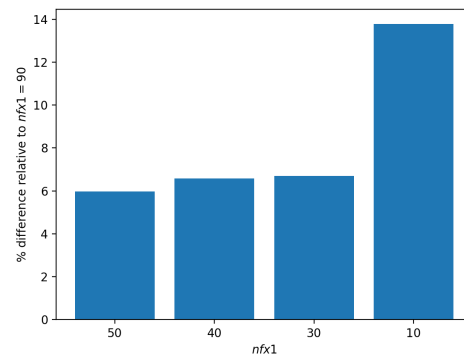
(a) RVEs with particle size $D_f = 30\mu m$



(b) Relative differences in ultimate stress between the curves in Fig. 6.9a



(c) v2 RVEs



(d) Relative differences in ultimate stress between the curves in Fig. 6.9c

Figure 6.9: Effect of number of particles $nfx1$

6.3. Behavior of the Debonding Model and Parameter Identification

The behavior of the Turon model for interface elements is investigated under the context of CH with the purpose of understanding the effect that micro-structural debonding damage has on the macroscopic response of the solid propellants. The matrix of the RVE is treated as linear elastic so that nonlinearities introduced by the Turon model can be explored in isolation of nonlinearities introduced by other constitutive models. The default debonding parameters of Table 6.1 and the default mesh are employed for all simulations.

Parameter	Value	Units
K	1.5×10^{14}	N/m^3
τ_I	5.0×10^6	N/m^2
τ_{II}	5.0×10^6	N/m^2
τ_{II}	2.5×10^6	N/m^2
G_{Ic}	1.125×10^2	J/m^2
G_{Ic}	1.125×10^3	J/m^2
G_{IIc}	1.125×10^2	J/m^2
G_{IIc}	1.125×10^1	J/m^2
η	0.5	-

Table 6.1: Debonding parameters for TNO's solid propellants. Blue value is used when both energies are equal to each other but the strengths are different. Green values are used when both strengths are equal to each other but the energies are different

Figures 6.10–6.12 show the effects that the debonding parameters have in the macroscopic response of the solid propellants. In general, the same patterns are observed here as in the investigation with the Turon model for the micro-structure only, Section 5.4.1. However, there are two major differences. The first one is that the responses observed here are more numerically stable than the microscopic responses observed in Section 5.4.1. In said section the tension response of the micro-structure exhibited early unconvergence for the cases where $G_{Ic} = G_{IIc} = 1.125 \times 10^1 J/m^2$ and where $K \geq 1.5 \times 10^{14} N/m^3$. In contrast, the simulations of this section do not become unconverged for these cases. As a consequence, when CH is applied the energies can have a significant effect in the macroscopic response, the linear elastic regime can accurately approximate the linear elastic BVP (where no interface elements are present), and ill-conditioning with respect to the dummy stiffness K can be avoided. All of this was not possible when only the micro-structure was investigated without CH. Note that when $G_{Ic} = G_{IIc} = 1.125 \times 10^1 J/m^2$ (Fig. 6.10c) debonding regime II exhibits a slight nonlinearity. This means that a few free surfaces are propagating, so regime III is interacting, although weakly, with regime II. Free surface propagation was not possible either for the default mesh when only the micro-structure was investigated. The second major difference when CH is applied is that when $G_{Ic} \neq G_{IIc}$ (Figures 6.10a–6.10b), lower values of either mode I or mode II energy can sometimes produce stiffer responses than higher values. This may be occurring because when the energies are different to each other, the macro-structural load path is forced into directions that are less efficient in minimizing potential energy than when the energies are equal to each other. If this is the case, this is a spurious effect introduced by CH since thermodynamics dictate that minimization of potential energy is always optimal.

The Turon model exhibits better numerical stability when CH is applied because the microscopic BCs are different than when only the micro-structure is investigated and because averaged macroscopic material tangents are employed. Microscopic BCs are periodic, which allow for a greater diversity of stress states than uniform BCs, which are more restrictive. The microscopic BCs are also adaptive because they change for each global time step. This allows the BCs of the current load step to "move along" with macroscopic deformation, which is in turn the manifestation of the microscopic stresses of the previous load step. Thus, microscopic BCs "move along" the load paths that they, along with macroscopic BCs, generate. The averaged macroscopic material tangents are extrapolated from the micro-structure (Eq.(6.5)), so they are different to the Turon model material tangent (Eq.(5.13)), and this difference affects the root-finding procedure.

All the figures presented in this section for investigating the Turon model are recreated in Appendix B.2 for the case where the modified damage model is applied to the matrix. The same investigation was done without CH in Section 5.4.1. The same contrasts and similarities that were mentioned in said

section between the case where the matrix is linear elastic and the case where the matrix experiences viscoelastic damage hold here, where CH is applied.

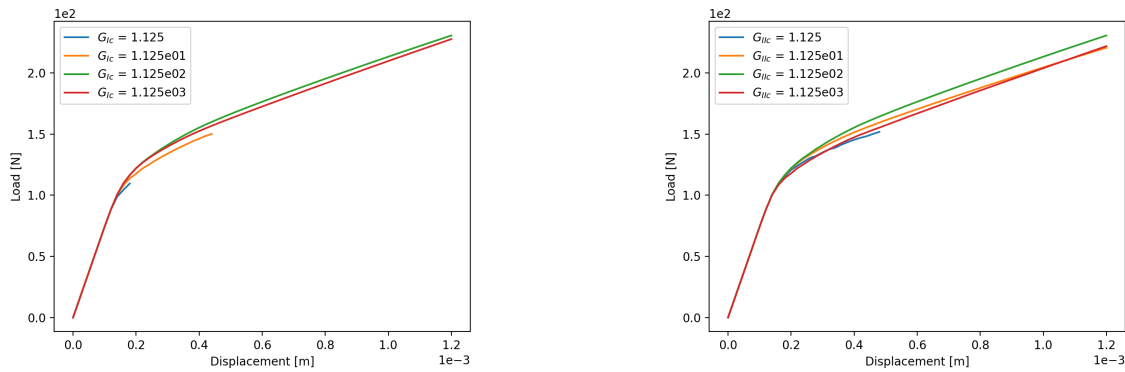
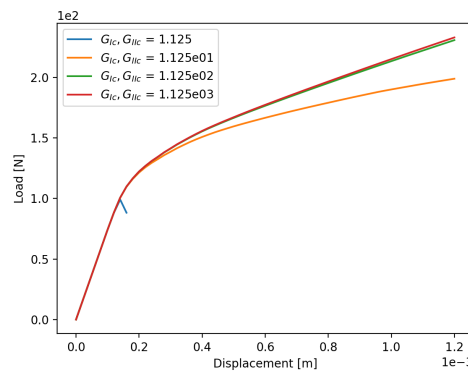
(a) Varying mode I energy G_{IC} (b) Varying mode II energy G_{IIC} (c) Varying mode I and mode II energies G_{IC} and G_{IIC}

Figure 6.10: Response of specimen for different values of the critical energy release rates

A set of debonding parameters that can provide a relatively reasonable approximation to the solid propellant preliminary experiment with strain rate $\dot{\epsilon} = 4.2 \mu\text{m/s}$ is identified. The identified parameters are the default parameters of Table 6.1. The approximation was not performed with the preliminary experiment with $\dot{\epsilon} = 4.5 \mu\text{m/s}$ because the corresponding experimental sample may have suffered from manufacturing imperfections, as was noted in Section 4.4.3. The debonding parameters were identified by simple trial and error and the viscoelastic damage model was employed for the matrix of the default microscopic mesh. The computational approximation is compared to the experiment in Fig. 6.14. The approximation is acceptable considering the scope and simplifications of this thesis. Recall that anisotropy, NLVE, nucleation damage, crack-growth for negative hydrostatic stresses, and a state dependent crack-growth equation are not considered in this study.

The approximation of Fig. 6.14 utilizes a dummy stiffness K for which the response of the linear elastic regime is softer than the response of the linear elastic BVP. This is clearly not ideal and it is a mistake which carried over to all the simulations of the next section. Even though the K of Table 6.1 is too low for the linear elastic regime to approximate the linear elastic BVP, it is still within a range where the solution for the default micro-structural mesh is well-conditioned, as shown in Fig. B.11 of Appendix B.2. However, note that this might not be the case for finer meshes. Most simulations of this chapter where debonding takes place are performed with the default mesh, so in general utilizing the default K does not have a detrimental effect.

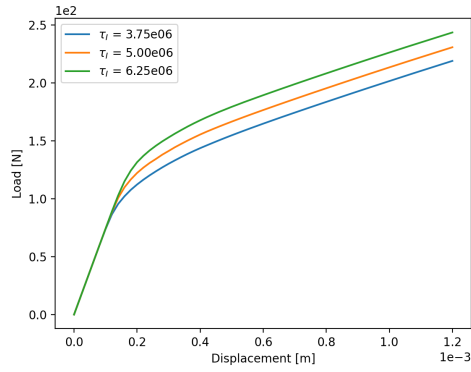
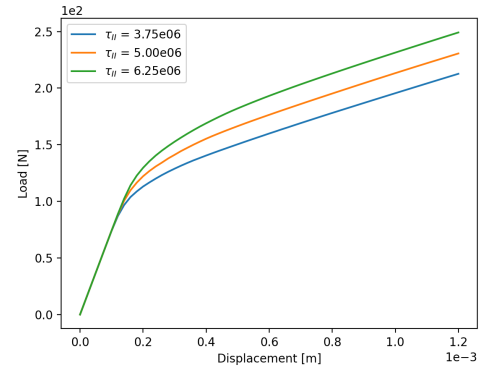
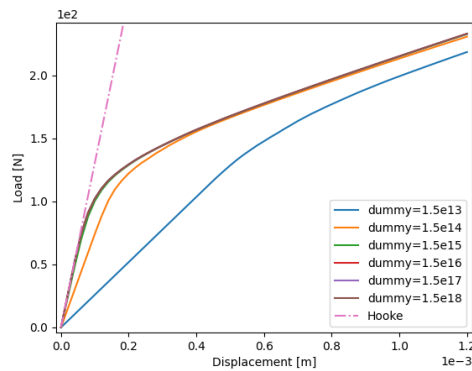
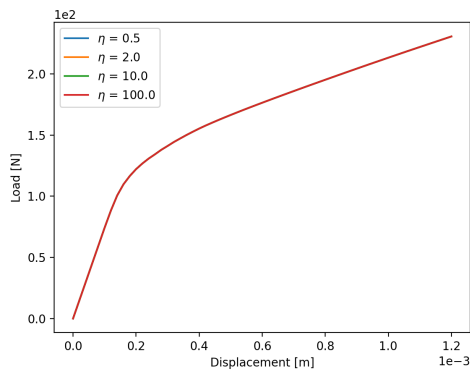
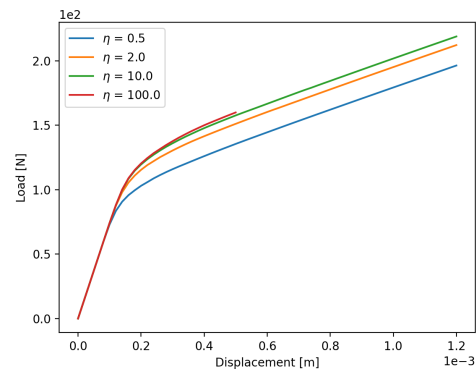
(a) Varying mode I strength τ_I (b) Varying mode II strength τ_{II}

Figure 6.11: Response of specimen for different values of the cohesive strengths

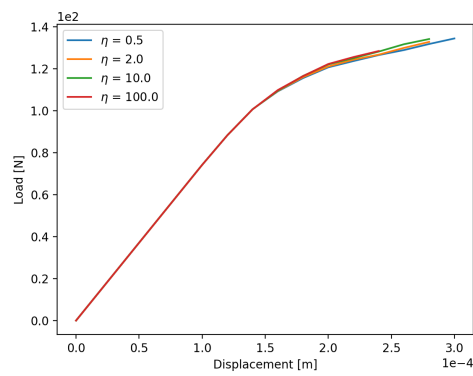
Figure 6.12: Response of specimen for different values of dummy stiffness K



(a) Both strengths and both energies are equal



(b) Both strengths are equal, but the energies are not



(c) Both energies are equal, but the strengths are not

Figure 6.13: Response of specimen for different values of the experimental parameter η

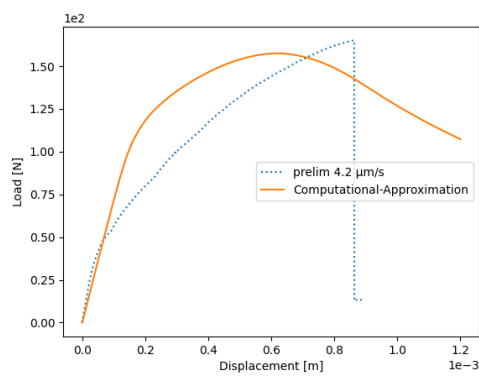


Figure 6.14: Computational approximation to the experiment for the identified debonding parameters

6.4. Damage-Viscoelastic, Debonding, and Combined Damage-Debonding-Viscoelastic Behaviors

The damage-viscoelastic, debonding, and combined damage-viscoelastic-debonding behaviors of solid propellants are investigated by applying the viscoelastic damage model to the matrix and the Turon model for interface elements to the matrix-particle interfaces. Results for different mesh refinements, particle size Df , and number of particles $nfx1$ are given in Appendix C. These results are not discussed in detail in this section because the same observations made in Chapter 5, where the same analyses were performed but for the micro-structure only, and Section 6.2, where macroscopic linear elastic results were discussed in detail, generally hold here. Only important differences and the most interesting results will be discussed. The debonding parameters of Table 6.1 and the continuum damage parameters of Table 4.3 were employed for all the simulations of this section and of Appendix C.

The macroscopic stress fields of Appendix C exhibit more symmetry than the macroscopic stress fields of the linear elastic BVP (Fig. 6.5). Damage, either in the matrix or the interfaces, improves the symmetry of the macroscopic solution because it reduces the intensity of stress concentrations. Therefore, damage reduces the influence that the direction of the macroscopic displacement gradients (and consequently, of the microscopic BCs) have on the accumulation of strain energy. Contrary to the linear elastic case, refining only the macro-structural mesh does affect the macroscopic distribution of stress in the presence of damage. This occurs because the constitutive laws may vary from one time step to the next.

CH and MH results are compared in Fig. 6.15 for different $nfx1$ when only matrix damage is considered (no debonding). The effects of stress concentrations on damage evolution are captured by CH, but not captured by MH. Nevertheless, the CH and MH results are quite similar to each other for all $nfx1$, especially in the pre-failure regime. This suggests that stress concentrations do not have a very large effect in damage evolution for the CH simulations. This is because damage is not concentrated in the micro-structure for the strain rate considered. Indeed, recall from Section 5.4.2 that when the microscopic strain rate is $\dot{\epsilon} = 3.36 \times 10^{-4} \text{ s}^{-1}$, damage is spread throughout the RVE. This same strain rate was applied here to the CH simulations of the macro-structure, which in turn means that similar strain rates are experienced by the micro-structure. Notice that CH results for particles with normally distributed Df are slightly closer to the MH result than CH results for uniformly distributed Df . This is unexpected, since the MH formulation assumes uniformly distributed Df . However, Df distribution is just one of the many assumptions within the CH and MH schemes.

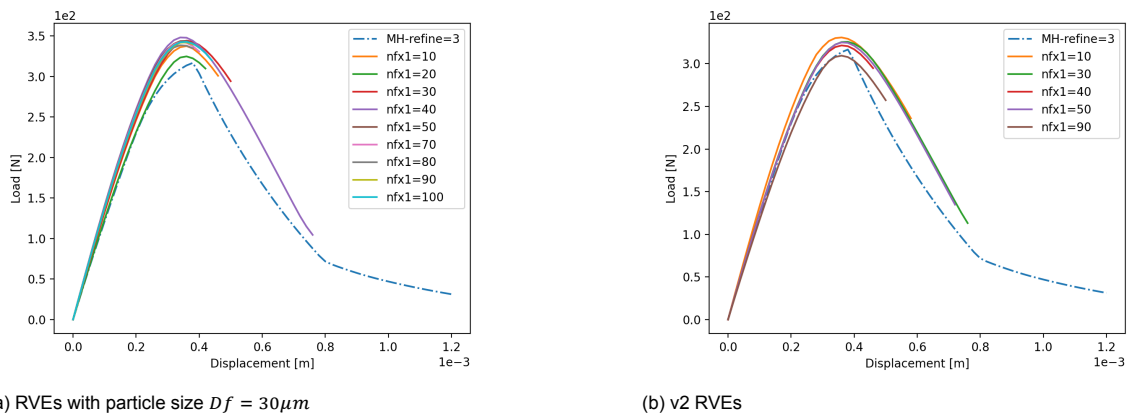


Figure 6.15: Comparison between CH results with different number of particles $nfx1$ and MH results

A computational modelling scheme that captures micro-structural viscoelasticity, continuum matrix damage, and particle debonding through means of CH was developed. This complete modelling scheme is applied for solid propellants for different strain rates and under tension, compression, and shear BCs. The results are shown in Fig. 6.16.

Tension computational results (Fig. 6.16a) show that ultimate strength increases and that the response becomes softer with increasing strain rate. TNO's matrix-only tension experiments (Fig. 1.4a) show that both ultimate strength and brittleness increase with increasing strain rate. The computational

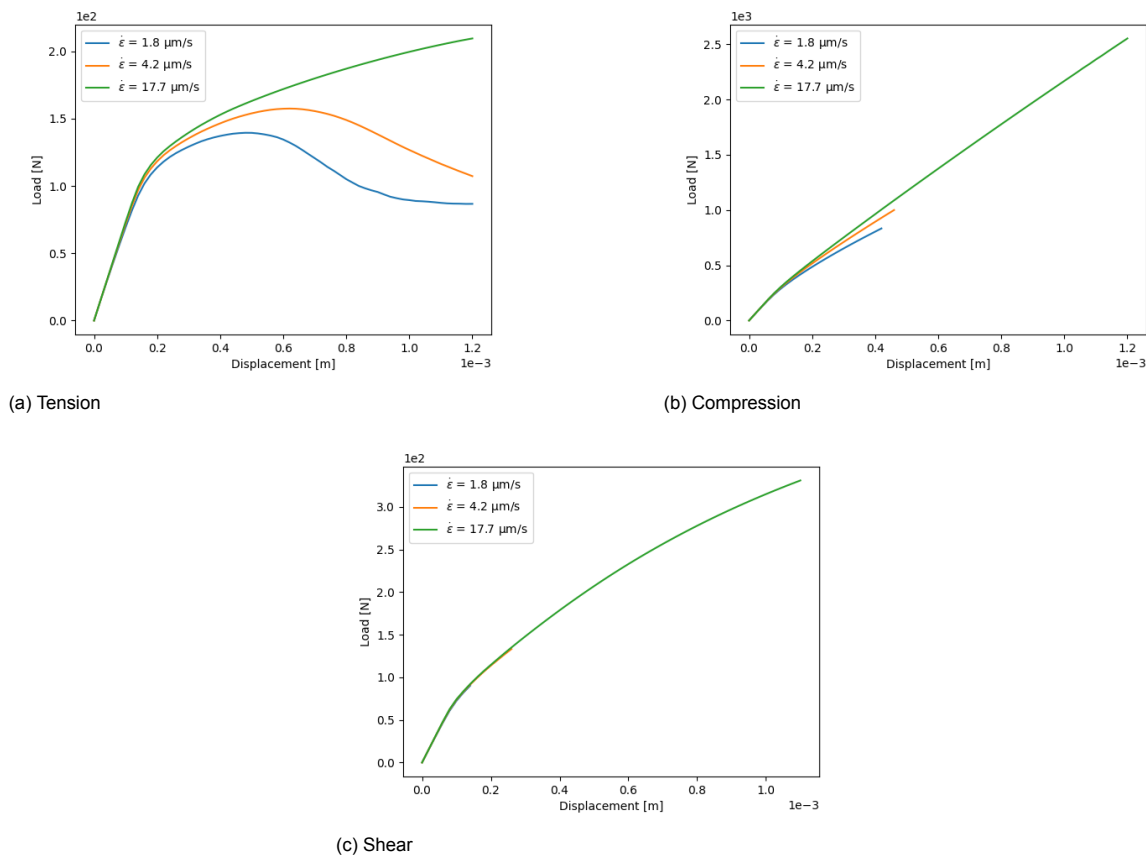


Figure 6.16: Macroscopic response of the solid propellants for different strain rates when continuum and debonding damage are considered

results exhibit a different brittleness trend than TNO's experiments, because the threshold micro-crack density ω_{n0} is non-zero. Recall from Section 4.4 that when $\omega_{n0} = 0.00$, the matrix-only computational results approximate the brittleness of the experiments better than when $\omega_{n0} \neq 0.00$. Also recall that $\omega_{n0} \neq 0.00$ is utilized to avoid excessive numerical instability. Note that the solid propellant computational results are compared to the matrix-only experiments, because TNO did not provide solid propellant data for significantly different strain rates. Nevertheless, solid propellants and matrix-only trends are expected to be similar in tension because both materials are related and because they both exhibit similar experimental responses (Figures 1.4a and 1.5a).

Compression (Fig. 6.16b) and shear (Fig. 6.16c) results are less numerically stable than tension results. They exhibit early unconvergence for relatively low strain rates. This occurs because the modified damage model is less stable for compression and shear than for tension, as was shown in Sections 4.3.2–4.3.3. The computational results for $\dot{\epsilon} = 17.7 \mu\text{m/s}$ suggest that the material is stronger in shear than in tension. However, this apparent difference between shear and tension strength is exaggerated because the continuum damage model does not allow damage to evolve in regions of negative hydrostatic stress. Which correspond to approximately half of the effective area of the RVEs subjected to shear. The computational modelling scheme is better suited for tension BCs than for other types of BCs.

6.5. Conclusion

The macro-structural behavior of solid propellants was investigated in this chapter by considering different combinations of micro-structural constitutive relations and geometries, various micro- and macro-structural mesh refinements, and CH for homogenizing the micro-structure. In general, the macro-structure exhibits similar trends and behaviors as those observed in Chapter 5 for the micro-structure. Only conclusions, not mentioned in said chapter are given here.

Results for different meshes and all combinations of constitutive models show that stress fields are significantly asymmetrical for coarse macro-structural meshes, even for symmetrical macroscopic BCs. This is particularly true for the linear elastic case, because the stress concentrations are strong. Asymmetries are reduced as macro-structural mesh refinement increases. This implies that relatively fine macro-structural meshes are necessary for locally reasonable results. Depending on the mesh resolution needed, this may be unfeasible because of the high computational demands of CH. The CH results of this chapter and the MH results of Chapter 4 are remarkably similar for the linear elastic case and for the perfect bond case. This implies that the MH framework may be regarded as a precise and computationally efficient approach when debonding is not considered. CH was shown to introduce a numerically stabilising effect whenever the Turon model was considered. Macro-structural CH results exhibit less sensitivity to mesh refinement than similar micro-structural results of Chapter 5, but do not converge upon mesh refinement either for relatively coarse RVE meshes. With CH ill-conditioning with respect to K can be avoided, because it is possible to use sufficiently high values of the dummy stiffness K to approximate the linear elastic BVPs (where no interface elements are present) with the linear elastic regimes. CH also allows to use values of the critical energy release rates G_{Ic} and G_{IIc} that are sufficiently small to capture significant softening. However, CH does introduce one drawback to the Turon model. Sometimes when $G_{Ic} \neq G_{IIc}$ internal potential energy is not minimized, which contradicts thermodynamic laws. These results lead to the encouraging conclusion that CH eliminates numerical issues associated with K , reduces RVE meshing requirements for capturing free surface propagation, and may reduce meshing requirements for achieving convergence upon refinement. However, even if CH allows the RVE to be less refined for achieving convergence, meshing requirements are still unfeasible. The results also point to the negative conclusion that materials with $G_{Ic} \neq G_{IIc}$ may not be well characterized with CH-Turon combinations.

The material's debonding parameters were identified through trial and error by fitting them to the solid propellant experiment with strain rate $\dot{\epsilon} = 4.2 \mu\text{m/s}$ while employing the matrix damage parameters found in Chapter 4. The approximation obtained with these parameters is satisfactory considering the scope of this study. However, better approximations are possible if limitations of the constitutive models employed are addressed, and if more thermomechanical aspects of the material are taken into account. Finally, the total damage-debonding-viscoelastic behavior of the solid propellants was computationally tested for different strain rates in tension, compression, and shear BCs. The numerical behavior of the computational modelling scheme is better in tension than in both compression and shear. This occurs because the modified viscoelastic damage model is less numerically stable in compression and shear and because ignoring damage for negative hydrostatic stresses prevents failure planes from forming in the micro-structure. Further work is needed for the computational scheme to be suitable for arbitrary loading conditions. However, its performance is good within the context of this thesis because the focus was to reproduce TNO's tension experiments.

Conclusion and Recommendations

7.1. Conclusions

This thesis identified and tested suitable material models for modelling the micro-structure of solid propellants and employed computational homogenization (CH) for characterizing the homogenized macro-structural behavior of the material. The Generalised Maxwell model was employed for viscoelasticity, modified versions of Lee and Shin [20] were proposed for matrix damage, and the Turon model for interface elements [30] was employed for matrix-particle debonding. The constructed computational modelling schemes were calibrated and compared with the tension experiments of the matrix and the solid propellants developed by TNO (i.e. Figures 1.4a and 1.5a). The aim of this thesis was to further understand the effects of the considered mechanical nonlinearities (i.e. viscoelasticity, matrix damage, and debonding) on the behavior of solid propellants, and to determine if CH and the material models considered are suitable for characterizing this material. The findings of this thesis are summarized as answers to the research questions (RQs) that guided this study.

1. *What are the effects of viscoelasticity and matrix continuum damage in solid propellants?*

TNO's experiments exhibit a clear rate dependence and a brittle failure, which were hypothesized to be caused by viscoelasticity and micro-crack damage in the matrix, respectively. The matrix was idealized as isotropic and linear viscoelastic, even though the experiments also exhibit anisotropic and state dependent behavior. The Generalised Maxwell model is employed for investigating viscoelasticity and the Lee and Shin continuum damage model for brittle particulate composites [20] was identified as a promising model for modelling micro-crack damage. The Lee and Shin model uses mathematical homogenization (MH) for modelling particulate composites, but it can also be used for the matrix-only. The model assumes that micro-cracks grow only in one direction, which is not in accordance with the matrix, and suffers from numerically unstable behavior. Two modified versions of the model were proposed for relaxing the direction of crack growth assumption and for improving numerical behavior. One version considers non-viscous damage and the other considers viscoelastic damage by applying the Generalised Maxwell model to the positive-definite term. The modified versions consider micro-crack growth in three orthogonal planes, a new parameter called the threshold micro-crack density ω_{n0} , and a different rate of crack growth equation as Lee and Shin [20]. The rate of crack growth equations employed by the modified models and by Lee's and Shin's original model describe crack growth damage as a state independent process. This causes numerical instabilities that are partially remedied by the newly introduced ω_{n0} . The modified damage models do not trigger early failure from loss of ellipticity because of their significant rate dependence.

The available experimental data was insufficient to reliably identify the model parameters introduced by the crack nucleation damage mechanism and by the crack growth initiation criterion for negative hydrostatic stresses. Therefore, the only damage mechanism that was considered in the characterization of the matrix was crack growth in regions of positive hydrostatic stress. This did not impose severe constraints in replicating the behavior of the matrix-only experiments. It was

shown that crack growth is significantly more relevant to brittle damage than crack nucleation, and that hydrostatic stress is positive everywhere in the matrix-only tension samples. The matrix-only experiment with strain rate $\dot{\epsilon} = 4.2 \mu\text{m/s}$, for which the model parameters were identified, was accurately replicated with the modified viscoelastic damage model. The viscoelastic parameters were identified with nonlinear least squares fitting and the damage parameters were identified by trial and error. Other matrix-only experiments with different strain rates were replicated with less accuracy. Loss of accuracy occurs because of discrepancies between the experimental samples, because of the isotropy and LVE simplifications, and as a consequence of the technique employed for reducing numerical instabilities. When $\omega_{n0} = 0.00$, the damage models agree with the experiments in that ultimate strength and brittleness are proportional to strain rate (i.e. $\sigma_u \propto \dot{\epsilon}$ and $\epsilon_u \propto \dot{\epsilon}^{-1}$). However, the models exhibit the opposite brittleness trend (i.e. $\epsilon_u \propto \dot{\epsilon}$) when $\omega_{n0} = 0.10$, which was chosen for modelling the solid propellants in Chapters 5 and 6 for improved numerical stability.

Perfectly bonded solid propellants were computationally investigated by embedding perfectly bonded particles into the matrix through both CH and MH. Both homogenization methods yielded remarkably similar responses even though the CH framework accounts for the effect of microscopic stress concentrations on damage evolution and the MH framework does not. This suggests that for the strain rate of $\dot{\epsilon} = 4.2 \mu\text{m/s}$ considered in the CH versus MH comparison, matrix damage is well distributed (i.e. not heavily localized) in the micro-structure. Indeed, the micro-structural damage fields of Chapter 5 confirm that damage is well distributed for $\dot{\epsilon} = 4.2 \mu\text{m/s}$. Damage localization would increase if the rate of crack growth equation was state dependent because damage would concentrate in regions of large overstress. Damage localization would also increase if damage was allowed in regions of negative hydrostatic stress, which do exist in solid propellants subjected to tension BCs, because localization bands would form more easily. Therefore, there is still some uncertainty about the precise effect that microscopic stress concentrations have on damage evolution.

Overall, the modified damage models are appropriate for modelling matrix damage in solid propellants. It is worth noting that the models could improve the material's characterization if crack growth for negative hydrostatic stress and nucleation damage were included. The main drawback of the models is that they often generate numerical instabilities, so caution and good intuitive and mathematical understanding of their behavior are necessary for successful application.

Matrix-only and solid propellant computational results confirm that viscoelasticity is a major source of rate dependence and that (continuum) matrix micro-crack damage causes brittle failure. They also lead to the unexpected result that continuum matrix damage is a significant source of rate dependence in the post-damage regime, which agrees with matrix-only experiments. The comparison between results for perfectly bonded solid propellants and solid propellant experiments clearly shows that other dissipative processes must also play important roles in determining ultimate strength, stiffness, and overall brittleness. However, the viscoelastic damage model should also be further modified for improving the characterization of these properties. In particular, state dependence and damage for negative hydrostatic stresses should be considered. Recommendations on how to improve the model are given in the next section.

2. *What is the effect of grain debonding in solid propellants?*

Particle debonding is observed in the electron microscope image (Fig.1.1) of the failure plane of TNO's solid propellants, and is hypothesized to significantly affect their behavior. The locations of particle debonding, the matrix-particle interfaces, are known 'a priori' of numerical computations, so zero-thickness interface elements were placed in these locations to model decohesion. The Turon model [30] was employed for describing the behavior of the interfaces with a bilinear traction separation law (TSL). A bilinear TSL is believed to be appropriate because the experiments suggest that interfacial softening can be approximated as constantly decreasing, provided that the matrix is appropriately modelled. The Turon model is thermodynamically consistent for mixed mode loading, which is important because the micro-structure is subjected to a variety of load states even for simple macroscopic BCs.

It was shown that when the Turon model is the only source of nonlinearities, the debonding dam-

age response of the micro-structure can be separated into four so-called debonding damage regimes that take place sequentially and sometimes interact weakly with each other. However, very fine RVE meshes are necessary for the four regimes to manifest. If the meshes are not sufficiently fine, the numerical solution becomes unconverged before regimes III and IV take place. Free surface propagation only occurs in these regimes. Mesh sensitivity is another important spatial discretization issue. RVE responses are highly mesh sensitive because fine meshes can characterize stress concentrations and their consequences better than coarse meshes. Very fine meshes are necessary to reduce mesh sensitivity and for RVE responses and converge upon mesh refinement. CH macro-structural responses are less mesh sensitive than RVE responses, but also require very fine RVE meshes to achieve convergence upon refinement. Using very fine RVE meshes is not feasible because the macroscopic behavior of the solid propellants is investigated with CH. Therefore, this study had to settle with characterizing debonding within the context of regimes I and II only, where interface softening occurs but free surface propagation does not, and with producing results that do not approach convergence upon mesh refinement.

It was shown that when only the micro-structure is analyzed with the meshes used for solid propellant analyses, assigning physically reasonable values to the dummy stiffness K and to the energy release rates G_{Ic} and G_{IIc} is not possible. The numerical solution becomes unconverged for high enough values of K and for low enough values of G_{Ic} and G_{IIc} . Consequently, the linear elastic regimes cannot approximate the linear elastic BVPs (where no interface elements are present), the solutions are ill-conditioned with respect to K , and the rates of softening are unreasonably slow. When CH is employed for modelling the macro-structure, numerical issues regarding K can be avoided and values of G_{Ic} and G_{IIc} that predict more reasonable rates of softening are possible.

TNO's solid propellant experiments are well approximated by the computational scheme that considers debonding and viscoelastic matrix damage under the CH framework. The approximation is not as accurate as the matrix-only approximation obtained with the damage-viscoelastic scheme, but is good considering the simplifications and scope of this thesis, and that free surface propagation is not well captured. The accuracy of the approximation is limited by the bilinear character of the Turon TSL, by the fact that regimes III and IV are not captured, and because anisotropy and other thermomechanical aspects of the solid propellants are not treated. Overall, the Turon model is appropriate for delivering functional results when a high degree of accuracy is not imperative, but it suffers from serious limitations for fully capturing the physical processes that solid propellants exhibit.

The answer to the previous RQ concluded that dissipative processes other than viscoelasticity and matrix damage also play important roles in determining the behavior of the solid propellants. The comparison between computational results for perfectly bonded solid propellants and results of the full CH damage-debonding-viscoelastic computational scheme show that debonding is certainly one of these processes. Thereby confirming the hypothesis about the high significance of debonding. This is because the simulations for perfectly bonded solid propellants exhibit much greater strength than the results of the CH damage-debonding-viscoelastic scheme. Comparing the results of the full scheme to the experiments it is evident that free surface propagation, which was not well captured, and additional dissipative processes are also important to the behavior of solid propellants.

3. *How can the micro/macro transition of solid propellants be modelled computationally?*

The macro-structural behavior of solid propellants is significantly affected by the behavior of the micro-structure. It is computationally unfeasible to directly consider the micro-structure in macro-structural FEM. Therefore, a method for approximating macro-structural behavior with a homogenized micro-structure is necessary. CH is hypothesized to be a suitable homogenization method for modelling the micro/macro transition of solid propellants. This homogenization technique extrapolates the evolving nonlinear behavior of the micro-structure to the macro-structure by linking both length scales through so-called averaging theorems. Its advantage over more computationally efficient homogenization methods, like MH, is that it allows to explicitly model debonding and is more precise.

Perfectly bonded solid propellants were investigated with CH and MH, both of which yielded similar results (mentioned in RQ 1). This implies that both homogenization methods validate each other and suggests that explicitly capturing the evolving state of the micro-structure is not essential for the strain rates considered in the investigation. However, CH may provide significantly better accuracy than MH for lower strain rates, for which stress concentrations and damage evolution interact more with each other. The use of CH was shown to have important consequences when interface elements with a Turon TSL are used for capturing micro-structural debonding damage. CH improves numerical stability, allows to use physically feasible values of the dummy stiffness K and of the energy release rates G_{Ic} and G_{IIc} , and reduces mesh sensitivity (mentioned in RQ 2). However, CH also necessitates very fine RVE meshes for capturing free surface propagation and for achieving convergence upon refinement, which is prohibitively computationally demanding.

Overall, CH is appropriate for extrapolating the behavior of the micro-structural material models investigated in this thesis to the macro-structure of solid propellants. It improves numerical stability, reduces mesh sensitivity, and allows to explicitly model debonding. In comparison to MH it allows to model more complex behavior (debonding cannot be explicitly modelled with MH), however its high computational cost imposes limitations. The hypothesis pertaining the suitability of CH for the macro/micro transition is correct.

7.2. Recommendations

Further research is necessary to improve the current understanding of the complex solid propellant material and to improve the computational modelling schemes employed for characterizing it. Recommendations on how to improve the computational scheme and on potential directions for future research are presented here.

7.2.1. Constitutive Modelling within the Numerical Schemes Employed

Recommendations for improving constitutive modelling within the context of the numerical schemes proposed in this thesis are given here.

State dependent rate of crack growth equation

The continuum damage model proposed by Lee and Shin [20] and the modified damage models proposed in this thesis employ rate of crack growth equations that are independent of the state of the material. State independence is the main reason for the numerical instability exhibited by the modified models. Employing a state dependent rate of crack growth equation would greatly reduce spurious loading-unloading oscillations, because the rate of damage evolution would increase smoothly as damage initiates and decrease smoothly as the material becomes highly degraded. Hence, the non-positive-definite softening terms would be regulated. A state dependent rate equation can be obtained by replacing the currently employed absolute overstress measure by a normalized overstress measure. Alternatively, new rate of crack growth formulations can be identified and their suitability can be tested for matrix materials.

Consistency between micro-crack size distributions assumed by the constitutive relation and by the crack growth equations

The constitutive relation and the crack growth (i.e. rate of crack growth and damage surface) equations employed by Lee and Shin [20] and by the modified damage models assume different micro-crack size distributions in the microscopic neighborhoods where cracks evolve. Ju and Tseng [18] assume uniform micro-crack size distribution for the constitutive relation with the purpose of keeping their mathematical expressions simple. However, this can lead to unexpected behavior. For example, increasing the number of micro-cracks N was shown to reduce brittleness because more energy is necessary for all cracks in a microscopic neighborhood to grow together. Conversely, Addessio and Johnson [20] assume exponential micro-crack size distribution for the crack growth equations based on experimental observation. Micro-crack size distribution should be the same for the constitutive relation and for the crack growth equations to improve the physical interpretation and numerical results. To see how to reformulate the constitutive relation for another micro-crack size distribution, refer to Ju and Tseng [18].

Micro-crack planes in different directions

The damage model proposed by Lee and Shin [20] considers crack growth only along micro-crack planes aligned in a single direction. In contrast, the modified damage models consider crack growth along micro-crack planes aligned to the three orthogonal Cartesian planes. Crack growth was extended from one to three directions because micro-cracks can grow in arbitrary directions in the matrix. This is a better representation than unidirectional crack growth, but is still a simplification. As the loading conditions are simple, this assumption has little effect. However, constitutive relations that better approximate micro-crack propagation in the matrix are necessary for employing the modified models for arbitrary loading conditions. Ju's and Tseng's constitutive relation [18] can be reformulated to allow crack growth for any number of arbitrary micro-crack plane directions. Matrix experimental data for a wide variety of loading conditions would be needed for finding the optimal number of crack growth directions and their orientations.

Micro-crack growth in regions of negative hydrostatic stress

Micro-crack growth in regions of negative hydrostatic stress was not considered, because the available experimental data is insufficient for identifying the parameters associated with this damage mechanism. For tension experiments, this was not an issue because the matrix-only and the solid propellant samples were mostly covered by regions of positive hydrostatic stress. In contrast, negative hydrostatic stresses were ubiquitous for compression and shear BCs, resulting in damage underprediction. Consequently, ultimate strength was overpredicted for these BCs and the numerical solutions exhibited early unconvergence. Allowing micro-crack growth damage to occur in regions of negative hydrostatic stress would improve numerical behavior. Matrix experimental data for identifying the friction coefficient μ_{fr} and the cohesive stress σ_0 is necessary for this purpose.

Anisotropy and nonlinear viscoelasticity in the matrix

TNO's experiments show that the matrix material exhibits different stiffnesses and state dependencies for tension and compression. The matrix was idealized as isotropic and linear viscoelastic (LVE) in this thesis. Consequently, the developed computational schemes cannot replicate the tension and compression experiments with the same set of model parameters. Different parameters must be found for each case, but only tension parameters were identified in this study. It is recommended to include anisotropy and nonlinear viscoelasticity (NLVE) into the computational schemes to characterize the behavior of the matrix for any arbitrary load state with a unique set of model parameters. This would greatly improve the generality of the computational schemes.

Interfacial transition zones

Interfacial transition zones (ITZs) were not considered for solid propellants, because their geometry and physical properties are not known. ITZs may have a significant effect on the response of the solid propellants. However, it is necessary to understand their effect to confidently elaborate a full computational characterization of the material. Considering ITZs may be particularly important to properly capture the effects of matrix and debonding damage because stress concentrations and debonding occur in the regions spanned by ITZs. It is recommended to investigate the properties of ITZs and if necessary to include ITZs in the computational schemes. Incorporating ITZs would improve current understanding of the solid propellants and may improve computational characterization.

Debonding properties as functions of particle size

The obtained results show that micro- and macro-structural responses vary significantly when the same debonding properties are employed for RVEs with different particle size. This occurs because debonding models for interface elements relate traction, a relative measure of force, to displacement jump, an absolute measure of translation. Debonding properties that do not depend on particle size were identified by fitting them to a solid propellant experiment through trial and error. This was not a major issue because the number of particles considered was high enough such that effects caused by large and small particles averaged out to produce a reasonable micro-structural response. If debonding properties would be identified as functions of particle size the resulting micro-structural responses would not only be correct in an averaged sense, but also locally within the micro-structure. Furthermore, this would partially reduce the necessity for considering large numbers of particles in the RVEs.

7.2.2. Numerical Schemes and Related Constitutive Modelling

Recommendations for improving numerical efficiency, solving related numerical issues, and improving characterization by improving and generalizing the numerical schemes proposed in this thesis are given here. Recommendations for addressing constitutive modelling issues linked to numerical scheme recommendations are also given.

Quasi-Newton Raphson methods for tangential stiffness

The damage rate constitutive equation (Eq. (4.29)) cannot analytically relate the strain rate to the stress rate with a linear system of equations, so a consistent tangent stiffness is not possible. Lee and Shin [20] proposed a pseudo-tangent stiffness (Eq. (4.34)) for carrying out the NR procedure. However, it was observed that this pseudo-tangent stiffness generally delivers worse computational performance than the secant stiffness, which is not ideal either. It is hypothesized that Quasi-NR methods can deliver good computational performance, better than those of the pseudo-tangent and secant stiffnesses. It is recommended to investigate which Quasi-NR method is most appropriate for the damage models and the computational schemes.

Characterize macro-structural damage-debonding-viscoelastic behavior only via mathematical homogenization

The purpose of this thesis was to characterize the macro-structural damage-debonding-viscoelastic behavior of solid propellants with CH. An MH framework for characterizing the macro-structural damage-viscoelastic behavior of perfectly bonded solid propellants was also briefly investigated, mostly for the purpose of academic comparison. Interestingly, the MH method produced similar results as the CH method for a fraction of the computational cost. This naturally raises the question of whether or not the MH method can be extended to include debonding and yield good results. This question is particularly interesting considering that computational efficiency limitations generally prevent the Turon model from capturing free surface propagation within a CH framework and prevent the use of mesh-insensitive meshes whenever the Turon model is employed. Yang et al [36] proposed a statistical debonding-viscoelastic model that is formulated within the same MH framework as the damage-viscoelastic MH model presented in this thesis. Therefore, both models are compatible. Combining both models into a unified damage-debonding-viscoelastic MH model may provide an accurate and cost effective alternative to model solid propellants. If the unified model proves unsuccessful for modelling the solid propellants, implementing and investigating it would still constitute an interesting academic endeavor. To further improve the damage-viscoelastic and the potential unified MH models, perturbed compliances that account for the interaction between matrix damage and particles could be formulated.

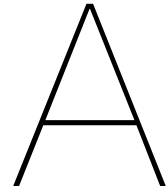
Machine learning for prediction of RVE behavior

Micro-structural RVE simulations that consider the Turon model for interface elements [30] require heavily refined meshes for capturing free surface propagation and for their numerical solutions to converge upon mesh refinement (i.e. to achieve mesh insensitivity). Macro-structural CH simulations with heavily refined micro-structures are unfeasible because of their high computational cost. Therefore, RVE meshes for which free surface propagation is generally not captured and which do not converge upon mesh refinement were employed in this thesis. As a solution to this issue, machine learning (ML) is recommended for predicting the behavior of heavily refined RVE meshes. 'A priori' micro-structural computations of RVEs with varying BCs and geometries can be used for predicting the averaged responses of arbitrary RVEs that are given arbitrary macro-structural inputs. This would make CH macro-structural simulations feasible because the macro- and micro-structures do not have to be evaluated concurrently; the micro-structural output is readily available from the ML predictions. The drawbacks of this approach are that devising an appropriate ML procedure is not a trivial task and that the 'a priori' ML process would be very computationally demanding. Nevertheless, the ML process only has to be performed once, so it is a more efficient approach in the long term than repeatedly performing the usual concurrent macro-micro CH computations.

Generalising the computational modelling schemes for capturing the effects of FDM

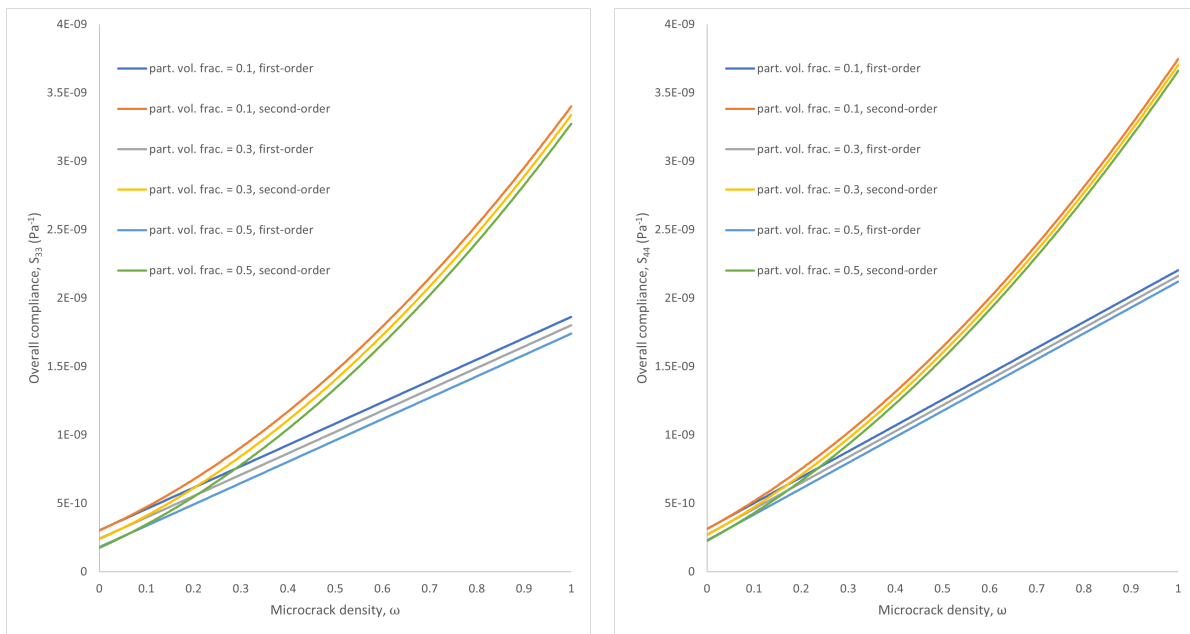
The computational modelling schemes given in this thesis analyze the macro-structures of solid propellants by homogenizing only their micro-structures. Therefore, the effects of the fused deposition modelling (FDM) manufacturing process employed by TNO, which introduces a mesoscale, were not

considered. Generalising the computational modelling schemes to schemes that consider a layered mesoscale is recommended for capturing the effects of FDM on solid propellants, and more generally, for analyzing any class of 3D-printed particulate composite. The meso-structure must account for the thermomechanical processes and effects that the manufacturing process introduces into the behavior of the solid propellants. Which include delamination damage, heterogeneous matrix properties caused by thermal gradients, among others. Meso-structural constitutive models must be identified and applied for capturing these processes and effects. For example, the Turon TSL [30] could be used by inter-laminar interface elements that capture delamination damage. A generalisation where CH is employed for concurrent macro-meso-micro computations would be very computationally demanding. It would clearly be unfeasible if the Turon model for interface elements [30] is employed for debonding because heavily refined micro-structural meshes would be necessary for capturing free surface propagation. Therefore, it is recommended to generalise the computational schemes by coupling concurrent macro-meso CH computations with either meso-micro computations that employ the unified damage-debonding-viscoelastic MH model or the ML approach proposed in the recommendations above. The principle of separation of scales must hold for these couplings to be valid. If it does not hold, the layered nature of the solid propellants must be directly incorporated in the macro-structure. This may still be feasible if the MH or ML approaches are employed because concurrent CH computations would not be necessary at any level.



Numerical Comparison Results

All the figures that Lee and Shin generated for exploring the behavior of their model are recreated here with the modified model. If the legend of some figure is unclear please refer to Lee and Shin [20], where the legends are almost identical.



(a) Longitudinal compliances

(b) Shear compliances

Figure A.1: First-order-only compliances and combination of first-order and second-order compliances for $\phi = 0.1$ and $\phi = 0.3$

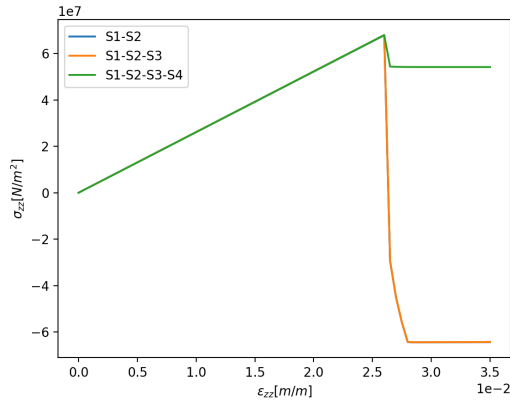
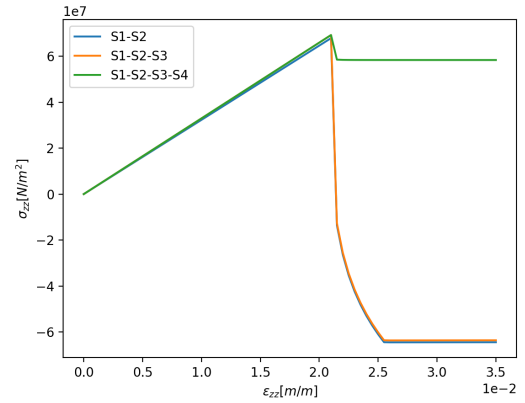
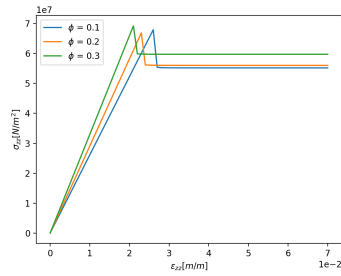
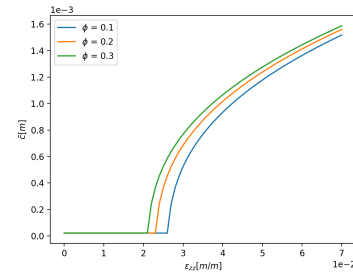
(a) Stress-strain curve for case with $\phi = 0.1$ (b) Stress-strain curve for case with $\phi = 0.3$

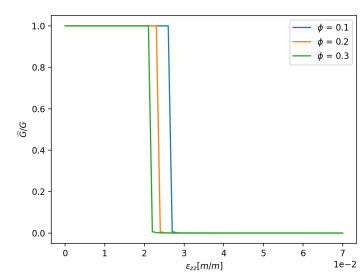
Figure A.2: Stress-strain response of element for first- and second-order contributions.



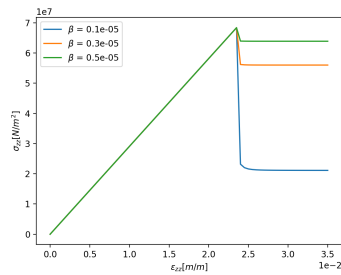
(a) Stress-strain curve



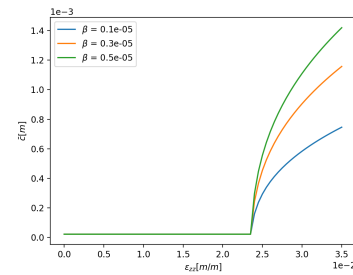
(b) Crack-size evolution versus strain



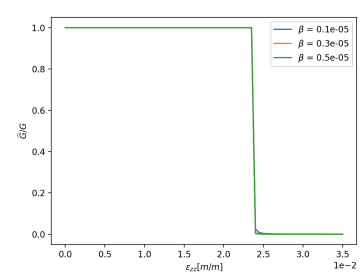
(c) Shear modulus degradation vs strain

Figure A.3: Response of element for different values of particle volume fraction ϕ .

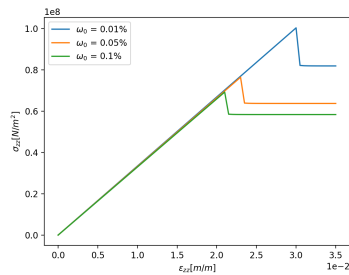
(a) Stress-strain curve



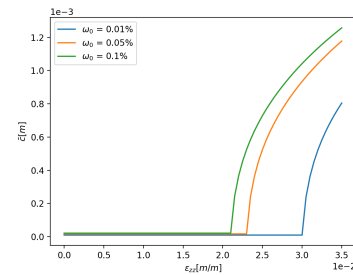
(b) Crack-size evolution versus strain



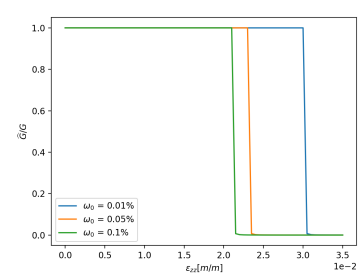
(c) Shear modulus degradation vs strain

Figure A.4: Response of element for different values of control parameter β .

(a) Stress-strain curve



(b) Crack-size evolution versus strain



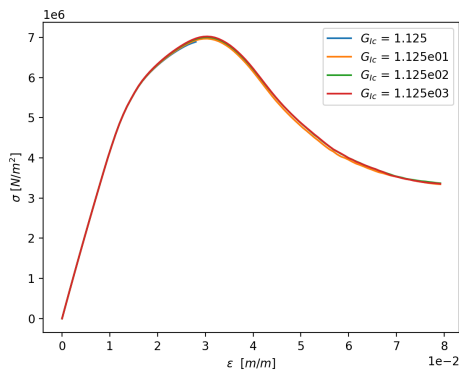
(c) Shear modulus degradation vs strain

Figure A.5: Response of element for different values of initial crack density ω_0 .

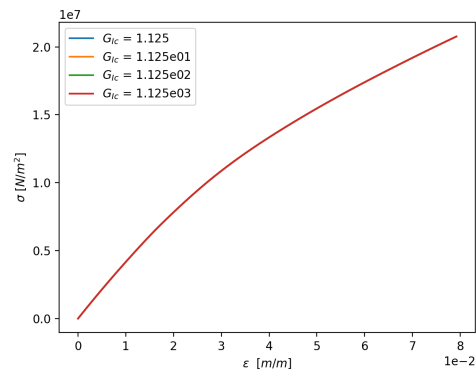
B

Effect of Turon Model Parameters on Composites with Matrix Damage

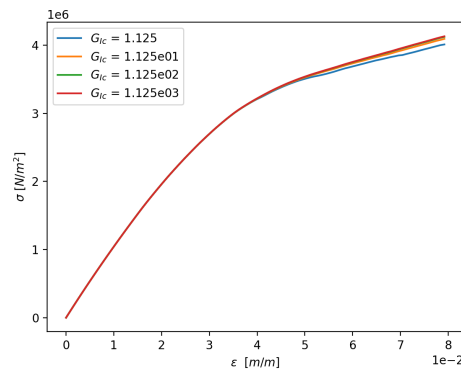
B.1. Effect on the Micro-Structure



(a) Tension

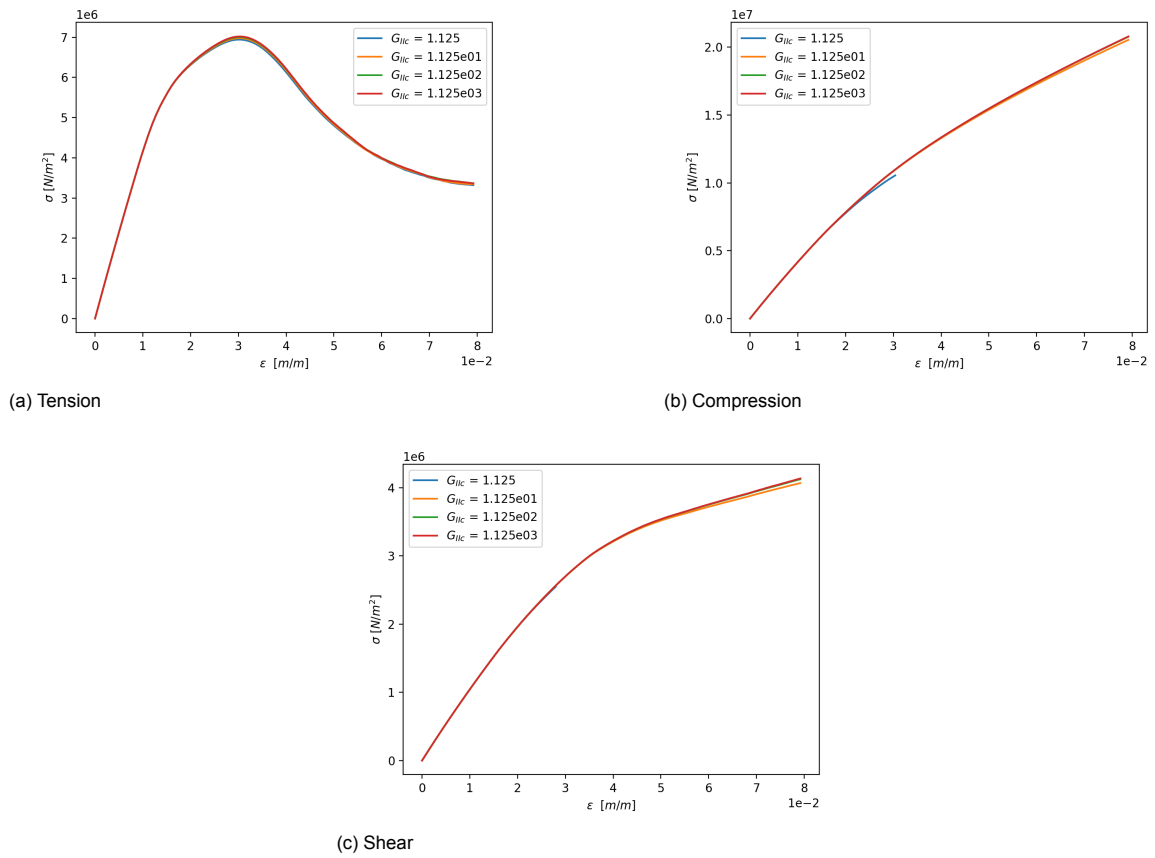


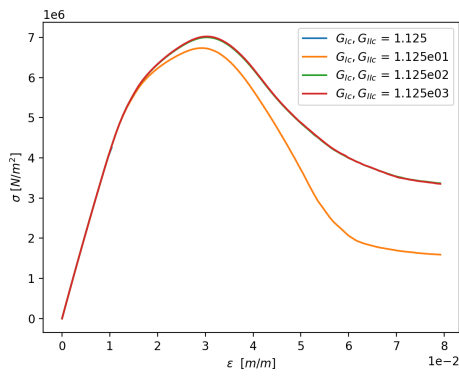
(b) Compression



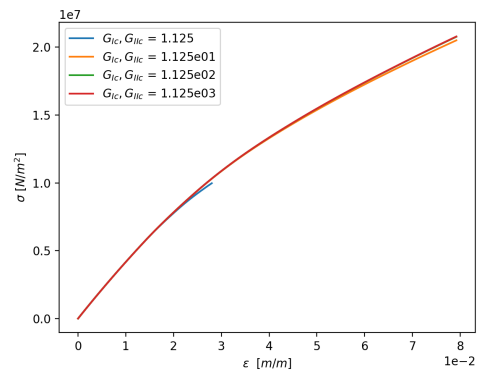
(c) Shear

Figure B.1: Response of specimen for different values of mode I energy G_{Ic}

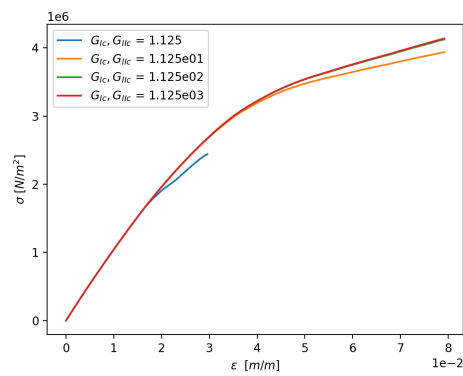
Figure B.2: Response of specimen for different values of mode II energy G_{IIc}



(a) Tension



(b) Compression



(c) Shear

Figure B.3: Response of specimen for different values of mode I and mode II energies G_{IC} and G_{IIC}

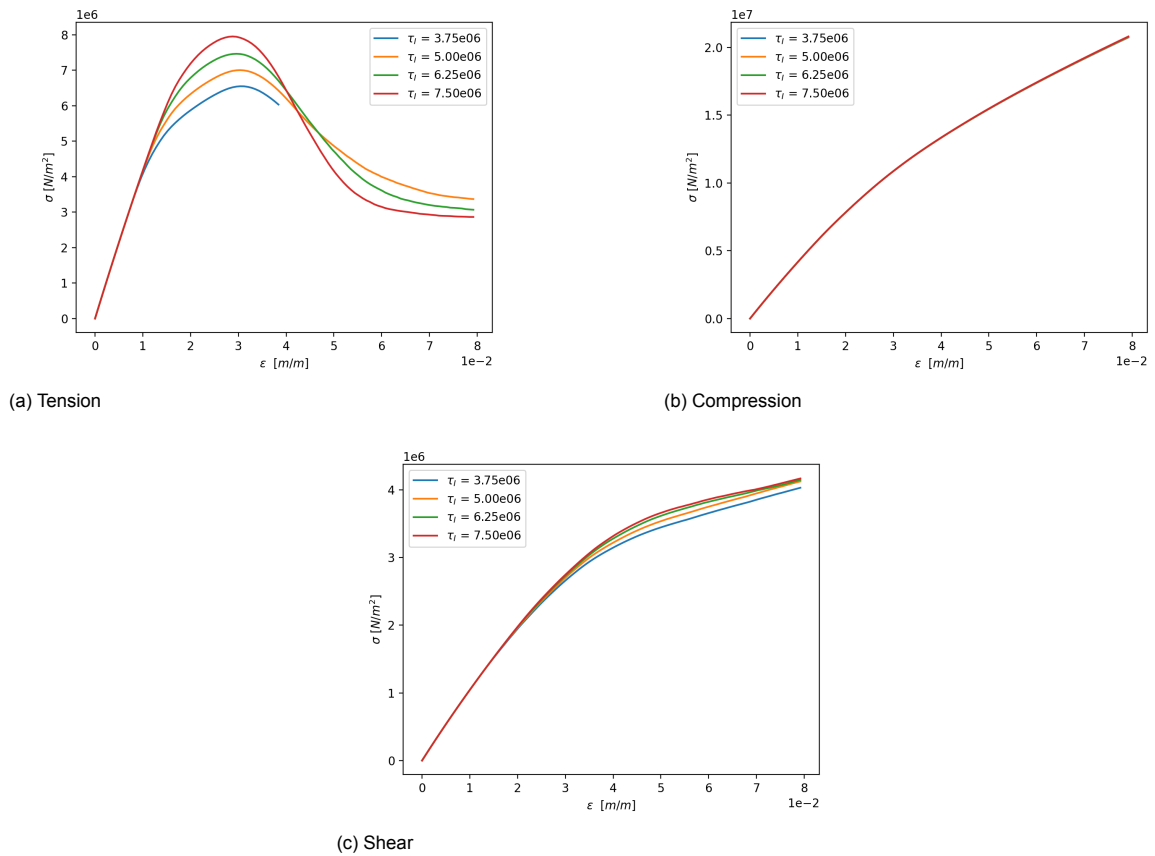
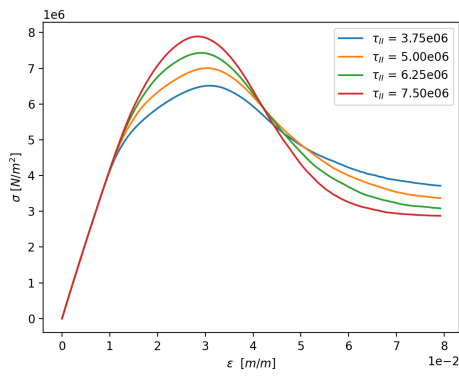
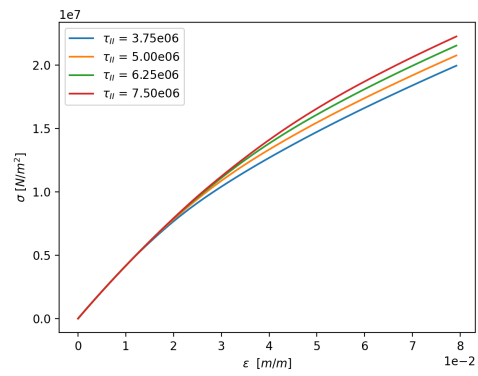


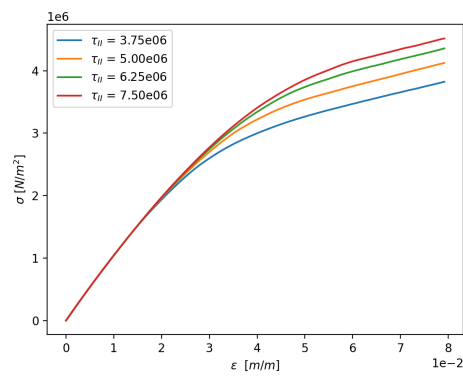
Figure B.4: Response of specimen for different values of mode I strength τ_I



(a) Tension

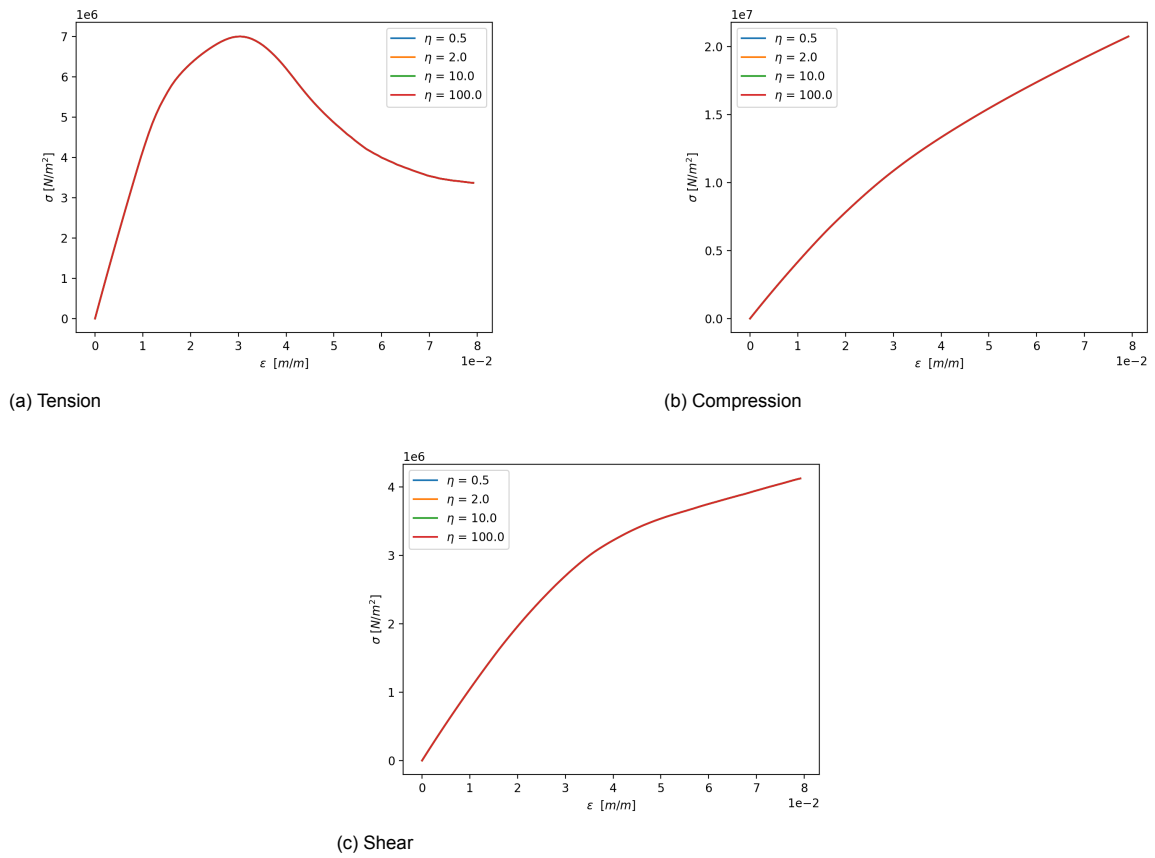


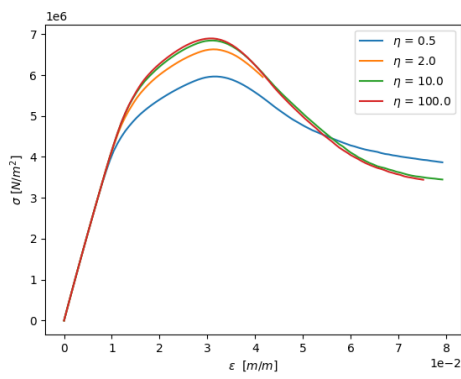
(b) Compression



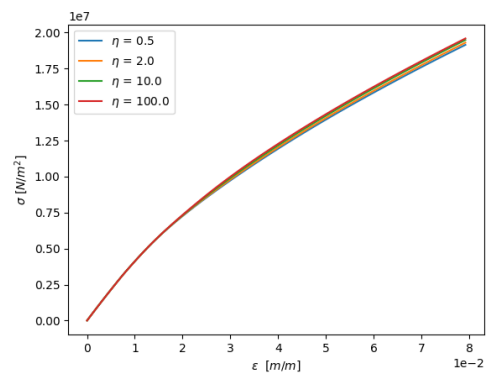
(c) Shear

Figure B.5: Response of specimen for different values of mode II strength τ_{II}

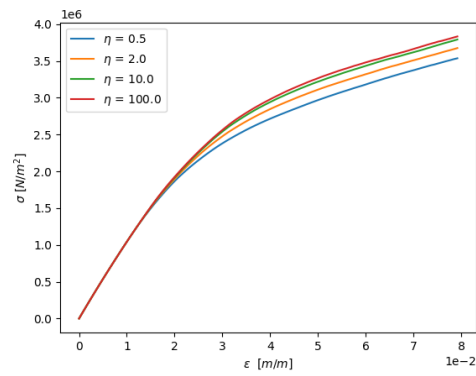
Figure B.6: Response of specimen for different values of experimental parameter η



(a) Tension



(b) Compression



(c) Shear

Figure B.7: Response of specimen for different values of experimental parameter η when both energies are equal to each other but the strengths are different

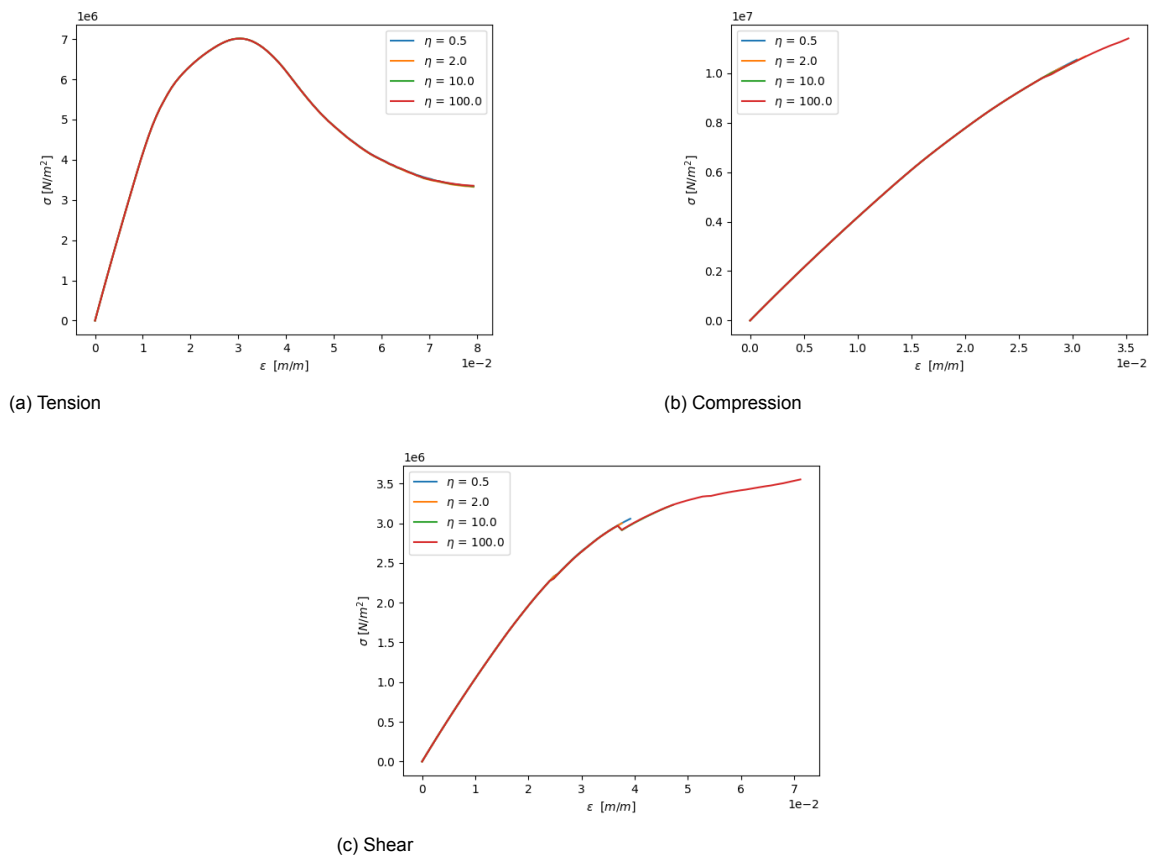
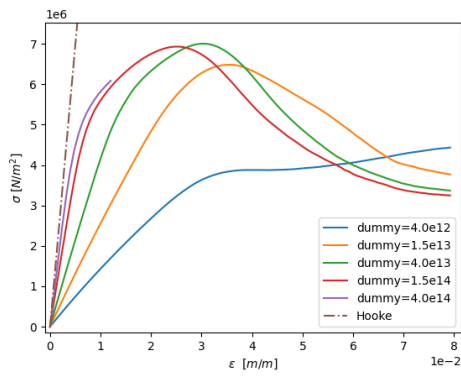
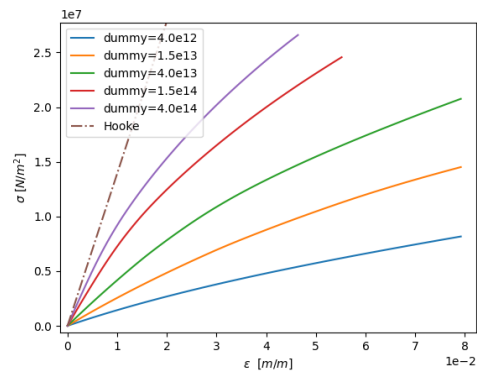


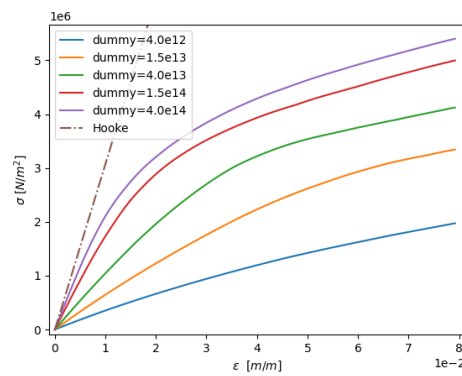
Figure B.8: Response of specimen for different values of experimental parameter η when both strengths are equal to each other but the energies are different



(a) Tension



(b) Compression



(c) Shear

Figure B.9: Response of specimen for different values of dummy stiffness K

B.2. Effect on the Macro-Structure

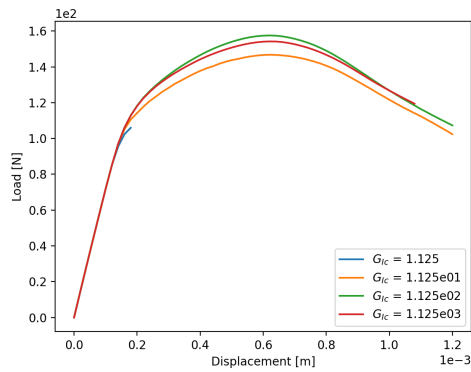
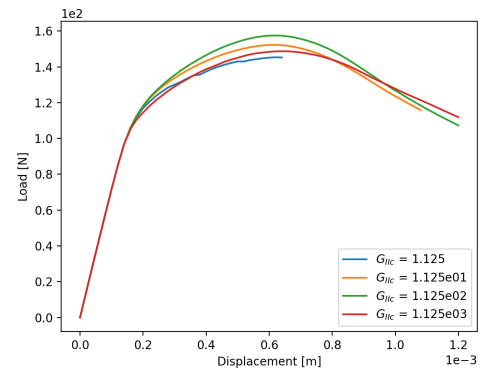
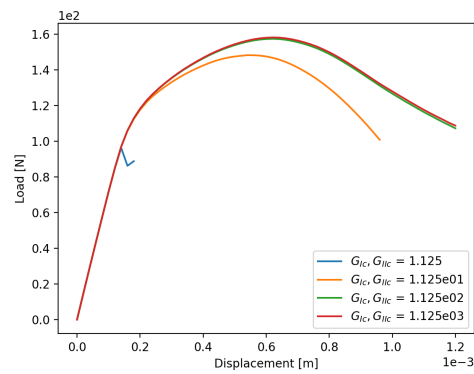
(a) Varying mode I energy G_{Ic} (b) Varying mode II energy G_{IIc} (c) Varying mode I and mode II energies G_{Ic} and G_{IIc}

Figure B.10: Response of specimen for different values of the critical energy release rates

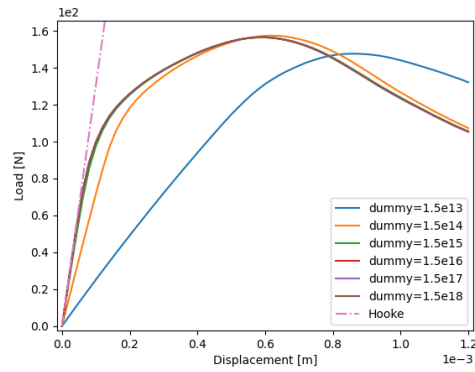
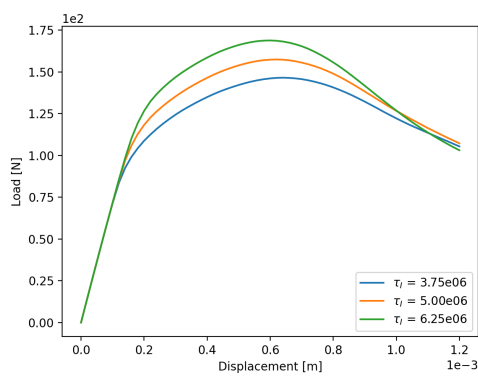
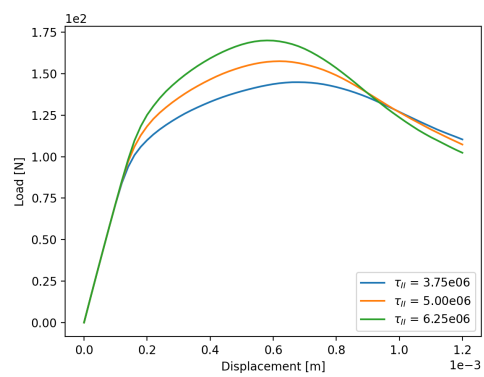


Figure B.11: Response of specimen for different values of dummy stiffness K

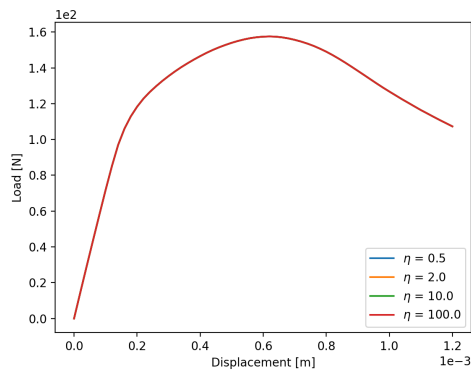


(a) Varying mode I strength τ_I

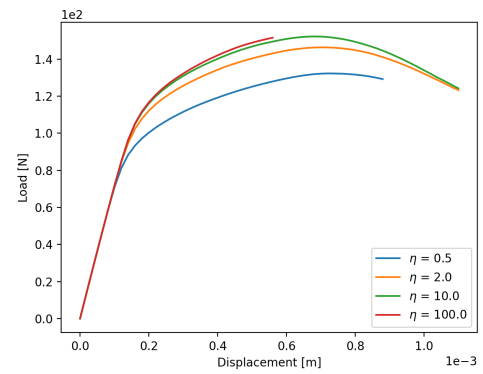


(b) Varying mode II strength τ_{II}

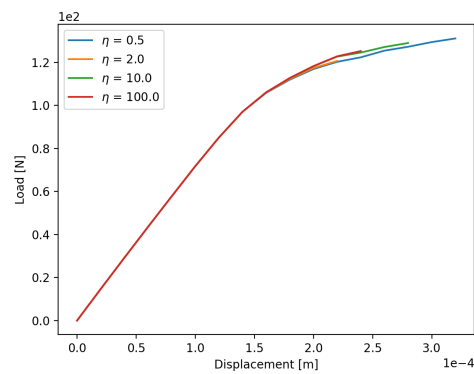
Figure B.12: Response of specimen for different values of the cohesive strengths



(a) Both strengths and both energies are equal

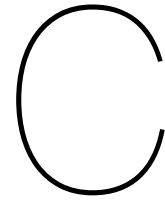


(b) Both strengths are equal, but the energies are not



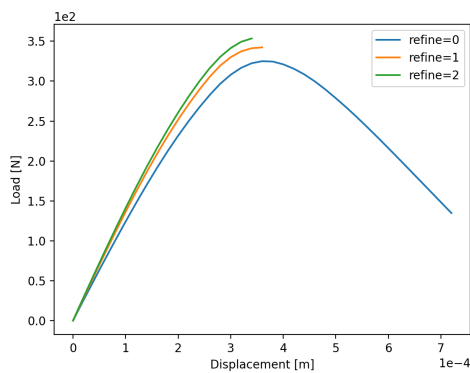
(c) Both energies are equal, but the strengths are not

Figure B.13: Response of specimen for different values of the experimental parameter η

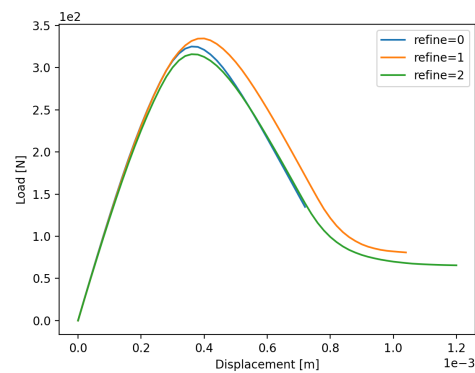


Computational Homogenization Analyses Results

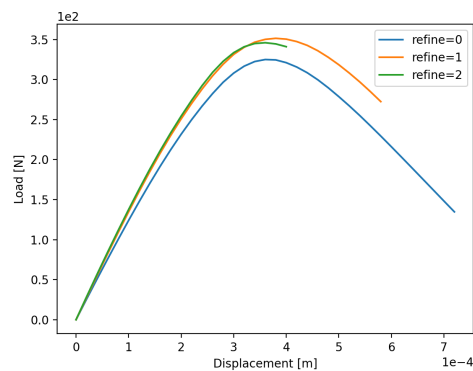
C.1. Damage-Viscoelastic Behavior



(a) Micro-structure only



(b) Macro-structure only



(c) Both micro-structure and macro-structure

Figure C.1: Effect of mesh refinement when v2 RVE with 50 particles is utilized. The subfigures show the number of refinements utilized for the specified length scales.

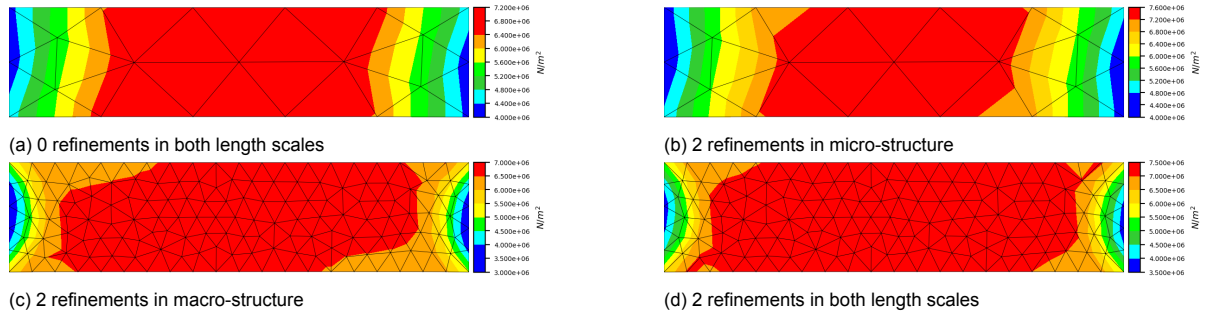
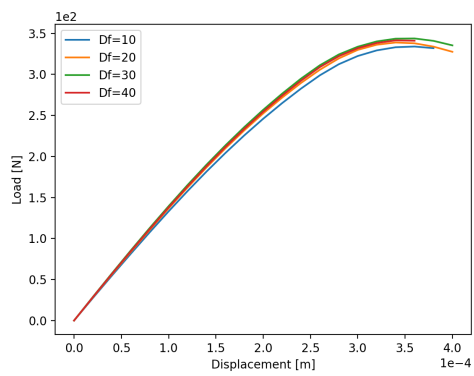
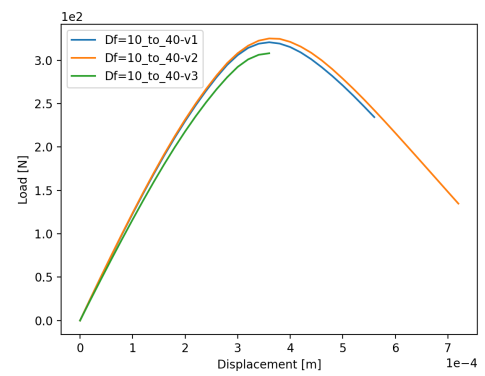


Figure C.2: Maximum principal stress fields at maximum displacement for v2 RVE with 50 particles when subjected to tension BCs. Different mesh refinements are considered.

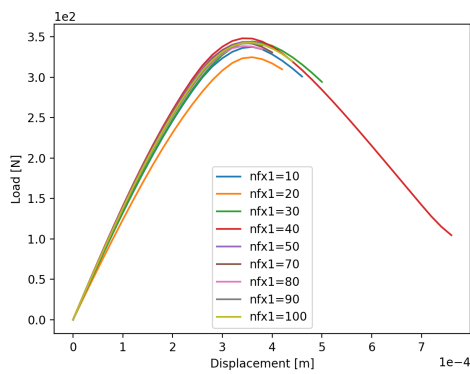


(a) RVEs with uniformly distributed particle size

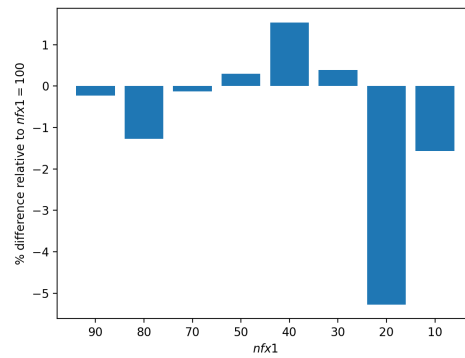


(b) RVEs with varying particle size

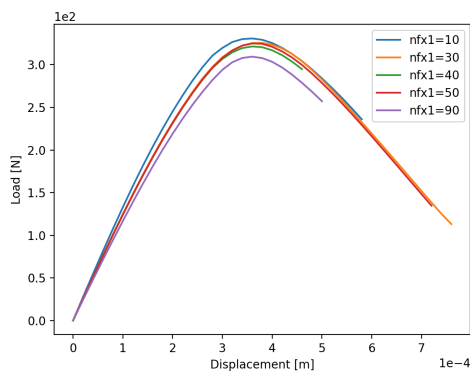
Figure C.3: Effect of particle distribution and particle size Df



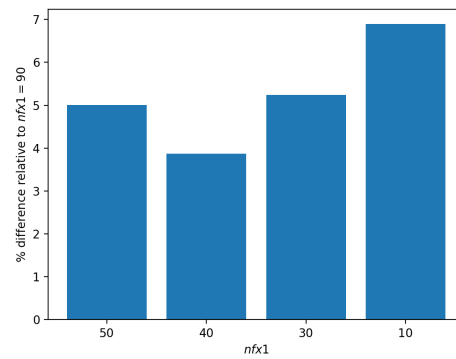
(a) RVEs with particle size $D_f = 30 \mu m$



(b) Relative differences in ultimate stress between the curves in Fig. C.4a



(c) v2 RVEs



(d) Relative differences in ultimate stress between the curves in Fig. C.4c

Figure C.4: Effect of number of particles $nfx1$

C.2. Debonding Behavior

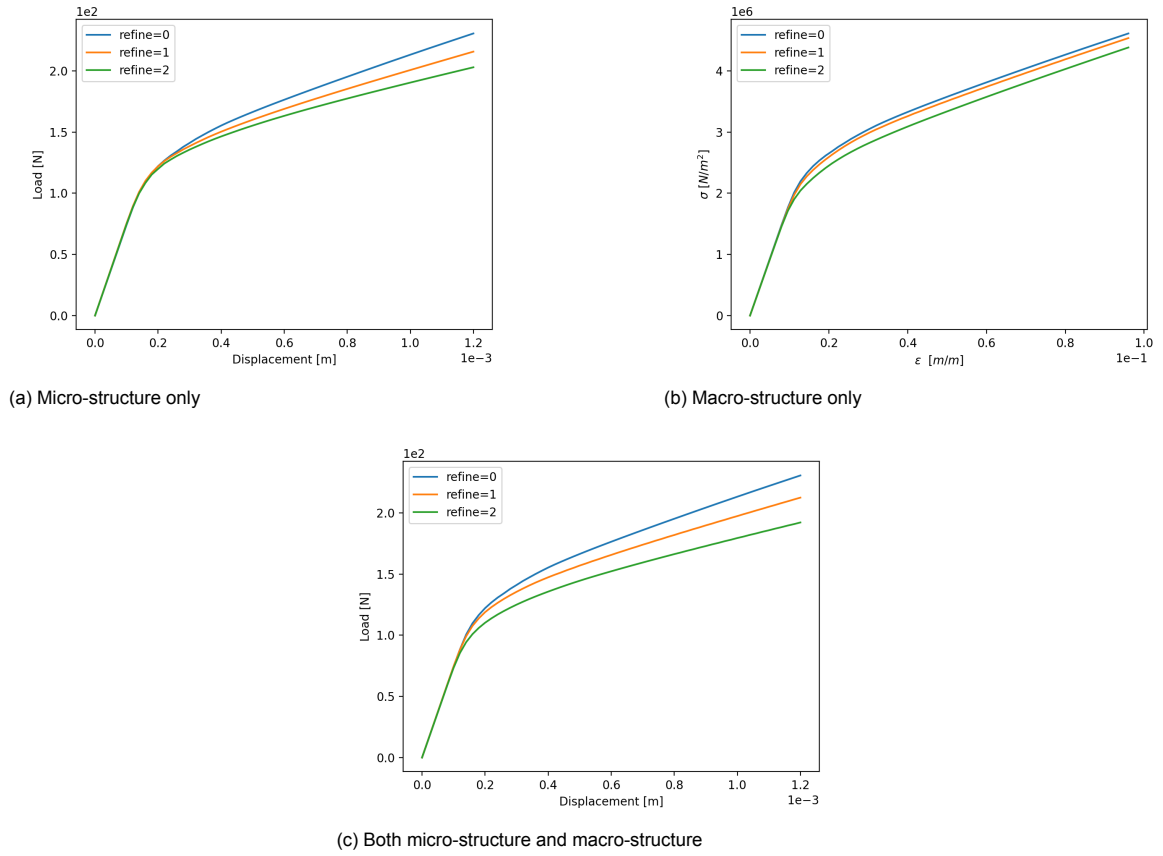


Figure C.5: Effect of mesh refinement when v2 RVE with 50 particles is utilized. The subfigures show the number of refinements utilized for the specified length scales.

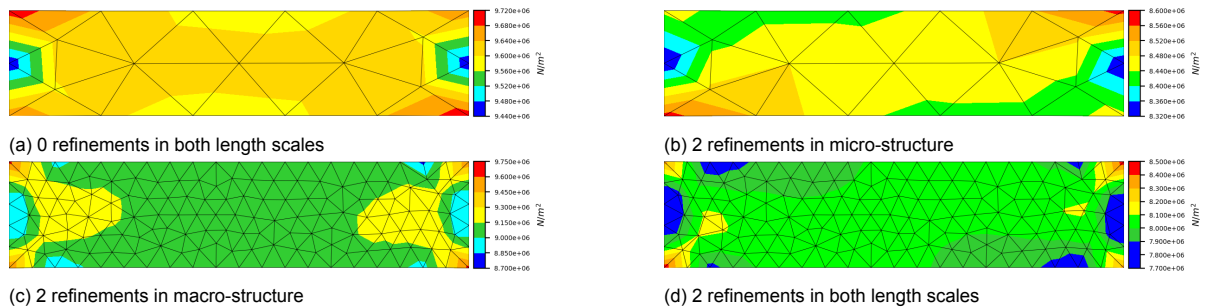
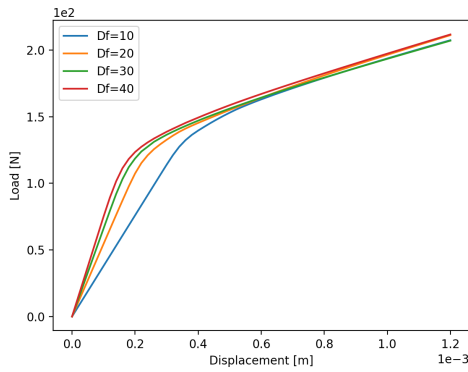
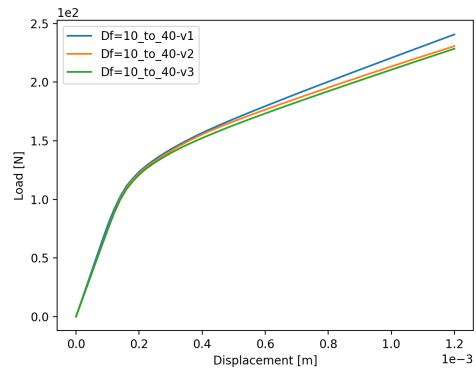


Figure C.6: Maximum principal stress fields at maximum displacement for v2 RVE with 50 particles when subjected to tension BCs. Different mesh refinements are considered.

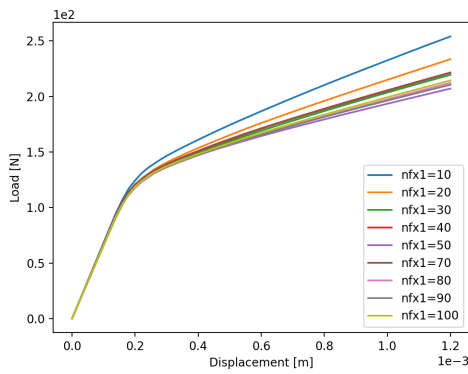


(a) RVEs with uniformly distributed particle size

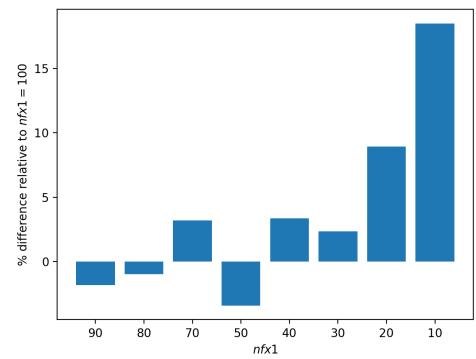


(b) RVEs with varying particle size

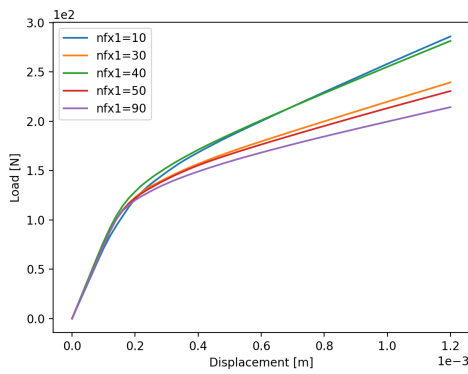
Figure C.7: Effect of particle distribution and particle size Df



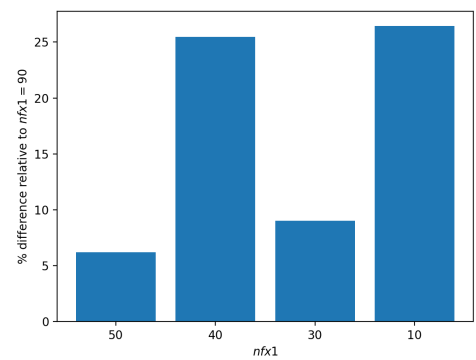
(a) RVEs with particle size $Df = 30\mu m$



(b) Relative differences in ultimate stress between the curves in Fig. C.8a



(c) v2 RVEs



(d) Relative differences in ultimate stress between the curves in Fig. C.8c

Figure C.8: Effect of number of particles $nfx1$

C.3. Damage-Debonding-Viscoelastic Behavior

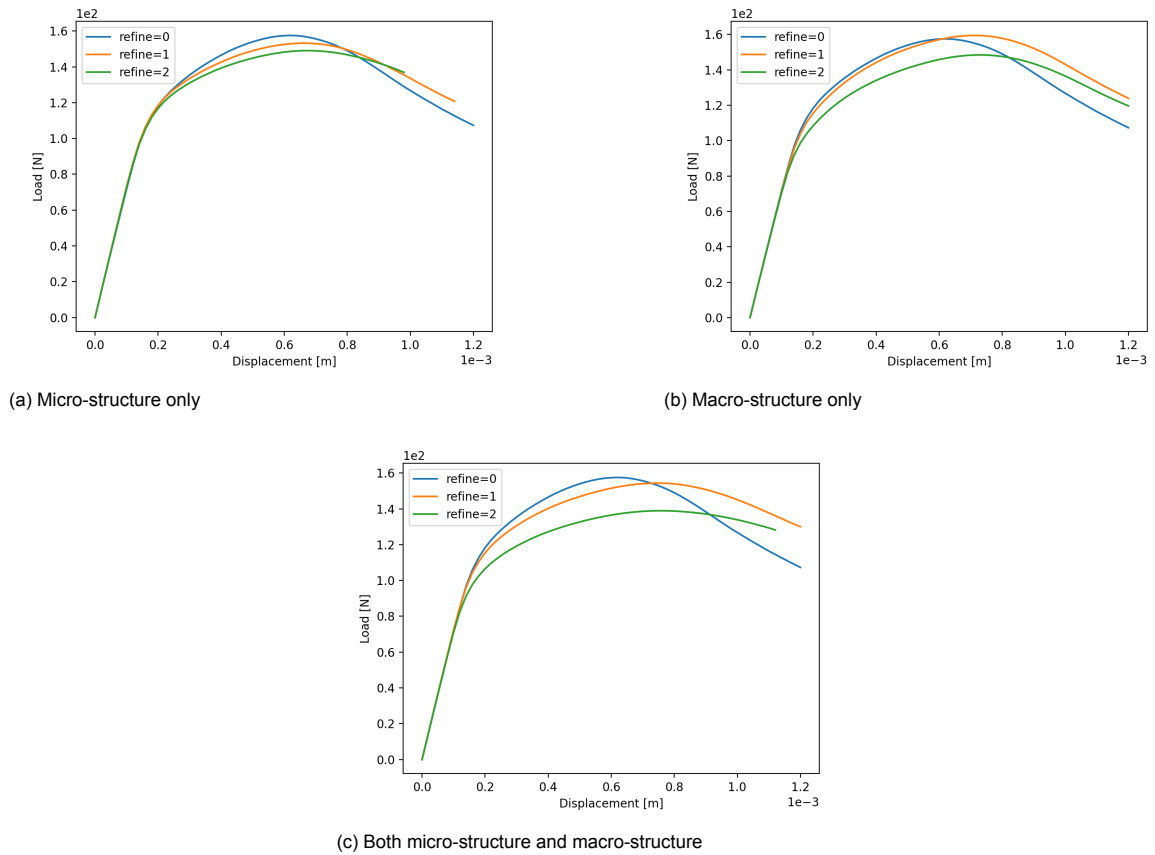


Figure C.9: Effect of mesh refinement when v2 RVE with 50 particles is utilized. The subfigures show the number of refinements utilized for the specified length scales.

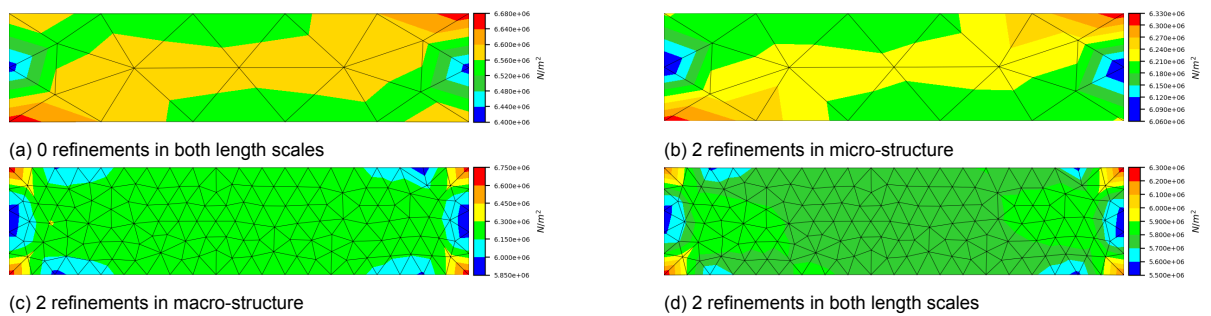
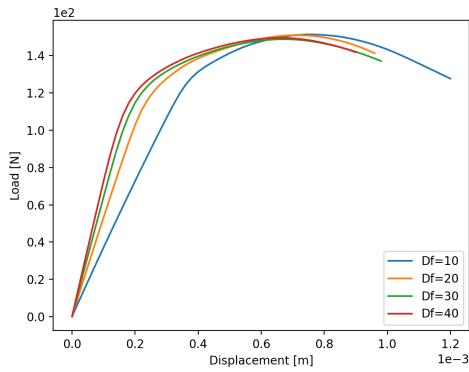
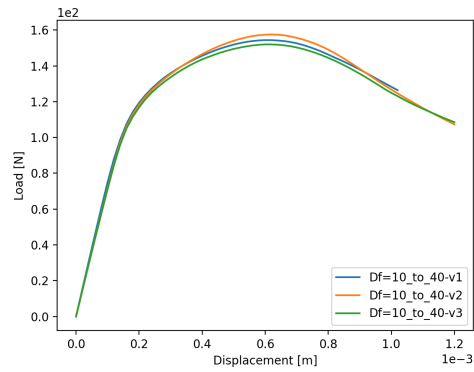


Figure C.10: Maximum principal stress fields at maximum displacement for v2 RVE with 50 particles when subjected to tension BCs. Different mesh refinements are considered.

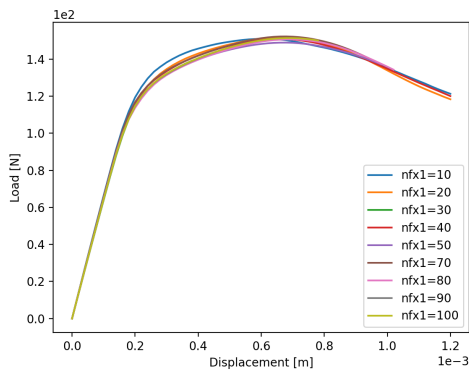


(a) RVEs with uniformly distributed particle size

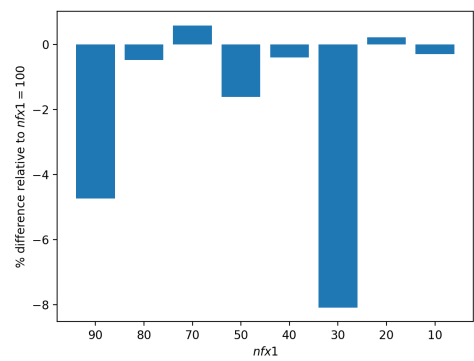


(b) RVEs with varying particle size

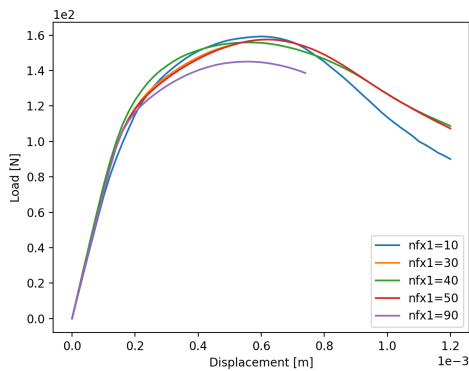
Figure C.11: Effect of particle distribution and particle size Df



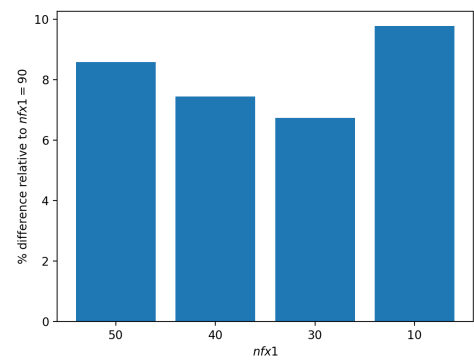
(a) RVEs with particle size $Df = 30\mu m$



(b) Relative differences in ultimate stress between the curves in Fig. C.12a

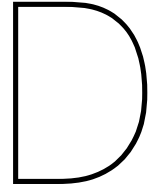


(c) v2 RVEs



(d) Relative differences in ultimate stress between the curves in Fig. C.12c

Figure C.12: Effect of number of particles $nfx1$



RVE Meshes

The RVE meshes with psuedo-random particle distributions employed in this thesis are given here. For these RVEs, the number of particles $nfx1$ varies from 10 to 100, the particle size Df varies from $10 \mu m$ to $40 \mu m$, and the mesh refinements define element size by applying *Gmsh* characteristic lengths defined by $L_m = 0.5Df/(n_m + 1)$. Where n_m is the number of times that a mesh has been refined relative to the base case $n_m = 0$. Particle size is either uniformly or normally distributed within an RVE. When particle size is normally distributed, $10 \mu m$ and $40 \mu m$ are the bounds of the Gaussian PDF from which Df is pseudo-randomly sampled. Different input versions $v1$, $v2$, and $v3$ are given to the mesh generating software for the pseudo-random sampling of Df for different RVEs.

The figures given here show the RVE meshes and Tables D.1–D.2 show the relevant details of these meshes when interface elements (IEs) are present and when they are not. The figures are captioned with the mesh ID. The IDs are composed of three elements separated by commas. The first element refers to the number of refinements n_m done on the mesh. The second element is either the particle size Df in μm when particle size is uniformly distributed or the input version vi (with $i = 1, 2, 3$) when particle size is normally distributed. The third element is the number of particles $nfx1$ in the mesh.

Note that there are more meshes with uniform particle distribution than meshes with normal particle distribution. This is because the meshes were generated automatically with *Gmsh*, and for some parameter combinations (of refinement, Df , and $nfx1$) the software generated unusable meshes where one or more T3 elements are represented by lines instead of triangles.

ID	Length	Nodes No IEs	Elements No IEs	Nodes With IEs	Elements With IEs
1,10,50	80.9	2009	3844	2736	4543
1,20,50	162	1973	3786	2693	4482
1,30,10	109	447	820	601	962
1,30,20	153	836	1578	1128	1858
1,30,30	188	1216	2386	1700	2805
1,30,40	217	1582	3020	2163	3579
1,30,50	243	1973	3798	2695	4500
1,30,70	287	2721	5245	3730	6233
1,30,80	307	3117	6026	4271	7150
1,30,90	326	3485	6746	4783	8010
1,30,100	343	3928	7632	5366	9036
1,40,50	324	1993	3832	2721	4536
0,20,20	102	438	818	NA	NA
1,20,20	102	765	1457	NA	NA
2,20,20	102	2099	4064	NA	NA

Table D.1: Details of RVE meshes where particle size is uniformly distributed

ID	Length	Nodes No IEs	Elements No IEs	Nodes With IEs	Elements With IEs
0,v1,50	171	1035	1976	1402	2321
0,v2,10	85.5	225	408	306	477
0,v2,30	115	614	1166	828	1366
0,v2,40	133	811	1544	1100	1813
0,v2,50	147	966	1860	1310	2188
0,v2,90	204	1753	3388	2375	3980
0,v3,50	162	989	1884	1359	2230
1,v2,50	147	1450	2770	1940	3244
2,v2,50	147	3724	7230	4639	8129
3,v2,50	147	13018	25630	14780	27376
4,v2,50	147	48968	97148	52421	100585

Table D.2: Details of RVE meshes where particle size is normally distributed

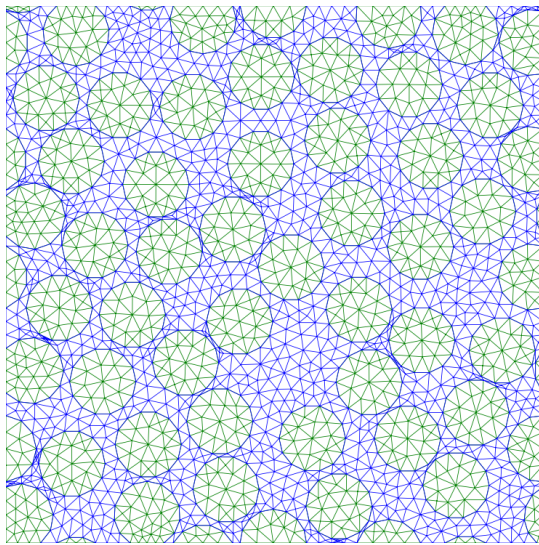


Figure D.1: ID: 0,10,50

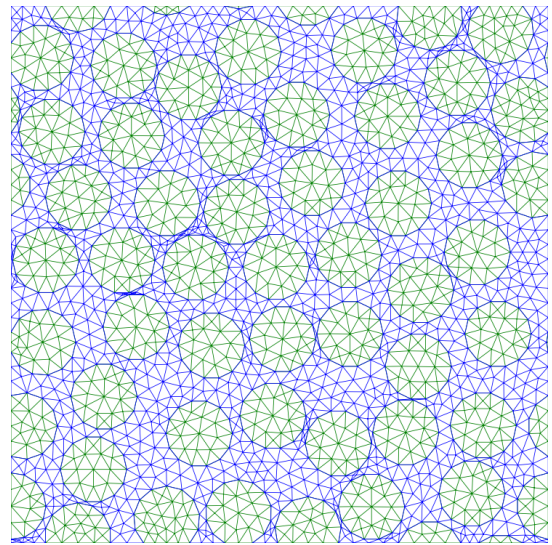


Figure D.2: ID: 0,20,50

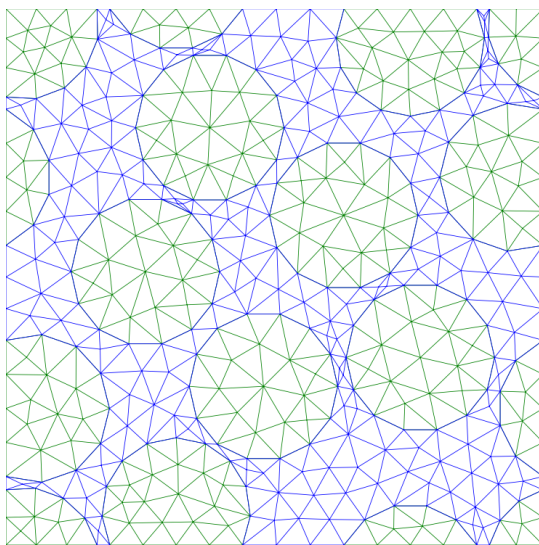


Figure D.3: ID: 0,30,10

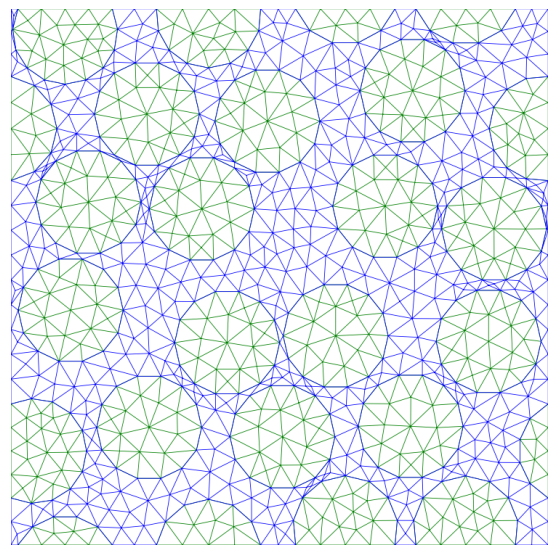


Figure D.4: ID: 0,30,20

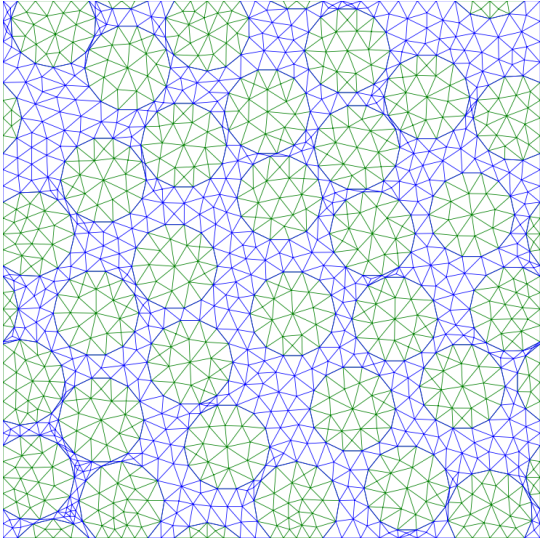


Figure D.5: ID: 0,30,30

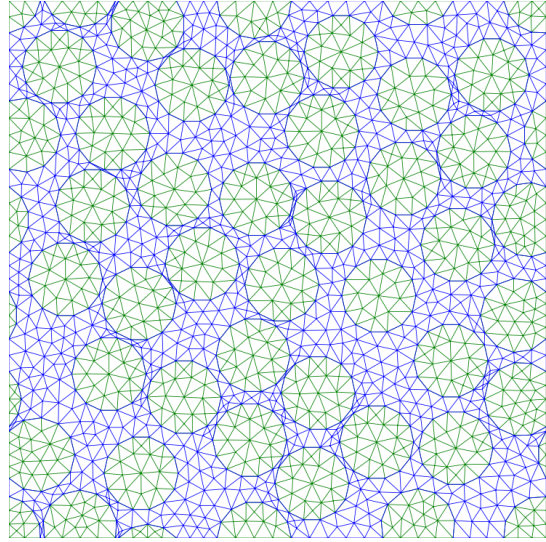


Figure D.6: ID: 0,30,40

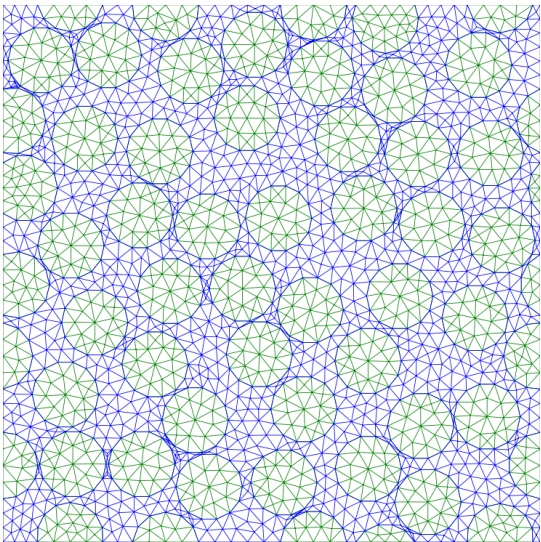


Figure D.7: ID: 0,30,50

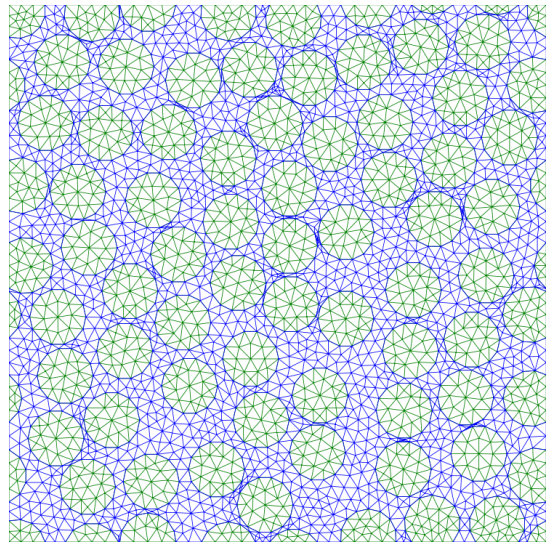


Figure D.8: ID: 0,30,70

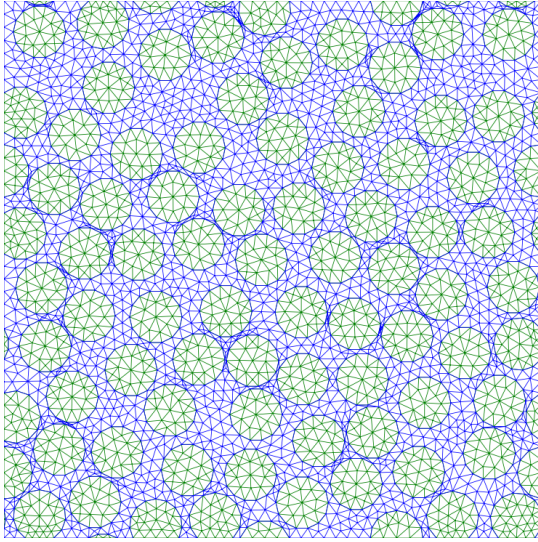


Figure D.9: ID: 0,30,80

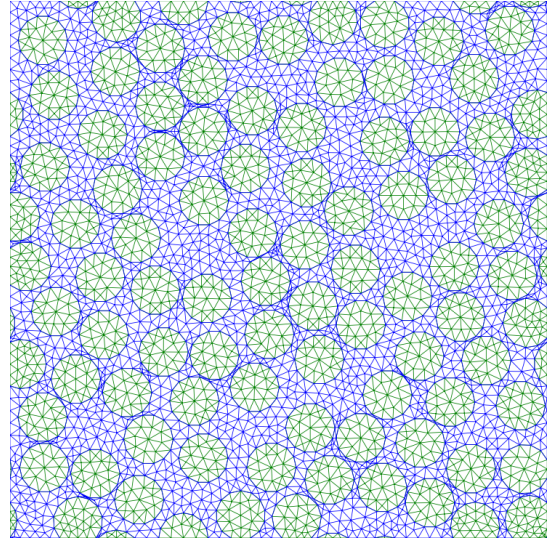


Figure D.10: ID: 0,30,90

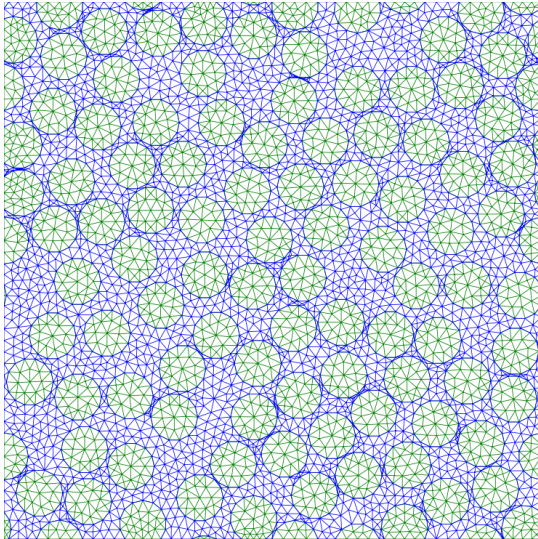


Figure D.11: ID: 0,30,100

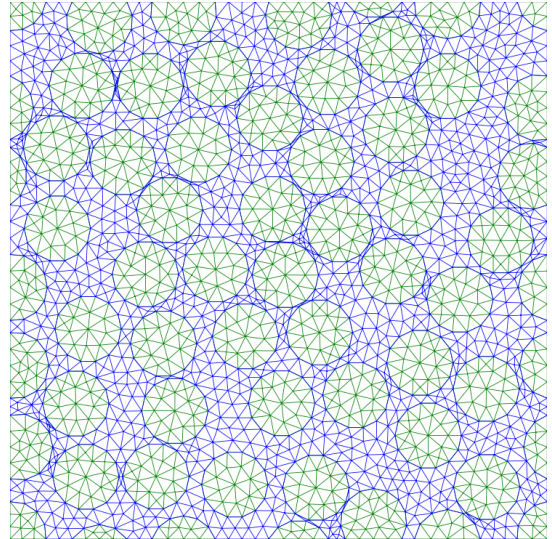


Figure D.12: ID: 0,40,50

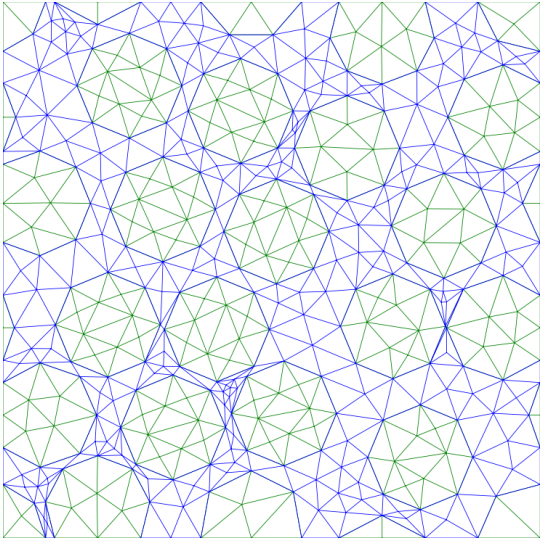


Figure D.13: ID: 0,20,20

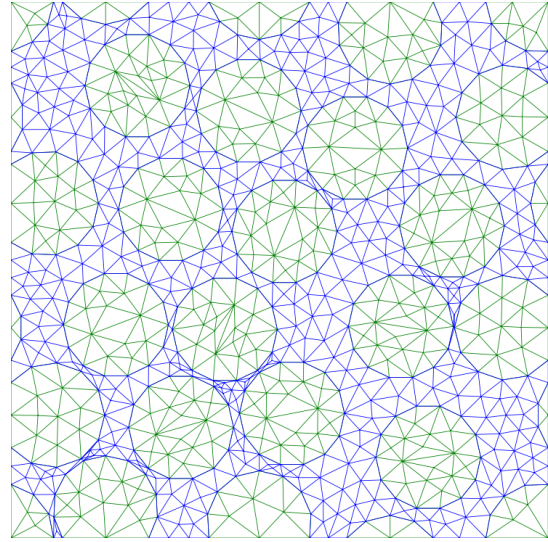


Figure D.14: ID: 1,20,20

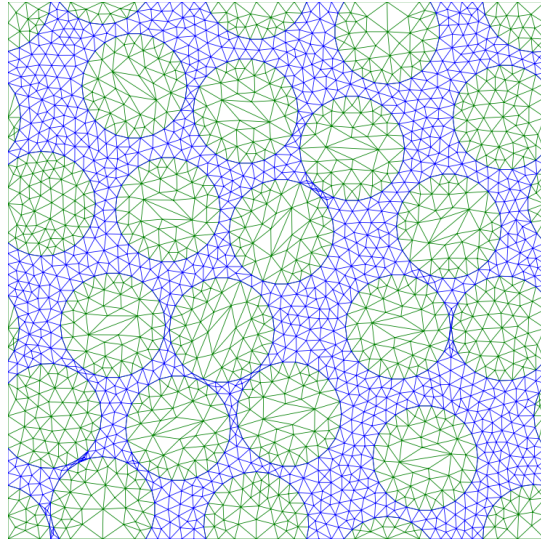


Figure D.15: ID: 2,20,20

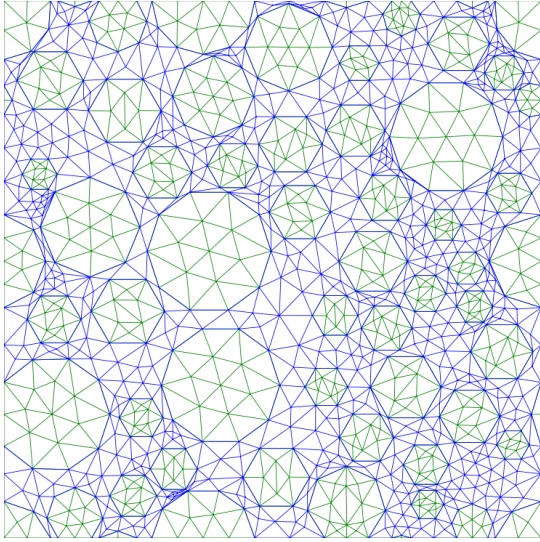


Figure D.16: ID: 0,v1,50

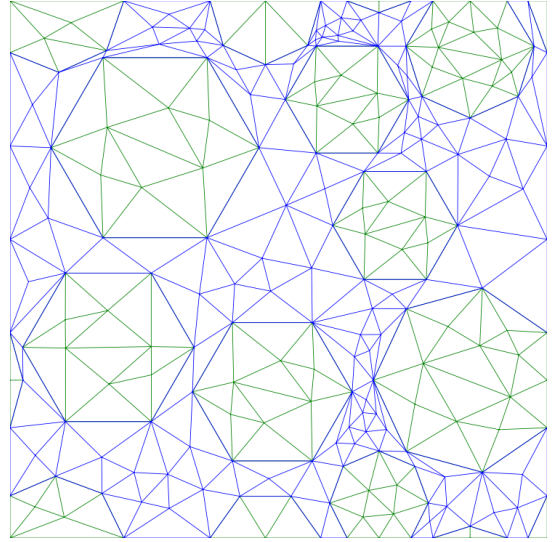


Figure D.17: ID: 0,v2,10

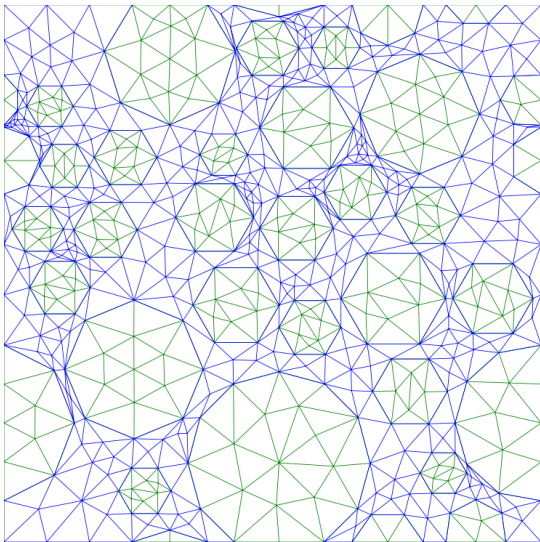


Figure D.18: ID: 0,v2,30

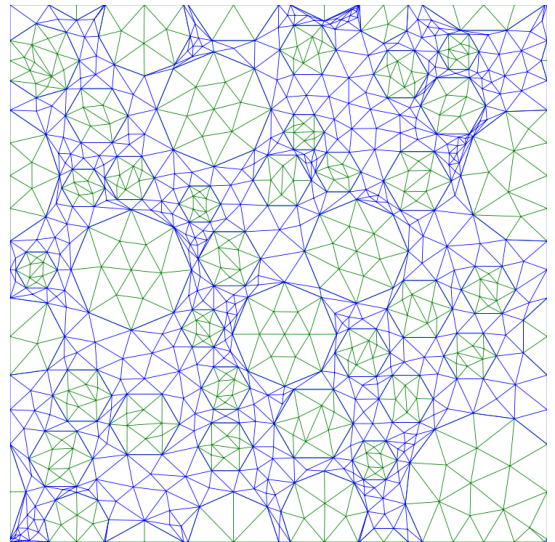


Figure D.19: ID: 0,v2,40

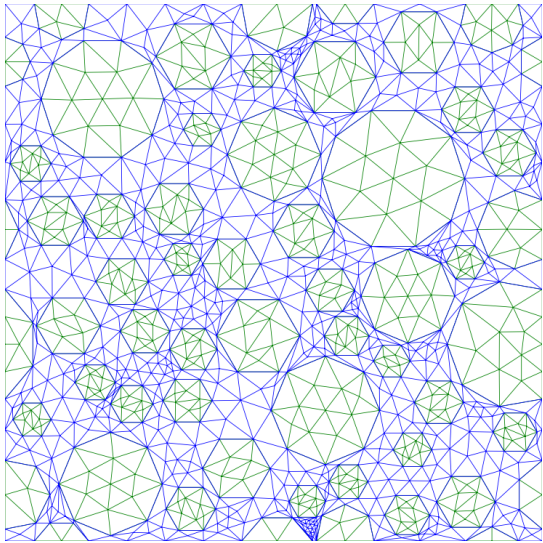


Figure D.20: ID: 0,v2,50

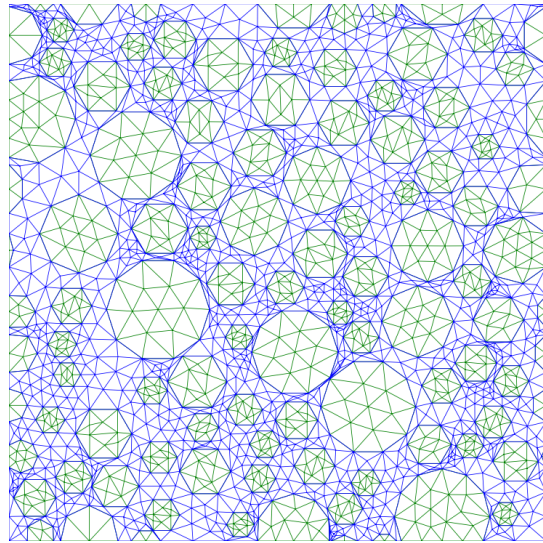


Figure D.21: ID: 0,v2,90

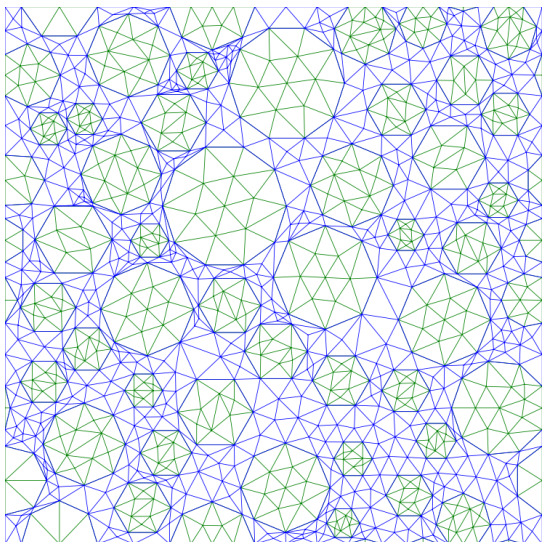


Figure D.22: ID: 0,v3,50

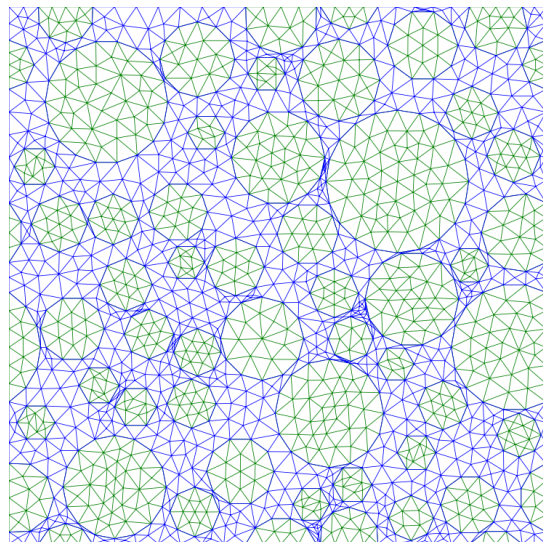


Figure D.23: ID: 1,v2,50

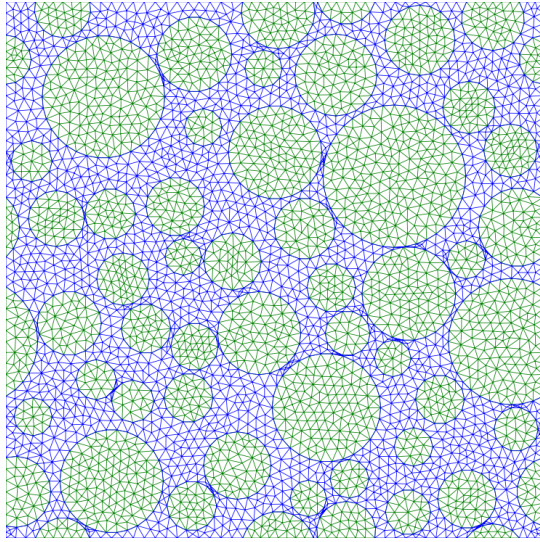


Figure D.24: ID: 2,v2,50

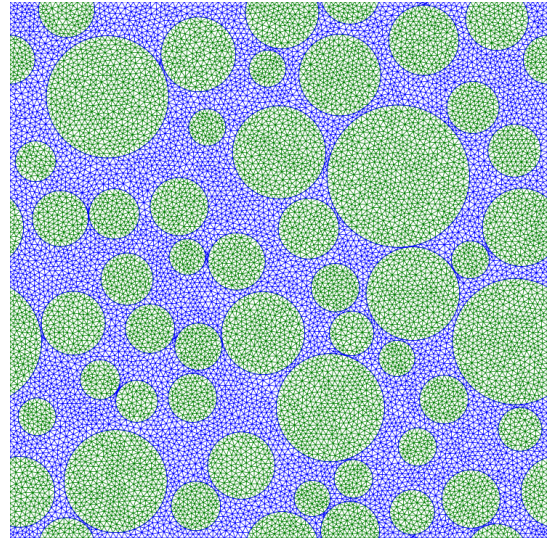


Figure D.25: ID: 3,v2,50

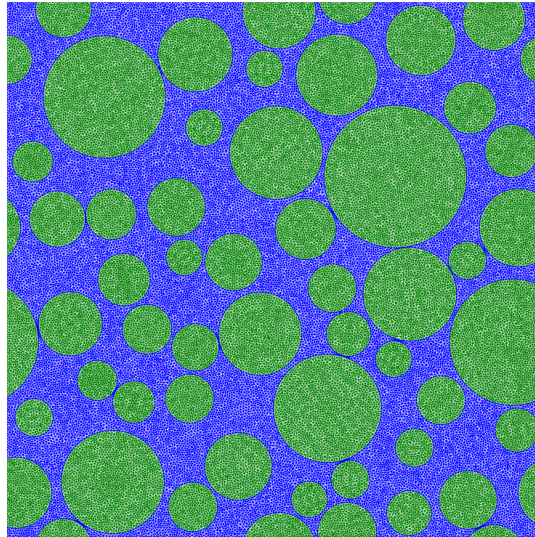


Figure D.26: ID: 4,v2,50

Bibliography

- [1] J D Achenbach, B Budiansky, H A Lauwerier, L V A N Wijngaarden, and J R Willis. *North-Holland Series in Applied Mathematics and Mechanics*, volume 6. 1969. ISBN 0444898816. doi: 10.1016/B978-0-7204-2356-3.50020-2.
- [2] Frank L. Addessio and James N. Johnson. A constitutive model for the dynamic response of brittle materials. *Journal of Applied Physics*, 67(7):3275–3286, 1990. ISSN 00218979. doi: 10.1063/1.346090.
- [3] Computational Approaches. *Computational and Experimental Methods in Structures — Vol. 3 MULTISCALE MODELING IN SOLID MECHANICS Computational Approaches*. 2010. ISBN 9781848163072.
- [4] A Barua and M Zhou. A Lagrangian framework for analyzing microstructural level response of polymer-bonded explosives. *Modelling and Simulation in Materials Science and Engineering*, pages 0–24, 2011. doi: 10.1088/0965-0393/19/5/055001.
- [5] E. Bouchbinder. *Non-Equilibrium Continuum Physics*. 2019.
- [6] Hal F. Brinson and L. Catherine Brinson. *Polymer engineering science and viscoelasticity: An introduction, Second edition*. 2015. ISBN 9781489974853. doi: 10.1007/978-1-4899-7485-3.
- [7] T. S. Chow. Stress–strain behavior of polymers in tension, compression, and shear. *Journal of Rheology*, 36(8):1707–1717, 1992. ISSN 0148-6055. doi: 10.1122/1.550281.
- [8] D. R. Curran, D. A. Shockey, and L. Seaman. Dynamic fracture criteria for a polycarbonate. *Journal of Applied Physics*, 44(9):4025–4038, 1973. ISSN 00218979. doi: 10.1063/1.1662891.
- [9] R. de Borst and L.J. Sluys. *Computational Methods in Non-Linear Solid Mechanics*. 2015.
- [10] R. de Borst, M. Crisfield, J. Remmers, and V. Verhoosel. *Non-linear Finite Element Analysis OF Solids and Structures*. 2 edition, 2012.
- [11] Frank Hild. Surface energy of plastics, Dec 2020. URL <https://www.tstar.com/blog/bid/33845/surface-energy-of-plastics>.
- [12] Sook-ying Ho. High Strain-Rate Constitutive Models Introduction. 18(5), 2002. doi: 10.2514/2.6041.
- [13] Ruize Hu, Chandra Prakash, Vikas Tomar, Michael Harr, and Ibrahim Emre. Experimentally-validated mesoscale modeling of the coupled mechanical – thermal response of AP – HTPB energetic material under dynamic loading. pages 277–298, 2017. doi: 10.1007/s10704-016-0141-7.
- [14] Robert J. Hudson, Peter Zioupos, and Philip P. Gill. Investigating the mechanical properties of RDX crystals using nano-indentation. *Propellants, Explosives, Pyrotechnics*, 37(2):191–197, 2012. ISSN 07213115. doi: 10.1002/prep.201100063.
- [15] Xu Jinsheng, Chen Xiong, Wang Hongli, Zheng Jian, and Zhou Changsheng. Thermo-damage-viscoelastic constitutive model of HTPB composite propellant. *International Journal of Solids and Structures*, 51(18):3209–3217, 2014. ISSN 0020-7683. doi: 10.1016/j.ijsolstr.2014.05.024. URL <http://dx.doi.org/10.1016/j.ijsolstr.2014.05.024>.
- [16] J. W. Ju and T. M. Chen. Micromechanics and effective moduli of elastic composites containing randomly dispersed ellipsoidal inhomogeneities. *Acta Mechanica*, 103(1-4):103–121, 1994. ISSN 00015970. doi: 10.1007/BF01180221.

- [17] J. W. Ju and T. M. Chen. Effective elastic moduli of two-phase composites containing randomly dispersed spherical inhomogeneities. *Acta Mechanica*, 103(1-4):123–144, 1994. ISSN 00015970. doi: 10.1007/BF01180222.
- [18] J.W. Ju and K.H. Tseng. A Three-Dimensional Statistical Micromechanical Theory for Brittle Solids with Interacting Microcracks. *International Journal of Damage Mechanics*, 1(1):102–131, 1992. ISSN 1056-7895. doi: 10.1177/105678959200100106.
- [19] Abraham Lasschuit. Tno 3d printed solid propellant summary. Summary of MSc thesis topic given by supervisor, 2019.
- [20] H K Lee and D K Shin. A computational investigation of crack evolution and interactions of microcracks and particles in particle-reinforced brittle composites. 64:419–431, 2004. doi: 10.1016/j.compstruct.2003.09.043.
- [21] H. K. Lee and S. Šimunović. Prediction of crack evolution and effective elastic behavior of damage-tolerant brittle composites. *Computer Methods in Applied Mechanics and Engineering*, 196(1-3): 118–133, 2006. ISSN 00457825. doi: 10.1016/j.cma.2006.02.008.
- [22] Wei-Guang Liu. *First-Principle Studies of the Initiation Mechanism of Energetic Materials. Dissertation*. PhD thesis, California Institute of Technology, 2014.
- [23] J Mergheim, E Kuhl, and P Steinmann. A hybrid discontinuous Galerkin / interface method for the computational modelling of failure. 519(814):511–519, 2004. doi: 10.1002/cnm.689.
- [24] Konstantinos Michalakis, Pasquale Calvani, and Hiroshi Hirayama. Biomechanical considerations on tooth-implant supported fixed partial dentures. *Journal of dental biomechanics*, 3: 1758736012462025, 08 2012. doi: 10.1177/1758736012462025.
- [25] A. Needleman. Some issues in cohesive surface modeling. *Procedia IUTAM*, 10:221–246, 2014. ISSN 22109838. doi: 10.1016/j.piutam.2014.01.020. URL <http://dx.doi.org/10.1016/j.piutam.2014.01.020>.
- [26] Vinh Phu Nguyen. *Multiscale failure modelling of quasi-brittle materials*. 2011. ISBN 9789461910110.
- [27] Vinh Phu Nguyen. An open source program to generate zero-thickness cohesive interface elements. *Advances in Engineering Software*, 74:27–39, 2014. ISSN 18735339. doi: 10.1016/j.advengsoft.2014.04.002. URL <http://dx.doi.org/10.1016/j.advengsoft.2014.04.002>.
- [28] R. H.J. Peerlings, R. De Borst, W. A.M. Brekelmans, and M. G.D. Geers. Localisation issues in local and nonlocal continuum approaches to fracture. *European Journal of Mechanics, A/Solids*, 21(2):175–189, 2002. ISSN 09977538. doi: 10.1016/S0997-7538(02)01211-1.
- [29] R. A. Schapery. Correspondence principles and a generalized J integral for large deformation and fracture analysis of viscoelastic media. *International Journal of Fracture*, 25(3):195–223, 1984. ISSN 03769429. doi: 10.1007/BF01140837.
- [30] A. Turon, P. P. Camanho, J. Costa, and C. G. Dávila. A damage model for the simulation of delamination in advanced composites under variable-mode loading. *Mechanics of Materials*, 38 (11):1072–1089, 2006. ISSN 01676636. doi: 10.1016/j.mechmat.2005.10.003.
- [31] O. Van Der Sluis, P. J.G. Schreurs, W. A.M. Brekelmans, and H. E.H. Meijer. Overall behaviour of heterogeneous elastoviscoplastic materials: Effect of microstructural modelling. *Mechanics of Materials*, 32(8):449–462, 2000. ISSN 01676636. doi: 10.1016/S0167-6636(00)00019-3.
- [32] Pieter van Mourik, Jaap van Dam, and Stephen Picken. *Materials Science in Design and Engineering*. 2012. ISBN 9789065623010. URL <http://www.vssd.nl/hlf/m017.htm>.

- [33] C V Verhoosel and M A Gutiérrez. Modelling inter- and transgranular fracture in piezoelectric polycrystals. *Engineering Fracture Mechanics*, 76(6):742–760, 2009. ISSN 0013-7944. doi: 10.1016/j.engfracmech.2008.07.004. URL <http://dx.doi.org/10.1016/j.engfracmech.2008.07.004>.
- [34] G.N. Wells. *The Finite Element Method: An Introduction*. 2009.
- [35] L Wu, D Tjahjanto, G Becker, A Makradi, A Jérusalem, and L Noels. A micro – meso-model of intra-laminar fracture in fiber-reinforced composites based on a discontinuous Galerkin / cohesive zone method. 104:162–183, 2013. doi: 10.1016/j.engfracmech.2013.03.018.
- [36] B. J. Yang, B. R. Kim, and H. K. Lee. Micromechanics-based viscoelastic damage model for particle-reinforced polymeric composites. *Acta Mechanica*, 223(6):1307–1321, 2012. ISSN 00015970. doi: 10.1007/s00707-012-0651-y.